

(1)

**The Photochemical Growth and Characterisation
of Thin SiO₂ Layers**

Vishal Nayar

A thesis submitted in fulfilment of the requirements for the degree of Ph.D
at University College London.

January 1991

ProQuest Number: 10609423

All rights reserved

INFORMATION TO ALL USERS

The quality of this reproduction is dependent upon the quality of the copy submitted.

In the unlikely event that the author did not send a complete manuscript and there are missing pages, these will be noted. Also, if material had to be removed, a note will indicate the deletion.



ProQuest 10609423

Published by ProQuest LLC (2017). Copyright of the Dissertation is held by the Author.

All rights reserved.

This work is protected against unauthorized copying under Title 17, United States Code
Microform Edition © ProQuest LLC.

ProQuest LLC.
789 East Eisenhower Parkway
P.O. Box 1346
Ann Arbor, MI 48106 – 1346

Abstract

This thesis reports a new method to grow thin silicon dioxide layers on silicon at low temperatures ($<550^{\circ}\text{C}$). Oxide growth was induced photochemically by ultraviolet (UV) excimer radiation, a near UV mercury-xenon lamp and a low pressure UV mercury lamp. The latter was found to be most successful and was used to generate ozone and excite the silicon surface electronically. Thin oxide layers of the dimensions required for future microelectronic devices were grown. The growth process and the materials and electronic properties of the oxides were also investigated by a variety of techniques. Oxide growth appeared to follow Cabrera-Mott type kinetics. The capacitance-voltage (C-V) and current-voltage response was measured for metal oxide semiconductor capacitors incorporating the oxide grown by the UV/ozone technique. High breakdown fields ($\approx 10\text{MV/cm}$) and typical C-V characteristics were observed. Infra-red spectroscopy, X-ray photoelectron spectroscopy and a new technique spectroscopic ellipsometry (SE) were used to assess the chemical and structural properties of the oxides grown. In almost all respects the low temperature oxides were found to be the same as conventional furnace grown (high temperature) layers. Previously thick ($>60\text{nm}$) silicon dioxide on silicon layers have been studied by SE. In the present work the technique has been applied to layers over the range 3-50nm. The accuracy and usefulness of the technique has been studied in detail to reveal hitherto unknown density changes in thin oxides grown at 900 and 1050°C . The capability of multi-angle SE to produce unambiguous results of improved accuracy was demonstrated for the thinnest layers in this investigation. It was found that oxide density increased as the thickness decreased for both oxidation temperatures. This suggests that single wavelength ellipsometry studies of oxide growth kinetics may be invalid because of the failure to take into account oxide density variations. The main contributions of this research are the development of low temperature UV/ozone oxidation of silicon surfaces and the application of SE and multi-angle SE to silicon dioxide/silicon structures. Both these techniques are applicable to silicon microelectronics as the oxide thickness diminishes due to increased miniaturisation and sophistication of integrated circuits.

Dedication

This thesis is dedicated to my dear parents (especially my mother who has had to cope with both my father's PhD. studies and now mine) for their support particularly during the struggle to write up.

Preface and Acknowledgements

This thesis addresses a field which has been investigated intensively for the last thirty years. Therefore the question arises what new is there left to be uncovered. Fortunately for myself and other research students many vital issues (some of which are discussed in the introductory chapter) are still unresolved. The importance of these issues lie in the "economic and technological" progress of the field of silicon microelectronics which provides the environment for research into the growth and properties of silicon dioxide layers on single crystal silicon (by growth, I mean the layer formed on reaction of an oxygen bearing ambient with the silicon surface rather than a film formed by deposition). With this background this thesis is technological in outlook and hopefully in result. The aim is that the information contained in this thesis will become useful in a technological sense. In addition to this the capability to grow oxides at low temperatures in relatively short periods allows the study of basic properties thin oxides which are not thermally relaxed.

The original "brief" for this project was to study ultraviolet (UV) enhanced oxidation and rapid thermal oxides/oxynitrides grown both at the Royal Signals and Radar Establishment (RSRE) and University College London (UCL). Typical of so much university research funding and facilities dominated the project totally. On arriving at UCL I started with an optical bench and an arc lamp (described below). Unfortunately the arc lamp was not functioning. During the run up period of the lamp I designed a small vacuum chamber which was used for the preliminary experiments (chapter one) carried out in the first year and a half. The excimer laser oxidation work was carried out at the Rutherford Appleton Laboratory for which I am indebted to R. Lawes, Francis Goodall and Graham Arthur. Both the arc lamp and excimer laser results eliminated these processes as viable oxidation technologies. Some interesting work on excimer patterned oxides, not included below, was however published (appendix G). Attempts to use the arc lamp in rapid thermal mode proved too unreliable due to the lack of in-situ temperature measurement. I must admit this period

appeared rather unproductive. Starting without much equipment and also lacking funds for apparatus combined to thwart some of the original aims.

However, the germs of the work during the final period of study were seeded. I was lucky enough to undertake a study of thin oxides using spectroscopic ellipsometry (chapter 3) at RSRE. Also as a final attempt at low temperature oxidation I pushed the idea of the UV/ozone oxidation in my transfer thesis. The idea of designing, manufacturing/obtaining components as well as commissioning and finally carrying out experiments all within one year was rather daunting. Chapters 2, 3 and 4 discuss the UV/ozone growth, ellipsometric and electrical characterisation work, respectively, carried out in the final hectic year. The growth kit became fully functional during the summer of 1989. As time passed the system performance was improved markedly but as with all research considerable time was lost due to equipment failures. These being the loss of cooling water and the failure of the clean room pure water supply. It should be added that the growth kit was installed in a typical dusty laboratory in London on the sixth floor of the engineering building. Hence given the physical environment it is all the more surprising that oxides so similar to those produced by the traditional thermal process were grown.

The "success" of the project (which is my biased opinion) was based upon the aid of a large group of people at UCL and RSRE. My gratitude goes to the SERC and RSRE for funding my studentship and to SERC and the Nuffield foundation for research grants to Dr. Ian W. Boyd. The sterling work of the Electronic Engineering workshop in producing solid objects from my designs and drawings will always leave me in their debt. On occasion their good humour raised my spirits. I can trace the origins of the equipment used in the UV/ozone experiments to many sources. For the main vacuum chamber my thanks to Dr. R. Newell (Dept. of Physics, UCL). The substrate heater and backing pump were borrowed from C. Glasse of Philips in Redhill, Surrey. The largest flanges for the system were borrowed from RSRE. I would also like to thank Parthiv Patel and Ian for

allowing me to hijack various vacuum fittings and the turbo pump which were bought for another experimental system. During the final year I had the pleasure of working with Parthiv and am grateful to him for helping me put together the UV/ozone system. Also my thanks to Prof. M. Green for access to the single wavelength ellipsometer at Imperial College without which collecting the growth data would have been impossible.

I am particularly grateful to Dr. C. Pickering for allowing me almost unlimited access to the spectroscopic ellipsometer at RSRE and his excellent guidance. The work done in this area was not envisaged at the outset but I believe has proved to be fruitful. The large number of oxides used in this study were grown at RSRE in the SPEL cleanroom and silicon wafers were also provided for the UV/ozone work. Most of the electrical characterisation was done at RSRE with the support and direction of Dr. M. J. Uren. I would also like to thank Dr. D. C. Rodway (RSRE) for the X-ray photoelectron spectroscopic analysis and Dr. R. Smith (RSRE) for access to the infrared spectrometer. The analysis of oxide growth data was carried out after some correspondence with Prof. A. M. Stoneham (Harwell Laboratories) whose suggestions proved to be very valuable in attempting to understand the growth mechanisms discussed in chapter 2.

Of the many people I have met and worked with I was lucky enough to gain a good friend and colleague in Dr. Francesca Micheli. We had many discussions and arguments about oxide growth. The voluminous literature on the subject would have been impossible to cover alone. The shared experience has provided me with many memorable and humorous incidents. Her diligence during her studies set a very good example.

Finally I would like to recognise Dr. Ian W. Boyd and Dr. Alison M. Hodge for their support throughout the project, the stipend from Ian and Alison's support for work at RSRE after the official studentship period was completed was very helpful. The present time is not an easy one for scientists and engineers working in British institutions. The time they have given me makes it all the more valuable.

Contents

	Page No.
Title	1
Abstract	2
Preface and Acknowledgements	4
Contents	7
Chapter 1, Introduction and Preliminary Experiments	
1.1 Introduction	10
1.2 Conventional oxide growth technology and its side effects	14
1.3 Reduced thermal budget oxidation techniques	20
.3.1 Co-oxidation species	20
.3.2 Rapid thermal oxidation	21
.3.3 High pressure oxidation	24
.3.4 Plasma anodisation	24
.3.5 Electron and ion stimulation	26
.3.6 Catalytic and acidic oxidation	26
.3.7 Photochemical oxidation	27
1.4 Near UV and excimer laser oxidation of silicon	29
.4.1 Near UV oxidation	31
.4.2 Excimer laser oxidation	37
1.5 Summary	42
Chapter 2, Low Temperature UV/Ozone Oxidation Experiments	
2.1 Introduction	44
2.2 UV/ozone oxidation system	48
2.3 Growth experiments	56
.3.1 Period 1 experiments	56
.3.2 Period 2 experiments	58
.3.3 Period 3 experiments	65
2.4 Analysis and identification of oxide growth mechanism	67
.4.1 Gas phase UV/ozone analysis	67

.4.2 Oxide growth mechanism	72
.4.3 Analysis of growth data	80
2.5 Summary	90
Chapter 3, Materials Characterisation of Thin Oxide Films	
3.1 Spectroscopic ellipsometric analysis	91
.1.1 Introduction	91
.1.2 Basic Ellipsometric Theory	94
.1.3 The sensitivity correlation analysis of Bu-Abbud et al.	97
.1.4 Ellipsometric data collection	108
.1.5 Single angle spectroscopic ellipsometry	110
.1.6 Multi-angle SE	122
3.2 Infrared Absorption Spectroscopy	124
3.2.1 Introduction	124
.2.2 Experimental	126
.2.3 Results	127
3.3 X-ray photoelectron spectroscopy	134
3.4 Discussion and Summary	137
Chapter 4, Electrical Analysis of UV/ozone Oxides	
4.1 Introduction	139
4.2 High frequency capacitance voltage characterisation	141
.2.1 Capacitor fabrication	141
.2.2 HFCV analysis	142
.2.3 Errors in extraction of parameters from HFCV	145
4.3 Thermal bias stressing behaviour	147
4.4 Current voltage characteristics	148
4.5 Summary	153
Chapter 5, Conclusions	155

Appendices

A Lifetime of atomic oxygen	162
B Stabilisation of lamp emission	162
C Bruggeman effective medium approximation	163
D Note added in proof to corroborate multi-angle SE results	164
E Electronic data relating to the Si/SiO ₂ Interface	165
F References	166
G Publications	175

Chapter 1

Introduction and Preliminary Experiments

1.1 Introduction

The oxidation of crystalline silicon is one of the most important processes in the fabrication of Si based integrated circuits (IC). The physical, chemical and electrical nature of Si/SiO₂ structures have been studied intensively for the last 30 years. Si ICs have become common place. Communications, computation, automation, the financial world and modern sciences are all heavily dependent upon IC technology. The world wide investment in IC technology is in the billions of pounds per annum. This investment has proved to be very profitable for society as a whole and the scientific understanding of various solid-state physical phenomena (Pepper, 1983). The basic building block of Si ICs is the metal oxide semiconductor field effect transistor (MOSFET), Fig.1.1. The behaviour of this device is strongly dependent upon the properties of the Si/SiO₂ interface. In particular the thermally grown (typically at 1000°C) oxide interface is favoured because of its relatively high perfection and ideal behaviour. A bare Si surface has approximately 10¹⁵cm⁻² surface states. Upon oxidation the number of states remaining at the Si/SiO₂ interface can fall below 10¹⁰cm⁻² (see the studies by Eastman and Grobman, 1972, Wagner and Spicer, 1972 and 1974 and Rowe and Ibach, 1974). However, as yet a full understanding of the mechanisms of the oxide formation and the many factors affecting the resulting interface does not exist. The large number of

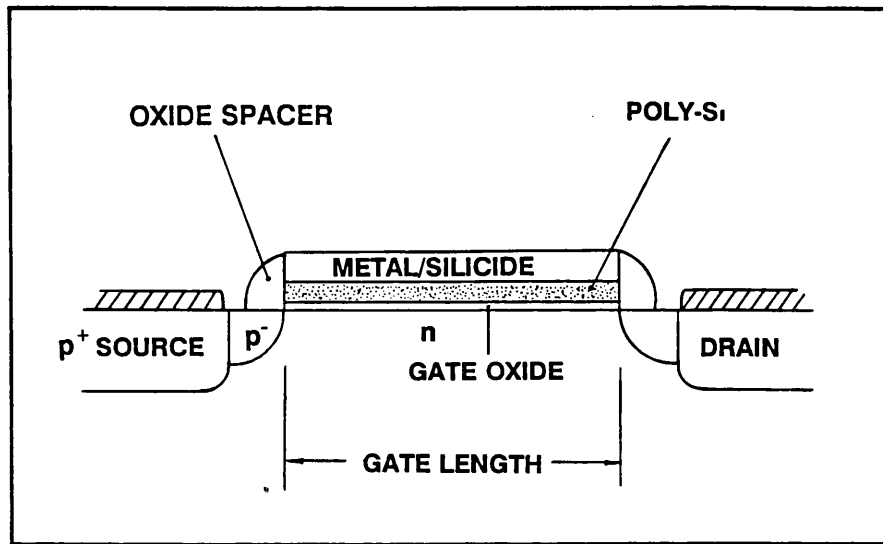


Fig.1.1 Cross-sectional structure of low doped drain/source MOSFET.

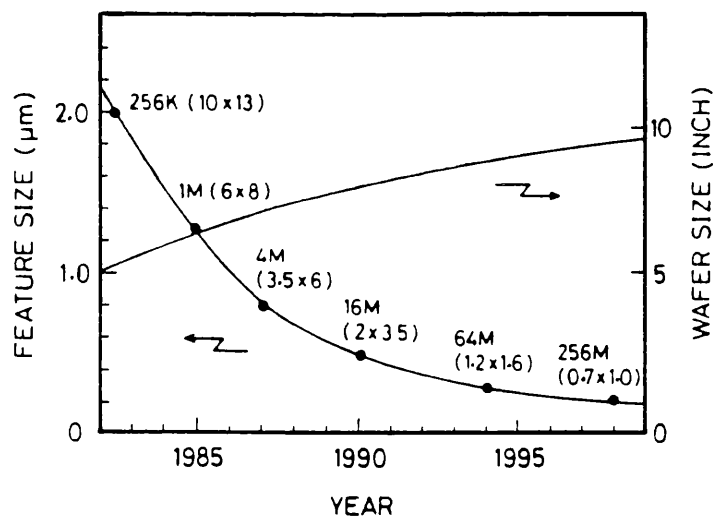


Fig.1.2 Future trend curve of experimental demonstration of the level of integration for dynamic random access memories (Hirose 1988). The numbers in brackets are the cell areas in μm^2 .

publications and conferences in the field provide evidence for this.

The demand for ICs with improved performance has produced one dominating trend. This is principally the increasing miniaturisation of electronic components and increased complexity of ICs. A critical dimension defined as the minimum feature size, i.e. the gate length (see Fig.1.1), is often used to indicate the level of integration. The historical trend of this parameter has been plotted by Hirose in 1988, Fig.1.2. He envisaged a 256Mbyte demonstration dynamic random access memory chip by the end of the century, based on $0.2\mu\text{m}$ minimum feature size. Presently $1\mu\text{m}$ devices are used routinely. The gate oxide thickness is typically in the region of 20nm for this gate width. For $0.5\mu\text{m}$ and $0.25\mu\text{m}$ the gate oxide thickness is expected to fall to 12nm and 7nm respectively. Fair and Ruggeles (1990) have also calculated that the oxide uniformity must be within $\pm 1\%$ of its nominal value. Presently, the very high quality of SiO_2 grown can only be achieved in an artificial environment with strict control of the exposure of wafers to impurities and contaminants. As the oxide thickness diminishes these effects become even more important (for example the first symposium on cleaning technology in semiconductor device manufacturing was held only recently, in the autumn of 1989, editors Ruzzylo and Novak) and can dominate device performance. To reach the projected levels of integration many problems must be solved, including the development of a suitable oxide growth technology which is discussed in the following chapters. However, the ultimate limit of miniaturisation is not known. Sai-Halasz et al. (1986) of IBM have demonstrated an experimental technology for $0.1\mu\text{m}$ gate length devices using a 4.5nm oxide (although 2.5nm would be more consistent for this gate length).

In line with the necessary development of fabrication technologies it is also vital that accurate techniques to quantify the processed layers and structures exist. The smallest dimension on any IC is the gate oxide thickness. Precise measurement of thickness is important because MOSFET characteristics are highly dependent on this parameter; especially the threshold voltage. The conventional method used is single wavelength

ellipsometry (SWE) at 633nm. Oxide thickness can be calculated only by assuming a refractive index for films thinner than ≈ 40 nm. It is well known oxide refractive index varies with growth conditions (Landsberger and Tiller, 1987). Hence the actual oxide thickness can be erroneous if the wrong refractive index is used. In the very thin oxide regime the accuracy with which thickness is calculated falls when using SWE. Another complication also affects thickness measurements. Evidence from infrared (Fitch and Lucovsky, 1989), radio-tracer (Rochet et al., 1986), X-ray photoelectron spectroscopy (Halbritter, 1988, Hattori et al., 1989, Grunthaner and Grunthaner, 1986), cross-sectional transmission electron microscopy (Ourmadz et al. 1987) and X-ray scattering (Fuoss et al., 1988) studies suggests that as the oxide grows its physical nature changes. For the very thin oxides noted above, the uncertainty of layer dimensions could easily invalidate operational model calculations of devices.

The aims of the investigations reported in this thesis are to address the issues of controllable oxide growth on Si at low temperatures; to thicknesses which are appropriate for future generations of ICs and to investigate both conventional and low temperature oxides. Measurements by spectroscopic ellipsometry as opposed to SWE are used to take into account oxide density changes in thermal oxides to improve the accuracy of oxide thickness results. The following discussion can broadly be divided into two parts. The remaining part of this chapter will look at conventional furnace growth technology and review the reduced thermal budget oxidation processes reported in the scientific literature. Additionally, preliminary experiments on the oxidation of silicon with near ultra-violet (UV) light and excimer laser radiation are described. Chapter 2 deals with UV/ozone growth experiments. Chapters 3 and 4 describe materials and electronic properties of the oxides grown. The final chapter is used to note any significant implications arising from the study and also future directions for investigation.

1.2 Conventional Oxide Growth Technology and Its Side Effects

Device quality gate oxides are presently grown in high temperature furnaces, typically, at around 1000°C in a highly purified oxygen ambient. The main advantage of the furnace oxidation has been reliable and uniform oxide growth with a large number of wafers processed simultaneously. High temperature oxidation and annealing in such furnaces produces well relaxed oxides and sharp interfaces.

Typically an oxidation furnace consists of a quartz walled tube which is resistively heated. Reaction gases are flushed in using flow controllers from one end. The wafers to be oxidised are inserted from the other end as shown in Fig.1.3. Such oxidation furnaces are large, energy intensive, high temperature and not always sealed to the atmosphere. The main difficulties associated with furnace growth are due to these intrinsic features and the oxide formation rate at high temperatures. As noted above the very thin oxides required for future generations of ICs are only a few tens of atomic layers thick. It is thus more important to control the oxide composition and uniformity to a greater degree and also reduce the defect density ($<0.5/\text{cm}^2$). The detrimental side effects of furnace and high thermal budget oxidation are:

- a) furnaces are hot wall and thus they are prone to rapid diffusion of impurities especially the light alkali metals and hydrogen generated from moisture. These species are then incorporated into the oxide and degrade its stability. The diffusion of impurities can be reduced by using double wall furnace tubes. In these the outer tube is flushed with nitrogen mixed with a small percentage of HCl.
- b) Ambient air infiltration (Philipossian et al., 1989) into the furnace can also occur and is known to be detrimental to the oxide leading to variations in the total oxide charge and thickness non-uniformity.

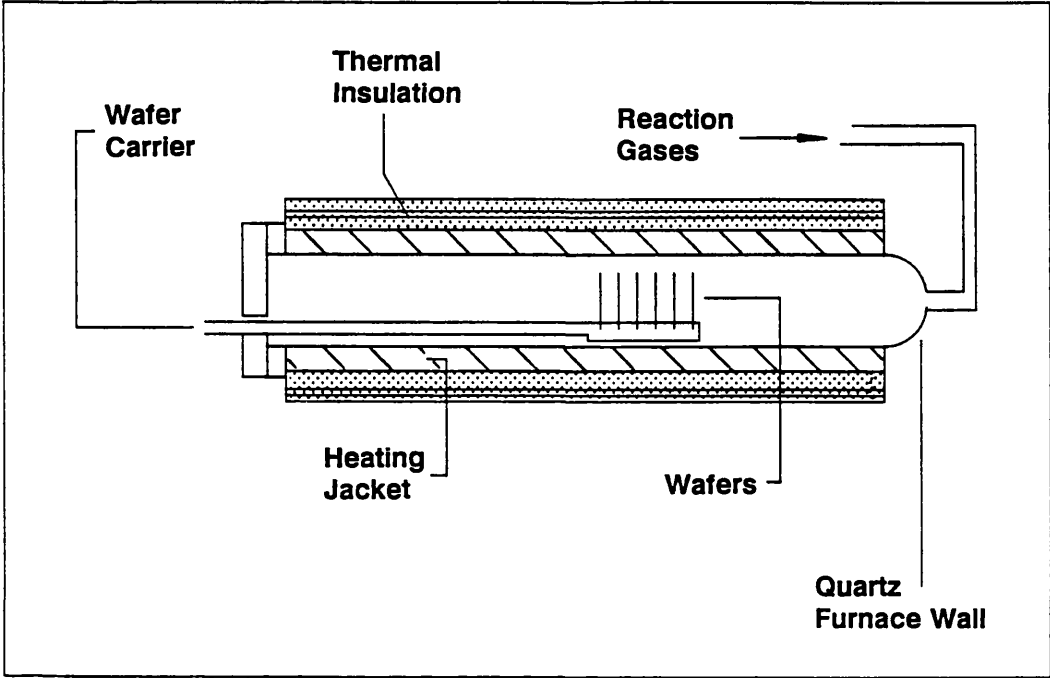


Fig.1.3 Typical Quartz hot wall oxidation furnace.

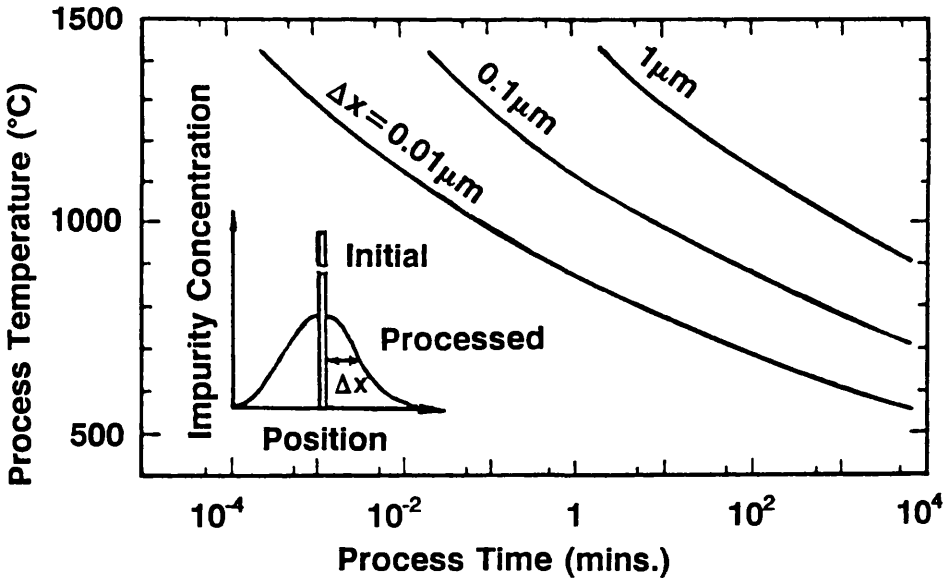


Fig.1.4 Broadening of impurity profiles in crystalline Si by thermal processing (Hirose 1988).

c) The high temperatures typical of thermal oxidation and annealing can also lead to roughening of the Si surface and pitting (Hahn et al., 1988, 1989 and Reisman et al., 1988, 1990). For Czochralski grown Si wafers the incorporated oxygen can form oxidation induced stacking faults, which are also believed to influence oxide breakdown properties (Rubloff et al., 1987 and Shirai et al., 1989).

d) The industry standard wafer size is increasing for economic reasons and is now typically 5 or 6 inches in diameter. Thermal stresses can be induced if heating or cooling is not uniform across the wafer. This can lead to wafer warpage and slip lines. Wafer distortions affect alignment in the lithographic processes while slip lines can also reduce carrier lifetimes and stop devices functioning.

e) Recently much interest has focussed on the effect of metallic impurities other than the alkali metals and their behaviour during oxidation. Ohsawa et al. (1990) and Hiramoto et al. (1989) have shown that gate oxide integrity is compromised by the presence of Ni, Cr, Cu and Fe. Heyns et al., (1990) have suggested that metallic contamination can lead to Si surface roughness which again impacts the oxide properties. At high temperatures these heavy metals become mobile and are able to diffuse throughout the Si/SiO₂ structure where they can reduce carrier lifetimes, breakdown fields, resistance to stressing and cause oxide thinning.

Most of the adverse affects of high temperature processes noted above can be avoided by careful processing and contamination control and are therefore classified as extrinsic. However, there are intrinsic side effects which are due to the large thermal budgets involved in furnace processing. Quite often oxide growth follows the formation of doped regions for source and drain by implantation. The dopant species redistribute during any exposure to high temperatures, Fig.1.4 (Hirose, 1988), and so as gate length falls the thermal budget must do so also to avoid dopant redistribution. The situation is often made worse because implant damage assists diffusion. A conventional thermal oxidation recipe is shown in Fig.1.5.

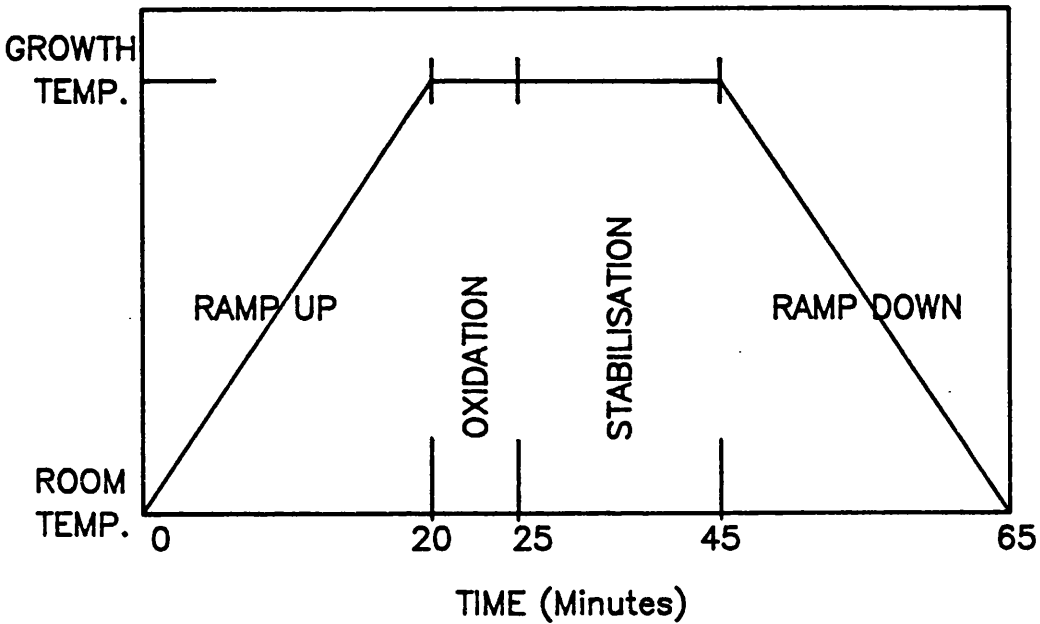


Fig.1.5 Conventional thermal furnace oxidation recipe.

A long ramp in period is required to avoid thermal stresses and allow the wafers and carrier to reach the growth temperature. The oxidation period is short for temperatures commonly used to grow gate oxides. Table I shows the time to grow 5nm and 10nm at 800°C, 900°C and 1000°C.

Growth Temperature (°C)	Growth Time (mins)	
	50Å	100Å
1000	≈ 2	≈ 4
900	≈ 7	≈ 22
800	≈ 60	≈ 140

Table I Oxide growth times for high temperatures.

The difficulty remains that to obtain good oxides high temperatures are necessary; while to control the growth process long times are desired. A simple method to achieve both is to reduce the partial pressure of O₂ by dilution with Ar. Unfortunately such treatments can cause interfacial roughness (Carim and Sinclair, 1987) which degrades oxide performance. Following oxidation a period of annealing in an inert ambient (N₂ or Ar) is used to stabilise the oxide interface before the wafer ramp out. It is clear from this that the total period during which the wafers are at high temperature is long in comparison to the growth time necessary to form the very thin oxides of interest. Uncontrolled oxide growth can also be incurred during the temperature ramps. Looking at **Fig.1.4** a reduction in temperature allows the process time to be increased. A reduction to 500°C means that the thermal budget for the oxidation process is small even for a 0.1µm gate width. Quite clearly processing at 500°C would be distinctly beneficial with respect to dopant redistribution.

Purely thermal oxidation at low temperature has been investigated but the formation rate is very slow (Taft 1984), once the temperature is reduced to 800°C and lower, **Fig.1.6**. Electronic properties of low temperature thermal oxides have also been poorer. Hence, there have been many attempts to develop alternative/enhanced oxide growth and deposition methods which are capable of producing layers of high electronic quality at low temperatures. It is important to note that the success of any low temperature method must be gauged by the comparison with oxides grown thermally at high temperatures. These are discussed in the next section.

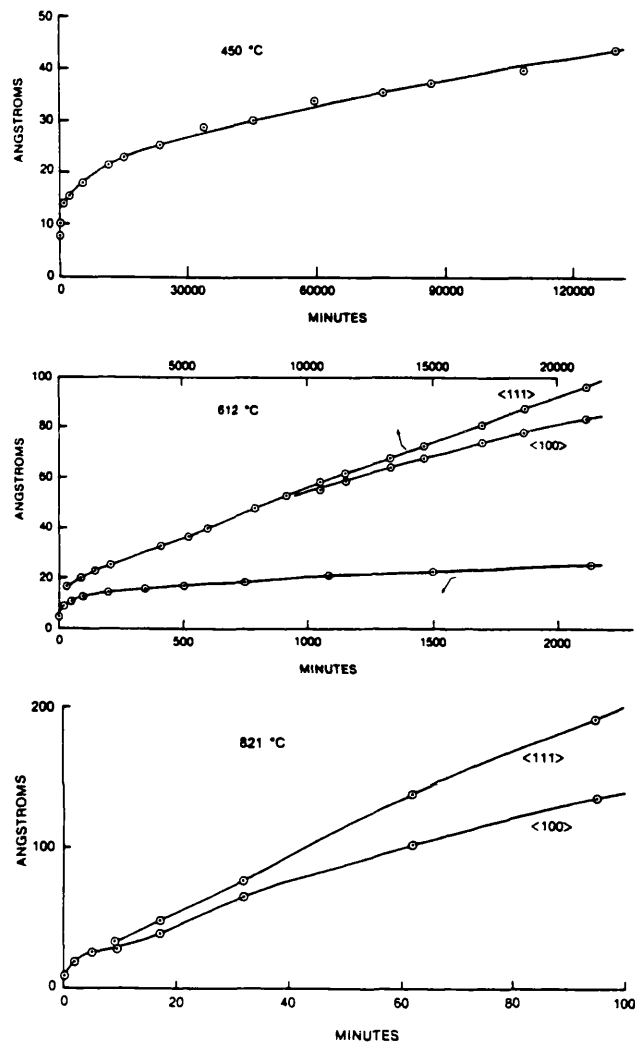


Fig.1.6 Thermal oxide growth on Si in dry oxygen at reduced temperatures (after Taft, 1984).

1.3 Reduced Thermal Budget Oxidation Techniques

The alternatives to high temperature thermal oxidation fall into several categories and are indicative of the many different approaches taken by researchers to overcome the problem.

1.3.1 Co-oxidation Species Enhancement

Firstly, there are the processes which are simply developments of atmospheric pressure furnace oxidation. In this group a hydrogen or halogen bearing species is added in small concentrations to the O₂. These methods in general operate at growth temperatures >800°C. The most commonly used species is H₂O. Oxidation in pyrogenic steam is well characterised, Deal and Grove (1965). The addition of even small concentrations, 10s of parts per million (ppm), can change the growth rate substantially as was shown by Irene and Ghez in 1977. While successfully improving the growth rate this method increases the presence of -OH bonds in the oxide and Si-H bonds at the interface, thus leaving it less resistant to electronic stressing than dry oxides.

The next most commonly used species is HCl (Hashimoto et al. and references therein, 1980) typically in concentrations of a few percent. The interest in HCl originated because of its use to getter metallic impurities from the gas phase and the oxide by the reaction of Cl to form volatile species. HCl was found to be less effective both as a getter and oxidation enhancer once the temperature was reduced to 800°C. Other methods to introduce Cl into the reaction ambient are Cl₂ or trichloroethane. However, it has been noted that by Hahn et al. (1988) that interfacial roughness is greater with Cl than for oxides formed using pure O₂ and they have also correlated bad electrical properties with increased roughness. It was also found that thin oxides grown in HCl appeared grainy and the Cl could in fact etch the Si through pin holes in the oxide.

Wei et al. (1988) found that the oxidation rate could be enhanced by an order of magnitude on the addition of HF in concentrations of ≈2000 ppm to the gas ambient. They also suggested that improved oxide properties were obtained in comparison to those grown at the same temperature in pure O₂.

However, a two step oxidation (initially with the mixed gas followed with pure O₂) was necessary to optimise the oxide properties and limit Si etching as was suggested by Hashimoto et al. for HCl. There is however a severe difficulty with using HF due to its well known reaction with SiO₂ in the presence of any traces of moisture. Miki et al. (1990) have shown that only surface adsorbed moisture is necessary to initiate the etching reaction. HF solutions are commonly used to etch SiO₂ in the semiconductor industry. Thus HF could attack the silica furnace walls and wafer boat releasing contaminants.

Another co-oxidation species which has been investigated is NF₃. Morita et al. (1984 and 1985) identified a large enhancement (nearly an order of magnitude given sufficient NF₃) in the growth rate for temperatures ranging between 600°C and 800°C. To enhance the oxidation rate, they found that higher concentrations of NF₃ were required as the substrate temperature was reduced. Increasing the concentration of NF₃ improved the growth rate until a critical value was reached when the etching effects of the fluorine (in the form of radicals) limited the oxide thickness. Fluorine atoms were incorporated into the oxide and believed not to degrade oxide properties drastically for the 800°C growths. However, a further anneal in oxygen was used to improve the breakdown field statistics and reduce the interface state density. For the 600°C oxides it was noted that the etch rate was much faster than that for layers grown in O₂. The oxide was thought to be of low density and thus less resistant. This is likely to affect the breakdown properties of the as grown oxide although these were not reported. Imai and Yamabe (1990) noted that an advantage of this gas mixture was that at 800°C the oxidation process effectively rounds corners and edges on Si surfaces. This is particularly important for oxidation of trench and hole structures, as envisaged for dynamic random access memory cells. The effect of fluorine addition on oxidation has been studied in more detail by Kim et al. (1990).

1.3.2 Rapid Thermal Oxidation

Another technique which also employs high temperatures is rapid

thermal oxidation (RTO). RTO has been studied for approximately 7 years and commercial machines capable of oxidising wafers up to 6" diameter are available. The thermal budget is reduced by raising the wafer temperature rapidly by radiant heating. An RTO process chamber is shown in Fig.1.7 (after Nulman, 1988). Only a single wafer is processed at one time. The wafer is held in thermal isolation on quartz pins and banks of lamps are used to heat it. High temperature ramp rates up to 100s of °C/s are common. This in effect removes the long ramp in times used in furnaces. After oxidation the wafer cools by radiation of heat and convection losses, again in a very short period of time. The rate of cooling can be controlled by keeping the lamps active at low power levels. By this technique the overall time that the wafer is "hot" is significantly lowered. Three recent reviews of the subject by Singh, Moslehi and Nulman all published in 1988 discuss RTO thoroughly. The types of gas mixtures discussed above have also been used in RTO although only the effect of HCl is well characterised. Fukada et al. (1990) have shown that very high quality thin (5nm) oxides can be grown in dry O₂.

A further development of RTO has been the growth of oxynitrides or reoxidised nitrides. In this case an oxide is grown followed by an anneal in NH₃ to form a nitrated layer. The advantage of the nitrated layer is the improved resistance to hot electron and radiation damage and as a barrier to impurity diffusion. It is often observed that the nitrogen atoms build up at the interfaces and increase the electrical leakage and oxide charge of the layer. To reduce these while still retaining the resistance to high fields the layer is reoxidised in oxygen. All these steps are carried out sequentially in a rapid thermal processor. The final product should then be a dielectric with the interfacial properties of an oxide but the bulk properties of an oxynitride. Such layers have been successfully grown and demonstrated in devices by Lo et al. (1990). The main difficulty with this procedure is that the NH₃ must be ultra-dry and the level of nitridation should not induce a high density of oxide charges.

A very recent development in the method of nitridation is the

substitution of N_2O for NH_3 . This appears to be a favourable process in that the presence of H is drastically reduced in the growth ambient. However the use of N_2O needs to be investigated further.

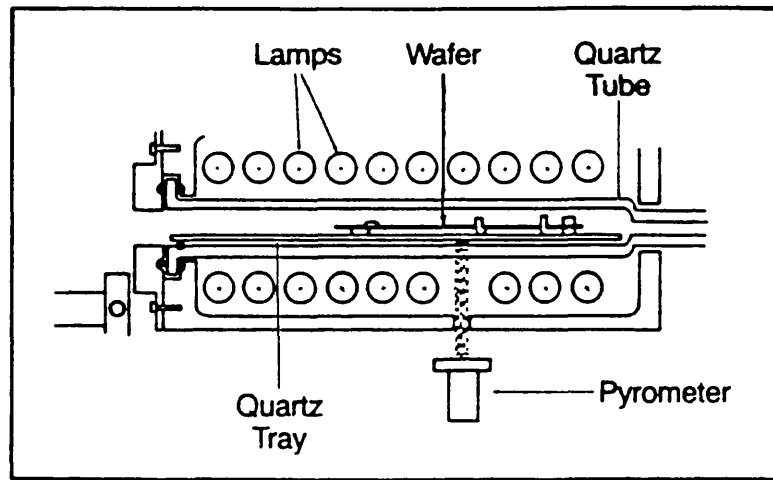


Fig.1.7 Schematic cross-section of tungsten filament lamp heated chamber (after Nulman, 1988).

RTO is a promising technology but still suffers from some draw backs specifically associated with rapid thermal processing (RTP) and of course processing temperatures are very high. The limitations of RTP are discussed by Moslehi in his review in detail. They are linked mainly to measurement of wafer temperature, the reproducibility and reliability of the equipment and the side-effects of the rapid thermal cycling. Accurate temperature measurement remains the most serious inadequacy without which it is impossible to repeat processes precisely. Normally a pyrometer is used to monitor temperature with an assumed value of the substrate emissivity which can vary with the wafer lot and any surface coatings as is likely. The fast heating and cooling can cause thermal shocks and stresses leading to wafer damage in the form of defects and slip dislocations. Temperature homogeneity across the wafer is not always maintained particularly during ramp up and ramp down so that oxide thickness variations over the wafer can exceed design tolerances (see section 3.3). Another problem that has not been significantly investigated is the impact of patterned layers on thermal homogeneity during processing, Vandenebee et al. (1989). These problems are exacerbated by the high temperatures

used because of the large changes in growth rate with small variations in temperature above 1000°C.

It was also suggested by Ponpon et al. (1986) and Saloui et al. (1987) that some photo-enhancement of oxidation was observed during RTO. Photo-enhanced and induced oxidation has indeed been conclusively observed and is discussed below. The issue of reaction enhancement in RTO is considered in section 1.4 and an experiment to resolve the situation is described.

1.3.3 High Pressure Oxidation

In 1.3.1 the growth rate was increased by chemical means. A physical mechanism of inducing faster oxidation has been invoked by heating the Si in a high pressure ambient, Tay et al. (1987) and Basu and Bhat (1988 and references therein). Pressures up to 100 atmospheres have been used to study oxidation kinetics (Reisman et al., 1987). Electrical properties are similar to thermal oxides for growth at 800°C. High pressure oxidation is not favoured because of the generally hazardous nature of the equipment. Also, at high pressures ambient gases circulate rapidly due to convection losses and thus cause large thickness non-uniformities in the oxides.

The oxidation methods noted above rely on controlling the period that the wafer is exposed to high temperatures. The remaining techniques that are discussed are truly low temperature.

1.3.4 Plasma Anodisation

Plasma anodisation of Si wafers has been used to grow oxide layers. However, these have tended to suffer from the very environment that encourages the growth. The oxygen is highly activated by radio-frequency or microwave discharge. The wafer is placed in the plasma region directly on one of the electrodes and is positively biased to enhance the diffusion of either Si or oxygen ions through the growing oxide. By accelerating the diffusion rate the growth rates that can be achieved are very high for low temperatures. Ho and Sugano (1982) obtained 1 μ m/hour at 600°C which is equivalent to oxidation in steam at 1200°C. Severe problems do exist with this method because of ion sputtering from the electrodes. Sputtered

species can then be incorporated into the oxide layers as it grows. Also energetic ions and the deep UV present in the plasma damage the oxide. The combination of these effects means that the oxides are unsuitable for electronic uses.

An alternative to direct anodisation is to place the Si on an anode outside (but close to) the discharge region. Thus exposure is limited to ions of lower energy and sputtering of the electrode is avoided. Kimura et al., (1985 and 1988) have demonstrated enhanced oxide growth at 580°C and produced 30nm in 60 minutes. Oxidation at an even lower temperature has been studied by Taylor et al. (1988). In this case although electronic properties are improved when compared to the anodic oxides they are still not close to the quality of thermal layers. Annealing can be used to further improve the oxides, Zhang et al. (1989).

A development of the anodisation process involves moving the Si to a longer distance down stream from the discharge into a vacuum compatible furnace tube. Vinckier et al. (1987) have demonstrated that the ion density reaching the Si is negligible in such an arrangement. Only atomic radicals and molecular oxygen remain in the afterglow after a distance of just 50mm from the discharge. Similar experiments have been carried out by Hoff and Ruzyllo (1988). Both reports show a much reduced oxide growth rate relative to plasma anodisation, for example, 6.5nm in 100 minutes at 550°C. Hoff in his thesis (1988) also studied the effect of adding NF_3 and H_2 to the discharge gas. Both gases had the effect of increasing the growth rate especially NF_3 . The oxidation rate has been strongly linked to the presence of atomic radicals in the gas ambient generated by the discharge rather than ionic species. The fluorine atoms are incorporated into the oxide and are suspected to change the local structure of the oxide allowing a more rapid motion of oxidation species towards the Si for reaction. In anodisation the high oxidation rate has been linked to the presence of O^- (Barlow et al., 1988). Vinckier et al. (1987) have noted the following order of reactivity for oxygen species; $\text{O}^- > \text{O} \cdot > \text{O}_2$. Kimura et al. (1988) have proposed that the O^- ions are formed by electron capture by O adsorbed on the oxide

surface. This is also supported by the calculations of Vinckier and De Jaegere (1990) who conclude that the O^- fluxes from the plasma toward the Si seem to be insufficient to explain the initial oxide growth rates. This subject is discussed in more detail in chapter 2 with respect to growth mechanisms for the UV/ozone experiments.

1.3.5 Electron and Ion Stimulation

In the previous section oxidation was induced apparently by the presence of charged species. Room temperature oxide growth has also been induced by Si surface excitation with low energy electrons by Collot et al. (1985) in a vacuum system with a low partial pressure of O_2 (10^{-7} torr). Very little information exists on the properties of these oxides. An O^- beam can also oxidise Si surfaces at room temperature as recognised by Todorov et al. (1986 and 1988). The energy of the ions ranged between 40 and 100eV. Oxide growth occurs by ion implantation into the surface and the dissipation of the energy to form Si-O bonds, until eventually sputtering limits the growth of the oxide. Electrical properties have been observed in MOSFET and capacitor structures. However, the oxides contain a notably larger concentration of sub-oxide species relative to thermal layers and are thus likely to be unstable with time. Additionally radiation damage to the layers is inevitable because of the energetic incident ions. More recently the effect of a very low energy O^- (5eV, Hecht et al. 1989) beam has also been investigated. In this case little or no implantation and hence resulting damage occurs, but the limiting thickness was only 2nm at room temperature.

1.3.6 Catalytic and Acidic Oxidation

Two other methods of encouraging the oxidation reaction use alkali metals, Oellig et al. (1987) and acid mixtures, Uchida et al. (1986). In the former the Si surface is coated with a few monolayers of an alkali metal in UHV. Following this it is exposed to O_2 for adsorption and reaction with the metal. It is next given a higher temperature anneal typically 600°C to reduce the metal oxide thus releasing the oxygen for reaction to the Si and desorbing the alkali species. Very thin oxides are formed with each

adsorption/desorption cycle although a 3nm film has been produced. A more recent analysis of the mechanism of oxide formation by Starnberg et al. (1989) suggested that a dissociative reaction occurred because of enhanced electron transfer into antibonding O₂ orbitals. The electron emission is made easier by the lowering of the work function by the metal coating. The acidic growth of oxide relies on a mixture of heated sulphuric and nitric acids in a pressure vessel. For a growth temperature of 250°C a 10nm layer was grown in 2 hours. Typically a pressure of 35 atmospheres was required. The oxides grown had a higher concentration of sub-oxide species than are normal in thermal layers and a reduced breakdown field. Both of these methods of oxidation are complex and lack the flexibility of the other techniques noted above.

1.3.7 Photochemical Oxidation

In this section growth techniques which are particularly relevant to the experiments reported within this and chapter 2 are introduced. They deal in the main with photochemically stimulated oxidation of Si. In the preceding section the effect of photo-irradiation was only mentioned with respect to RTO. Laser oxidation has been studied by a number of researchers with a variety of sources. The original observation that radiation from a high pressure mercury lamp could affect the oxide growth rate was made by Oren and Ghandi in 1971 for thermal oxidation at normal furnace temperatures. Since then a variety of lasers of different wavelength output have also been used. There are essentially two categories of experiments; firstly the Si is irradiated at high temperature in a furnace and secondly only the laser is used as the energy source. The former arrangement was used by Schafer and Lyon (1981 and 1982), Boyd and Wilson (1981 and 1982) and Young and Tiller (1983, 1987) to study the effect of visible and near UV light generated from an argon laser. Young and Tiller also extended their studies to UV excimer laser radiation down to a wavelength of 193nm. The deep UV is reported to increase the oxidation rate by as much as 300% relative to visible light for a background substrate temperature of 850 and 900°C. This was suggested to be due to the efficient creation of atomic oxygen

species by photo-induced dissociation of O_2 . The effect of visible light on growth enhancement was small. A more precise study of the enhancement was carried out by Micheli and Boyd in 1987 (see also the thesis by F. Micheli, University College London 1990). These experiments fall into the second category noted above. The laser was used to heat the Si to temperatures in the range 700 to 1000°C. As the temperature was increased the enhancing effect diminished as purely thermal oxidation became dominant.

Once again the experiments noted in the previous paragraph were carried out at high temperatures. Photo-oxidation, without substrate heating, using an excimer laser was first demonstrated by Orłowski and Richter (1984). However, they used energy densities sufficiently high to melt the Si surface. The rapid oxidation of molten Si is well known and therefore the process cannot be said to be low temperature. Solid phase oxidation was induced at much lower incident fluences (thus limiting the Si surface temperature rise to less than 600°C) by Fiori (1984) and Fogarassy et al. (1987) using 248 and 193nm radiation respectively. An attempt to compare the effectiveness of the two wavelengths is described in the following section.

Morita et al. (1986), in addition to studying the thermal oxidation of Si using O_2/NF_3 mixtures, have applied excimer laser stimulation to the Si surface simultaneously at a temperature of 400°C. A 6nm oxide was grown, after 20 minutes, using a laser pulse energy density and repetition rate of 20mJ/cm² and 50Hz respectively. The NF_3 concentration was 2000ppm in O_2 . The high growth rate was caused by the photo-dissociation of NF_3 to form F radicals which were thought to modify the interface structure. No information on the electrical properties was published.

Two other methods which are chronologically contemporary with the experiments reported below are oxide growth by the photo-decomposition products of N_2O and the thermal reaction of O_3 . Namiki et al. (1988 and 1989) used 193nm laser radiation to dissociate N_2O to study the initial stages of oxygen bonding at room temperature. Similar thicknesses to

native oxide were grown. Thicker oxides, $\approx 5\text{nm}$ were grown by Ishikawa et al. (1989) using substrates heated to 500°C in N_2O which was simultaneously irradiated by a low pressure mercury lamp. This experiment is quite similar to the UV/ozone technique discussed in detail in chapter 2, although ultimately not as effective. What is interesting is that the form of the growth curves for the two processes is similar. This suggests that the mechanism of oxide formation may be the same.

Ozone enhancement at room temperature was noted by Tabe in 1984 and further studied by Ruzzylo et al. (1987). A 15 minute exposure under a low pressure Hg lamp was found to reproducibly grow 1.2nm and 1.4nm in dry and wet oxygen respectively. Thermal oxidation in O_3 was very recently studied by Chao et al. (1989) at temperatures ranging between 700 and 950°C . The concentration of O_3 used was 2.25ppm however a notable enhancement occurred at temperatures below 900°C for films less than 70nm.

1.4 Near UV and Excimer Laser Oxidation of Silicon

In this section oxidation studies using a broad band arc lamp and an excimer laser as the photon sources are described. The aim of these photo-oxidation studies was to identify wavelength ranges that increase the reaction rate, beyond the conventional thermal process, so that the overall growth temperature could be reduced. In particular it was important to learn whether near UV light induced any extra oxidation. The reason for this is that intense photon sources for UV light become both more complex and expensive for shorter wavelengths of light. It was emphasised in the previous section that UV irradiation was effective for high silicon substrate temperatures but that low temperature studies were very limited (Fiori 1984, Fogarassy 1987).

Oxide growth enhancement was first observed by Oren and Ghandi in 1971 when ultraviolet (UV) light was applied to the Si surface at high temperature. Since their photon flux was small, the experiment suggested that the UV induced some photo-chemical mechanisms to encourage the oxidation reaction. Studies of rapid thermal oxidation (Singh, 1988, Hodge

et al., 1986, Ponpon et al., 1986) using lamp systems have also suggested that some photoenhancement of the reaction was evident. In particular, it was found that arc lamp systems (Gelpey et al., 1986) induced a faster reaction than tungsten filament lamp systems because of their greater near UV output. These differences have more recently been attributed to unreliable measurement of silicon temperature (at high temperatures) during oxide growth (Dilac, et al. 1989). However, it is still not apparent whether at low temperatures ($<800^{\circ}\text{C}$) growth is enhanced beyond the thermal rate.

Experiments by Schafer and Lyon (1983) and Young and Tiller (1983 and 1987) have noted oxide growth enhancement for longer wavelengths of light in the visible range. Micheli and Boyd (1988, 1990) using a continuous wave argon laser to induce Si oxidation have concluded that for visible wavelengths of light the reaction is primarily dependent upon the induced temperature, but is also affected by the incident photon flux density. This flux density increases the instantaneous electron population in the near surface region of the Si (Young and Tiller, 1987), which appears to be important in the overall oxidation reaction (Irene and Lewis, 1987). Thus, for the same initial absorbed beam power (and thus initial surface temperature), green (514nm) laser light causes more "photonic" growth than the blue (488nm) due to the greater electron population induced by the green light. However, the major effect of the high powers applied is purely heating. At high temperatures ($>800^{\circ}\text{C}$) the enhancement due to irradiation is thought to be masked by the fast thermal oxide growth reaction, Boyd (1983).

Experiments applying pulsed UV laser light have been performed by Orłowski and Mantell (1988) and Fogarassy et al. (1987) to increase the oxidation rate. The former especially achieved very high oxide growth rates which were not reproduced by Fogarassy et al. Under pulsed conditions only the near surface region was heated significantly and notable reaction enhancement was observed when either 249nm or 193nm radiation was used. Additionally 193nm radiation was found to be more effective than 249nm. Attempts to compare pulsed (i.e. very high peak power) irradiation

successful because the precise surface temperature rise is difficult to determine (theoretical calculations of the surface temperature rise do exist though and are briefly discussed below). Additionally the effect of the high peak power density upon interface bond restructuring remains uncertain (Fiori 1984). The area of low temperature excimer laser oxidation is not well understood and the data available is rather limited and controversial.

The following discussion is divided into two main sections. The first section describes the investigation of near UV (260-370nm) while the second the effect of excimer laser radiation at 248nm and 193nm on low temperature oxidation.

1.4.1 Near UV Oxidation of Silicon

Experimental System

The experiment recorded here was devised to overcome the difficulties of comparing pulsed UV and cw visible laser irradiation. The use a short arc 1000W cw (Hg-Xe) lamp source (Photon Technology International) allowed a direct comparison of the effect of cw UV and visible light. The broad spectral output of the lamp is shown in **Fig.1.8** (supplied by the manufacturer).

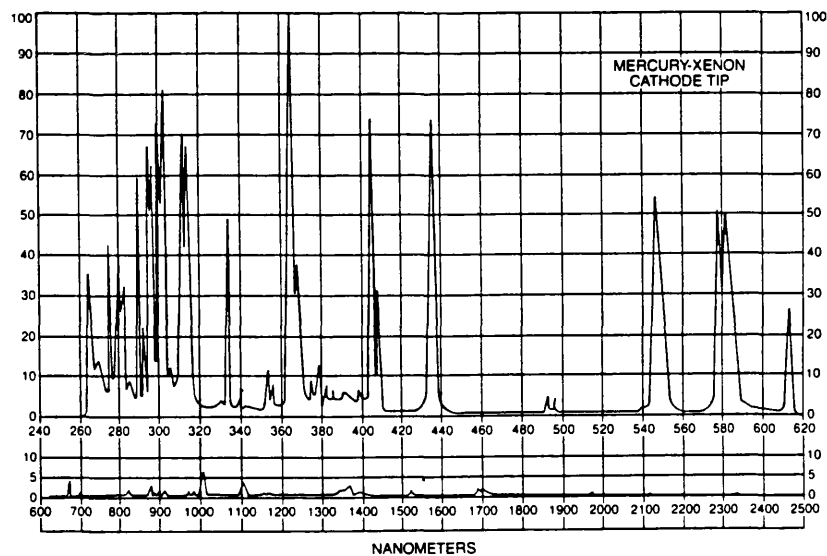


Fig.1.8 Spectral output of Hg-Xe arc lamp.

Its total output was approximately 160W over the wavelength range 260-2000nm. The beam from the lamp was focused by a parabolic mirror to

a spot of 10mm diameter at a distance of approximately 200mm. A profile of the arc beam is shown in Fig.1.9. It was taken at approximately 15mm from the focal plane with a $200\mu\text{m}$ diameter pin hole using a broad band thermopile detector. The beam was measured in several translations and found to be radially symmetric.

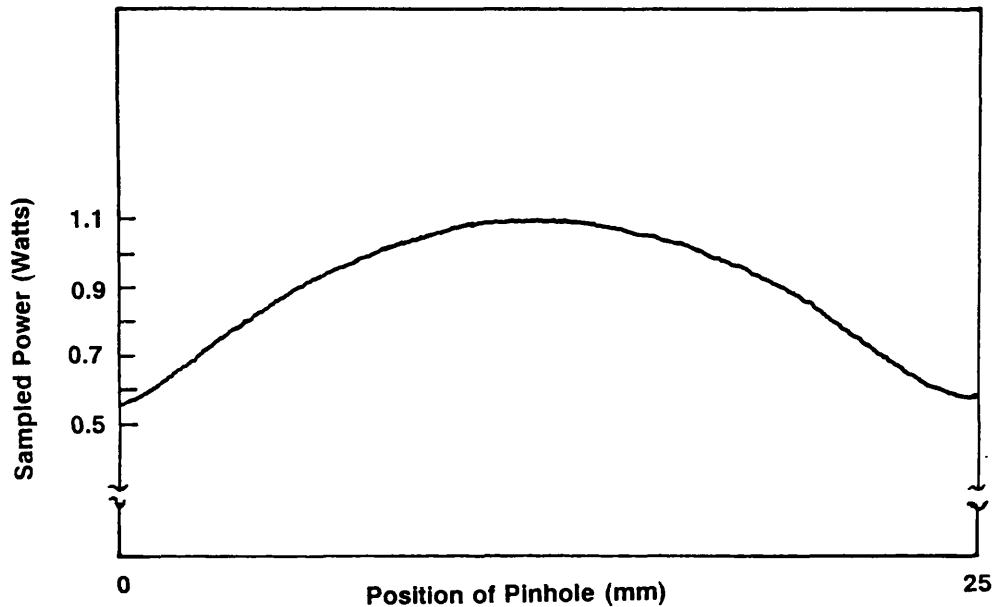


Fig.1.9 Arc lamp beam energy density profile.

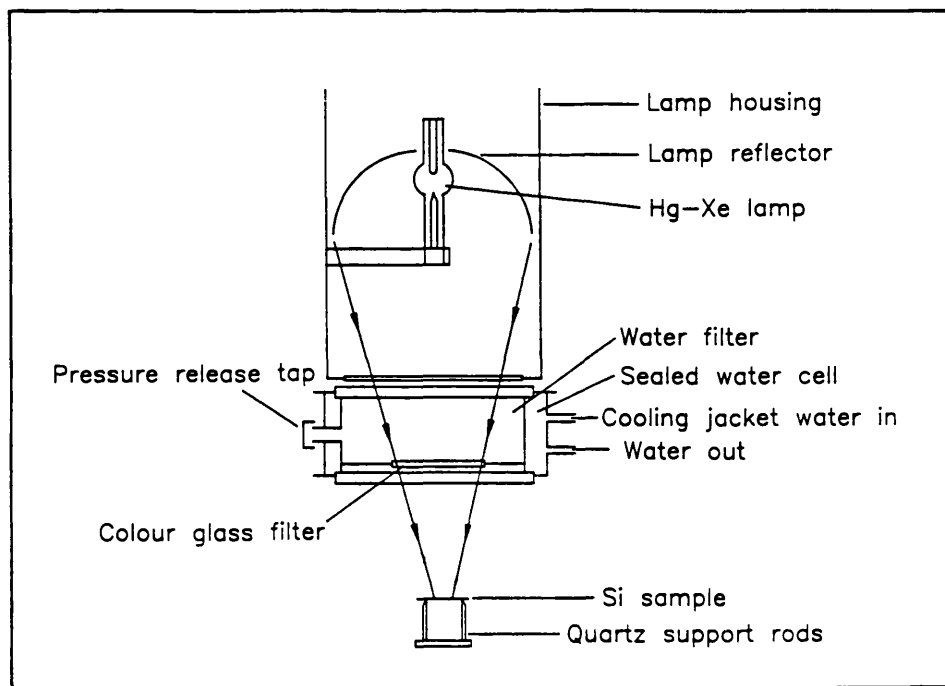


Fig.1.10 Experimental arrangement for low temperature near UV oxidation.

Originally it was thought that the wide bandwidth could be spectrally selected by a monochromator. However, the throughput energy in such an arrangement was severely reduced to the point that it was useless. As alternatives dichroic mirrors and dielectric filters were also investigated but were found to be unable to survive the high energy density incident from the lamp. The solution to the problems of reduced energy transmission and the fragile nature of thin film filters is shown in **Fig.1.10**. Wavelength regions of interest were selected by means of a water filter and colour glass filters. The water filter absorbed wavelengths greater than 1000nm, a very small amount of the UV was also absorbed by the water. UV and visible light ranges were obtained using the standard colour glass filters UG5 and GG495 respectively. These filters work by absorption and the absorbed energy must be dissipated to avoid damage. Hence the filters were inserted into the water enclosure where the surrounding water kept them cool. Thermal stress caused the filters to crack without the water cooling. Transmission curves for the two filters are shown in **Fig.1.11** and the relative colour spectra transmitted by each filter are shown in **Fig.1.12**. The fraction of red light transmitted by the UG5 filter ($\pm 14\%$ of the total) is relatively small.

By irradiating individual Si samples in air with the two colour bands of light, the oxide growth resulting was determined as a function of time. The Si samples were $\langle 100 \rangle$ oriented, p-type (2-10 Ω cm) squares (20x20mm²) and 125 μ m thick. Samples were placed on quartz pins to reduce thermal loss. Four pins, especially fabricated such that their tips were extremely fine were held in a home-made jig. Prior to irradiation the Si samples were cleaned with H₂SO₄/H₂O₂ (1:1) solution (here after called the "bomb" clean) and had an average native oxide of 2nm. All samples were placed at the lamp focus (beam diameter 10mm) so that all the light transmitted by the filters was incident upon the Si. The oxide thicknesses were measured with an ellipsometer (Rudolph AutoEL2) at fixed refractive index (1.462, 12 measurements per sample).

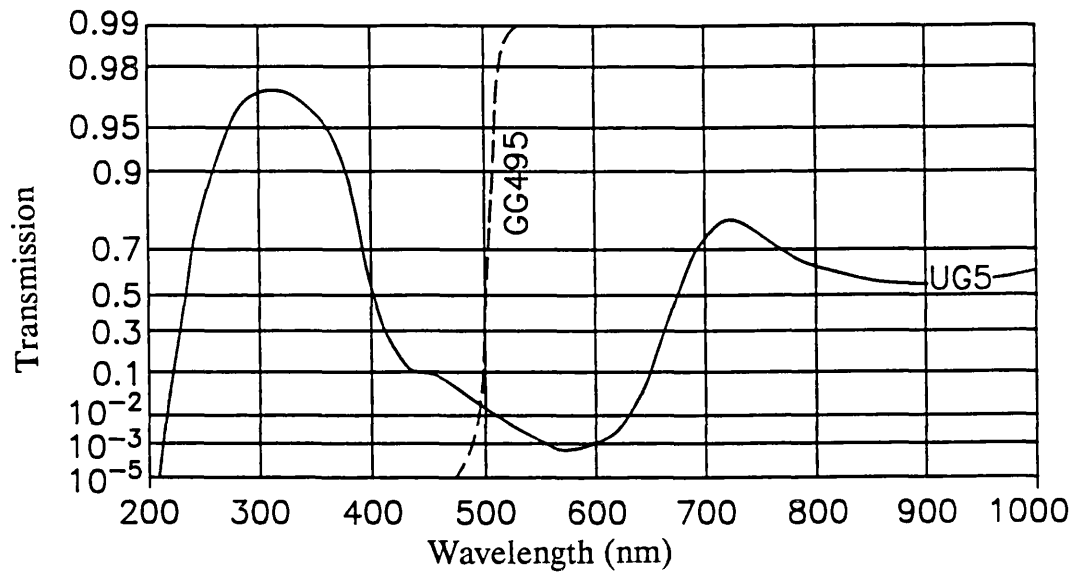


Fig.1.11 Transmission curves for UV (UG5) and visible (GG495) filters.

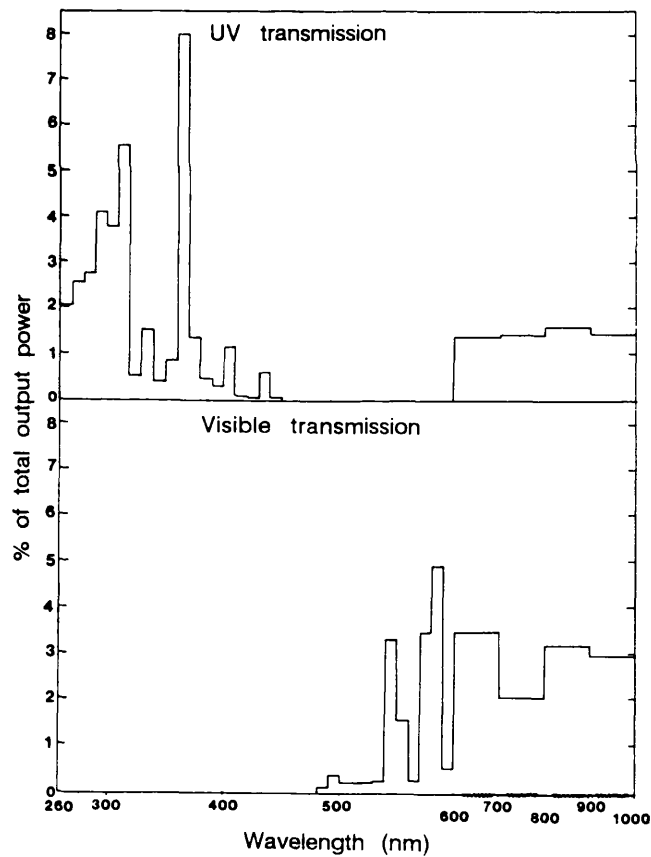


Fig.1.12 Relative colour spectra transmitted by each filter.

In order to isolate differences in the non-thermal contribution to the reaction a calibration experiment was performed to determine the heating effect of the two colour ranges. To achieve this, a Si sample with an embedded thermocouple (bonded with a ceramic cement) was placed in the normal processing position. The temperature from the thermocouple was then recorded as a function of the power input to the lamp, **Fig.1.13**. Although the temperatures noted may not be precisely those induced during oxidation due to thermal losses via the thermocouple itself, the lamp input power required to produce the same temperature with either filter could be found from **Fig.1.13**. To induce a temperature of 400°C with visible light only 885W input power was necessary in comparison to 980W for the UV. The difference between the power levels is principally indicative of the difference in Si reflectivity between the two broad wavelength regions.

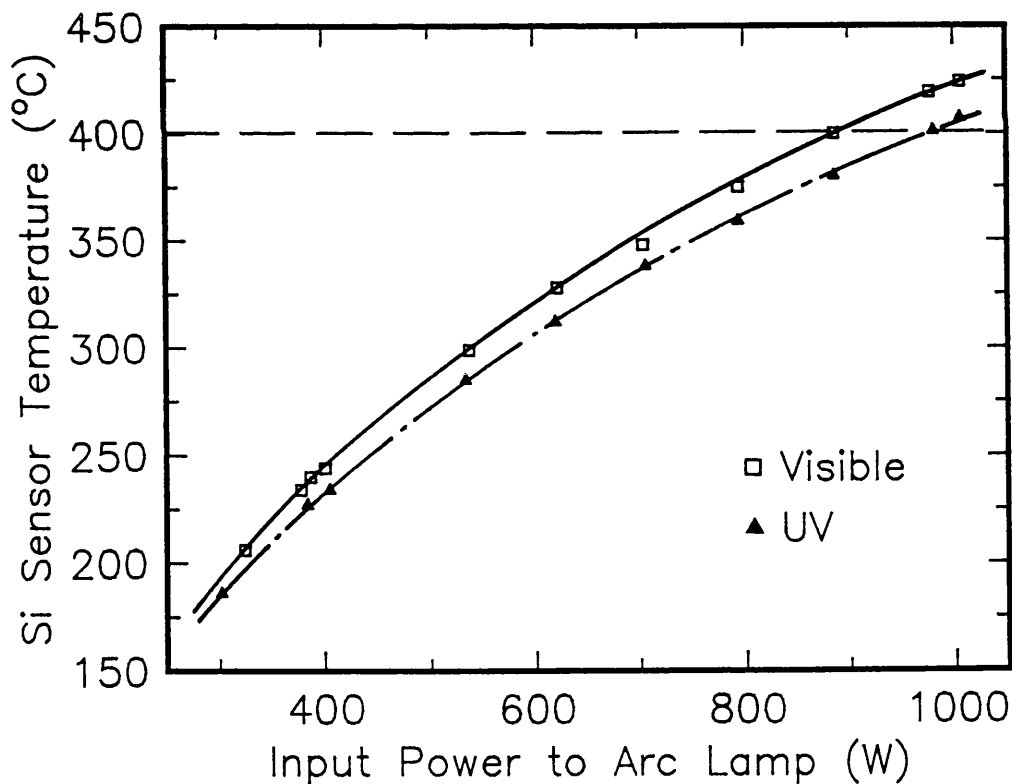


Fig.1.13 Si sensor temperature as a function of the arc lamp input power.

Results and Analysis

Having ascertained that these power levels induced the same temperature rise in the Si ($\approx 400^\circ\text{C}$) then any variation in the oxide growth for the two filters could be ascribed to non-thermal or photonic phenomena. Fig.1.14 shows the oxide thickness (standard deviation of $\pm 1\text{Angstrom}$ over 12 measurements) as a function of irradiation time for the two photon bands together with a previously published curves (Taft, 1984) of the oxide grown thermally at 450°C and 612°C . Whilst a purely thermal oxidation reaction would only induce the growth of 2Angstroms or so after 6 hours at 612°C , the light induced reactions encouraged between 6 and 9Angstroms in the same time. Indeed, it was observed that the UV light induced faster growth than the visible radiation.

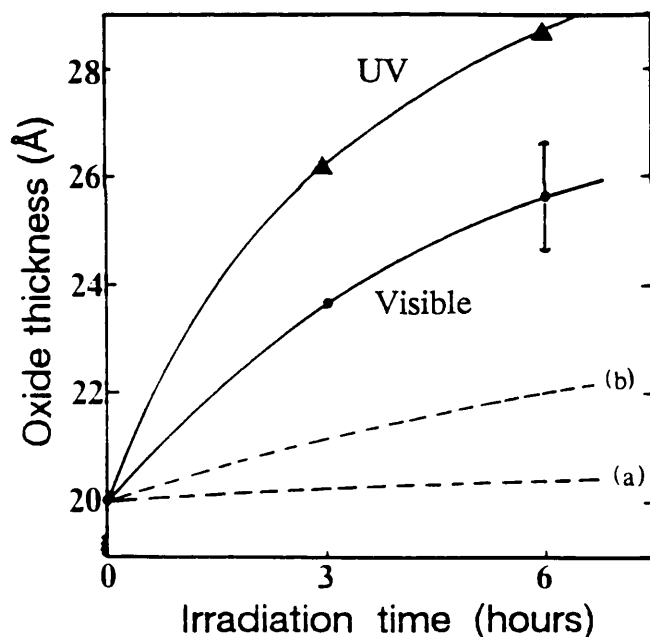


Fig.1.14 Oxide thickness against growth time for the two wavelength ranges (curves a and b are for thermal oxide growth at 450°C and 612°C respectively after Taft, 1984).

By way of interpreting the data, it was noted above that the photon flux is important in introducing non-thermal effects to the oxidation process. If this principle is applied here, then the photonic enhancement would be expected to be stronger for visible exposure, due to the greater number of photons incident. This statement is qualified by noting that to produce the same sample temperature the total absorbed power must be equal for both

wavelength ranges. Thus if one considers the average photon energy to be $\approx 3.8\text{eV}$ (325nm) in the UV and $\approx 1.7\text{eV}$ in the visible then clearly the visible flux is ≈ 2.25 times greater. Since the result shows faster UV growth then fewer UV photons must induce a stronger "photonic" enhancement than the visible light. This suggests that the precise energy of the photo-generated electrons rather than their absolute number may become important above a certain level, this effect is not evident with visible photons.

Mechanisms for UV enhancement have been linked to carrier generation in the near Si surface (Oren and Ghandi, 1971, Young and Tiller, 1987). Photo-emission of electrons (in addition to thermionic emission which is always present at high temperatures) from the Si into the oxide conduction band requires a minimum photon energy of 4.3eV (around 290nm, this is the energy difference between the Si valence band and the oxide conduction band). An inspection of **Fig.1.11** reveals that the number of photons available with at least this energy is small. Additionally photoemission "efficiency" for these wavelengths is very low, $< 10^{-5}$ electrons/absorbed photon according to Dressendorfer and Barker (1980). At around 3.4eV direct electron transitions can be excited in the Si and the absorption coefficient becomes larger. Therefore the relative carrier population in the near surface is greater than for the visible case. Hence this greater population of electrons which are also more excited may lead to an increase in thermionic emission for the UV case. It has also been postulated, by Yu et al. (1988), that direct photo-dissociation of O_2^- by $\approx 4.1\text{eV}$ photons can lead to more reactive oxygen species, however, this process is also limited by the formation of charged oxygen which also requires photoemission of electrons from the Si. Ultimately all these mechanisms are limited as is evident from the small oxide growth rates.

1.4.2 Excimer Laser Oxidation

Experimental System

Oxides were grown using the simple experimental configuration shown in **Fig.1.15**. Increased energy density was achieved by inserting two

Spectrosil lenses into the beam path. Si with a surface orientation of $\langle 111 \rangle$, a resistivity of 6-10 Ω cm and p-type (boron) doping was used in this study for both wavelengths. The Si samples were prepared with 10% hydrofluoric acid dip and a 15 minute flush in deionised water.* After a period of storage a stable native oxide (of an average thickness of 19Angstroms for 249nm samples and 15Angstroms for 193nm samples) was measured on the silicon prior to oxidation. The samples were loaded into the oxidation chamber in a clean room environment. Electrograde oxygen was flushed into the chamber and the Si oxidised at atmospheric pressure. Oxide thickness was determined using an ellipsometer as noted above.

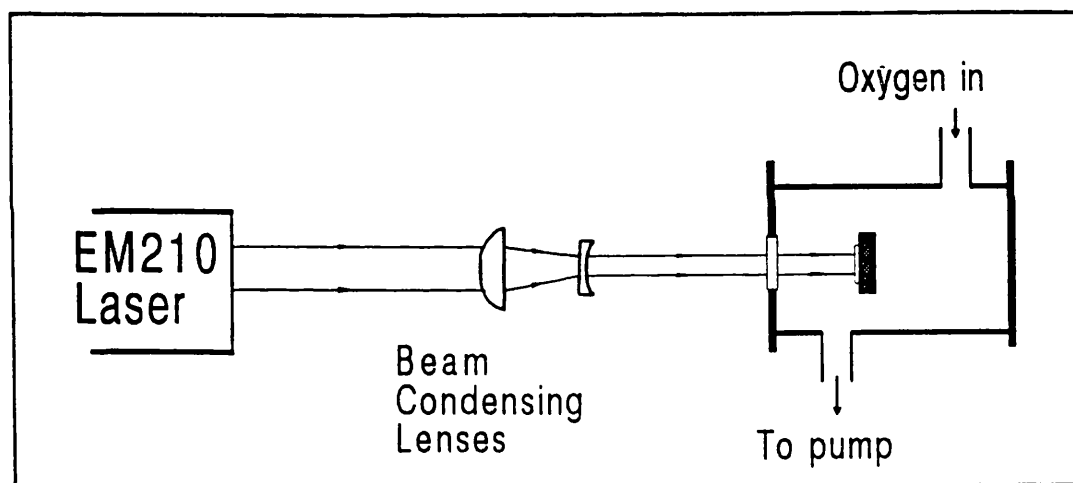


Fig.1.15 Excimer laser oxidation system.

All of the oxidations were carried out at a laser repetition rate of 10Hz. The pulsewidth at both wavelengths (249nm and 193nm) is around 23ns. With the Lambda Physik laser model EMG210 the pulse energy drops both as a function of the repetition rate and the total number of laser shots. For example, the low repetition rate pulse energy after each oxidation run was measured and found to decrease by less than 5% even after the longest runs at 249nm. However, at 193nm the pulse energy was very much more difficult to maintain at a constant value. This is a well known problem with the excimer emission at 193nm from ArF gas. The effect of this is discussed below.

Since the beam fluence strongly influenced the oxide growth rate, it was ensured that the energy density during processing was much less than $0.45\text{J}/\text{cm}^2$ (Fogarassy et al., 1988) which is the energy required to induce surface melting leading to rapid oxidation. By melting the surface severe damage to the oxide/Si interface results leading to bad electrical properties and increasing surface roughness. The energy density prior to oxidation was set to approximately $0.23\text{J}/\text{cm}^2$ using a Gentec Joule meter at low repetition rate ($< 1\text{Hz}$).

Results and Analysis

Fig.1.16 shows the oxide thickness variation as a function of the number of shots delivered to the surface. The oxide thickness increased to 30Å after 40000 shots at 249nm. The standard deviation of the data points was calculated to be less than $\pm 2\text{Å}$. Using a similar energy density, a series of oxides were grown with 193nm radiation for comparison of the growth rate. The 193nm data are also plotted in the **Fig.1.16**. At 193nm growth appears to proceed at the same initial rate as at 249nm. However, only a small increase after 20000 shots is observed.

It should be noted that the unreliability of the excimer laser system may well mask true oxidation behaviour in particular at 193nm. It has been noted above that the pulse energy at this wavelength falls quite drastically as the total number of pulses increases and much more so beyond 20000 shots (by up to 40% after 40000 shots) in comparison to 249nm. Another problem was identified after the experiments were carried out. A new power meter was purchased which relies on a pyroelectric detector. This meter was capable of a much higher frequency response than the Gentec and thus it was possible to measure the average pulse at the operating frequency of 10Hz. It was found that the average pulse energy decreased by 20% at 249nm and by 35% at 193nm. Thus the actual average power densities were $0.18\text{mJ}/\text{cm}^2$ and $0.16\text{mJ}/\text{cm}^2$ for 249nm and 193nm respectively.

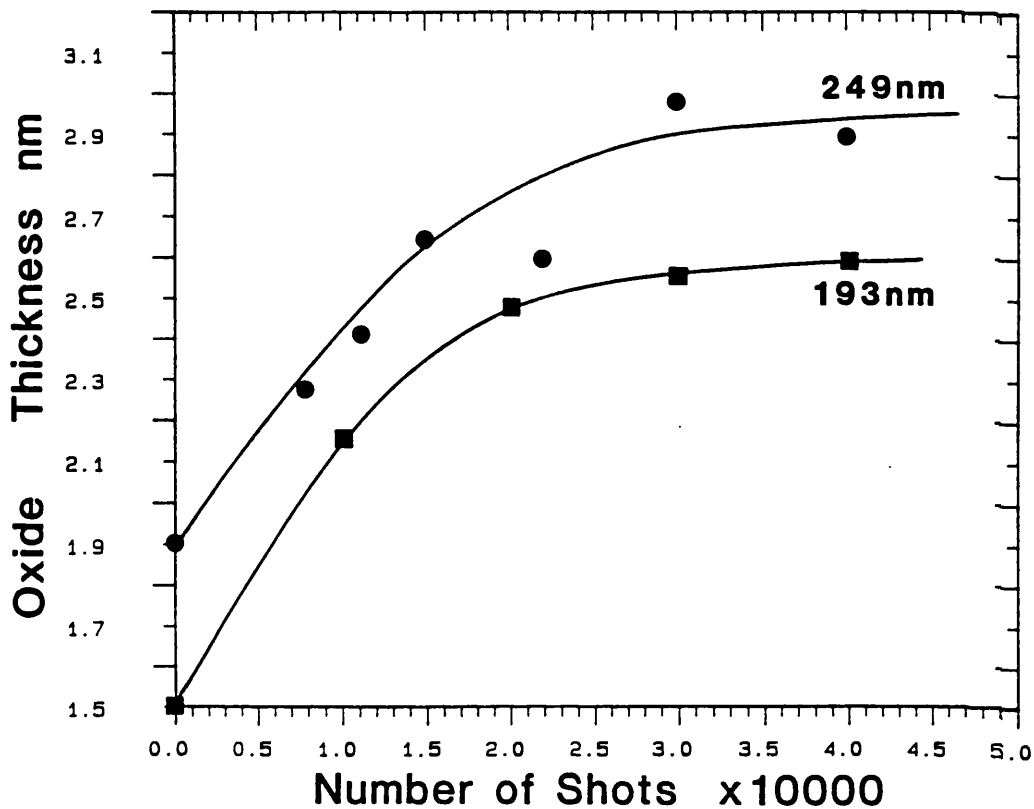


Fig.1.16 Excimer laser induced oxidation at 193 and 249nm.

Therefore the very small increase in oxide thickness at 193nm for more than 20000 shots is more likely to be a result of the fall of the pulse energy rather than a fundamental limitation on the oxide growth. Fogarassy (1987) has reported the growth of 50Angstroms of oxide using similar energy densities with a large number of shots (10^5).

It was not possible to measure the surface temperature rise during the laser pulses. However, the surface temperature rise has been calculated by several authors using a theoretical finite element model of the laser-surface interaction (Baeri et al., 1979, Ong et al., 1986, Fogarassy, 1987, Unamuno and Fogarassy, 1989). It was only recently that the thermal models were confirmed as being capable of describing the pulsed laser excitation of surfaces by Hicks et al. (1988). Theoretically the maximum temperature induced on the Si surface in this experiment (for a pulse energy density $<0.25\text{mJ}/\text{cm}^2$) is less than 500°C (Fogarassy, 1987). The total exposure time during 40000 shots is less than 1ms. From a purely thermal stand-point one would not expect an oxide thickness increase up to 30Angstroms during

the millisecond at the elevated temperature estimated above. In fact even by extrapolating the known temperature dependence of thermal oxidation of solid Si (Taft, 1984) one cannot achieve the result observed at an oxidation temperature of 600°C in less than 500 minutes. Therefore there must be a non-thermal oxidation process inducing the growth. From the form of the curve the oxidation appears to be self-limiting.

In comparison with visible laser oxidation UV light has a much greater enhancement in the low temperature regime. Previous studies have linked this to the generation of a highly non-thermalised carrier plasma in or near the interfacial region and laser induced bond breaking in the interfacial region (Wautelet, 1988). Afterglow oxidation of Si (Vinckier et al., 1987, and Hoff and Ruzyllo, 1988) at low temperatures suggests that growth is controlled by the availability of atomic oxygen for temperatures below 750°C. It is possible that the oxide growth observed in this study may be due to a process which creates atomic oxygen which can diffuse quickly through the ultrathin oxide at low temperatures, until itself diffusion-limiting the reaction. One should therefore expect that at 193nm the oxide would grow faster because it can more efficiently cause molecular oxygen to dissociate into atomic species (see section 2.1). However this effect may be small at atmospheric pressure because the lifetime of atomic oxygen is less than a millisecond (see appendix A). Hence because the initial growth rates for the two wavelengths are similar it is likely that the same mechanism dominates oxide formation. In the present case the laser photon energy exceeds the energy necessary to photoemit carriers from the Si into the oxide conduction band. The possible effects of carrier injection into the oxide were noted above and are further discussed in chapter 2. Another more unusual effect has also been observed by Chen et al. (1988). Si irradiated in vacuum under excimer laser fluences well below those required to induce melting was found to eject Si ions from the surface for energy densities $>12\text{mJ}/\text{cm}^2$. This certainly suggests that surface bond breaking is likely to play an important part in the oxidation process

promoted by excimer laser irradiation.

1.5 Summary

Previous studies which observed little difference when comparing the growth rates from UV arc lamps and visible/infrared rapid thermal processing (RTP) systems can now be explained. The high temperatures induced during RTP easily mask the small near UV enhancement because thermal growth mechanisms dominate. In the case where the thermal contribution to oxidation is minimised it was shown that the near UV can increase the oxide formation rate. A definite but apparently self-limiting enhancement of the oxide growth was observed with the excimer laser. The actual mechanism of oxide growth is as yet unresolved although surface bond cracking seems likely. Unfortunately the excimer laser experiments were curtailed by the failure of the laser itself and lack of laser time. The main conclusion that can be drawn is that near UV is not a useful regime for low temperature oxidation but deeper UV does offers some advantage.

It is obvious from the discussion above that many techniques have been developed to replace thermal oxidation and reduce the thermal budget. However not one of these has yet been able to meet the requirements of MOS scaling fully, that is to produce a high quality gate oxide at low temperature. This leaves the field open to further investigations. The main aim of this thesis is to discover and exploit UV photo-chemical reaction mechanisms which can induce low temperature oxide formation. It is important to note that all of the low temperature processes described above employ photo-excitation, electronic excitation or reactive atomic radicals. Charged species and charge transfer are implicated in many of the reaction mechanisms. Secondly, although just as important, a quantitative optical non-destructive technique is required for gate oxide analysis as its thickness falls. Spectroscopic ellipsometry is a technique which may meet these requirements. Its use and limitations remain to be investigated further. [The field of SiO₂ growth and its properties have attracted much attention

over the past 30 years. Some recent conference proceedings specialising on this subject are listed at the beginning of the references.]

Chapter 2

Low Temperature UV/Ozone Oxidation Experiments

2.1 Introduction

As has been noted in the preceding chapter oxide growth was observed to increase for thin films when either UV radiation was incident or a source of atomic oxygen was available for the reaction. It was in this light that the UV/ozone oxidation experiment was developed. The inherent advantage of this method of oxidation lies in applying both UV photons of energy sufficient (4.5eV) for surface excitation and the creation of ozone (O_3) which is simultaneously a source (or store) of atomic oxygen.

Both UV light and ozone can be obtained by using a low pressure mercury lamp constructed from Suprasil B silica glass (which is a very deep UV transmitting glass). To create ozone it is necessary to first dissociate molecular oxygen into atomic radicals which can, on reaction with O_2 , form O_3 . Low pressure mercury discharges radiate a number of wavelengths but the principle UV lines are 254nm and 185nm. A typical Hg emission spectrum is shown in Fig.2.1. Power output at 254nm is normally much higher than at 185nm. Figs.2.2,3 show the absorption coefficients of O_2 and O_3 as a function of wavelength. To directly photo-dissociate O_2 to ground state radicals photons of at least 242.4nm (4.99eV, see the books by Okabe, 1978 and Calvert and Pitts) are necessary. Thus 185nm light is capable of producing oxygen radicals although the absorption coefficient at this wavelength is still rather small. Photochemical and gas phase reactions

between oxygen species are listed below (and in more detail in the book by Okabe and the paper by Baulch et al., 1984). It is assumed that all reactions are dominated by oxygen chemistry.

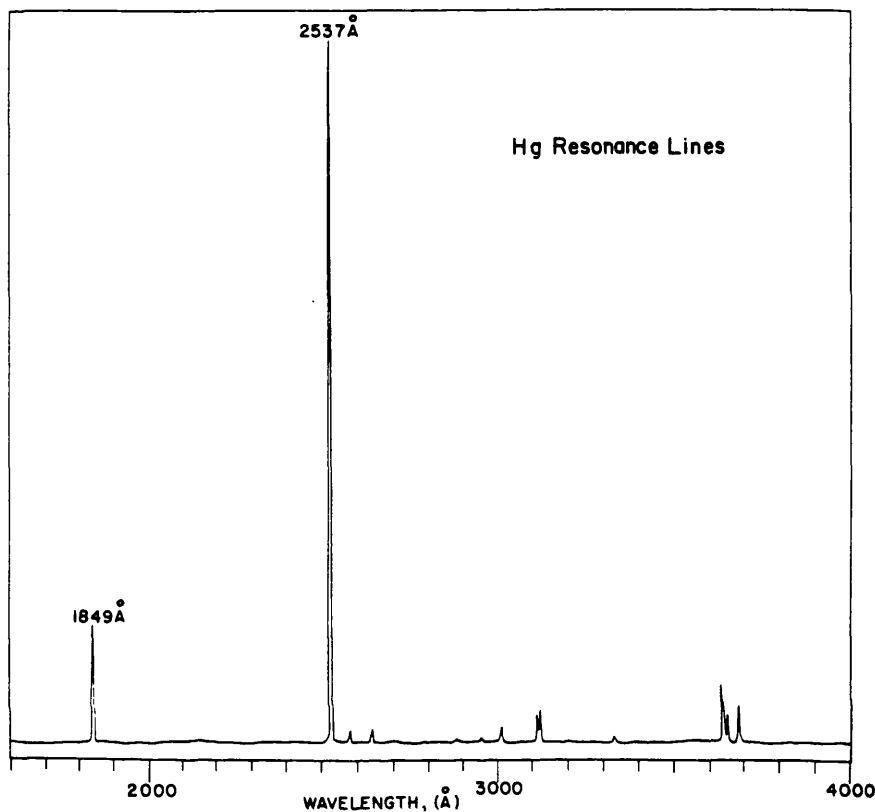
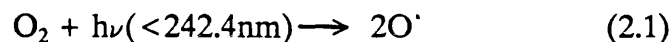
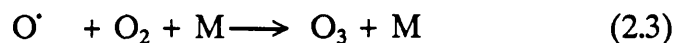
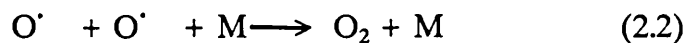


Fig.2.1 Typical emission spectrum of a low pressure Hg discharge (Okabe p110).



O' is a ground state oxygen atom. Both the recombination of atomic oxygen and the formation of O_3 are three body processes. The third body (M) is required to absorb both energy and momentum.



These reactions essentially consume atomic oxygen. The concentrations of atomic oxygen and ozone are much smaller than molecular oxygen (see section 2.4.1 below) and thus the dominant reaction is (2.3), that is ozone formation. Ozone photodissociation is possible with light of wavelengths $< 900\text{nm}$ (see Fig.2.3). For wavelengths $< 310\text{nm}$ excited states of molecular and atomic oxygen are produced.

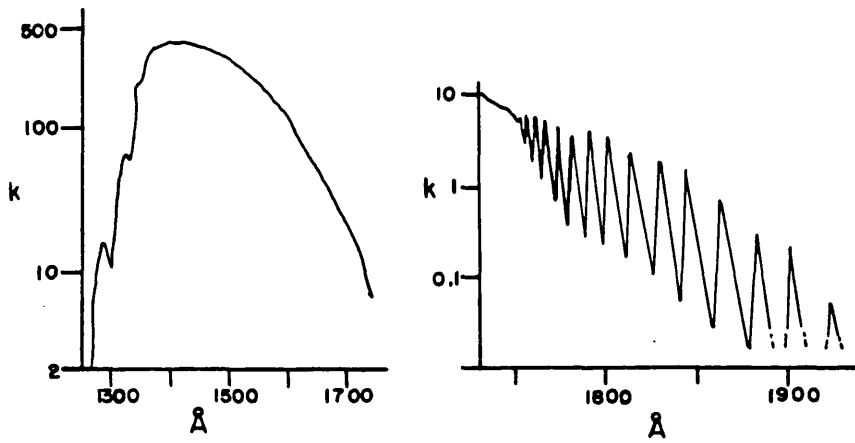


Fig.2.2 Absorption coefficient for O_2 ($\text{atm}^{-1} \text{cm}^{-1}$) (Okabe p178).

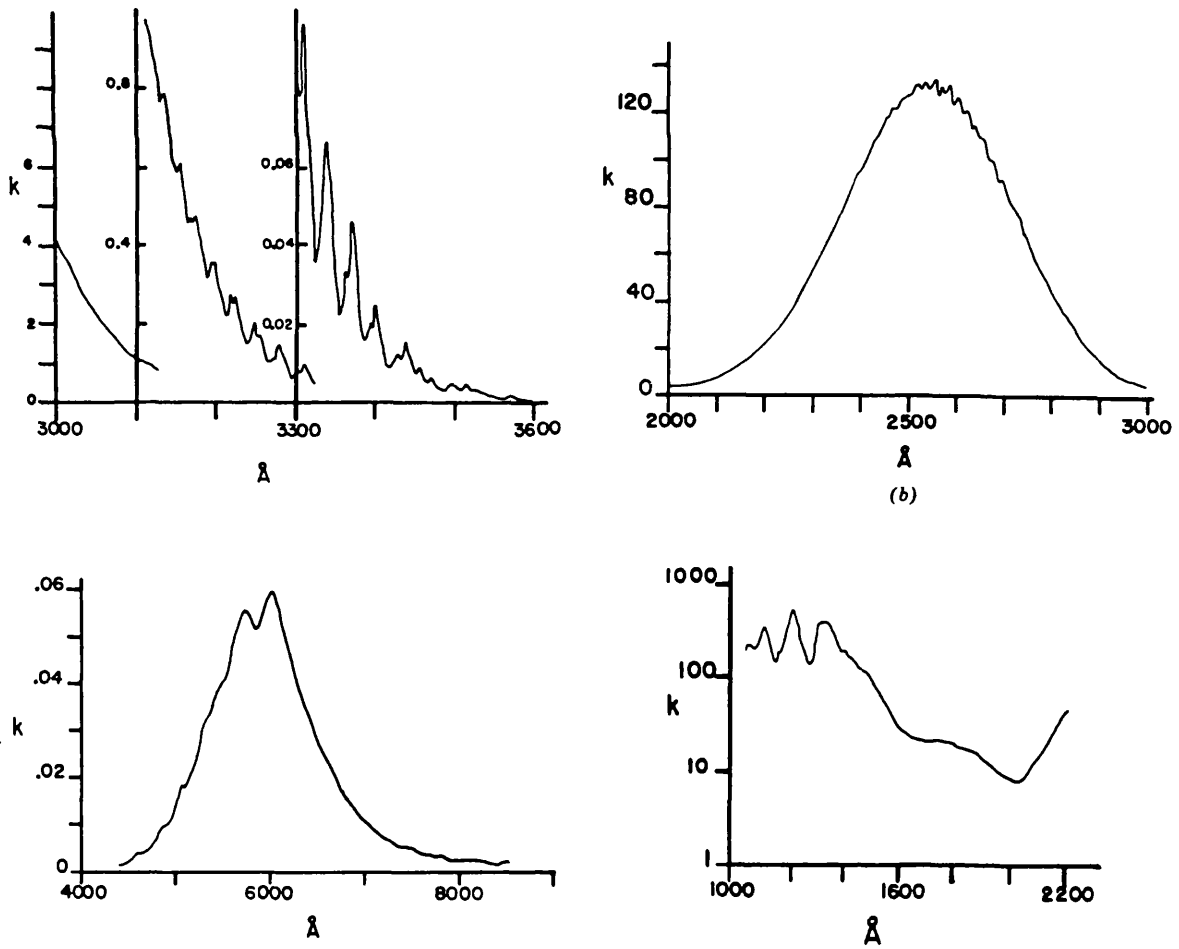


Fig.2.3 Absorption coefficient for O_3 ($\text{atm}^{-1} \text{cm}^{-1}$) (Okabe p238).



The secondary reactions between radicals and other oxygen species determine O lifetime and are dependent on the partial pressures of the other species (mainly O₂) because the reaction probability is high. The pseudo-first order calculation of O lifetime is given in appendix A and shows that the lifetime of O is short. However the lifetime of O₃ is long, the rate constant (k_d) for decomposition takes the form:

$$k_d = 4.6 \times 10^{15} \exp(-2400/RT) \text{ cc}(\text{mole sec})^{-1} \quad (2.6)$$

Where R is the gas constant and T the absolute temperature. The O₃ absorption spectra peaks at approximately the 254nm Hg lamp emission line as shown in Fig.2.3. A direct dissociation reaction occurs producing molecular and radical species. Therefore the composition of the gas phase is strongly dependent upon the incident light flux and gas pressure. The absorption coefficients (for 1 atmosphere of gas) at the two wavelengths are;

$$\alpha_{185}(\text{O}_2) = 0.15\text{cm}^{-1} : \alpha_{254}(\text{O}_3) = 120\text{cm}^{-1} \quad (2.7)$$

This means that light levels are a strong function of distance from the lamp. Only small concentrations of the respective species are required to reduce the flux (at both 185nm and 254nm) arriving at the silicon surface to very low levels for typical lamp to substrate spacing (which was determined by other experimental constraints). Fig.2.4 shows the variation of light intensity for the 254nm line as a function of distance and ozone concentration. The importance of sample distance and ozone concentration are discussed below.

In the experiments described below the growth of ultra-thin oxide was investigated as a function of growth temperature and Si surface orientation (<111> and <100>). In addition experiments to determine the effect of incident light flux and initial surface preparation were also carried out. Oxides formed by UV/ozone treatment were characterised using high frequency capacitance-voltage (C-V), current voltage (I-V) measurements and spectroscopic ellipsometry, X-ray photoelectron spectroscopy and infra-red spectroscopy (see chapters 3 and 4).

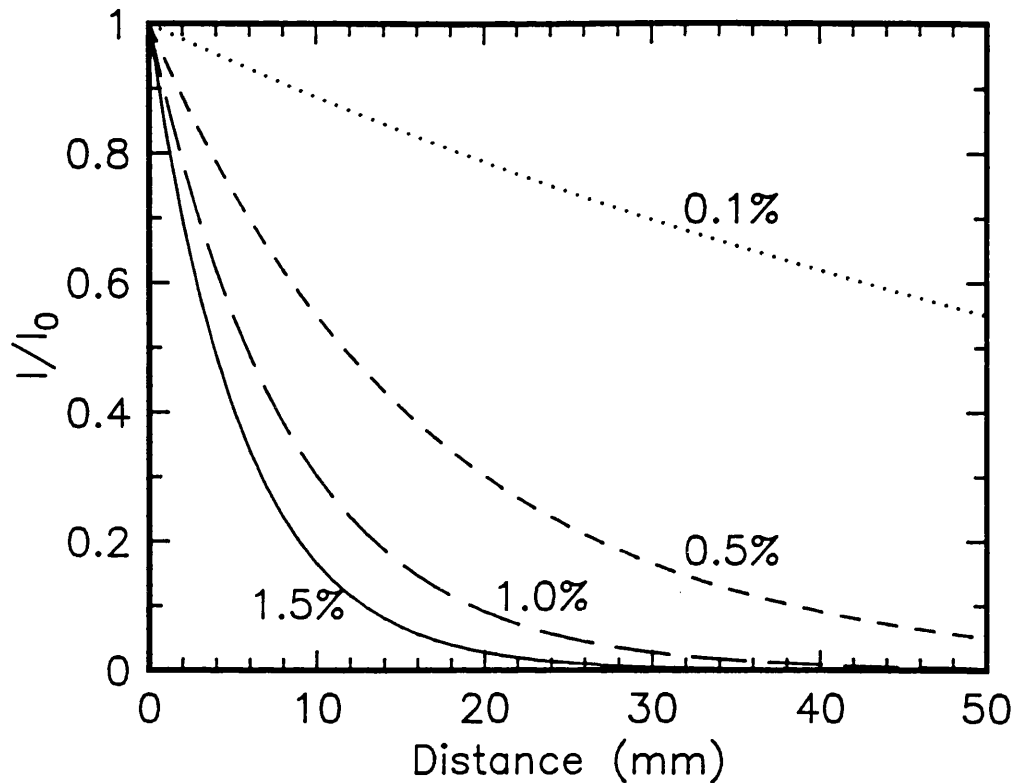


Fig.2.4 Variation of light intensity with $[O_3]$ and distance from lamp.

2.2 UV/ozone Oxidation System

A schematic diagram of the experimental arrangement is shown in Fig.2.5. The experimental apparatus can be divided into several sub-systems which were designed and constructed in-house. These are;

- a) lamp assembly, cooling and power supply,
- b) substrate heating and temperature control,
- c) vacuum chamber, pumps and pressure monitoring,
- d) gas supply and flow control.

a) The essential component of the system was the UV grid lamp purchased from the Jelight Co., California. It was constructed from suprasil glass tube (to allow emission at 185nm) in the form of a serpentine. This allows a large tube length to be used thus maximising output emission while minimising the area (approximately $20 \times 19 \text{cm}^2$) of the grid conveniently. The discharge gas was a low pressure ($< 0.1 \text{ torr}$) mixture of mercury and argon (used as the buffer gas) and was custom designed to fit into the vacuum chamber available. Principally the area of the grid was determined

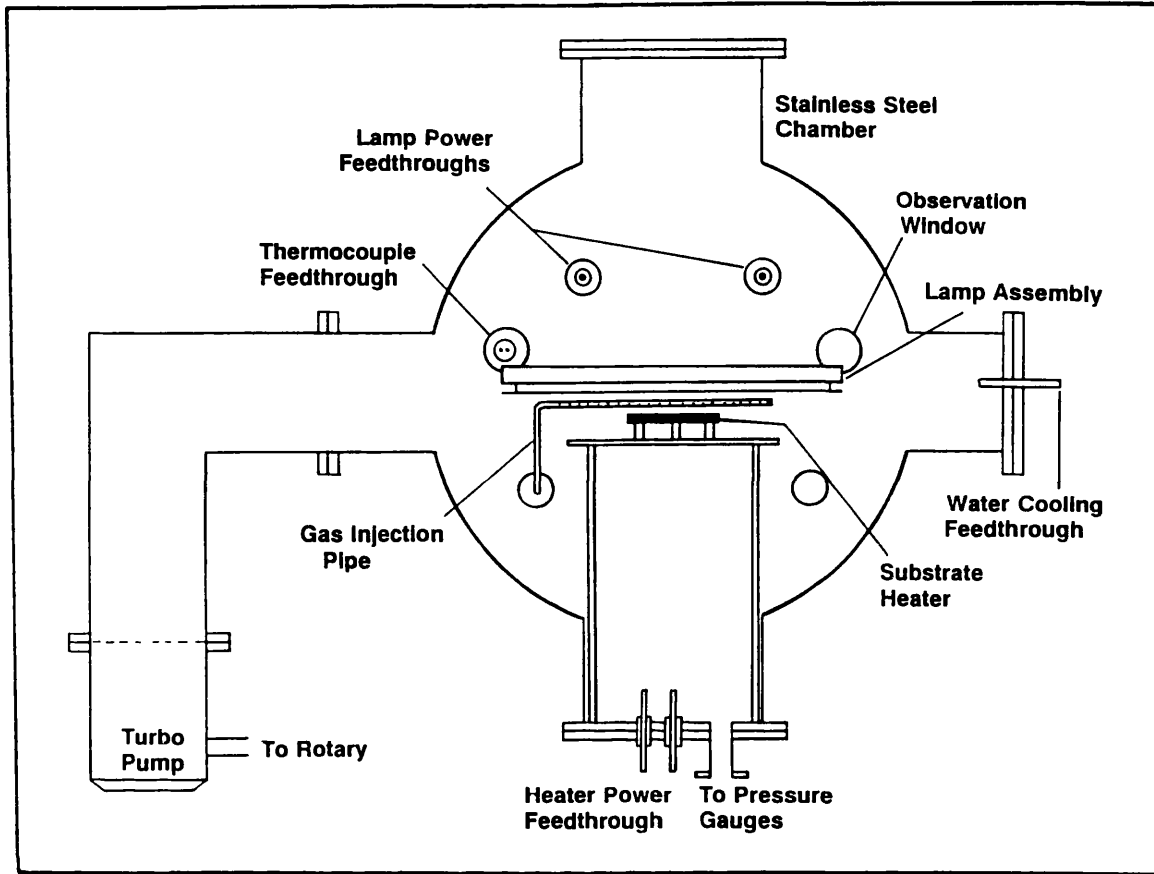


Fig.2.5 Schematic outline of UV/ozone oxidation system.

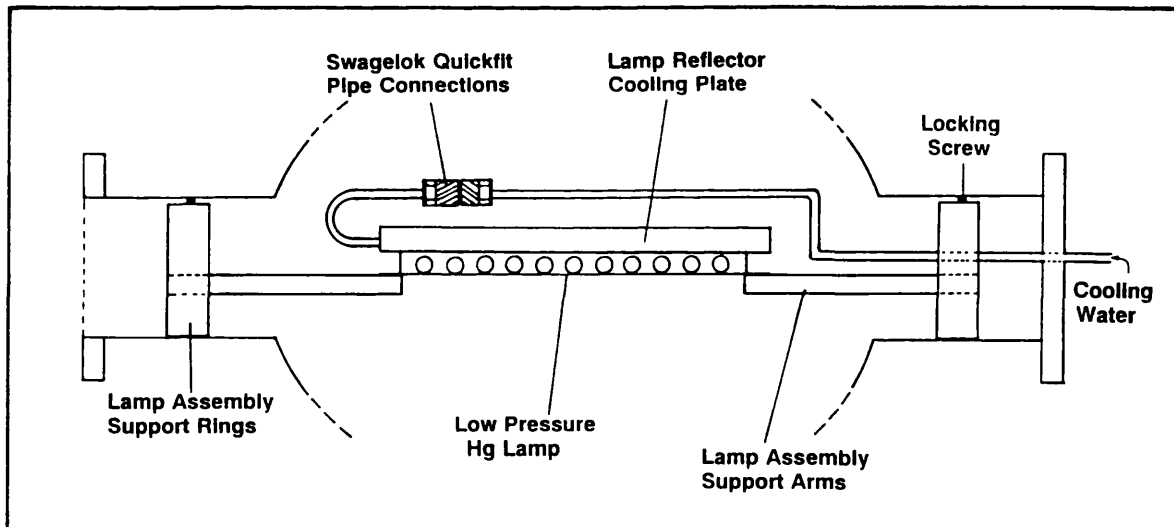


Fig.2.6 Schematic outline of lamp support structure and reflector cooling supply.

by the internal diameter and length of the chamber. The lamp was held to its aluminium reflector by thin steel wire. Lamp efficiency was strongly determined by grid temperature and was recommended to lie between 40-60°C. To cool both the reflector and lamp a large copper cooling plate was constructed and cooling water was flushed through the plate. Reflector and cooling plate are held together in contact by screws. Power to the lamp was supplied via high voltage (stable to a signal of 10^5V) ceramic insulator feedthroughs. Electrical cables inside the chamber were insulated with alumina ceramic beads. A spark voltage of nominally 7.5kV was necessary to ignite the lamp. After the initial start up the voltage dropped to 3kV and the current flowing was 120mA (a.c.). Stable output was achieved after approximately 3-4 minutes.

The lamp assembly was held in position by two support arms emerging from the smallest opposing chamber ports. This is shown in more detail in Fig.2.6, along with the water cooling pipe connections. The water supply pipes were 1/4inch diameter stainless steel. Swagelok quickfit vacuum compatible fittings were used to connect the supply pipes to the cooling plate inlet and outlet. Cooling plate temperature was maintained between 12-15°C. Initially the lamp operation was severely limited by over- heating. However, by increasing the flow rate of cooling water so that the reflector temperature was $<15^\circ\text{C}$ stable operation was possible over most experimental conditions with the exception of reduced external gas pressure. Heat loss from the grid was mainly convective because the contact area between it and the reflector was small. Therefore, by reducing external gas pressure, heat loss was also decreased causing the lamp to overheat. An increase in lamp temperature had the effect of raising the internal mercury gas pressure. In control experiments it was found that the lamp would operate continuously up to a critical grid temperature of around 110°C. Beyond this temperature the internal gas pressure rises sufficiently to reduce the mean free path of the mercury ions to the point that the current flowing via the discharge falls. The lamp then begins to flicker randomly or even switch off. During this period the lamp cools and internal gas pressure

diminishes until the lamp reignites. Lamp temperature also controls its efficiency and thus the output flux density. It was very important to maintain the reflector temperature to a stable value during oxidation experiments. For most of the experimental period the cooling water was obtained from a shared recirculator. On occasions when other demands on the system were high the efficiency of the lamp dropped. By operating when demand was low it was possible to obtain reproducible results. In the final series of experiments a dedicated water supply with a high flow rate was used improving lamp efficiency. A simple visual check of the lamp emission colour indicated whether the lamp was warm. At lower lamp temperatures the emission appeared white with a bluish tinge. Once the lamp warmed up (typically $>55^{\circ}\text{C}$) a greenish tinge was observed. In the experiments detailed below it was found that lamp temperature was influenced by the substrate heater temperature (particularly when $>400^{\circ}\text{C}$) and thus the likely light output was slightly different for the various growth temperatures under study. A method to overcome this difficulty is described below in appendix B.

The grid lamp functioned under two external pressure ranges. Near atmospheric pressure (and higher) it ran continuously if cooling water was maintained to hold the reflector temperature at $<15^{\circ}\text{C}$. The other pressure range lies below $=10^{-3}\text{mbar}$ but only for a limited period ≈ 40 minutes. This was the time it took for the lamp to reach its critical temperature. In the intermediate pressure range (500mbar to 10^{-3}mbar), the high voltage necessary to discharge the lamp actually discharged the external gas because its resistance to current flow was smaller than that of the lamp gas. Such a discharge should be avoided under all circumstances due to its detrimental effects on electronic components in the system, reactive gas ions formed can attack hydrocarbons, fluorocarbons and even corrode metal surfaces severely. Deposits of a hard carbon-like material were noted after accidental external gas discharge. These proved very difficult to remove and reduced system cleanliness.

Although the main difficulty of overheating was overcome problems still

occurred when the substrate heater, Fig.2.5, reached temperatures $\approx 550^{\circ}\text{C}$. Infrared radiation from the heater was absorbed by both the lamp and the reflector and given sufficient time could lead to the overheating noted above. For such high heater temperatures small decreases in the flow of coolant pushed the lamp into instability. On occasion this happened when other demands on the cooling supply were high.

(b) Sample temperature control was achieved using the configuration illustrated in Fig.2.7.

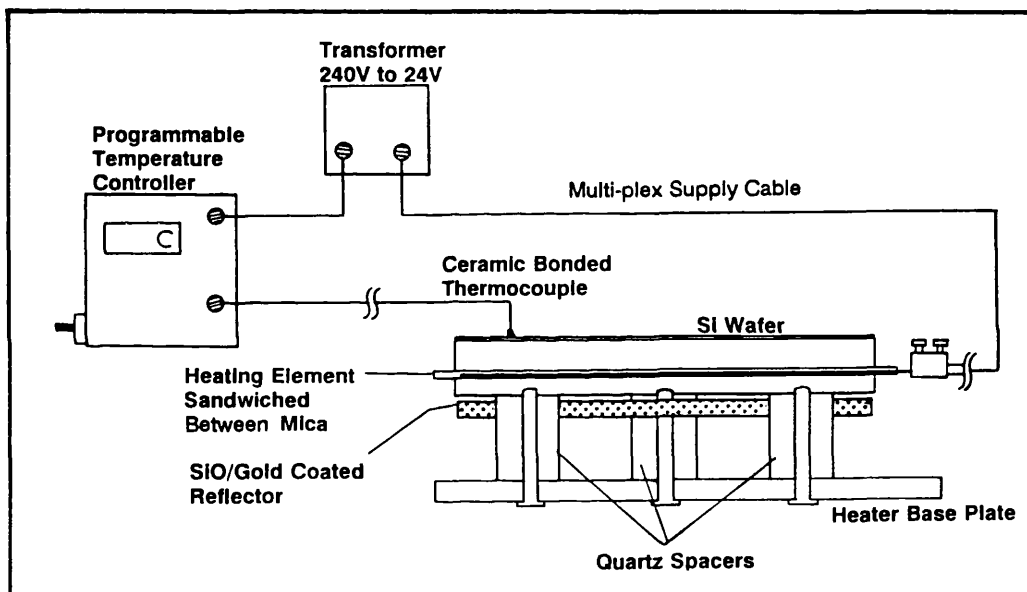


Fig.2.7 Substrate heater and temperature control configuration.

A type K (chromel/alumel) thermocouple was connected to a programmable controller which both monitored and maintained sample temperature at a given value. Resistive heating of a molybdenum filament clamped between two stainless steel plates was used to raise sample temperature. The filament had a resistance of 2Ω and a 24V, 15A signal was applied to it. The maximum temperature possible was just $>550^{\circ}\text{C}$. A curve of time to temperature is plotted in Fig.2.8. Clearly temperatures below 450°C are achieved in a relatively short time. This finite period has an important consequence for the experimental growth data particularly for times <40 minutes and more so for higher growth temperatures. To study this "heating up" period several control samples were grown and are

discussed below. Beyond 550°C the temperature was difficult to maintain and also caused lamp overheating. Initially using the original heater arrangement it was difficult to heat samples to even 500°C. Also, although the heater was held 20mm above the support base by 3 quartz spacers, the base temperature was very rather high, >300°C. Much of the energy from the filament was emitted downwards because the lower heater plate was thinner than the upper plate. To overcome this difficulty a thin film IR mirror was placed just below the heater. The mirror was produced by vacuum evaporation of a visibly opaque gold layer on to quartz. A thin SiO layer was then evaporated to act as a protective coating. Gold is an efficient IR reflector and was chosen both for convenience of fabrication and because of its unreactive nature in the ozone ambient. It was found that with the mirror in place the base temperature was reduced to about 100°C.

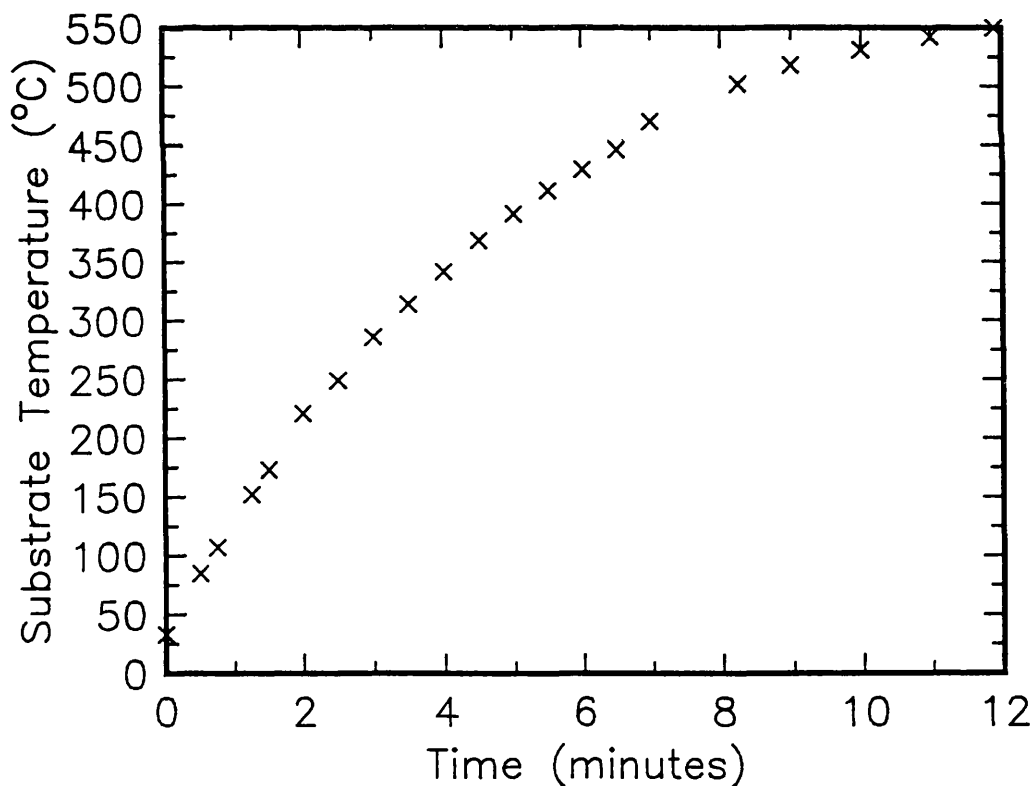


Fig.2.8 Substrate heating time required to achieve growth temperature.

As noted above sample temperature was monitored with a thermocouple. The thermocouple was bonded to a silicon wafer (with ceramic adhesive) which was mechanically held on to the top of the heater.

Silicon samples placed on the wafer were therefore less likely to pick up contamination from the hot stainless steel surface and any small heating effect due to radiation from the lamp was also accounted for. By temperature profiling the heater surface the variation was found to be $\pm 5^{\circ}\text{C}$. In addition the controller maintained temperature to within $\pm 5^{\circ}\text{C}$ of the set value.

(c) The preferred material of construction for all the components was stainless steel (type 316). Vig (1985) has shown that it is more resistant to attack from ozone than aluminium. However, the use of copper and aluminium was unavoidable for some components. Only parts that remained cool during the ozone oxidation experiments were constructed from these materials. Copper especially, oxidises very rapidly when heated in ozone and should be avoided where possible. All parts of the system were solvent and detergent cleaned prior to assembly after which the chamber was pumped down to 10^{-6} mbar for 48 hours and internally heated by the substrate heater. For short periods the lamp was also switched on to assist out-gassing. UV light is known to assist removal of surface adsorbates, particularly water, which is the major surface contaminant.

To avoid oil vapour contamination in the system a turbo-molecular high vacuum pump (backed by a conventional fomblinised rotary pump) was used. In general O-ring seals were used where convenient, but on fittings requiring little or no disassembly either copper gasket or indium wire seals were used. Care was taken to avoid excessive heating ($> 100^{\circ}\text{C}$) of parts with indium seals due their limited temperature stability. The chamber pressure was measured using a Pirani gauge from atmosphere to 10^{-3} mbar and a Penning from 10^{-3} to 10^{-7} mbar. Most of the vacuum assembly including the cooling plate, vacuum flanges/fittings, the lamp and heater support structures gas transport and injection systems were designed by myself and manufactured by the engineering workshop.

d) Only N_2 and O_2 were used in the system. Both gases were electrograde as supplied by the British Oxygen Company. High purity regulators and

electropolished stainless steel pipes were installed to transport the gases from the bottles to reaction chamber. Because only non-corrosive gases were transferred Swagelok connections were used where necessary. **Fig.2.9** shows the gas system schematically. A high vacuum stop valve was installed so that the gas line could be shut off during chamber pumping. The gas flow rate was controlled by adjusting the regulator pressure and fine metering needle valve. When all impediments to gas flow were removed up to the gas bottle regulator it was found that a chamber pressure of $<10^{-6}$ mbar could be maintained by the turbo pump indicating a low leak rate from the gas lines. Prior to injection the gas was filtered with a 0.1micron "point of use filter" to reduce any particulates originating from the gas system. The gas was injected into the chamber immediately below the lamp (see **Fig.2.5**) to ensure that a build up of gas impurities did not occur in the vicinity of the sample because of low gas flow rates during growth experiments ($<40\text{mls}^{-1}$).

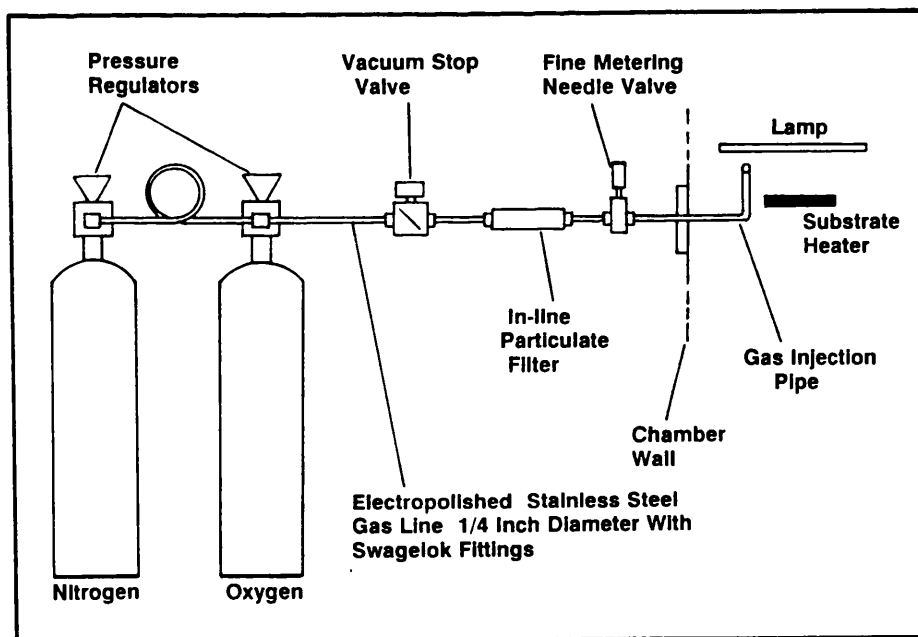


Fig.2.9 Gas delivery system to reaction chamber.

2.3 Growth Experiments

The UV/ozone growth experiments can be divided into three sections chronologically. As with all new apparatus the system and operational procedures evolved during the whole period of study. The ultimate goal was to increase the oxide thickness grown in as short a time as possible at temperatures less than 550°C. From design to initial operation a period of 6 months was required. After this two major modifications of the system were carried out and these delineate the experimental growth sections.

2.3.1 Period 1 experiments

During this period the system pumping efficiency was low because only a small 25mm diameter port was available. It was difficult to reduce the chamber pressure below 7×10^{-6} mbar even after several hours of pumping. Also because of the limited cooling water available from the recirculator lamp output was not optimised. To reduce IR energy radiated by the substrate heater reaching the lamp a suprasil quartz window was placed between them. UV was transmitted by the window but the IR blocked. Even with this configuration at high substrate temperatures the lamp temperature could rise to 110°C. The sample to lamp distance was 55mm. This distance was fixed to avoid excessive lamp heating. Separate silicon substrates* of the type used in the arc lamp studies were oxidised at temperatures ranging between 150-550°C as received from the manufacturer (Virginia). The normal growth procedure was to place the samples into the system and pump the chamber out 10^{-5} mbar for at least an hour. The chamber was then filled to atmospheric pressure with oxygen and the gas flow rate was set to approximately 70mls⁻¹. The samples were irradiated initially at near room temperature for 5 minutes. During this time the lamp stabilised and the ozone concentration increased. It is well known that low temperature UV/ozone treatments tend to remove surface hydrocarbon contaminants (see for example Vig, 1985, Ruzyllo et al., 1987 and Krusor et al., 1989). Next the substrate heater was turned on. Growth time as recorded in all the figures below is the processing time once growth temperature was achieved. After oxidation the chamber was again pumped

* Sample area was 5-7cm².

out with the rotary pump to remove any O_3 and halt the reaction and finally filled with nitrogen to atmospheric pressure. A nitrogen flow was maintained through the chamber until the sample temperature dropped to $<100^\circ\text{C}$. The sample was then removed and stored for measurement.

Results

The results of the initial growth experiments are plotted in Fig.2.10*. It was observed that the growth of oxide, while slow, was very much temperature dependent. However the difference in oxide growth at 500°C and 550°C became small. This indicates that thermal processes may be influencing the gas dynamics in the chamber.

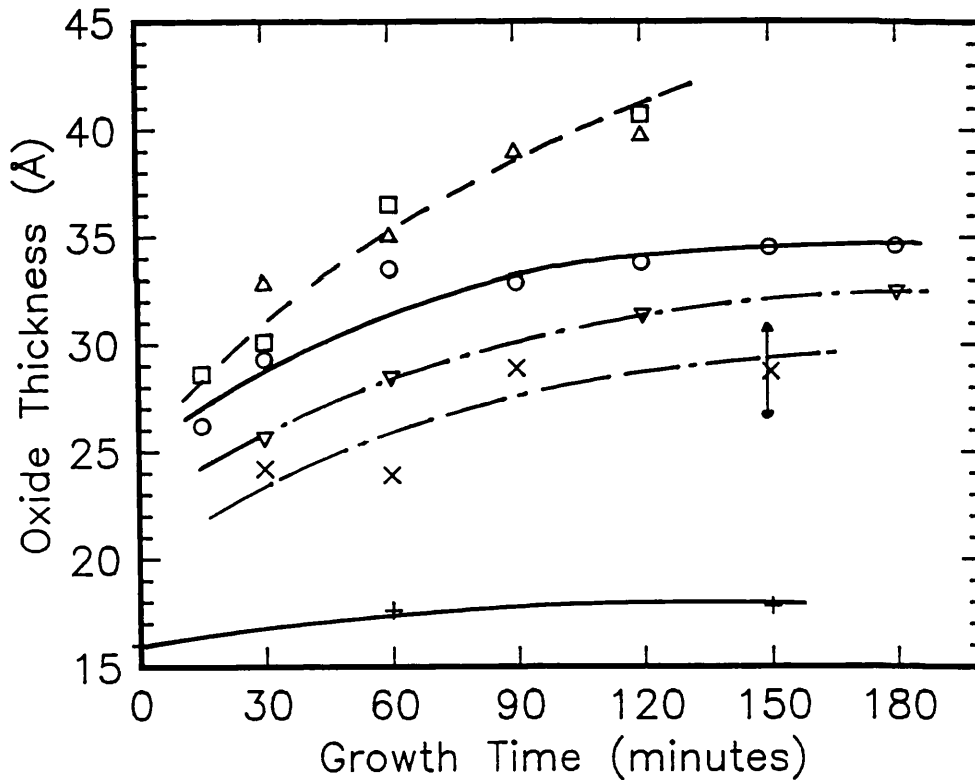


Fig.2.10 Period 1 UV/ozone oxide growth as a function of substrate temperature, \square 550°C , Δ , 500°C , \circ , 450°C , ∇ , 350°C , \times , 250°C , $+$, 150°C .

It is well known that the O_3 molecule lifetime is strongly dependent upon its temperature (equation 2.6). Thus gas heating at substrate temperatures beyond 500°C may be sufficient to reduce O_3 concentrations substantially. Certainly thermal oxidation of Si to produce layers of the thickness observed at the respective temperatures would require periods of

* Where curves are drawn on the data in this section (2.3) they are simply as an aid to the eye.

time that are orders of magnitude greater (see Fig.1.6).

2.3.2 Period 2 Experiments

During the initial experiments it was also found that the growth results were affected by the native oxide layer present on the Si. The effect of the uncontrolled air ambient during storage was removed by stripping the native oxide with a dilute (0.5%) HF dip. This improved the reproducibility of the data. The heater reflector was introduced into the system to reduce heat loss from the heater and therefore also reduce the total heat input to the reaction chamber. Also the flow rate of cooling water was increased so that the maximum lamp temperature did not rise above 90°C. Finally a large diameter, 100mm, vacuum elbow was installed to improve the pumping efficiency of the system. The turbo pump input also had a 100mm diameter orifice.

Oxidation was carried out on a variety of samples to compare the effects of:

- a) surface orientation between Si $\langle 111 \rangle$ (p-type 2-6 Ω cm) and $\langle 100 \rangle$ (p-type 0.1-1 Ω cm). Prior to growth the oxide was stripped and the Si was washed for 5 minutes in deionised (DI) water (13-14M Ω cm).
- b) Si $\langle 100 \rangle$ which had 2 different surface treatments , dilute HF(5 minutes) followed by DI H₂O rinsing for 5 minutes or dilute HF(5 minutes) followed by the bomb clean (H₂O₂:H₂SO₄ for 5 minutes) and 5 minutes rinsing in DI H₂O.
- c) The effect of surface irradiation with light from the lamp. This was done by shadowing samples on the heater with a stainless steel sheet approximately 5mm above their surface but still allowing the O₃ ambient to reach them. These samples will be identified as covered (c) and uncovered (uc) in the discussion below. In all comparative experiments oxides were grown simultaneously to avoid any process repeatability problems. This ensured that the growth process was always the same for comparison experiments.
- d) a series of control experiments was also carried out to observe the thermal oxide growth in the system at 500°C. These were particularly

important because they allowed the effect of any system peculiarities such as a possible excess of moisture in the oxygen to be determined. Also the oxide thickness grown during the warm up period for different oxidation temperatures was noted.

The growth procedure was modified slightly for this series of experiments. All samples were loaded into the growth chamber after chemical processing within 20 minutes; however, because the growth kit was not in a clean room environment, particulate or adsorbed contaminants could not be avoided. After loading the chamber was pumped down to 10^{-5} mbar and the Hg lamp switched on for 10 minutes. UV radiation from the lamp both directly and by warming the Si surface was observed to reduce adsorbates. During this low pressure radiant heating the temperature of the sample was observed to rise to $\pm 100^{\circ}\text{C}$ and the gas pressure increased typically to 5×10^{-5} mbar implying desorption from the internal surfaces. Chamber pressure was again allowed to fall to 1×10^{-5} mbar before being filled to atmospheric pressure. Gas flow rate was set to 37ml/s. The remaining steps were the same as in period 1. Oxides were grown at substrate temperatures of 350°C and 500°C . During this period of experiments it was noted that occasionally large random discrepancies occurred in the growth data. For some time it was believed that these originated from processing irreproducibility. On investigation it was discovered that they could be traced to the sample storage containers (commercial "chip" trays). Oxide growths were carried out at University College but thickness measurements were taken at Imperial College. Often samples were stored for a few days prior to measurement. The thinner layers produced with very short oxidation times were stored for as small a time as possible. Samples showing a high degree of non-uniformity and unusually high thicknesses were washed in iso-propyl alcohol to remove hydrocarbon layers adsorbed from the storage containers. It was also possible that with such thin layers the oxide would continue growing in the air. To examine this possibility some 350°C growths were repeated and the samples taken to IC immediately for measurement. All the growth data

presented in Fig.2.15,16 was taken without any storage delay after growth (i.e. on the same day within 2 hours).

Results

a) Fig.2.11 shows the growth of oxide on HF dipped water washed Si for both $\langle 111 \rangle$ and $\langle 100 \rangle$ orientations. As with thermal oxidation at high temperature the $\langle 111 \rangle$ surface has a higher reaction rate. This result is contrary to the oxidation study by Taft in O_2 which shows no orientation dependence at low temperatures for such thin layers. It is important to note that for short times i.e. <40 minutes the oxide thickness tends to be more of a result of pre-growth time oxidation. Room temperature oxide growth in an ozone environment is well known. The growth rates in such thin layers are very high and therefore the influence of the lamp stabilisation and heat up periods are more significant for shorter growth times. The growth rates appear to be very similar.

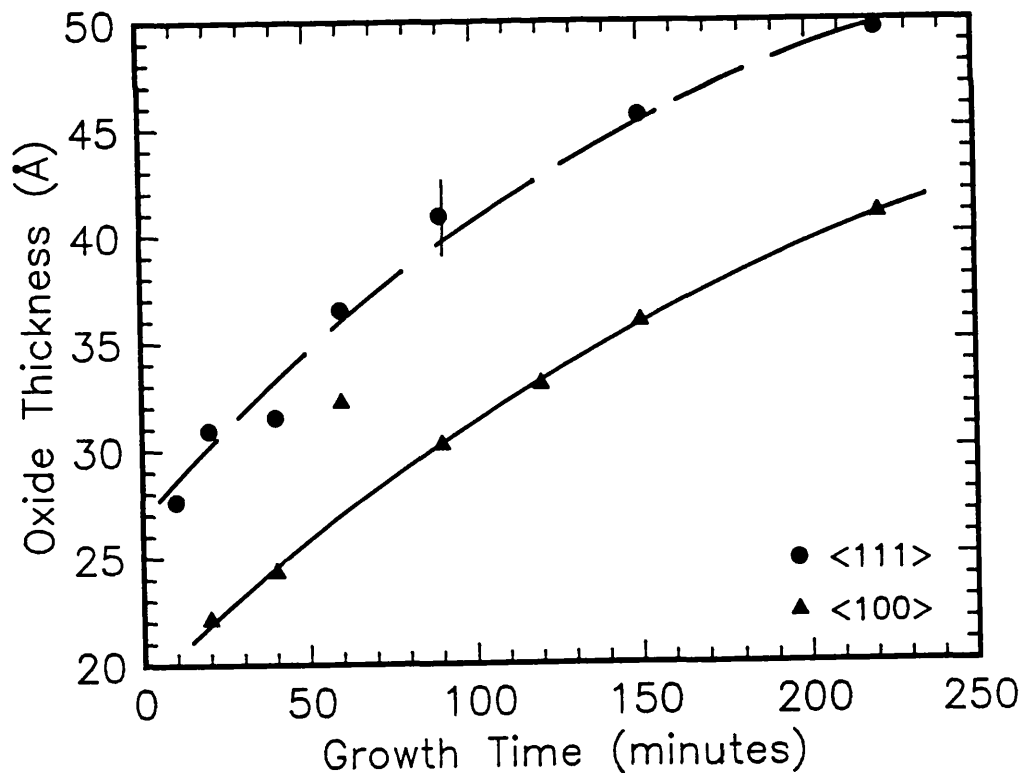


Fig.2.11 Orientation dependence of oxide growth at 350°C.

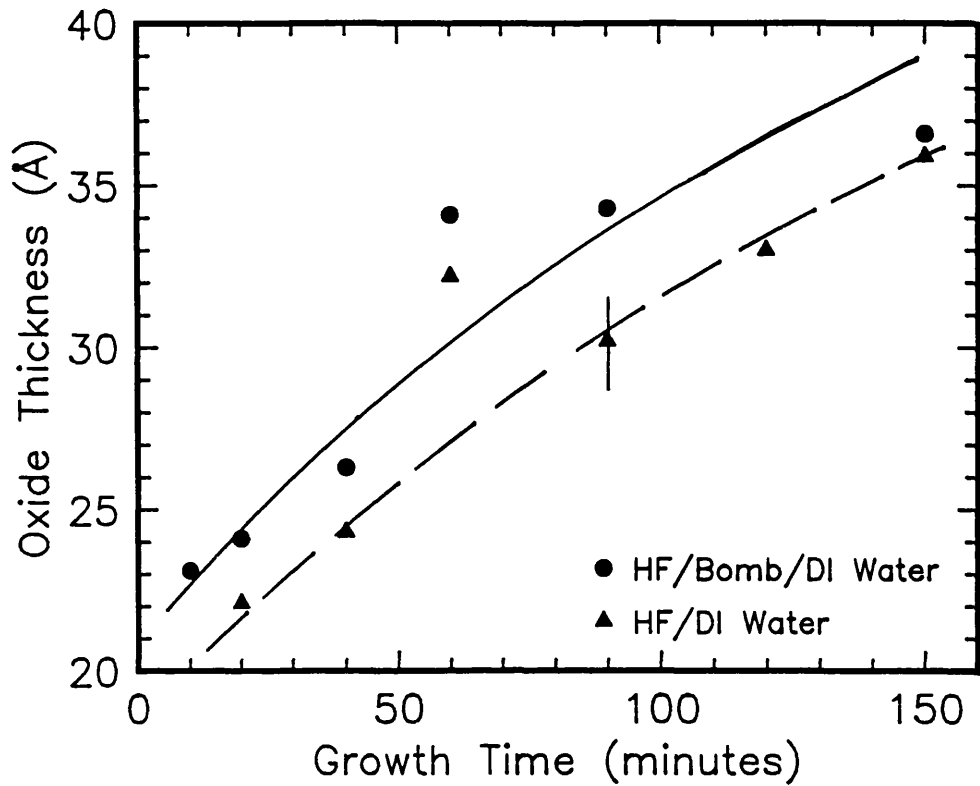


Fig.2.12 The effect of surface preparation on oxide growth at 350°C.

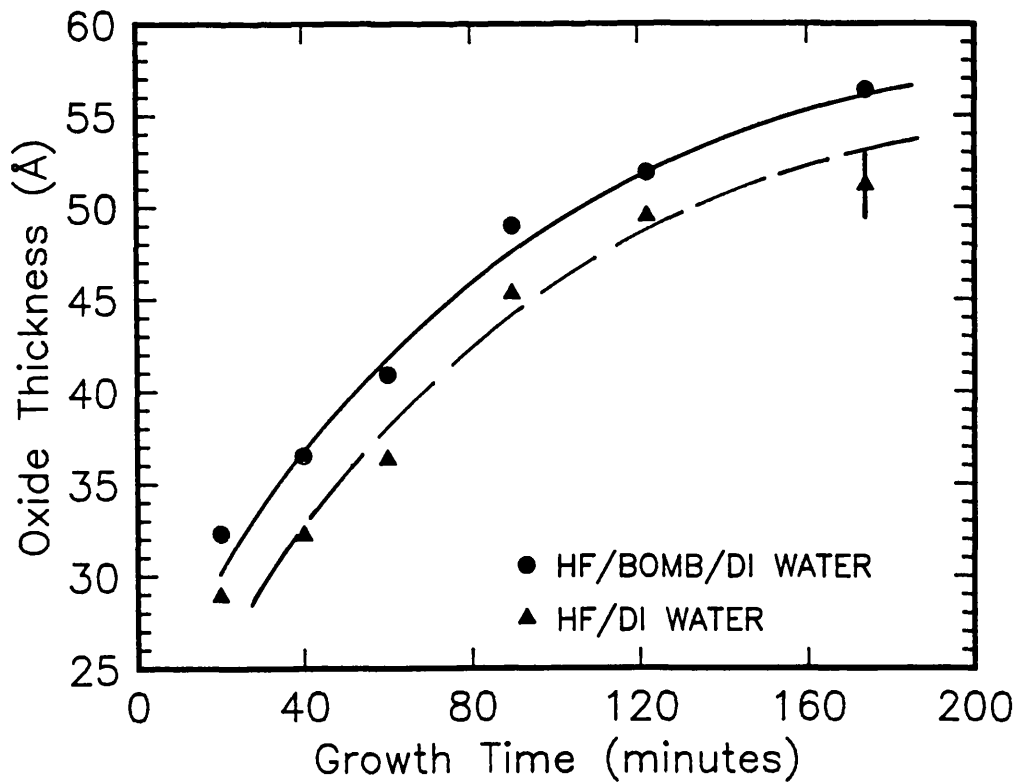


Fig.2.13 The effect of surface preparation on oxide growth at 500°C.

b) The effect of surface preparation is noted in **Figs.2.12,13** for 350°C and 500°C respectively on <100> Si. At 350°C the difference in the two surface preparations was small although on average the bomb cleaned samples were thicker. At 500°C the trend was much more distinct. Bomb samples were thicker by an almost constant value (≈ 4 Angstroms). This suggested that any offset was just the difference in the initial oxide produced by the chemical preparations. Growth kinetics for bomb and HF dipped Si appeared to be very similar. From **Fig.2.12** it can be seen that the data for 60 minutes are high. This is a typical example of one of the spurious "growth runs" and is most likely linked to contamination but the difference in thickness between the different preparations is still evident (similarly the data for 60 minutes in **Fig.2.14** from this run is also "high").

c) To observe the effect of UV surface irradiation covered and uncovered samples were grown simultaneously at 350°C on <100> Si after native oxide removal by dilute HF. In **Fig.2.14** the (c) and (uc) data are plotted upto a growth time of 220 minutes. The main conclusion one can draw was that below ≈ 30 Angstroms (100 minutes) surface irradiation did not affect growth substantially. Beyond 30 Angstroms there was a notable divergence between the (c) and (uc) oxides. As noted above it was suspected that long delays after oxidation and before measurement could affect the thickness values measured particularly for very thin oxides (<30 Angstroms). To test this hypothesis the (c) and (uc) oxidations were repeated for growth times between 20-120 minutes, **Fig.2.15**. Once again the results for the two lots were similar with the (c) being just thinner. As stated previously every data point plotted is the mean of at least 12 measurements over 4 points on the samples. The standard deviation from the mean was typically between 1-1.5 Angstroms. What is important to note is that the second set of oxides are only marginally thinner than the stored batch suggesting that further oxidation is small, but occasional contamination can occur. Similar experiments at 500°C for long growth times (>3 hours) also showed that (uc) samples had thicker oxides, but, there was insufficient time to obtain a full data set.

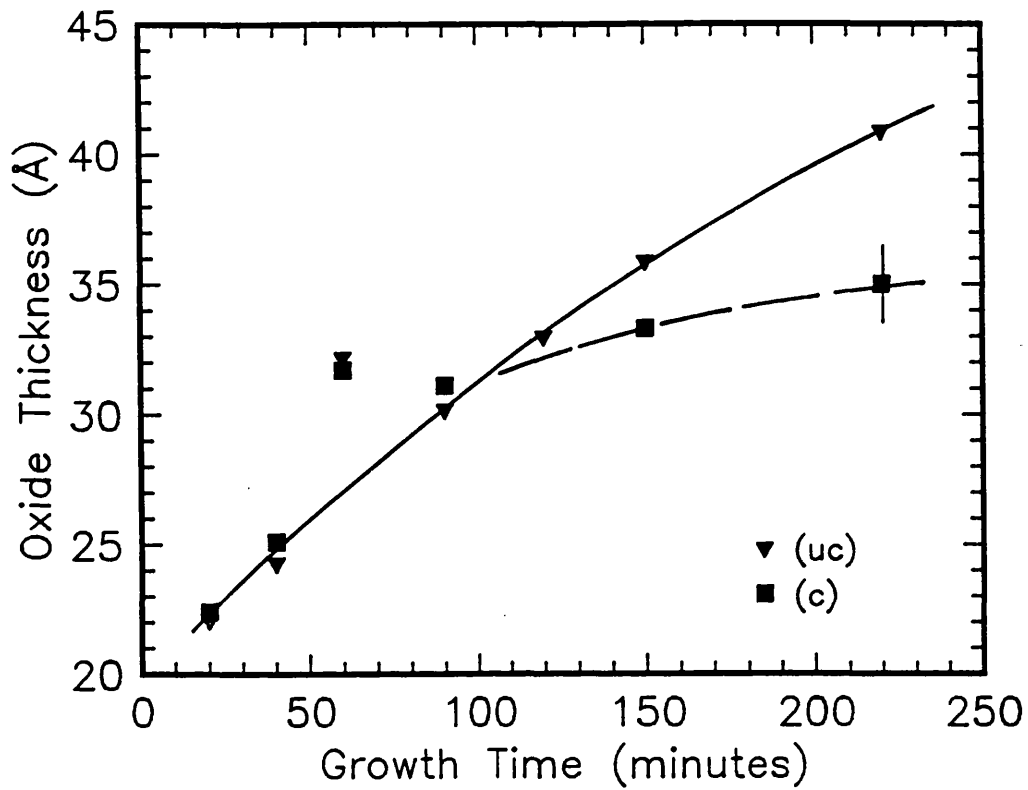


Fig.2.14 Oxide growth on covered (c) and uncovered (uc) Si at 350°C (stored samples).

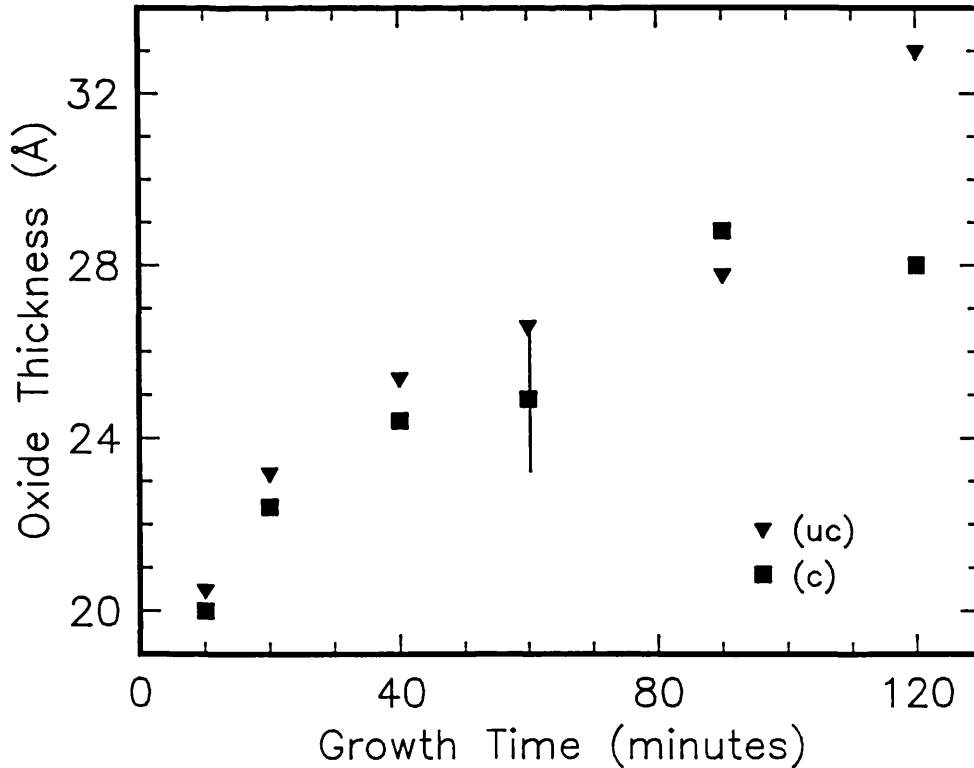


Fig.2.15 Repeated (c) and (uc) growth at 350°C (measured without any sample storage time).

d) For control experiments Si samples prepared in a similar fashion to the UV/ozone experiments were oxidised at 500°C, Fig.2.16. All the processing steps were carried out as above except that the lamp was not switched on after the chamber was refilled with oxygen to atmospheric pressure. As expected the oxide growth rate is extremely slow after the initial formation of about 20Å. Also plotted are the thickness of oxide formed during the warm up period to 350 and 500°C, plotted at 0 growth time (the outline symbols are for 350°C). It is quite clear that a very thin oxide layer can be formed very rapidly in comparison to native oxide growth (this agrees with the study of Ruzyllo et al., 1987) and that substantially faster oxide growth is a direct result of the presence of UV/ozone. Thermal oxidation at 500°C follows that observed by Taft (see Fig.1.6).

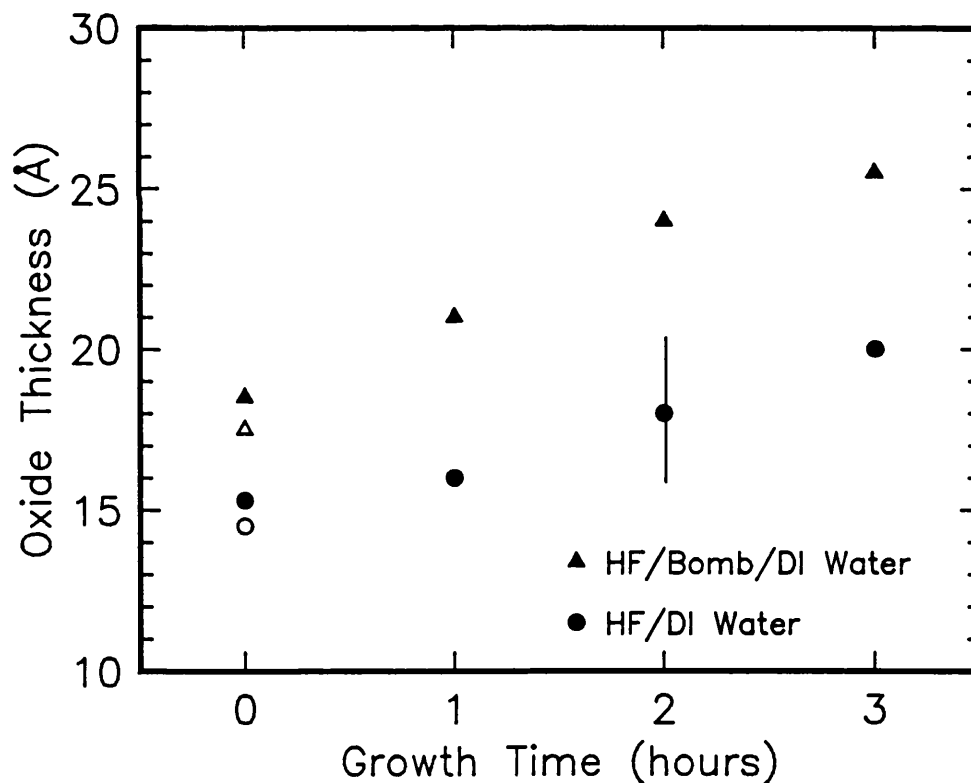


Fig.2.16 Thermal oxide growth (i.e. without UV/ozone) at 500°C in the reaction chamber. The data at 0 time are the oxides grown during the period for the sample to reach growth temperature (outline symbols are for temperature to reach 350°C only).

2.3.3 Period Three Experiments

The final series of oxidations were performed after two major changes to the experimental system. Firstly a new oxygen gas bottle was installed and secondly due to failure of the cooling water recirculator a direct independent tap water line was installed. The tap water had a higher flow rate than the recirculator and maintained reflector temperature at $\pm 12^{\circ}\text{C}$. Previously the lowest reflector temperature was $\pm 15^{\circ}\text{C}$. This meant that the lamp temperature during operation was stabilised to $\pm 65^{\circ}\text{C}$. Oxygen gas was again specified as Electrograde (semiconductor industry standard), however it was noted that the new bottle was 99.997% O_2 in comparison to 99.7% previously purchased.

Most oxides grown during this period were aimed toward capacitor fabrication for electrical measurements. Unfortunately due to the long installation time for the tap water supply only a limited number of growth runs was possible. The gas flow rate was believed to be an important factor with respect to the O_3 density generated in the reaction zone. Oxides were therefore grown at 500°C with gas flow rates of 8mls^{-1} and 24mls^{-1} .

Results

With the improved lamp cooling maintaining lamp temperatures close to the manufacturers recommended values and the lower gas flow rates substantially thicker oxides were produced for growth times and substrate temperatures similar to those used in periods 1 and 2. Oxide thickness grown in 1 hour with a gas flow rate of 8mls^{-1} over the temperature range $350\text{-}550^{\circ}\text{C}$ is plotted in Fig.2.17. Previously at 350°C ± 27 Angstroms was grown under period 2 conditions. This was improved to ± 30 Angstroms. For higher temperatures though the oxidation process was much more efficient, e.g. at 500°C a ± 55 Angstrom oxide was produced in comparison to ± 36 Angstrom in period 2.

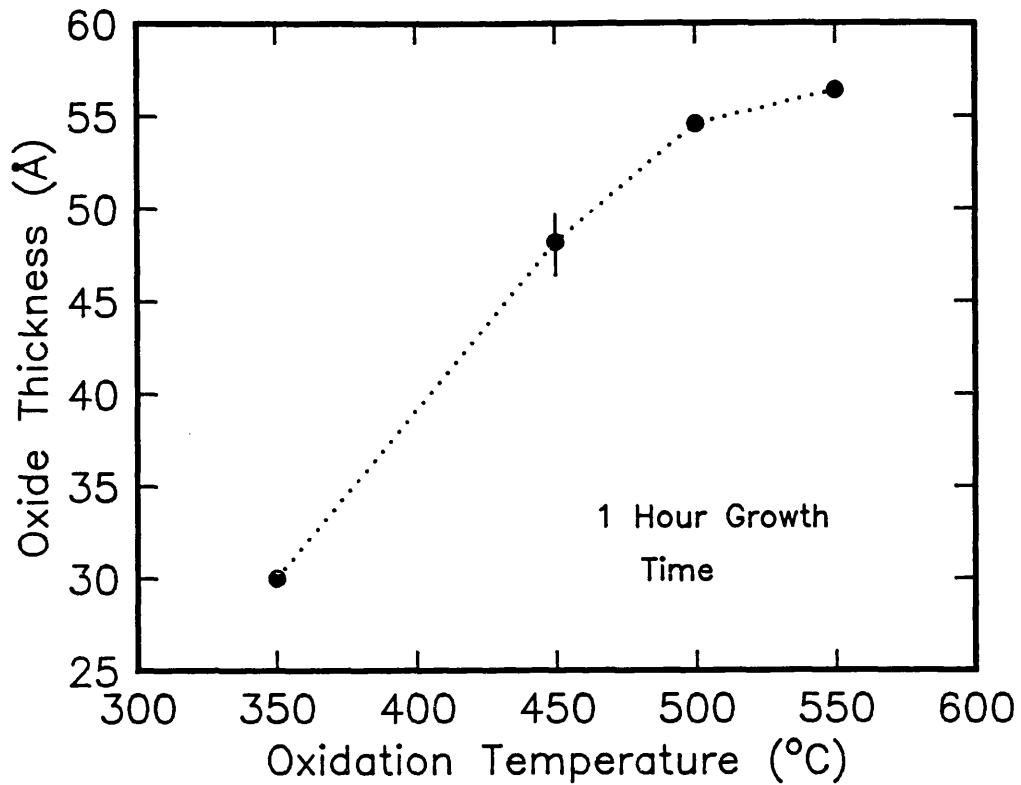


Fig.2.17 Oxide grown in 1 hour as a function of substrate temperature for a very low gas flow rate (8ml/s).

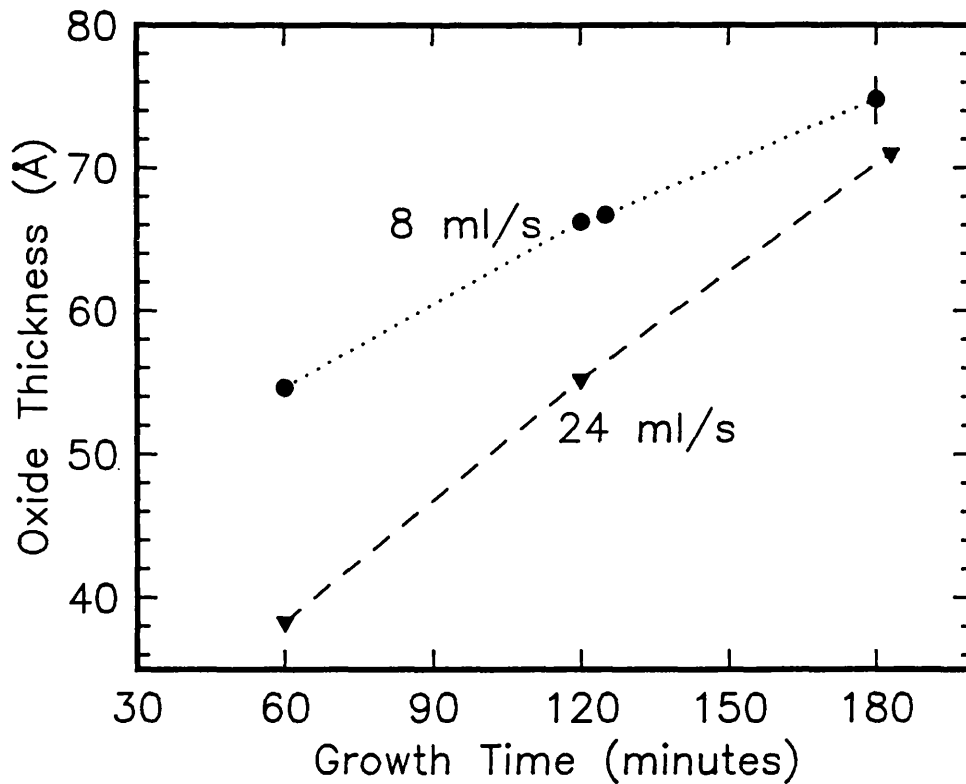


Fig.2.18 Oxide grown with a substrate temperature of 500°C for two gas flow rates.

Fig.2.18 shows the oxide grown at a temperature of 500°C with two gas flow rates. With 24mls⁻¹ the oxide growth was diminished particularly for shorter growth times. Therefore it was likely that increasing gas flow reduced the O₃ content of the reaction zone and thus the oxidation rate fell. What is important to note is that oxides of electronically "useful" thickness can now be grown using the UV/ozone technique.

2.4 Analysis and Identification of Oxide Growth Mechanism

From section 2.3 certain conclusions can be drawn about both the experimental apparatus and more generally UV/ozone stimulated oxide growth. These are:

- i) Oxide formation increases with substrate temperature but as the oxide gets thicker the growth rate falls.
- ii) Substrate temperature increases above 500°C only improve growth rates slightly.
- iii) The effect of different surface preparations on growth rate is small.
- iv) Oxide thickness increases with decreasing gas flow rate and improved lamp efficiency.
- v) Oxide growth on both covered and uncovered surfaces is similar but diverges significantly (**Fig.2.14**) as thickness increases (covered Si oxidation is slower).

In this first half of this section the relationship between gas flow rate and ozone concentration is explored. The time dependent build up of O₃ was measured by UV absorbance. The O₃ concentration was noted and an upper limit on this was calculated. The second half of this section is used to try to identify the actual growth mechanism. Previously low temperature oxidation of Si in O₂ was suggested to follow Cabrera-Mott (CM) kinetics by Fehlner (1972).

2.4.1 Gas Phase UV/ozone Analysis

The O₃ concentration below the lamp was found by measuring the level of 254nm light reaching a UV sensitive photodiode placed under the lamp. As shown in **Fig.2.3** 254nm wavelength light is strongly absorbed by O₃. A

wide bandwidth of light was emitted by the lamp ranging from the UV to visible. To select the 254nm line a thin film narrow band filter was employed. The current generated by the diode was amplified and converted to a voltage read by a digital multimeter. Fig.2.19 illustrates the arrangement. The absorption coefficient (α) for an atmosphere of O_3 at 254nm is 120cm^{-1} . The diode output was linear, and hence directly proportional to the incident flux. By applying the expression for the propagation of light intensity I , through an absorbing medium,

$$I = I_0 \exp(-\alpha d) \quad (2.8)$$

an effective α (α_e) can be calculated for a known distance from lamp to detector d .

$$(\alpha_e/120\text{cm}^{-1}) \times 100 = \% \text{ of } O_3 \text{ under the lamp} \quad (2.9)$$

A large gas flow rate of 140ml/s was used to demonstrate its effect on $[O_3]$ clearly. The diode distance was either 25mm or 50mm from the lamp. To determine the output of the lamp (I_0) measurements were taken in nitrogen.

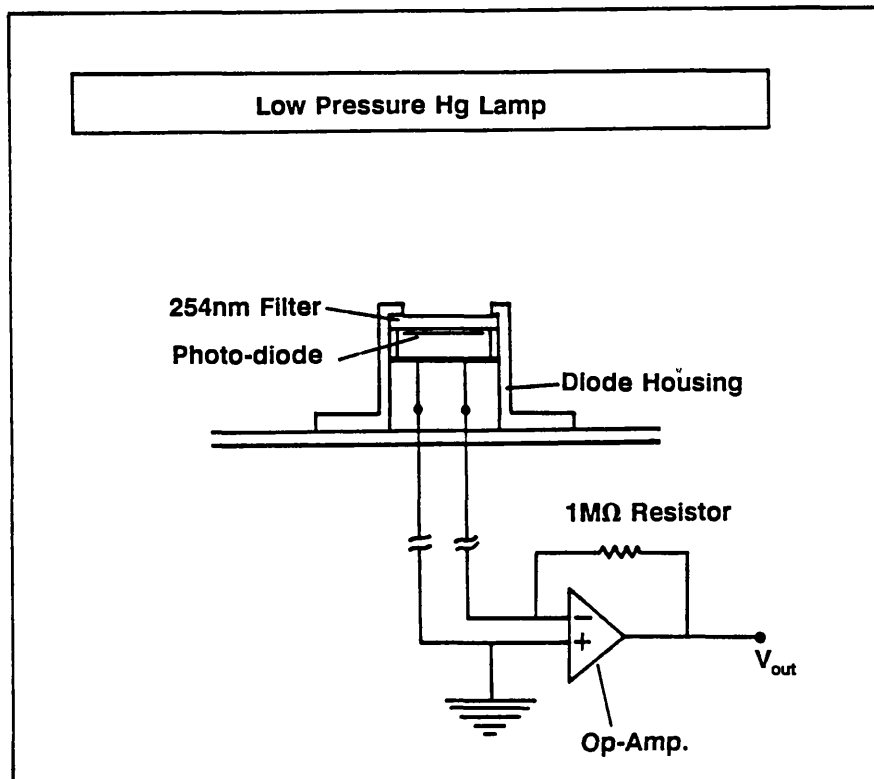


Fig.2.19 Experimental arrangement for UV/ozone gas phase analysis.

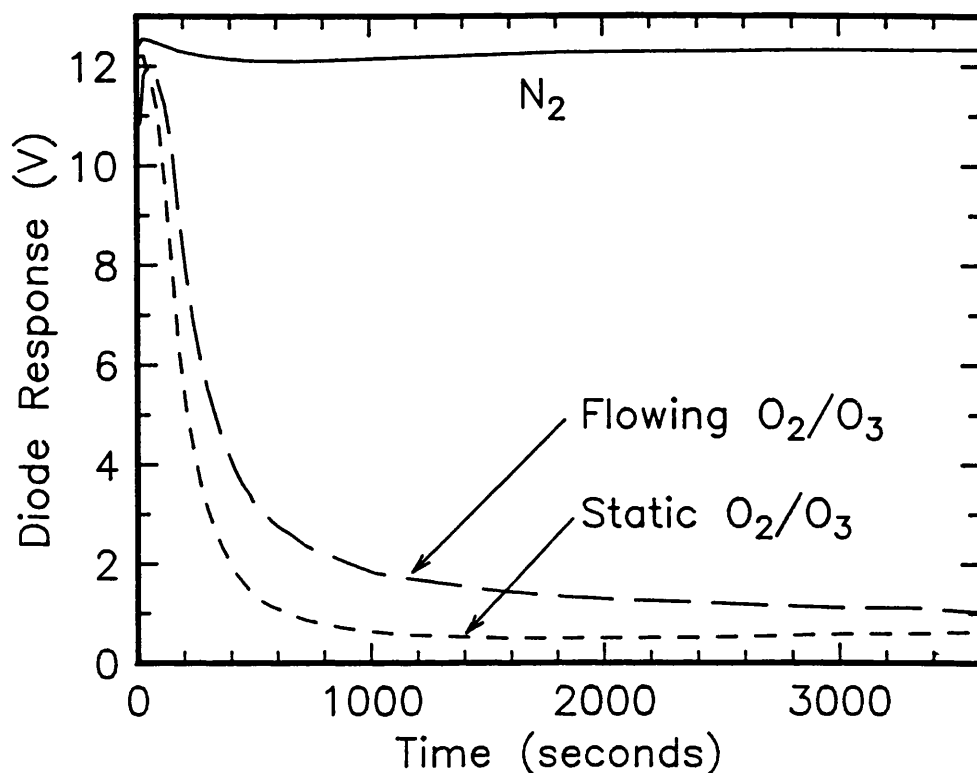


Fig.2.20 Diode response showing ozone build for different gas conditions in reaction chamber.

Fig.2.20 shows the diode voltage for a) an N₂ ambient, b) flowing O₂/O₃ and c) static O₂/O₃. It was immediately obvious that gas flow reduced the O₃ concentration because the higher diode voltage, curve b), simply implied that less of the light was absorbed. Therefore there were less absorbing molecules of O₃ than in static oxygen. **Fig.2.21a,b** show that once gas phase equilibrium is established the light intensity falls by an order of magnitude as the distance from the lamp increases from 25mm to 50mm. The flux of 254nm light reaching the Si surface is therefore likely to be very low even in flowing oxygen. It is interesting to note that the disparity in flux for the two diode distances was greater for flowing oxygen.

After the data shown in **Fig.2.20,21** was collected it was noted that the high diode sensitivity and the non-zero transmission of the narrow band filter for visible wavelengths of light was modifying the results. To avoid visible light reaching the diode a small section of the UV transmitting but visible blocking glass UG5 (as used in the arc lamp experiments) was placed over the 254nm filter. This reduced the total light intensity reaching the diode as plotted in **Fig.2.22**.

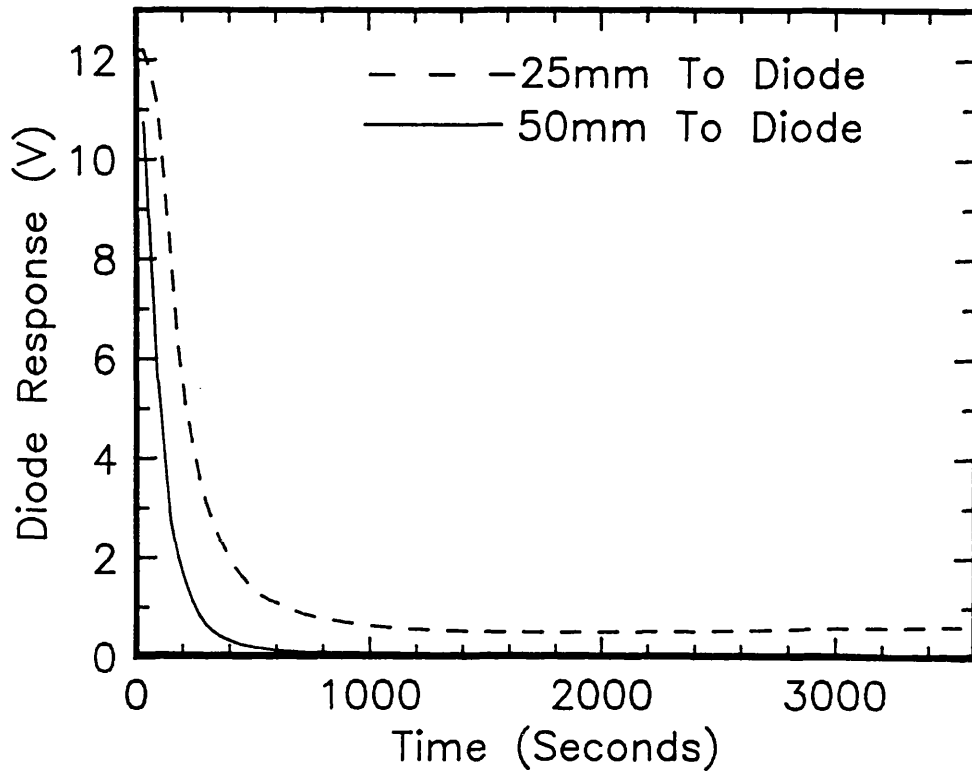


Fig.2.21a Diode response showing ozone build up for static gas for two diode to lamp spacings.

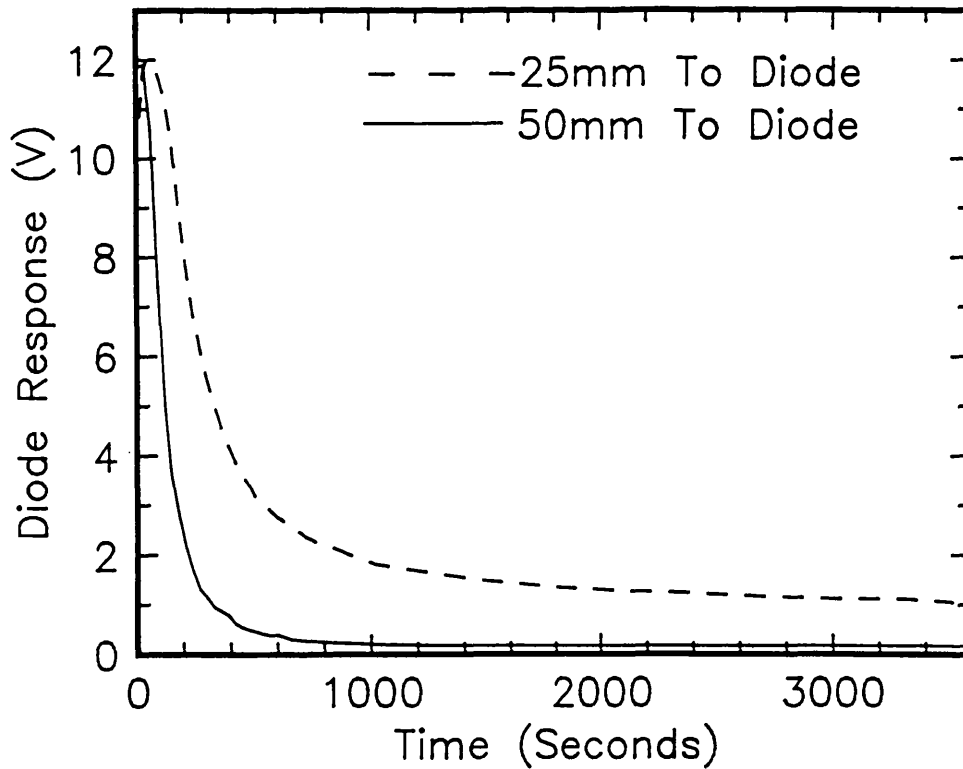


Fig.2.21b Diode response showing ozone build up for flowing gas for two diode to lamp spacings.

From the data of Fig.2.22 a correction factor and hence the corrected α_e and $[O_3]$ were calculated, shown in table 2.I, for the different measurement conditions.

Diode Distance (mm)	Ambient Condition	α_e (cm^{-1})	% O_3
25	Static O_2/O_3	1.47	1.23
25	Flowing O_2/O_3	1.25	1.04
50	Static O_2/O_3	1.36	1.08
50	Flowing O_2/O_3	1.01	0.88

Table 2.I

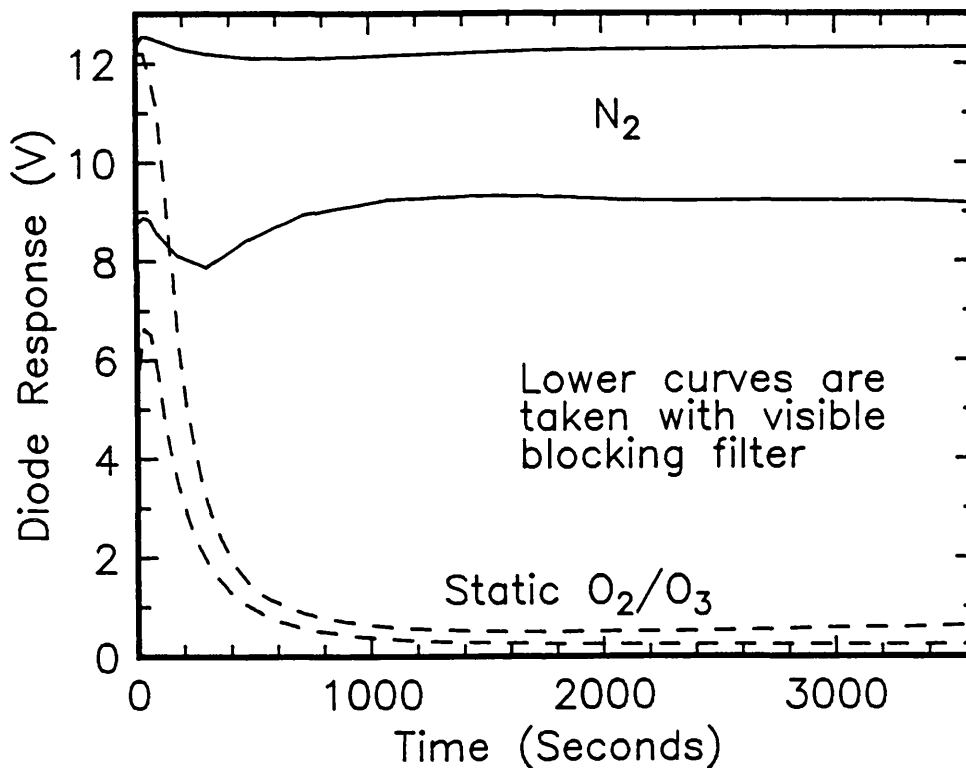


Fig.2.22 Diode response showing ozone build up with visible blocking filter in place (lower curves) compared to just the 254nm filter.

The O_3 concentration during growth would no doubt have been modified by the presence of the heater but was unlikely to exceed 1-1.2%. The effect of the heater during growth would be to circulate the gases above it. Heated gas would rise and displace gas in the vicinity of the lamp thus having a homogenising effect on the ambient ensuring that O_3 reached the

Si surface. Certainly for the final series of growth experiments (section 2.3.3) with the minimal flow rates used (8ml/s) the O₃ concentration was likely to approach 1%. In conclusion the O₃ concentration was very dependent on experimental parameters which suggests that the growth process was strongly linked to the O₃ concentration.

2.4.2 Oxide Growth Mechanism

As discussed in chapter 1 high temperature (>800°C) oxide growth kinetics have been investigated by many people for a variety of growth conditions. Many models have been formulated with a wide variety of starting assumptions. These models invariably fit parameters in the expressions to replicate the experimental data. There now exists a large body of growth data collected from in-situ ellipsometry studies on oxidation in dry O₂ over a range of gas pressures and oxidation temperatures. However no one model has been accepted although it is now believed that contrary to the linear-parabolic model of Deal and Grove (1965) the interface reaction rate is not limiting in the initial growth regime (see for example the review by Irene, 1988, and the papers by Han and Helms, 1988, and Massoud and Plummer, 1987). Data fitting to models with a large number of variable parameters is not a reliable method of identifying kinetics and therefore the growth mechanism. This was demonstrated by Ling et al. (1989) using a correlation analysis of parameter extraction (similar to the analysis discussed in chapter 3 on ellipsometric data).

In the case of low temperature oxidation very few studies have been carried out because of the long times required to grow oxide layers. Fehlner reviews the low temperature oxidation process for a variety of materials in his book (1986). The data published by Taft (1984) represent the most recent and extensive work on low temperature thermal oxides. Fehlner suggests that Cabrera-Mott growth kinetics apply to the low temperature (and reduced O₂ pressure, <10⁻²atm at high temperatures) oxidation process. In this section I attempt to evaluate which mechanism is a good candidate and propose the reason why O₃ stimulates oxidation. Recently

Reisman et al. (1987) collated thickness data for high temperature oxidation and found that the growth could be described by a power law. Following this they suggested that a power law dependence originated from the oxide stress developed by growth. Wolters et al. (1989) put forward an alternative which assumed that the fixed oxide charge dominated the transport of a negatively charged oxidant species. In the light of these recent developments the discussion below will consider linear-parabolic (LP), power law (PL) and Cabrera-Mott (CM) kinetics.

In the present study the growth data was rather limited because in-situ growth monitoring was not available. Therefore for the reasons outlined above direct fitting is not an appropriate technique for mechanism identification. There does exist another method which can be used to eliminate certain models. This is a qualitative test developed by Stoneham and Tasker (1987 and was suggested by Stoneham in a private communication). Three sets of growth data are analysed using this technique. These are the 450°C data from period 1, 350°C <111> data and the repeated 350°C <100> data from period 2. Prior to the analysis and by way of an introduction the three models noted above will be briefly discussed to high-light their differences.

Linear-Parabolic:

The discussion below follows the "classic" Deal-Grove model and can be found in any number of texts. The basic assumptions for the LP model are that the oxidant (O₂) moves from the gas-oxide boundary to the Si/oxide interface. In equilibrium the flux of oxidant across the two boundaries is equal (after the formation of an initial oxide thickness x_i). Molecular oxygen is the diffusing species under the influence of a concentration gradient. Reaction at the Si interface is a first order process. The expression derived then becomes

$$x^2 + Ax = B(t + \tau) \quad (2.10)$$

$$\text{where } A \triangleq 2D_{\text{eff}} (1/k_c + 1/h) \quad (2.11)$$

$$B \triangleq 2D_{\text{eff}} C^* / N_1 \text{ and} \quad (2.12)$$

$$\tau \triangleq (x_i^2 + Ax_i)/B \quad (2.13)$$

D_{eff} is the effective diffusion coefficient within the oxide, C^* is the equilibrium concentration of oxidant at the oxide surface and N_1 is the number of oxidant molecules incorporated into a unit volume of the oxide layer. τ is defined as the initial time (as opposed to initial oxide thickness x_i). A "characteristic" time can be defined for the process i.e.

$$A^2/4B = D_{\text{eff}}N_1/[2C^*(1/k_c + 1/h)] \quad (2.14)$$

and characteristic oxide thickness as,

$$A/2 = D_{\text{eff}}/(1/k_c + 1/h) \quad (2.15)$$

For time or oxide thickness less than the above the equation for growth (2.10) reduces to

$$x \triangleq B(t + \tau)/A \quad (2.16)$$

i.e. linear growth for $t < A^2/4B$. When $t \gg A^2/4B$ and $t \gg \tau$ then a parabolic law is evident.

$$x^2 \triangleq Bt \quad (2.17)$$

x_i is typically in the range 20-30nm. The range of interest here is much smaller thus one should observe a linear growth process. Looking back at the data it is clear that it does not "appear" to be linear. The linear rate constant is

$$B/A = k_c h (C^*/N_1) / (k_c + h) \quad (2.18)$$

k_c is the interface reaction rate and h the gas phase transfer coefficient. The LP model is known to fail for x less than about 20nm if the rate constants are extrapolated from temperatures greater than 850°C to lower temperatures. However, this does not preclude the existence of a LP regime which has different diffusing species rather than O_2 .

Power Law:

These type of kinetics do not have a firm physical basis. As yet there have been two explanations offered which lead to power law (PL) kinetics. These are the visco-elastic deformation model of Nicollian and Reisman (1988) and the oxide internal field model of Wolters and Zegers-van Duynhoven (1989). Both start from completely different premises to

produce similar kinetics. Other models incorporating an internal oxide field are also discussed in the literature but just add the effect of a field to the LP model (for example Naito et al., 1986, Wong and Cheng, 1988 Beck and Majkusiak, 1989). The PL function is essentially,

$$x = (Pt)^\alpha \quad \text{where } P^\alpha \text{ is a constant.} \quad (2.19)$$

It was assumed by Nicollian and Reisman that the oxide viscosity varied with its thickness. The viscous flow leads to density modifications in the oxide which control the diffusion of oxidant species. The oxide field model assumes the oxidant to be negatively charged and its diffusion moderated by the generation of fixed oxide charge. The charged species is suggested to be O^{2-} based upon the transport studies of Srivastava et al. (1985). It is also assumed that the rate limiting step is the flow of charged oxidant. A charged species is formed by electron flow from the silicon into the oxide by thermionic emission and electron capture by the oxidant. However, the formation mechanism of O^{2-} is not discussed and it is not obvious that this species is the prevailing oxidant. The formation of such a species would require a high energy input. It is suggested that O^- and O_2^- can also exist in thermal equilibrium at high temperature. Certainly the population of a molecular species is likely to be much larger than an atomic one. It is important to note here that the model has only been validated for high temperature ($>800^\circ\text{C}$) thermal oxidation. It is in the interest of completeness and the possibility (see the studies by Young and Tiller, Micheli and Boyd, Schaffer and Lyon discussed in chapter 1) that enhanced low temperature oxidation is controlled by electronic processes that the power law model is included. Needless to say both models deriving PL kinetics are regarded as controversial.

Cabrera-Mott:

This mechanism of oxide formation was originally proposed during the late 1940's. Since then many studies have reformulated the basic mechanism to include particular effects such as the nature of the oxide, the diffusion of species, the effect of coupled currents, etc. Recently these

various studies have been reviewed by F. F. Felhner in his book entitled "Low Temperature Oxidation". In chapter 2 of this book rate expressions for oxide growth are discussed quite exhaustively and it was found that most lead to logarithmic-type kinetics. Below, the basic CM model is described followed by a brief discussion of the kinetics derived for two modified mechanisms dominated by a) surface controlled reaction and b) the electron flow into the oxide. The discussion is drawn from Felhner's book and is included here because of its relevance to this study.

Fig.2.23 shows the band structure of the semiconductor-oxide-surface adsorbed gas system before and after equilibrium is formed. The essence of CM lies in the fact that it assumes that an electron trap site is formed on the oxide surface by an adsorbed oxidant species. Electrons can pass easily through the very thin oxide films to populate these sites by tunnelling, defect site conduction or Schottky emission into the oxide conduction band. The oxidation process then proceeds by the high field transport of an ion from one interface to the other. Under such high fields there is no equilibrium of ions at the interfaces and oxidation is controlled by either defect generation at the interface or bond breaking within the oxide to allow the incorporation of the oxidant ion.

From **Fig.2.23** we see that the field is just $E = V/x$. The rate determining step then becomes the incorporation of an ion into an interstitial site of the oxide (not part of the oxide network). In the general case it is possible for both cations and anions to be mobile. Additionally ionic movement in a vitreous oxide may be defect dominated rather than via interstitial sites. Many studies of the oxidation of Si at high temperatures have shown that the oxidant is the mobile species and the Si atoms essentially remain very close to the interface (see the radio-tracer experiments of Han and Helms, 1988 and Rochet et al., 1986 and 1989). It was observed that there was little interaction between the diffusing species and the oxide network under typical furnace oxidation conditions. This condition is believed to be maintained for low temperature growth also.

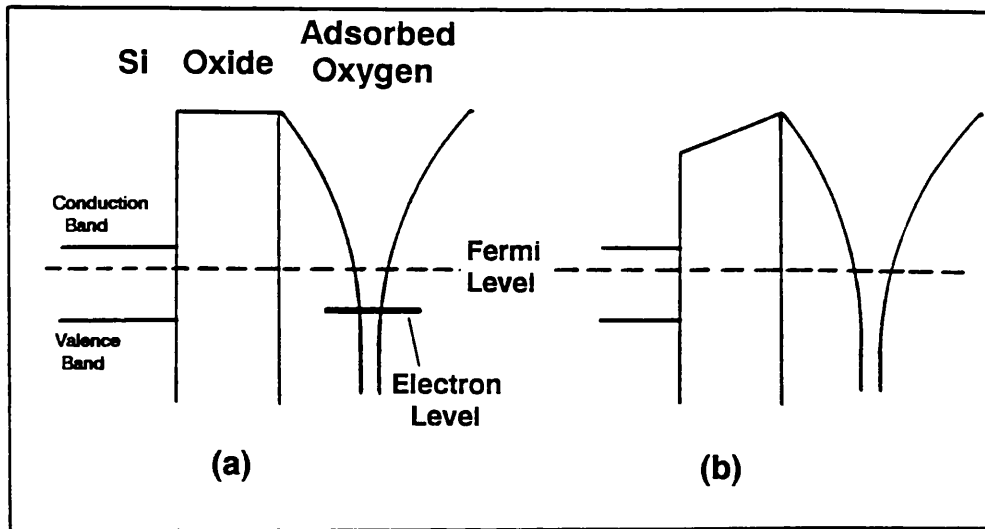


Fig.2.23 Electronic energy levels in the semiconductor, oxide and adsorbed oxygen structure: a) before electronic equilibrium b) after equilibrium is achieved. After Cabrera and Mott, 1948.

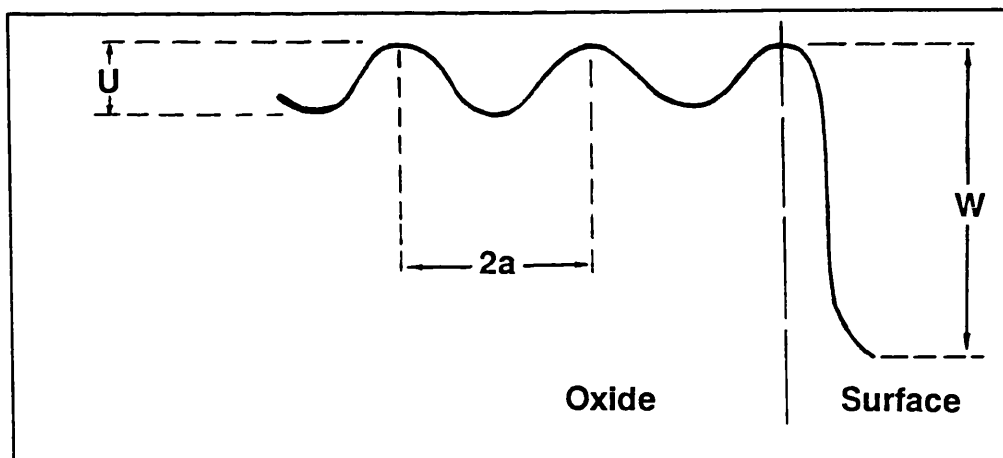


Fig.2.24 Potential energy structure of oxide/surface where the energy barrier to ion injection into the oxide is W and the activation energy for diffusion is U . After Cabrera and Mott, 1948.

The potential energy diagram of the oxide and its surface is shown in **Fig.2.24**. The probability of an ion surmounting a potential barrier U and moving a distance $2a$ from interstitial site to interstitial site is

$$\nu \exp[-U/kT] \quad (2.20)$$

according to Cabrera and Mott, where ν is the atomic vibration frequency (typically taken to be 10^{12}s^{-1}). The presence of a field E lowers the barrier U by qaE in the direction of the field and conversely raises it by the same value in the opposite direction. The drift velocity v_d then becomes

$$v_d \approx 2\nu a \exp[-(U-qaE)/kT] \quad (2.21)$$

for large E . For the very thin oxide layers of interest in this work it is this case of high E field that is believed to be relevant. Once the ion is injected into the oxide the high field sweeps it to the other interface rapidly. Interfacial properties dominate the injection of ions into the oxide and therefore determine which ion is mobile. For an ion to be injected the barrier to be surmounted is W (Fig.2.24). With the assumption that the first jump distance is half the spacing of interstitial sites the probability of transition is

$$\nu \exp[-W/kT] \exp[qaE/kt] \quad (2.22)$$

Hence the oxide formation rate can be expressed as

$$dx/dt = N\Omega\nu \exp[-(W - qaE)/kT] \quad (2.23)$$

Ω is the oxide volume per substrate atom and was calculated to be 45Angstroms^3 for vitreous silica, N is the number of potentially mobile ions at the surface and is suggested to be related to the number of surface states although this has not been quantified well directly. It has been calculated to be 10^6cm^{-2} for low temperature thermal oxidation. One would expect N to vary with the adsorbing species. A detailed discussion of the adsorption of oxygen was given by Hu (1984) with respect to oxidation. From the expression above it appears that a logarithmic type growth curve should be observed. Cabrera and Mott also define a limiting thickness x_l taken when the growth rate slows to one atom layer in 10^5 seconds:

$$x_l \approx Vaq/(W-39kT) \quad (2.24)$$

This in turn defines a critical temperature $W/39k$ below which the film grows rapidly to the limiting thickness x_l and then essentially stops growing. For higher temperatures there is no limiting thickness and a transition to

another type of kinetics can occur. This temperature is estimated to be $\approx 500^\circ\text{C}$ for Si (see Felhner 1972). It is interesting to note at this point that the growth data collected for temperatures around 450°C and lower oxide thickness limits whereas at 500°C this does not appear to be the case (Figs.2.11 to 2.16). Further growths for longer times are required to clarify the situation. Cabrera and Mott give an expression for the growth of oxide derived from the above rate equation which is an inverse ln of time i.e.,

$$x_1/x = K - \ln(t) \quad (2.25)$$

$x_1 = qaV/kT$ and K is a constant. A more precise integration of the growth rate expression was carried out by Ghez (1973) yielding

$$x_1/x = -\ln[(t + \tau)/x^2] - \ln(x_1 u) \quad (2.26)$$

where $\tau = \text{constant}$, $u = N\Omega\nu\exp(-W/kT)$ and $x_1 = |ZeaV/kT|$. Z is the charge on the mobile ion and e the electronic charge. Even with the more accurate formulation conclusive determination of kinetics is not possible in most cases because of the similarity of fits of direct ln and inverse ln over most data sets as noted below.

Finally, it is important to note that the CM model assumes a homogeneous oxide layer across which there is no space charge. This may not necessarily be the case for SiO_2 because it is well known that the growth process creates fixed oxide charge in the layer. The possible effect of this charge will be discussed later. For the more recent formulations including modified growth mechanisms noted above a) when a surface reaction is rate limiting and much slower than the other processes involved in oxide formation then a linear growth rate is predicted (see Felhner, 1986). More interestingly if the rate is controlled by the addition of an electron to form a charged species a logarithmic law is derived. b) when the controlling process is the flow of electrons the ion current is close to equilibrium. For very thin oxide layers electron tunnelling current dominates the growth. Therefore the number of electrons having energy E_e and passing through a barrier of height ϕ and width x is

$$Q \exp \{(-2x[2m^*(\phi - E_e)]^{1/2})/h\} \quad (2.27)$$

where Q is a constant, m^* the effective electron mass and $dx/dt = [\text{Const. exp}(-Kx)]$ leading to direct logarithmic kinetics.

2.4.3 Analysis of Growth Data

It is obvious from this discussion that kinetics cannot be used purely to infer the growth mechanism directly and knowledge about the "system" from other sources is necessary. To illustrate the difficulty in identifying kinetics **Figs.2.25-27*** are plots of ln-linear, ln-ln and inverse ln function transformations of the three data sets noted above. It is clear that both logarithmic and PL produce similar levels of fit. However, the inverse ln plots in **Fig.2.27** are quite good and indicative that a CM type reaction may indeed be operating particularly in the case of 350°C growth data.

To try to further discriminate between the types of kinetics the method developed by A. M. Stoneham (private communication, 1989) is used. Stoneham defined a parameter g_0 at a time t_0 and oxide thickness x_0 at which one growth or rate limiting mechanism dominates;

$$g_0 = -d(\ln y)/d(\ln x) |_{t_0} = (x/y)(dy/dx) |_{t_0} \quad (2.28)$$

$y = dx/dt$, g_0 is assumed to be constant for all oxide thickness values where the mechanism dominates. However in reality g_0 is a function of time and hence the oxide thickness because the growth mechanism often is a combination of effects or changes with the oxidation regime. Normalised growth velocity (Y) and thickness (X) are then defined as

$$Y = y(t)/y(t_0) \text{ and } X = x(t)/x(t_0) \quad (2.29)$$

Stoneham then converted the expressions for LP, CM and PL to relate Y , X and g_0 .

$$Y_{LP} = [1 + g_0(X - 1)]^{-1} \quad (2.30)$$

$$Y_{CM} = \exp\{g_0[(X^{-1} - 1)]\} \quad (2.31)$$

$$Y_{PL} = X^{-g_0} \quad (2.32)$$

He noted that plotting Y against X should allow one to eliminate models and in the case of similar kinetics check whether they can be distinguished with the available data. Any discontinuity in the X, Y curves is indicative that the kinetics are inappropriate.

* Straight lines are best fit lines by the least squares method.

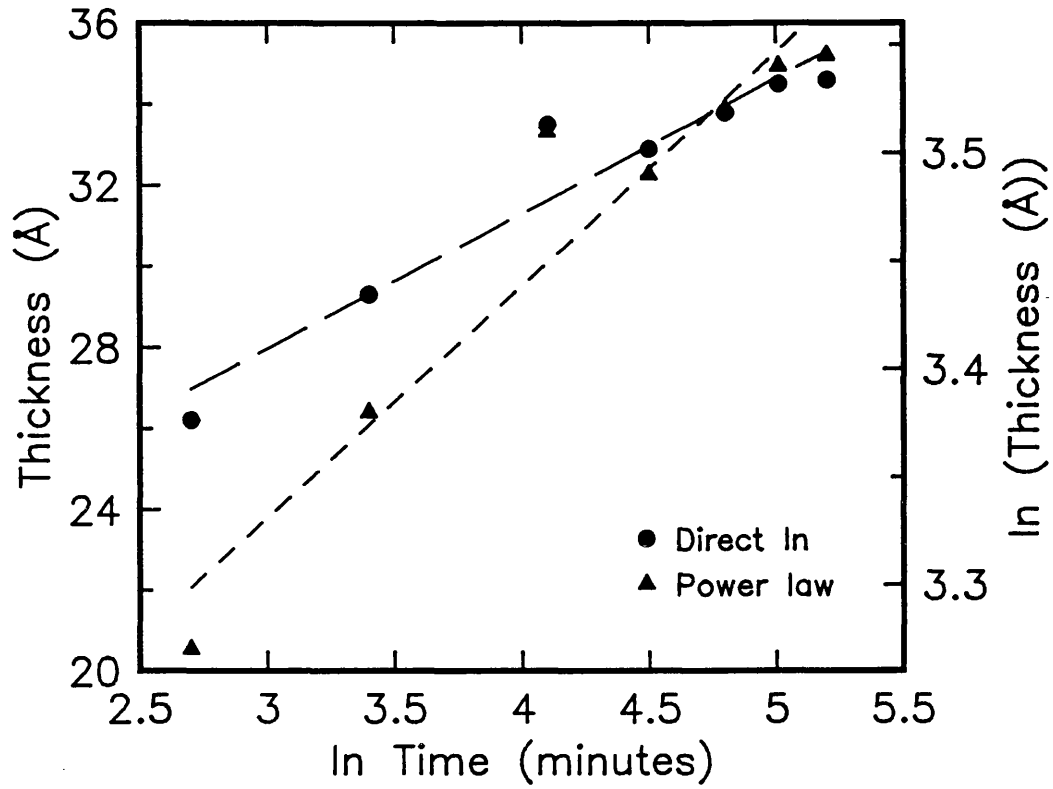


Fig.2.25a Direct ln of time and power law fits of data set (a), see table 2.II.

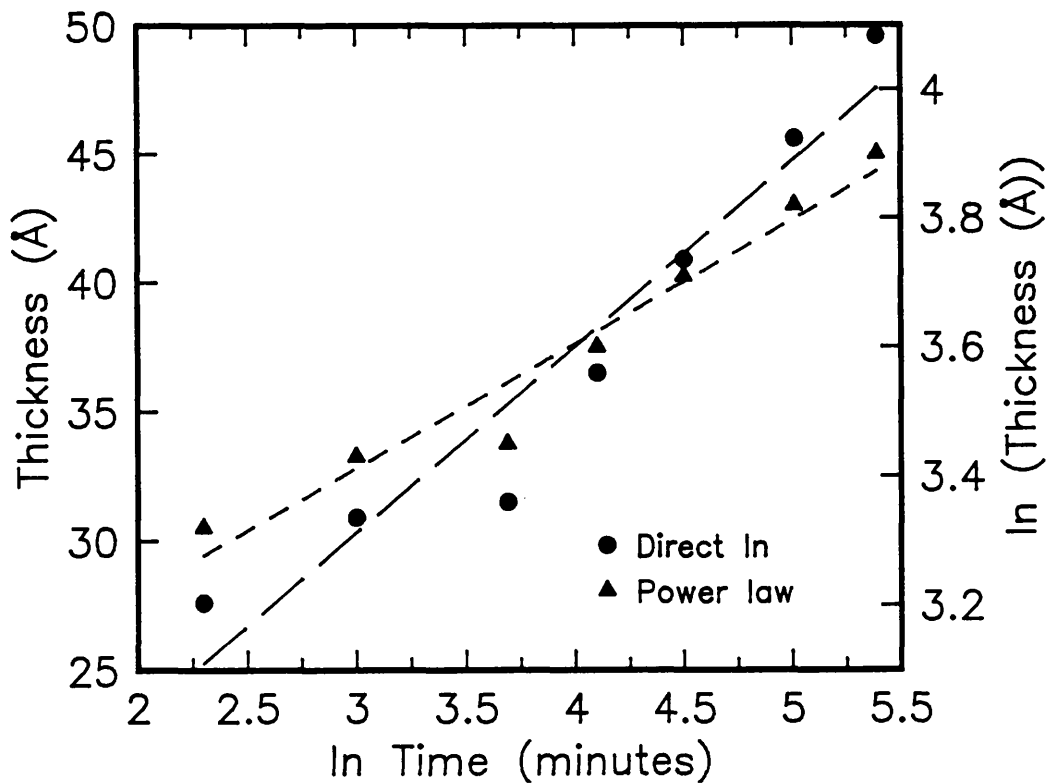


Fig.2.25b Direct ln of time and power law fits of data set (b) see table 2.II.

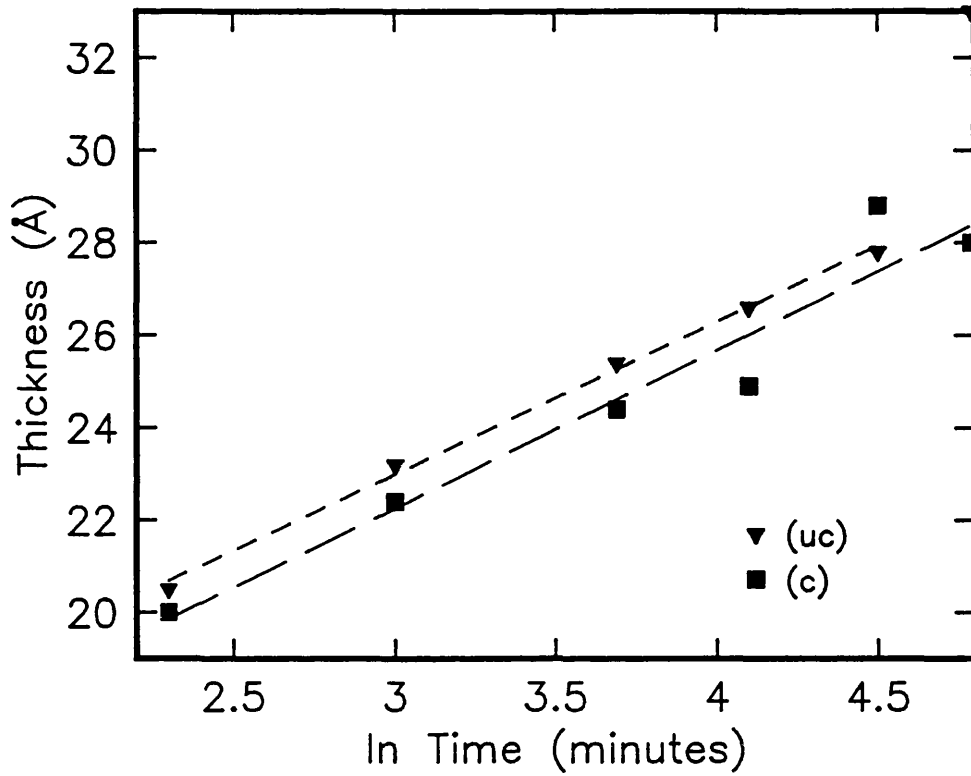


Fig.2.26 Direct ln of time fits to data set (c) (table 2.II) for covered and uncovered oxide growth.

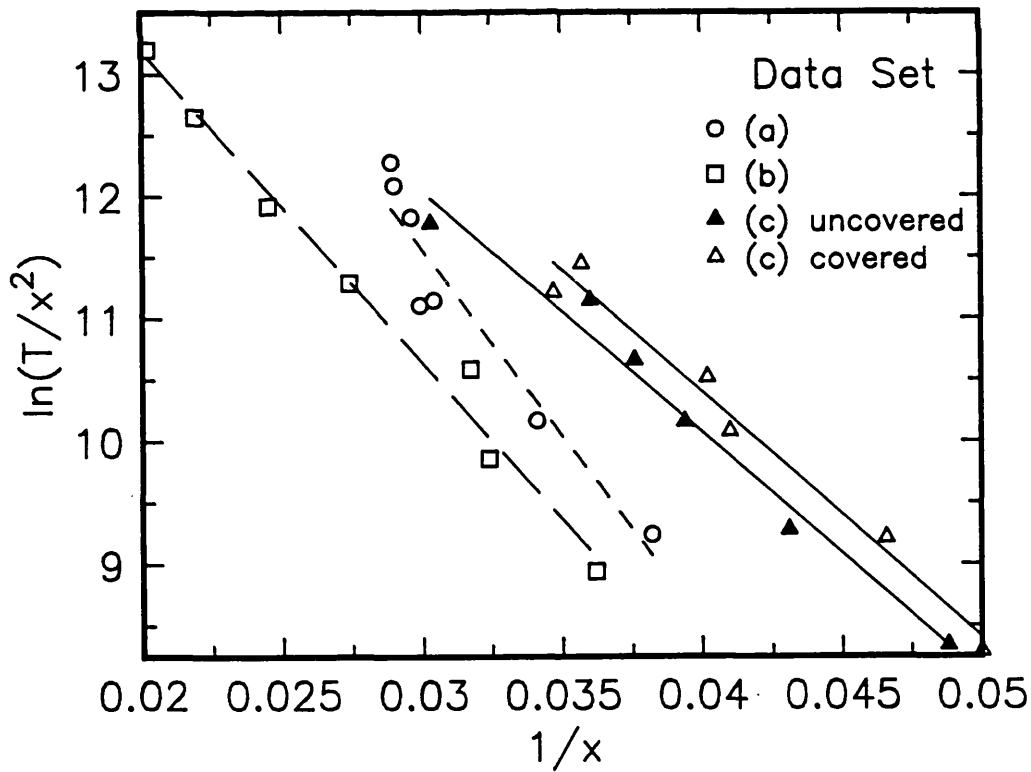


Fig.2.27 Inverse ln growth law fits according to the solution of Ghez, equation 2.26.

In the discussion that follows the data sets were converted to X and Y using g_0 values calculated graphically. The precise value of g_0 is not important rather it is the order of magnitude which is indicative of the type of kinetics. Values of g_0 for the three data sets are tabulated below, table 2.II.

Data Set	Growth Temperature (°C)	g_0	x (Å)
a) <100>	450	11.6	33.5
b) <111>	350	5.0	43.5
c) <100>	350	13.0	27.2
c) <100>	350	8.0	22.5

Table 2.II

It was observed that for both a) and b) g_0 was essentially constant with thickness. However for c) g_0 did change as the oxide thickness increased. This suggests that the dominating growth mechanism changes as the oxide becomes thicker. In all cases g_0 was greater than 1 meaning that oxide growth can not be described by LP kinetics. This is more clearly displayed in Figs.2.28-30 because Y_{LP} in all cases has a discontinuity and the growth velocity curve is non-physical. What is interesting is that the problem of distinguishing between PL and CM kinetics is also not resolved definitely. PL predicts slightly lower growth rates than CM but the form of the curves is similar. Thus it seems that within the available data it is not possible to infer the growth process directly. Further more detailed data is necessary particularly for thinner oxides at shorter times. Unfortunately this regime is very difficult to study without in-situ measurement techniques. A better way to obtain information on the process of oxidation would be to modify the experiment. Further experiments will be discussed in the concluding chapter.

As yet the answer to the question of what growth mechanism is active in a UV/ozone environment remains uncertain, however some insight can be gained by reconsidering the general results and looking at the possible

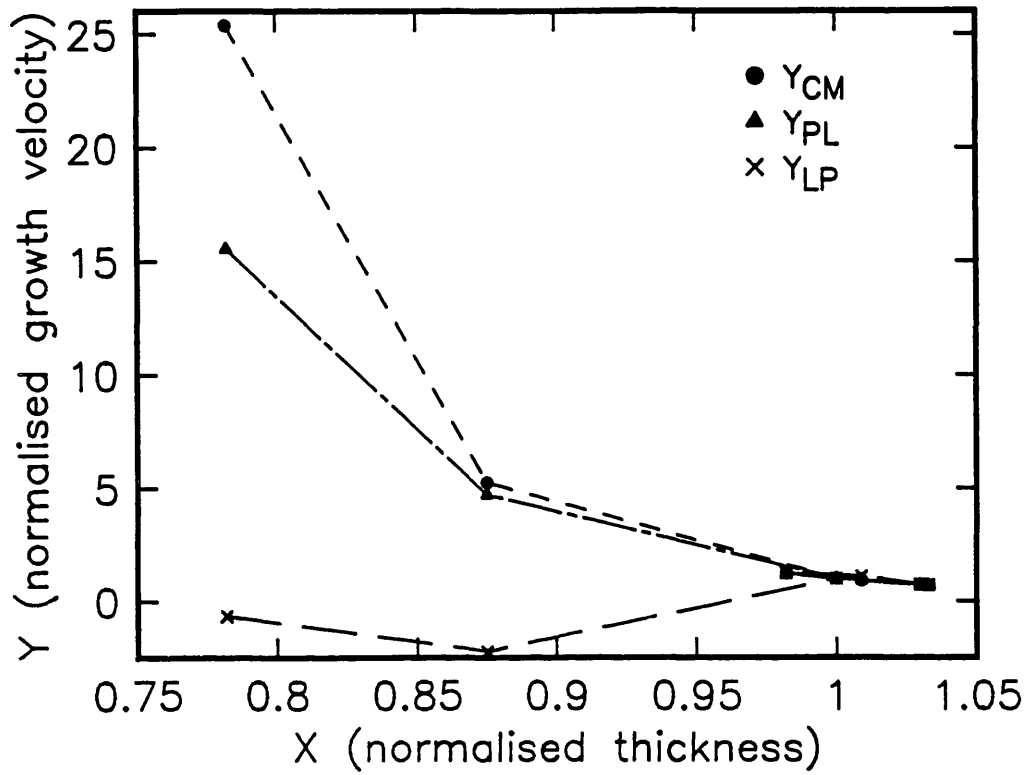


Fig.2.28 Functional fitting of kinetics for data set (a), $g_0 = 11.6$.

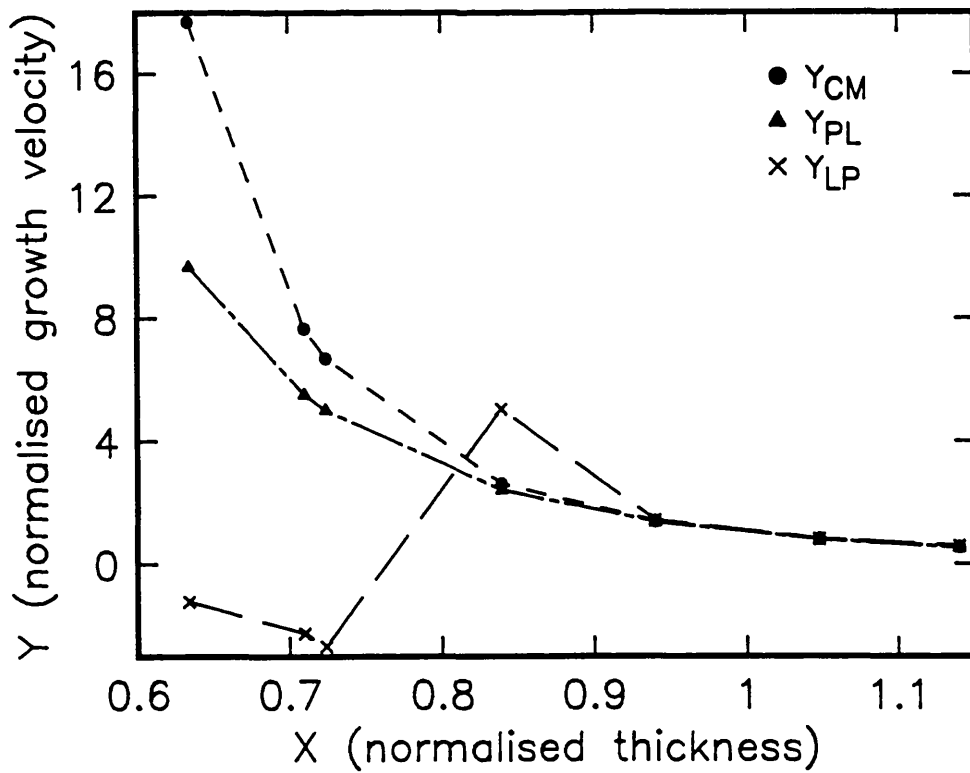


Fig.2.29 Functional fitting of kinetics for data set (b), $g_0 = 5$.

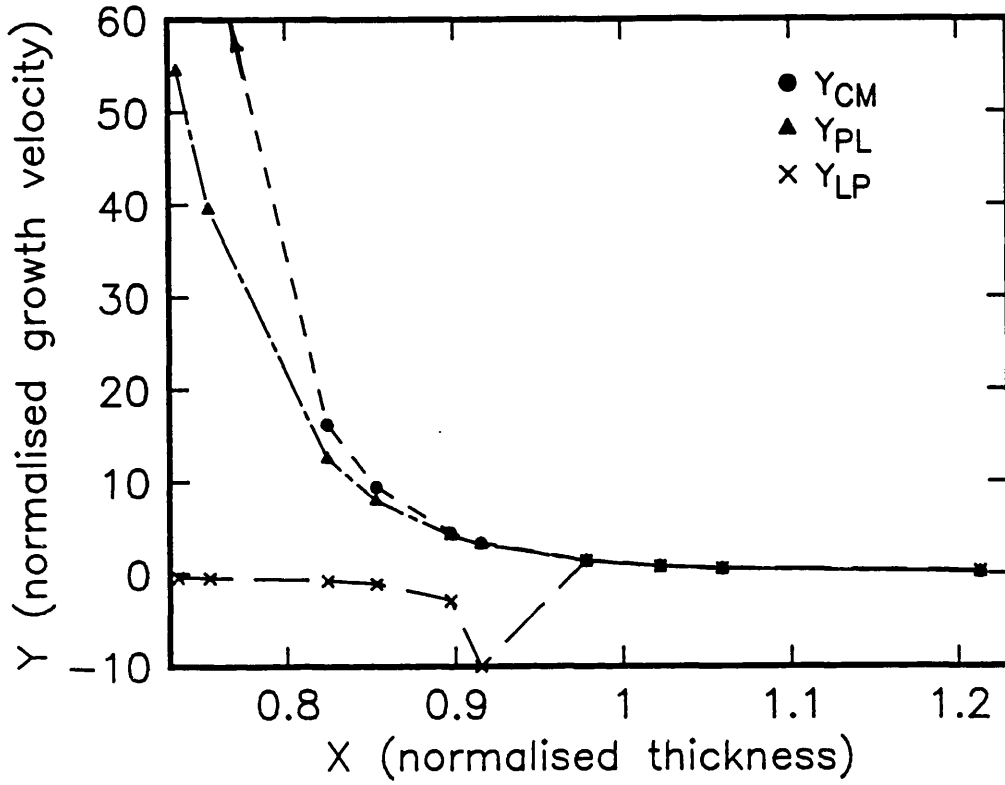


Fig.2.30a Functional fitting of kinetics for data set (c), $g_0 = 13$.

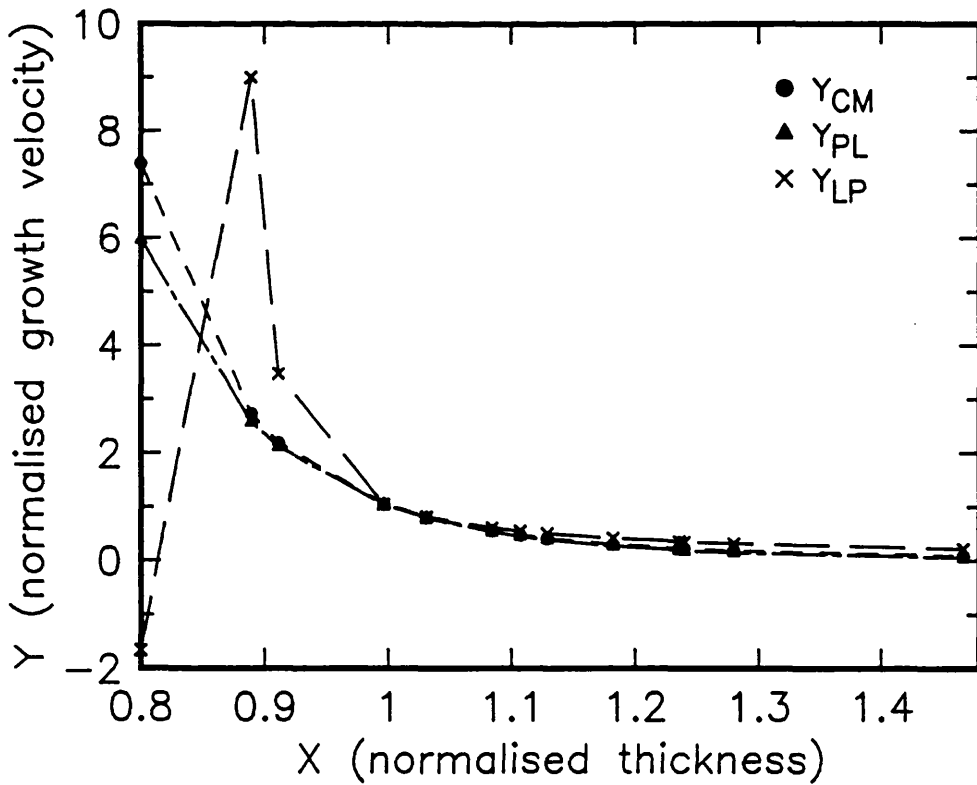


Fig.2.30b Functional fitting of kinetics for data set (c), $g_0 = 8$.

reaction steps to oxide formation. In both PL (as derived by Wolters et al., 1989) and CM electrons are assumed to flow to the oxide surface for negative oxygen ions to form (it is not known if these ions are molecular or atomic). Thus an electric field is induced and the ions drift back to the Si for reaction. In thermal oxidation it is believed that the oxidant is molecular but the growth rates observed in the present study are much greater than in the thermal case. From analogous (to UV/ozone) low temperature studies using oxygen plasma afterglows (see section 1.3 iv) and direct plasma anodisation it has been concluded that rapid oxide growth is due to the presence of dissociated oxygen species. The high reactivity of atomic oxygen in comparison to molecular oxygen to Si surfaces is well known (Madix and Susu, 1970). Ozone is the only other species which is present. It is not a likely oxidant because it is a larger molecule than O_2 and thus its diffusion through the oxide should be even more restricted than for molecular oxygen. Hence the proposed oxidant is an atomic oxygen species.

The next question is whether the oxidant is charged or not. Oxidation appears to be thermally activated and could be due to the higher decomposition rate of O_3 releasing more O near the oxide surface. O radicals then diffuse to the Si and react. Thus the oxide growth rate would be a function of the temperature and not the oxide thickness assuming that oxide was not a barrier to O diffusion. Hence the oxide thickness would increase linearly with time. In fact oxidation is very much a function of thickness and the relationship with temperature does not appear to be straight-forward. It is interesting to note that as predicted by the CM model for temperatures below 500°C rapid growth occurs followed by an almost static plateau while for $500\text{-}550^\circ\text{C}$ oxide growth continues and the plateau is not so evident even after 3 hours growth time. Additionally, the recent work of Rochet et al. (1986) suggests that for very thin layers some interaction between the diffusion species and oxide network does occur. In their study they used very low water content molecular oxygen. With the high reactivity of atomic oxygen some interaction between the radical and the oxide

network is highly likely. Thus the proposition is that a driving force for the motion of oxidant is necessary to ensure that it reaches the Si rapidly. The source of this is the intrinsic field generated by the formation of ionic species. A very recent study by Rechtein et al. (1990) identified the existence of oxygen ions on Si surfaces formed by charge transfer to adsorbed molecules prior to their dissociation and reaction. Both O^- and O^{2-} were identified as being present. The substantially higher electron affinities of both O and O_3 in comparison to O_2 are much more likely to "draw" out electrons from the Si thus accelerating the growth reaction.

In the model proposed by Wolters et al. (1989) electrons are thermionically emitted into the oxide while in CM they tunnel to the oxide surface. SiO_2 is a vitreous solid and highly homogeneous. It has no grain boundaries and thus one would not expect any preferential routes for charge flow. Thermionic emission of electrons at high temperatures is large but because it is an exponentially activated process at the temperatures of interest to this study it is very limited. For Si/ SiO_2 the emission current is,

$$I_d = 110 T^2 \exp(-\phi/kT) \text{ A/cm}^2 \quad (2.33)$$

At $\sim 1100K$ and $\sim 800K$ the number of electrons emitted is 3×10^{12} and $6.4 \times 10^6 \text{ cm}^{-2} \text{ s}^{-1}$ respectively assuming a barrier height of $\sim 3.15 \text{ eV}$. Wolters (1989) suggests that positive fixed oxide charge dominates the flow of oxygen ions. In chapter 4 electronic properties of the oxides are discussed. It was found that "bomb" cleaned samples did not have the same positive oxide charge as HF dipped samples however the growth rates for the two preparations were very similar (Figs.2.12-13). In both cases the calculated oxide charge density was large ($Q_{ss}/q \approx 10^{12} \text{ cm}^{-2}$). Accordingly positive oxide charge seems not to be a dominant factor and does not restrict oxide growth. It may play a role though in assisting electron motion when the tunnelling current falls due to the width of the oxide barrier.

On the basis of the preceding discussion of the growth data a reaction sequence applying a modified CM mechanism can be constructed.

- 1) O_3 (or O) is adsorbed onto the oxide surface (much more

efficiently than O_2 because of its larger sticking coefficient).

2) Charge flow to equilibrate the Fermi level with the adsorbed electrons state occurs by tunnelling.

3) Either $O_3 + e^- \longrightarrow O_2 + O^-$
or $O + e^- \longrightarrow O^-$

Both of these processes are known to be energetically favourable (see Baulch et al., 1984, and Steinfield et al., 1987) and capture by either O_3 or O is much more probable than with O_2 because the electron affinities for the three species are 2.1, 1.45 and 0.4eV respectively.

4) O^- drifts through the oxide and reacts rapidly with the Si to join the network.

5) When the tunnelling emission of electrons diminishes to small values ($< \sim 10^7 \text{cm}^{-2}\text{s}^{-1}$, at around 3nm for 350°C and $< 100 >$ surfaces) then UV photoemission of electrons into the oxide allows the reaction to continue.

In the initial part of the growth process inverse ln kinetics should be observed if a classical CM mechanism is dominant. Following this a direct ln regime should be entered according to the modified mechanisms discussed in the previous section. Because of the difficulty in distinguishing between direct and inverse ln kinetics all the growth data can be fitted with either type of kinetics equally well. It is interesting to note that both Vinckier et al. (1987) and Hoff and Ruzyllo (1987) report ln type kinetics for afterglow oxidation of Si.

It is very important to note that experimentally a difference was observed in the reaction for covered and uncovered Si surfaces beyond a certain oxide thickness. It is this which suggests that the emission of electrons into the oxide by whatever process plays an important role in oxide growth. For the most detailed data set, i.e. 350°C, $< 100 >$ g_o was observed to be changing as the oxide thickness increased. The implication of this is that the growth rate limiting mechanism changes as the oxide

grows, see Fig.2.31, from tunnelling of electrons to their photo-emission.

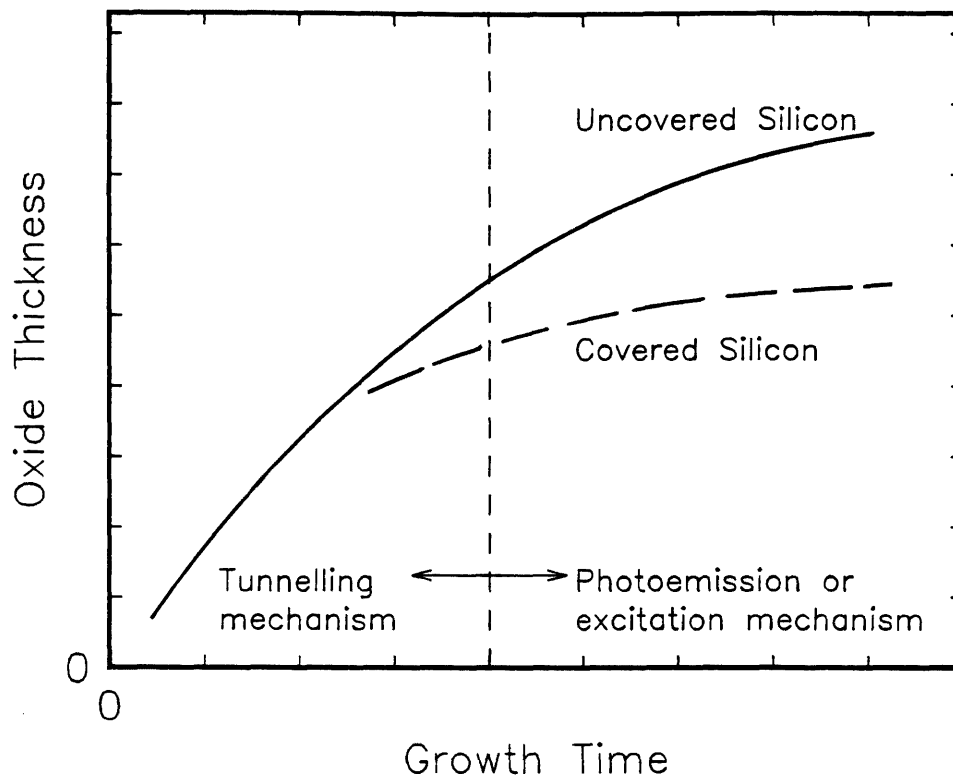


Fig.2.31 Schematic illustration of the dominant growth mechanism for different thicknesses.

UV photoemission of electrons into and through the oxide is well known. Dressendorfer and Barker (1980) observed the photocurrent in MOS structures for a wide range of photon energies. The photoemission (into vacuum) studies of Eastman and Grobman and Spicer (discussed in chapter 1) were looking at very thin oxide layers of a few Angstroms and used photon energies significantly greater than the Hg lamp. A very recent investigation (Pidduck and Nayar, 1990) of photoelectron emission in air induced by a low pressure Hg lamp observed charge flow. Additionally Goshu and Saeki (1989) noted the appearance of photoelectrons from quartz surfaces also with a low pressure Hg lamp.

To conclude, oxidation is influenced by a combination of factors. These include the reactivity of the oxidant and its ability to move through the oxide rapidly. Studies of plasma and afterglow systems show that the efficiency of oxidant species follows the order $O^{\cdot-} > O > O_2$ (Vinckier et al., 1987). Oxide charge (positive) can be expected to assist electron flow into the oxide by

lowering the barrier height at the Si/SiO₂ interface due to image charge effects or providing tunnelling sites in the oxide. Additionally Stoneham (1987) has shown that charge near an interface can assist injection of species due to the induction of image potentials. Certainly in the present case the restraining effect of positive oxide charges on negative ion motion to the Si seems limited.

Understanding the growth mechanism is particularly important if the growth rates for low temperatures using the UV/ozone technique are to be improved. The effect of electron affinity on the diffusion of species through a thin oxide layer has been observed by Ocal et al. (1985) for Al₂O₃ on Al. They found that Au atoms ($E_a=2.8\text{eV}$) diffused through a chemically reduced oxide while K atoms ($E_a=0.6\text{eV}$) did not. The difference was ascribed to the high electron affinity of Au atoms in comparison to K atoms. If electron affinity is such an important parameter as their work suggests, then the enhanced oxidation of Si in the presence of F and Cl atoms could be explained by noting that both have an E_a around 3.5eV. Methods to improve the growth rate and obtain more information about the formation process are discussed in the chapter 5.

2.5 Summary

In this chapter the UV/ozone route to thin oxide growth has been developed. It has been shown to be effective at temperatures <550°C. The oxide growth rate recorded at 500°C by this technique is equivalent to thermal oxidation at approximately 775°C in dry oxygen. An attempt to analyse the growth data suggests a Cabrera-Mott, logarithmic type oxidation process although it is not possible at this stage to show this conclusively. However, LP kinetics can be excluded. UV irradiation plays an important part in extending oxidation beyond 2.5-3nm. Oxides up to ~8nm have been grown at a temperature of 500°C. This is typically the thickness that will be required for future generations of deep submicron MOS integrated circuits.

Chapter 3

Materials Characterisation of Thin Oxide Films

3.1 Spectroscopic Ellipsometric Analysis

3.1.1 Introduction

Single wavelength ellipsometry (SWE) at 632.8nm has been used to characterise oxide growth and the optical properties of thin films for several decades. The technique relies on the change in polarisation of light which is specularly reflected from the surface of interest. Once the change in polarisation is quantified then it is related to optical (and thus material) properties of the layers under study. A comprehensive description of the theoretical basis of the subject including experimental measurement techniques and data analysis is given in the book by Azzam and Bashara. However their monograph does not deal with recent developments in the field of spectroscopic and multiple angle spectroscopic ellipsometry (SE and MASE respectively). Since the initial work of Aspnes and et al. in 1979 on the development of SE as opposed to multi-wavelength ellipsometry discussed by Azzam and Bashara the usefulness of the technique has been recognised in a diverse range of fields (see McMarr et al., 1986, Snyder et al., 1986, Pickering et al., 1986, 1990, and Vanhellefont et al., 1989). This has led to the commercial production of fast, accurate and highly reproducible ellipsometers. Additionally the recent availability of a wide body of very accurate optical reference spectra allows ellipsometric data to be reduced to verifiable material parameters (such as thickness (x), density

(D), interfacial layers and surface roughness).

It is well known that the density of grown oxides can vary with the growth conditions. An expression relating density and the real part of the refractive index (n) is given by Ravindra et al. (1987) which shows that an increase in density is analogous to an increase in n according to the equation 3.1, plotted in Fig.3.1. This is particularly interesting for very thin oxides because it has been suggested that thin oxides are denser because of the proximity of the substrate.

$$\rho = \frac{3M}{4\pi N\alpha_t} \left[\frac{n^2 - 1}{n^2 + 2} \right] \quad (3.1)$$

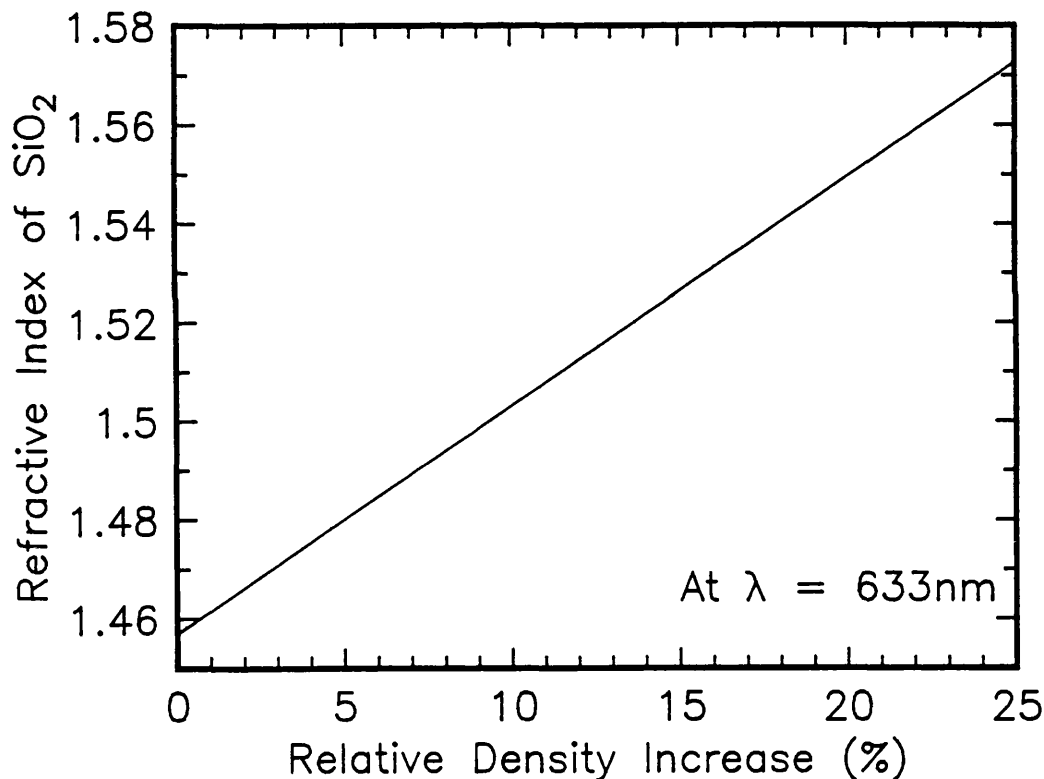


Fig.3.1 Relationship between refractive index and relative oxide density.

N is Avogadro's number, α_t is the total electronic polarisability and M the molecular weight. During oxidation a large volume expansion occurs at the growing interface of the oxide. There is also a large bonding mismatch between the crystalline Si and amorphous oxide. This mismatch is believed to be accommodated by the presence of an interfacial layer of sub-stoichiometric oxide and a densification of the oxide. As the distance

between the grown oxide and the Si-oxide interface increases, the oxide becomes more relaxed. Therefore the observed density of a grown oxide is likely to be a memory effect from interfacial bonding.

Many oxidation studies have used in-situ SWE (at fixed n) to obtain growth rate data and various models have been fitted to this data (see the studies of Massoud and Plummer, 1985, and also Irene, 1987). If oxide density does indeed vary with x then the fitting parameters derived in such studies may need to be revised. Typically if n is fixed to that for relaxed vitreous silica then for very thin oxides (of higher density) the value of x calculated will be greater than the actual value. An ex-situ study by Aspnes and Theeten (1980) used SE on thicker oxides ($>200\text{nm}$ furnace oxides, grown at 1000°C) and showed that their density was $\approx 0.6\%$ greater than that of fused silica. They also found that an interfacial layer of $\approx 0.6\text{nm}$ with a composition of $\text{SiO}_{0.4}$ existed between the Si and oxide. More recently, a theoretical examination of ellipsometric data sensitivity by Bu-Abbud et al. (1986) illustrated the difficulty in determining material parameters for thin SiO_2 films on Si.

Thin SiO_2 layers on Si have been studied intensively by a variety of techniques. However, SWE is the most commonly used method to determine oxide thickness and refractive index. For layers $<50\text{nm}$ SWE results are generally ambiguous due to the lack of "sensitivity" theoretically of the technique rather than just instrumental accuracy. The change in Δ and ψ at 632.8nm with the oxide thickness is small. The following sections present,

- a) an outline of the theory of the technique (following the discussion in the book by Azzam and Bashara and Bu-Abbud et al.),
- b) a brief description of the experimental ellipsometry apparatus,
- c) an experimental test of the technique to discover both its limitations and obtain information on the physical properties of thin oxides ($<50\text{nm}$). The main interest of this study is the characterisation of ultra-thin layers less than 10nm thickness. The aim of the first and second sections is to introduce the subject rather than present a detailed

discussion.

3.1.2 Basic Ellipsometric Theory

A monochromatic collimated linearly polarised light beam is directed at an angle of incidence ϕ on to the surface of the sample under study. Upon reflection the beam becomes elliptically polarised and is analysed using a polariser and photodetector. Fig.3.2 shows the geometric arrangement. ϕ , is required to be accurately determined. Linearly polarised light can be described by two vector components, one of which lies in the plane of incidence (p polarisation) while the other is perpendicular to the plane of incidence (s polarisation).

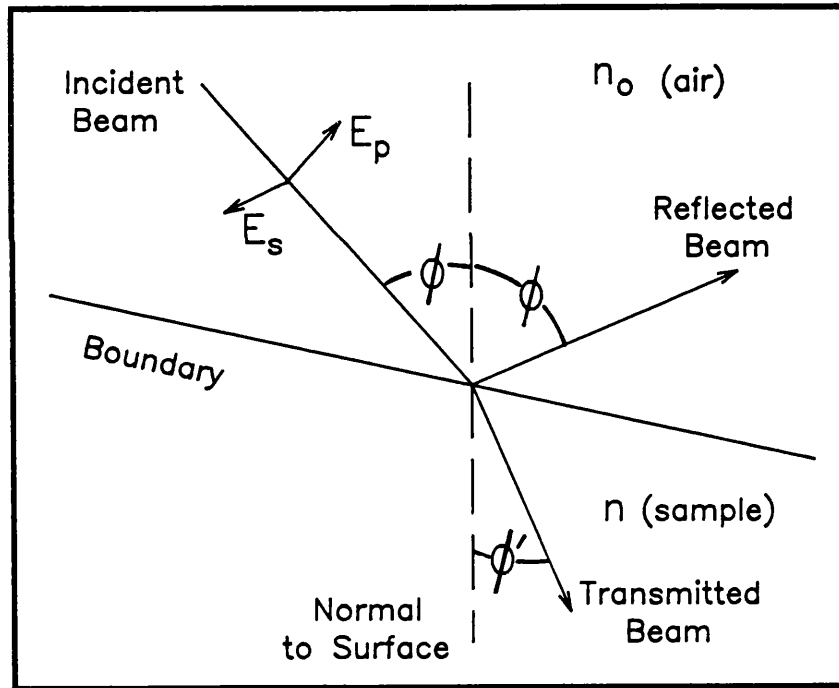


Fig.3.2 Geometrical arrangement of ellipsometric measurement.

By applying Maxwell's equations to the boundary between the sample and ambient the complex reflectances, r_p and r_s , can be determined.

$$E_p^{ref} = r_p E_p^{inc} \quad E_s^{ref} = r_s E_s^{inc} \quad (3.2)$$

$$\text{where } r_p = \frac{n \cos\phi - n_o \cos\phi' E_p^{ref}}{n \cos\phi - n_o \cos\phi' E_p^{inc}} \quad (3.3)$$

$$r_s = \frac{n_o \cos\phi - n \cos\phi' E_s^{ref}}{n_o \cos\phi + n \cos\phi' E_s^{inc}} \quad (3.4)$$

E is the electric field strength for incident (inc) and reflected (ref) waves, n and n_o are the complex refractive indices as defined in Fig.3.2. ϕ and ϕ' are related by Snell's law,

$$n_o \sin\phi = n \sin\phi' \quad (3.5)$$

Ellipsometric instruments measure the property r_p/r_s . This ratio can be redefined as

$$\frac{r_p}{r_s} = \rho = \tan\psi \exp(i\Delta) \quad (3.6)$$

$\tan\psi$ and $\cos\Delta$ are the parameters most used in SE to describe the optical properties of a sample because these are the data that are actually collected. However it is necessary to convert these to more common optical functions such as the refractive index. In the case of a bare substrate,

$$n = n_o \tan\phi [1 - 4\rho(1 + \rho)^{-2} \sin^2\phi]^{1/2} \quad (3.7)$$

This can be done with ease only in this the simplest of cases. For even the situation of a single layer on a substrate the expressions become very complex. A detailed discussion of the ambient-film-substrate case can be found in chapter 4 of the book by Azzam and Bashara. An alternative to direct solution of the theoretical expressions for the optical functions is to model the experimental data using an assumed sample structure and reference spectra for the constituents of the model. The optical properties of a layer of more than one constituent can be calculated using the Bruggeman effective medium approximation (see appendix C). Thus the density of a film can be simulated by mixing positive or negative "voids" for lower or higher density respectively. When the model is sufficiently close to the actual data it is assumed to be representative of the sample under investigation. Typically a regression analysis is applied to the model. Various means are used to determine the "quality of fit" (defined in detail below). The main method is the minimisation of the unbiased estimator (σ).

Calculation of optical functions such as n by the fitting route requires an accurate knowledge of $\tan\psi$ and $\cos\Delta$ (or ψ and Δ in the case of conventional SWE instruments) to obtain a high confidence result. However, there arises another difficulty, one which so far has attracted little attention but is high-lighted by Bu-Abbud et al. very well in their study of 1986. There are as with all analyses theoretical bounds on the sensitivity of both instrument and technique. Given that instrumental sensitivity is sufficient to "see" a change caused by an arbitrarily small perturbation in an experimental parameter (e.g. wavelength or ϕ) then $\tan\psi$ and $\cos\Delta$ can be determined within certain limits. Thus the smallest value of these limits can be defined as the precision of the instrument. These values are known for the ellipsometer used in the present study. This leaves the issue of the theoretical limit on the sensitivity of the method (particularly with respect to data extraction) which is a critical difficulty with ellipsometry particularly for situations when very thin films or multi-layer structures are under study. Typically in SWE the accurate calculation of both refractive index and oxide thickness is not possible for layers of less than 50nm. The cause of this is that the changes in ψ and Δ with respect to layer thickness and refractive index are very similar i.e.

$$\frac{\partial \tan\psi}{\partial n} \sim \frac{\partial \tan\psi}{\partial x} ; \frac{\partial \cos\Delta}{\partial n} \sim \frac{\partial \cos\Delta}{\partial x} \quad (3.8)$$

In particular the sensitivity of ψ for thin oxides is very low and therefore one is attempting to calculate n and x from just one well defined datum. These points are illustrated in the Fig.3.3 to 3.9 below showing the effect on $\cos\Delta$ and $\tan\psi$ when small variations in the layer are introduced. In multi-angle SE (MASE) calculations an initial sensitivity (or response surface) analysis is particularly important because it allows one to chose the wavelength and angle ranges so as to maximise measurement sensitivity. In the present discussion a brief introduction and the conclusions of the analysis of Bu-Abbud et al. (1986) are noted. The aim of this work being to both verify their methods and obtain information on thin oxide films.

3.1.3 The Sensitivity Correlation Analysis of Bu-Abbud et al.

In ellipsometry data reduction and parameter extraction can lead to ambiguous results without an assessment of the sensitivity of the modelling technique used. The sensitivities correlation test allows one to "judge" the confidence one can place in the results obtained. It is important to ensure that the number of independently obtained data are greater than or equal to the number of unknown parameters. To increase the data set both SE and MASE can be used with respect to SWE. In SE the results of measurements at a fixed angle yield $\tan\psi$ and $\cos\Delta$ for each wavelength (λ), i.e. two independent numbers. For a bare, smooth surface n and k can thus be determined at each λ . If a homogeneous film exists on a substrate and assuming the substrate parameters are known then three unknowns exist. These being the film thickness, n and k . Hence because only two data points are being used to calculate 3 unknowns SWE cannot be used without producing some ambiguity in the result. However, the situation is improved in SE by the fact that in data fitting reference spectra for both substrate and film constituents are used and data are taken over a wide range of wavelengths and the layer thickness is a constant for all wavelengths. Thus reasonable results are achieved as shown below except in the case of very thin films ($<6\text{nm}$) or attempts to model multilayer structures.

Multiangle Ellipsometry

It should be noted that sensitivity correlations cannot be calculated from parameter correlation coefficients. Bu-Abbud and co-authors first discuss multiangle measurements at a single λ . This example illustrates their analysis very well. They found that for a weakly absorbing film on an absorbing substrate (as in the case of SiO_2 on Si) that

$$\frac{\partial\psi}{\partial x_f} = \frac{\partial\psi}{\partial n_f} \quad \frac{\partial\Delta/\partial x_f}{\partial\Delta/\partial n_f} = \frac{(n_f^2 - n_s^2)(n_f^2 - 1)}{2[n_f - (n_s^2/n_f^3)]x_f n_f^2} \quad (3.9)$$

i.e. ψ was insensitive to changes in x_f and n_f while the sensitivities of Δ to n_f and x_f were proportional as long as

$$\lambda > \frac{x_f}{n_s^2 - \tan^2\phi} \quad (3.10)$$

For $\phi \approx 75^\circ$ and $n_{Si} = 3.85 - j0.02$ then for the above inequality to fail the layer thickness needs to be large, typically more than 50nm (at $\lambda \approx 633\text{nm}$), which is much thicker than the layers of interest here. Δ is more sensitive than ψ and therefore there are strong correlations between n_f and x_f sensitivities. It is clear from this that multiple angle measurements at a single wavelength will fail to uniquely determine the film parameters even though the substrate parameters are known.

A high sensitivity correlation coefficient between any two parameters leads to a reduced accuracy in the values calculated for them. If a parameter X_i is observed L times ($i = 1, \dots, L$ and X represents either Δ or ψ or $\cos\Delta$ and $\tan\psi$) and the unknown variables vector is $B = (b_1, \dots, b_k)$ then the "sensitivity matrix" is

$$P_{L \times k} = [p_{ij}] : \quad p_{ij} = \partial X_i / \partial b_j \quad (3.11)$$

(i.e. the rate of change of an experimental parameter with an unknown or fitted parameter) and the sensitivity correlation coefficients between any two unknowns b_j and $b_{j'}$ is

$$A = a_{jj'}^* = \frac{\sum_{i=1}^L [p_{ij} p_{ij'} - L(L-1) \langle p_{ij} \rangle \langle p_{ij'} \rangle]}{\left[\sum_{i=1}^L ((p_{ij})^2 - L(L-1) \langle p_{ij} \rangle^2) \right]^{1/2} \left[\sum_{i=1}^L ((p_{ij'})^2 - L(L-1) \langle p_{ij'} \rangle^2) \right]^{1/2}} \quad (3.12)$$

$$\text{and} \quad \langle p_{ij} \rangle = \sum_{i=1}^L \frac{p_{ij}}{L} \quad \text{i.e. the average.} \quad (3.13)$$

The sensitivity matrix can be calculated as demonstrated by Bu-Abbud and Bashara (1981) using the Marquardt algorithm (1963). To calculate the error in extracted variables the procedure is to take the inverse of A : $A^{-1} = C$ and compute the standard deviation of errors from the residual

$$\sigma = [G(B)/(L-k)]^{1/2} \quad (3.14)$$

($G(\mathbf{B})$ is defined below as the mean square error). Finally to obtain the estimated error in each parameter assuming a normal distribution take

$$\sigma_{bj} \propto \sigma C_{jj}^{1/2} \quad (3.15)$$

If a_{ij}^* the (sensitivity correlation coefficient) between 2 parameters is close to 1 then the above method for calculating errors can fail. The solution calculated varies with the initial estimates for the model. Consequently accurate values for the two parameters are difficult to extract. It was also found that in the case of a thin SiO_2 layer on Si with a single wavelength multiangle data set sensitivity correlations are near ± 1 for the following pairs of parameters,

$$\begin{aligned} & n_s \text{ and } k_f, \\ & k_s \text{ and } n_f \\ & n_f \text{ and } x_f \\ & k_s \text{ and } x_f. \end{aligned}$$

In the case of SE using data fitting with reference spectra for all the materials involved the aim initially was to determine n_f and x_f assuming a single layer model. However these are still strongly correlated with the correlation varying as a function of oxide thickness (see section 3.1.5).

Multiple Angle Spectroscopic Ellipsometry

$$\text{In this case } \rho = \rho[\lambda, \phi \text{ and } \mathbf{B}(\lambda)] = \tan\psi \exp(i\Delta) \quad (3.16)$$

$$\text{and } \mathbf{B} = [b_1(\lambda), b_2(\lambda), \dots, b_K(\lambda)] \quad (3.17)$$

$$\text{and } b_j(\lambda) = \sum_{i=1}^K b_{ji} \delta_{\lambda'\lambda} \quad (3.18)$$

Where $\delta_{\lambda'\lambda} = 0$ for $\lambda \neq \lambda'$, 1 for $\lambda' = \lambda$

in the case of discrete wavelengths. \mathbf{B} is the parameter vector constructed from the modelled variables b_i . Discrete values for these parameters are calculated from the reference spectra. The Marquardt (non-linear least square) algorithm noted above has been incorporated into commercial software supplied by the J. Woollam Co. (Nebraska University) and minimises

$$G\{B(\lambda)\} = \sum_{i=1}^n [\{\cos\Delta'_i - \cos\Delta_i(B_i, \phi_i)\}^2 + \{\tan\Psi'_i - \tan\Psi_i(B_i, \phi_i)\}^2] \quad (3.19)$$

Here the primes indicate experimental observation while the other parameters are calculated from the fitted model. For a data set combining M measurement wavelengths at J angles of incidence then the number of observations is

$$L = 2JM \quad (3.20)$$

and the number of undetermined parameters is

$$K = 2M(P + 1) + P \quad (3.21)$$

where P is the number of layers in the structure. To precisely determine the nature of the sample under study it is necessary for $L > K$ at least. In the case of single angle measurements $L = 2M$ and thus

$$L < 2M(P + 1) + P \text{ for } P > 0. \quad (3.22)$$

With a single layer of SiO_2 $K = 4M + 1$. With the inclusion of an interface layer between the oxide and Si $P = 2$ then $K = 6M + 2$. Therefore to ensure that the conditions for determination are met

$$2JM > 4M + 1 \text{ in the case of 1 layer and} \quad (3.23)$$

$$2JM > 6M + 2 \text{ in the case of 2 layers.}$$

This means that for a two layered structure at least 4 measuring angles are necessary in spectroscopic ellipsometry. Results from multiangle analyses of thin oxide layers are given in section 3.1.6. It is important to note that the above rules of thumb apply particularly when the correlations are high and the sensitivity of the measurement parameters of interest is low. Correlations occur for MASE data when

$$\frac{\partial X}{\partial b_i} = C \frac{\partial X}{\partial b_k} \quad (3.24)$$

where C is a constant over the range of experimental observations, X is either measured parameter and $\partial b_k = C\partial b_j$. The parameters b are functions of λ and it follows that for correlation

$$\frac{\partial b_k}{\partial \lambda} = C \frac{\partial b_j}{\partial \lambda} \quad (3.25)$$

Correlation can occur between the parameters of any one layer and the parameters of another layer and C can be a function of λ . However, film thickness is constant i.e. $\partial x_f / \partial \lambda = 0$ always and therefore the correlation between n_f and x_f is broken allowing its accurate determination in the case of a single layer. This is because the rate of change of $\tan\psi$ and $\cos\Delta$ is not proportional to the rate of change of x_f and n_f . In the case of a two layer model if $\partial n_{f1} / \partial \lambda \propto \partial n_{f2} / \partial \lambda$ over the wavelength range measured. Then n_{f1} and n_{f2} (the refractive index for layers one and two respectively) are correlated and x_{f1} and x_{f2} can be if

$$\frac{\partial x_{f1} / \partial n_{f1}}{\partial x_{f2} / \partial n_{f2}} = \text{constant for all } \lambda \quad (3.26)$$

This results in all parameters of the two layers being correlated to each other. For a sufficiently wide range of wavelengths this is unlikely in many material structures. In the case of SiO_2 layers on Si parameter correlation between the oxide thickness and density is high because C is nearly constant over the whole wavelength range particularly when the oxide thickness is below 50nm. Thus the advantage of a wide range of spectroscopic and multiangle measurements cannot be underestimated because the probability that expressions 3.24 to 3.26 hold is reduced significantly.

To illustrate the problem of correlation between changes of density and thickness for thin oxide layers we need only consider the theoretical values calculated from an abrupt layer model using reference spectra. In Fig.3.3 the expected $\tan\psi$ and $\cos\Delta$ are plotted for layers with a 10% difference in either the thickness (nominally 5nm) or the density of a layer of SiO_2 on Si. The density is compared to that of fully relaxed vitreous silica (Malitson 1965). All further references to density will in fact be this relative effective density (D).

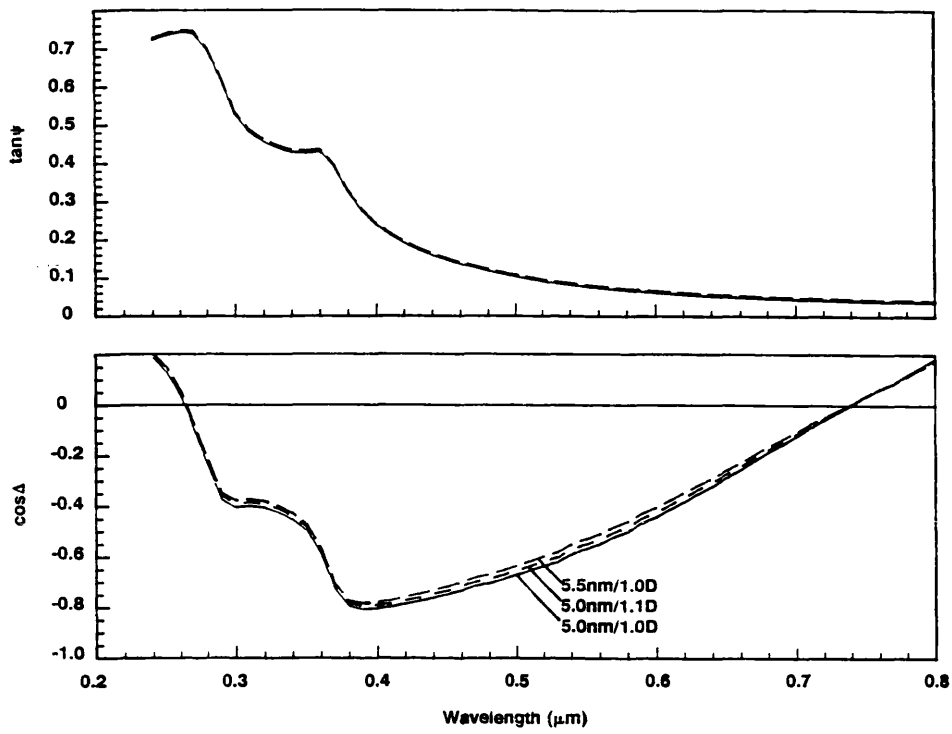


Fig.3.3 Modelled data for a 5nm (nominally) SiO₂ layer on Si and with a 10% increase in either thickness or density.

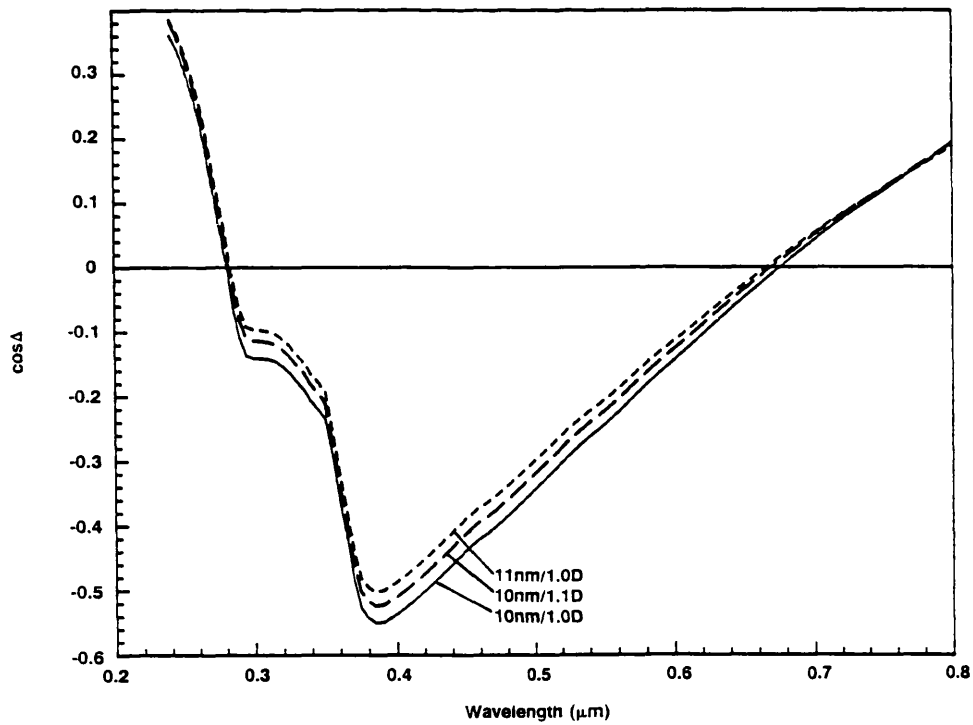


Fig.3.4 Modelled data for a 10nm (nominally) SiO₂ layer on Si and with a 10% increase in either thickness or density.

The first striking feature is that $\tan\psi$ is almost unchanged by the small modifications in film parameters. Because all the curves are rather close it obviously becomes difficult to distinguish between the two variants. $\text{Cos}\Delta$ does show some variation and therefore any attempt to calculate n or density is mostly dependent upon its variation. In the remaining figures only $\text{cos}\Delta$ values are plotted. Fig.3.4 shows the effect on $\text{cos}\Delta$ of 10% variations in x and density for a 10nm layer. A plot for a thicker 15nm film is also included (Fig.3.5). The lower curve is calculated for a 15nm film with a relative density of 1, while the upper curve is actually two overlapping plots for $\text{cos}\Delta$ calculated for a film of 15.5nm/1D and the other for a film of 15nm/1.05D. Clearly even with this thicker film there is difficulty in distinguishing between small differences in thickness and density.

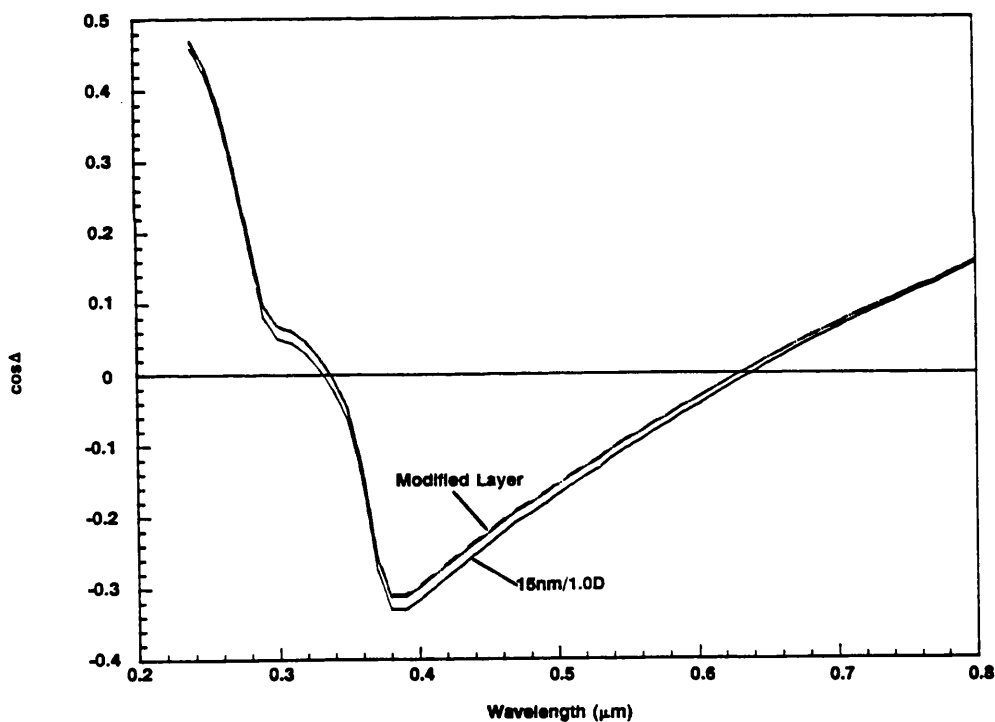


Fig.3.5 Modelled data for a 15nm (nominally) SiO_2 layer on Si and with a 0.5nm or 5% increase in thickness and density respectively.

As yet the case of a two layer sample i.e. one including an interfacial region has not been mentioned. Attempts to calculate the existence of such a layer are not feasible for the very thin layers of interest ($<20\text{nm}$) and the method becomes untenable because the sample is severely under-determined by SE. Thus more information about the sample is

required to extract any interfacial layer properties using multi-angle SE. One can attempt to break (or reduce) the correlation in calculated values by taking and analysing multi-angle spectra. The simultaneous analysis of such spectra is a difficult task. Fortunately the availability of the commercial software from Nebraska University allowed an investigation of the technique to be carried out.

It is important to look at the range over which measurements can be taken to maximise sensitivity. The multi-angle SE software has a facility which allows a theoretical simulation from which sensitivity plots can be generated. The plots are generated by simulating data for particular models as a function of both wavelength and angle of incidence (using reference spectra for the constituents of the model). To determine if experimental measurements will be able to differentiate between any two structures the difference between the two data sets (of either $\cos\Delta$ or $\tan\psi$ is calculated. As noted above $\tan\psi$ is not very sensitive for thin oxide films and so only the difference in $\cos\Delta$ ($\partial\cos\Delta$) is plotted. $\partial\cos\Delta$ contour plots are shown in **Fig.3.6-8** for two different thicknesses. **Fig.3.6** is a plot of the difference of two films of thickness 5.0 and 5.2nm with a relative density of 1 as compared to fully relaxed vitreous silica. What is evident from the contours is that the values of $\partial\cos\Delta$ are significantly greater than the instrumental precision ($\approx\pm 0.0015$ in $\cos\Delta$) over a large part of the range and therefore a 0.2nm accuracy in the experimental data extraction can theoretically be achieved. Thus the contour plots are useful in showing the regions of high sensitivity precisely. The effect of changes in density are shown in **Figs.3.7a,b** for a 5.0nm film with densities of 1.05 and 1.1 in comparison to a fully relaxed film respectively. The change in $\partial\cos\Delta$ obviously increases with a greater difference between the two layers being compared. However, an important point arises here when one compares **Fig.3.6** to **Fig.3.7**. The general form of the plots is quite similar; the effects of small changes in density and thickness on $\cos\Delta$ are similar and thus one can understand the origin of correlation between the film's parameters. The next contour plot included,

Fig.3.8, shows the difference between thickness and density effects.

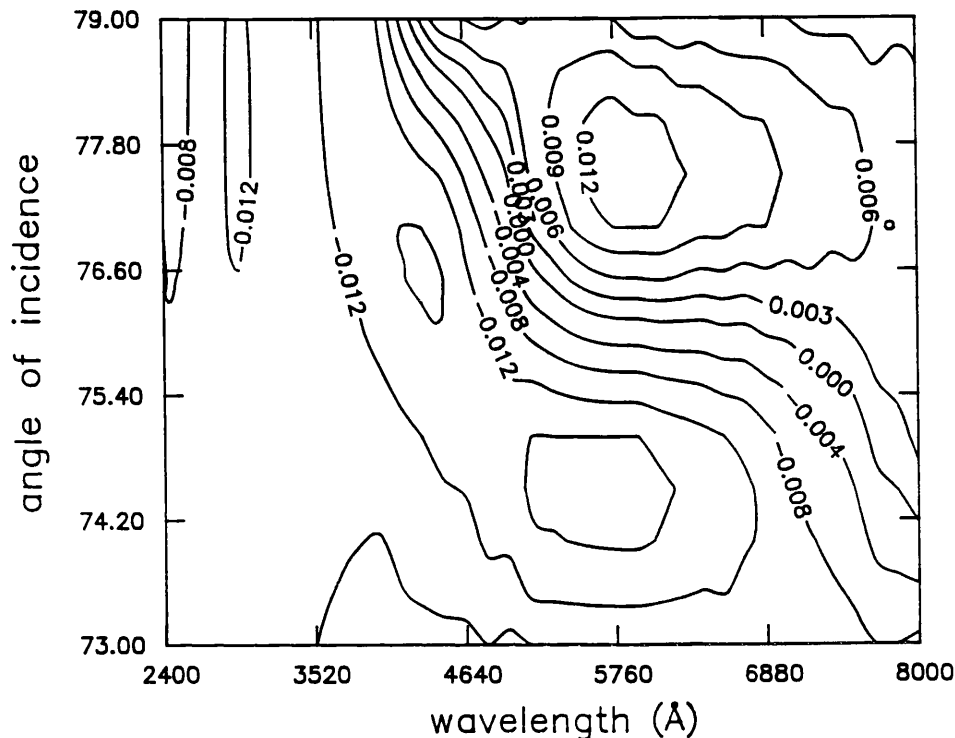
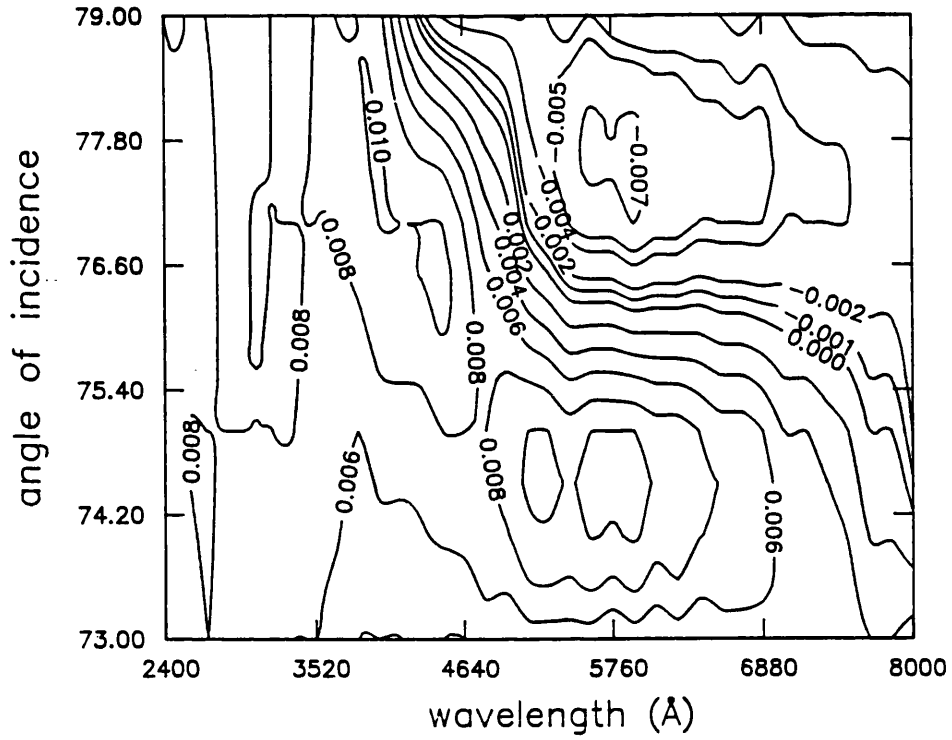
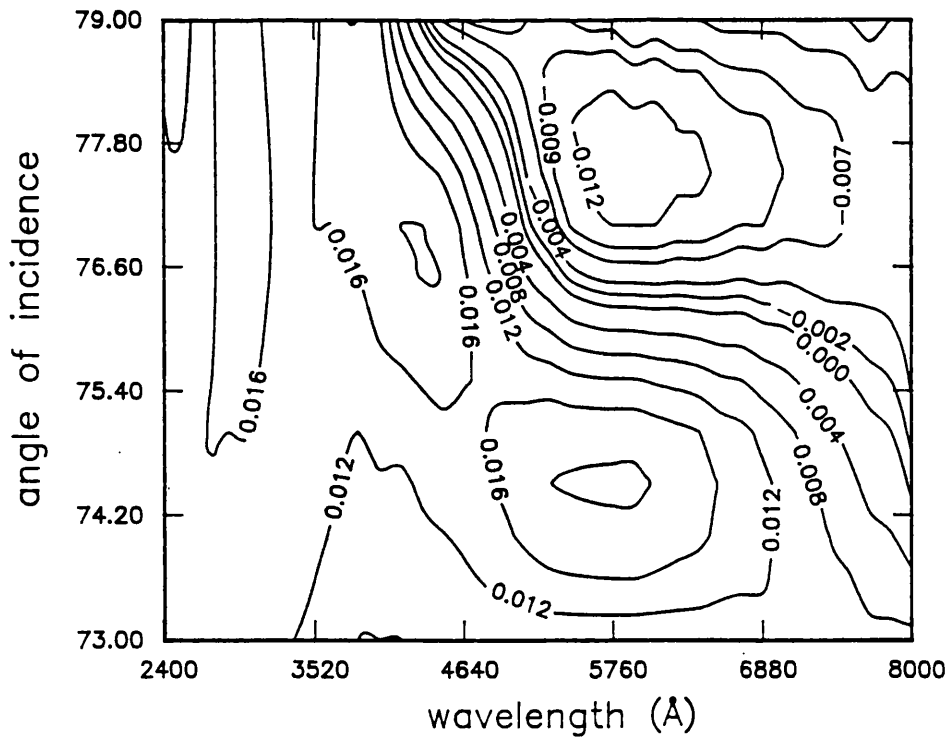


Fig.3.6 $\Delta \cos \Delta$ for two oxides of thickness 5.0 and 5.2nm both with a relative density of 1.

It is well known that an interfacial substoichiometric layer exists between the Si and oxide. Fig.3.9 is a sensitivity plot of the difference between a relaxed SiO_2 layer and one with a 1nm transition layer (of effectively SiO calculated using the Bruggeman effective medium approximation for physical mixing, see appendix), i.e. a two layer system. Although it has been shown above that it is not possible to resolve the parameters of a two layer structure using SE for thin oxide films it is important to note that the region of high sensitivity is in the ultraviolet (240-450nm). Beyond this range sensitivity is low because the penetration depth of the probing light into the Si surface is large. Thus the interaction with the interlayer is limited. However, as wavelength decreases the penetration depth falls because the extinction coefficient (k) of both the Si substrate and interlayer rises, Fig.3.10.



(a)



(b)

Fig.3.7 $\Delta\cos\Delta$ for two oxides of thickness 5nm and (a) relative density of 1 and 1.05 (b) relative density of 1 and 1.1.

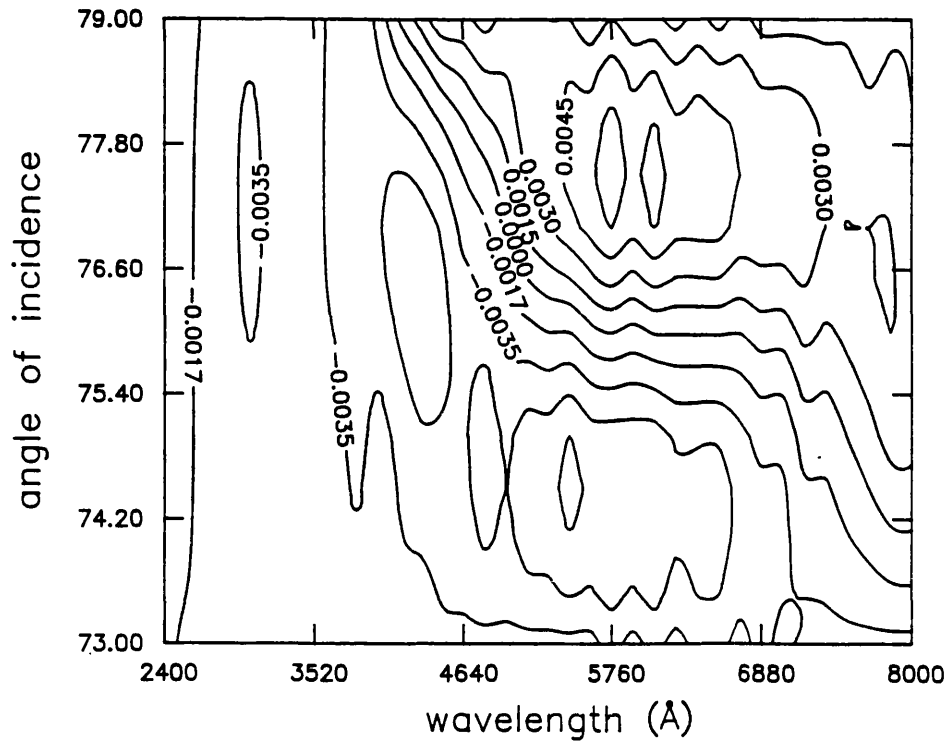


Fig.3.8 $\Delta \cos \Delta$ for two oxides, 5nm with a relative density of 1.05 and the other, 5.2nm with a relative density of 1.

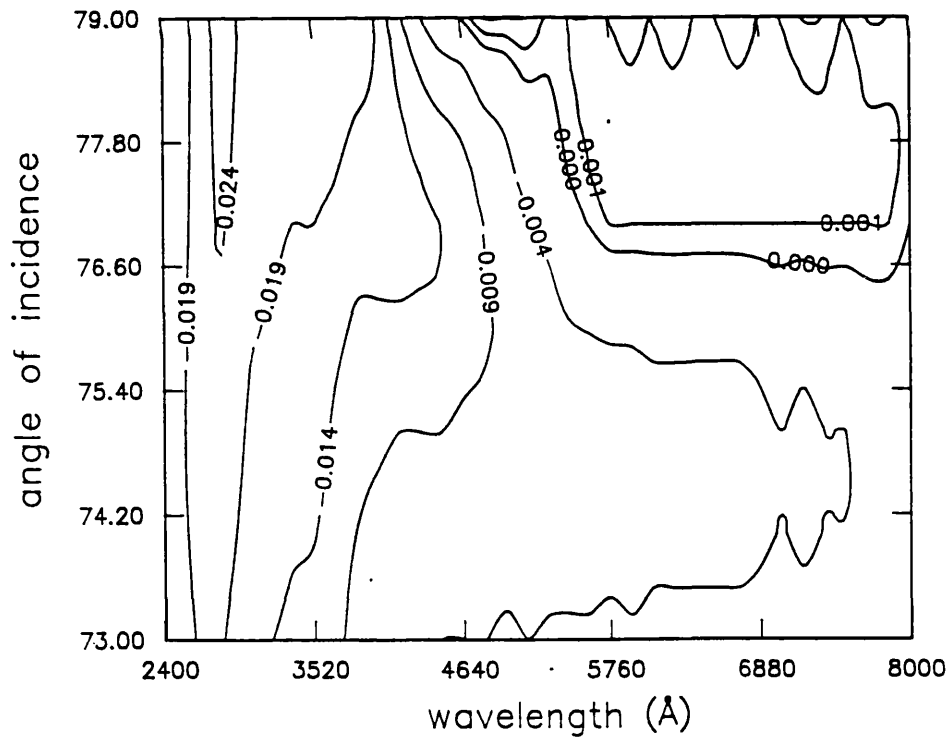


Fig.3.9 $\Delta \cos \Delta$ for two oxides, 5nm with a relative density of 1 and the other 4nm of oxide with a 1nm (SiO) interfacial layer.

An additional conclusion can also be drawn from the preceding discussion. An angle of 75° is at or near the peak sensitivity over most of the spectral range and thus justifies its general use. Sensitivity is at its maximum because 75° is near the Brewster angle for silicon. Thus for the multiangle measurements described below the angles chosen were between 72° and 80° .

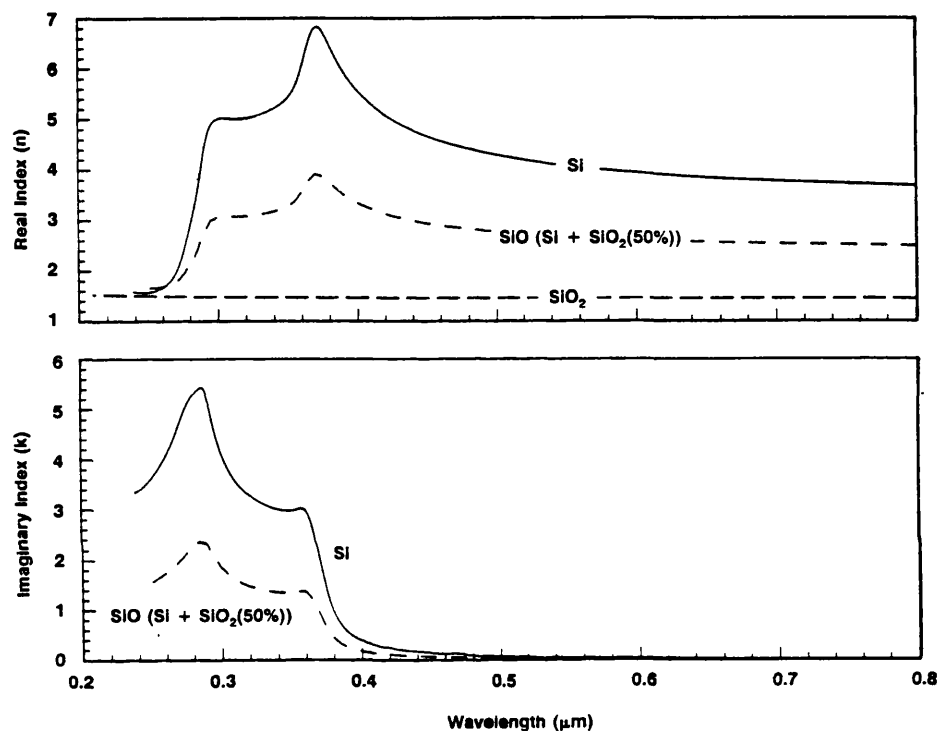


Fig.3.10 n and k for Si, SiO₂ and SiO (generated from the effective medium approximation) and SiO₂.

3.1.4 Ellipsometric Data Collection

The instrument used in the acquisition of $\tan\psi$ and $\cos\Delta$ data was commercially produced by the SOPRA company. The principle of its operation is documented very well elsewhere (see the recent review by Collins, 1990 and references therein). Here only a basic outline is given. The optical arrangement is shown in Figs.3.11,12.

In SWE a monochromatic beam (typically from a laser) of known polarisation is incident on the sample; however in SE a wideband Xe lamp is used as the source. Incident light is collimated (beam divergence of $<0.5\text{mrad}$.) to produce a highly parallel beam. Although a 3mm diameter

beam is nominally incident the sampled area is smaller, typically 1mm^2 . The polarisation is modulated by rotating the polariser. After reflection it passes through the analyser before entering the spectrometer via a quartz optical fibre. A wide lamp emission range (210-2500nm) allows spectroscopic measurements but the practical lower wavelength limit is 240nm because of the fibre transmission. The lamp is powered by a stabilised supply. Polariser and analyser positions are defined to better than 5.5×10^{-3} degrees. The optical bench precision allowed the incident angle to be set to an accuracy of 0.01° . Wavelength of measurement was also very precisely determined by the use of a spectrometer with a double monochromator (i.e. with a prism and a grating giving a resolution of 0.1nm with the slits open). For signal detection a multialkali photomultiplier tube with a range of 185-930nm was used as a photon counter. Thus the overall precision of the the instrument was ± 0.001 in $\tan\psi$ and ± 0.0015 in $\cos\Delta$ at an analyser angle of 45° and wavelength of 600nm.

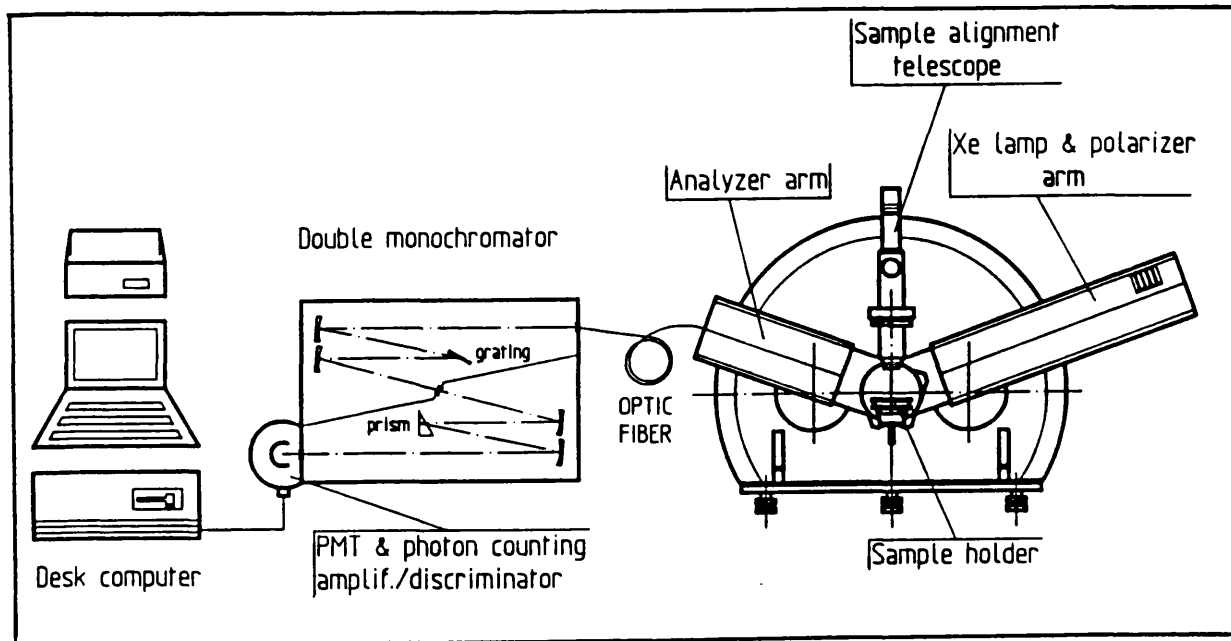


Fig.3.11 Schematic of the ellipsometric measurement system.

Ellipsometer operation and data transformation was computer controlled. The major requirement in "setting up" was sample alignment to ensure that the measurement plane was reproduced from sample to sample. This was done by using an auto-collimator and finally by adjusting the sample orientation to maximise the detected signal in real time.

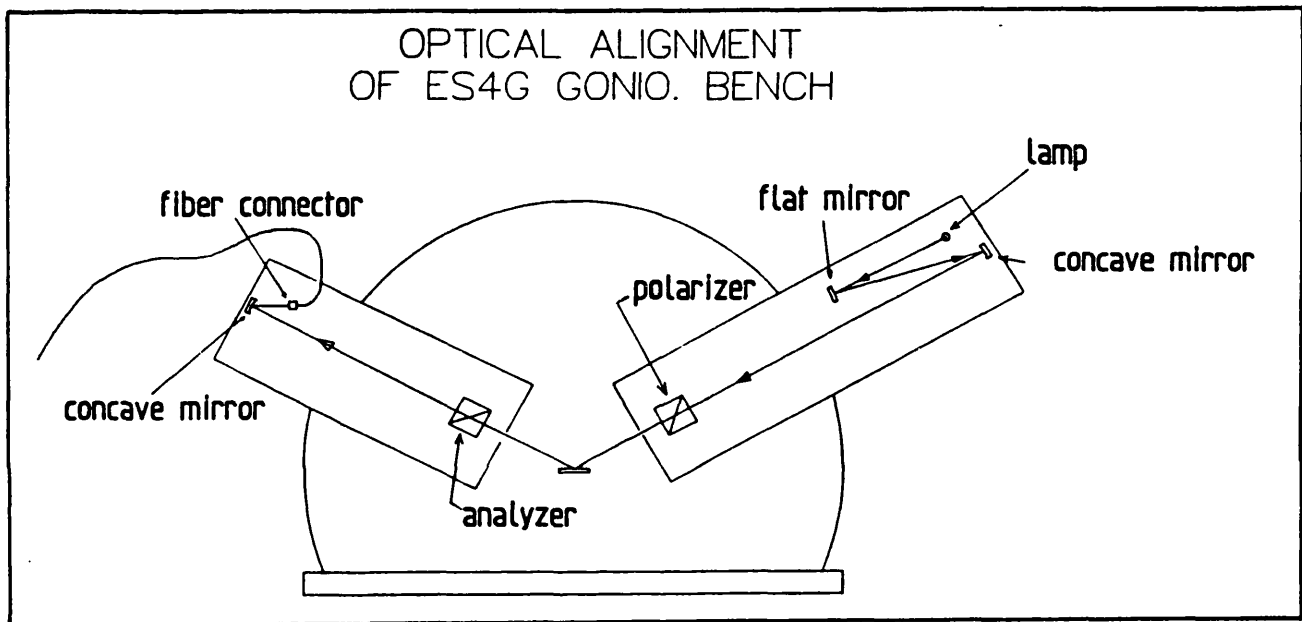


Fig.3.12 Schematic of ellipsometer optical path.

3.1.5 Single Angle Spectroscopic Ellipsometry

Oxide Growth for SE Analysis

In this section the growth of oxides specifically for ellipsometric analysis is described. Oxides were grown at 1050°C using an AG Associates Heatpulse 2101 and in a conventional furnace at 900°C in dry oxygen (the latter for direct comparison with the RTO oxides over a similar thickness range). Oxides grown by the UV/ozone technique (see chapter 2.3) were also studied. Wafer temperature in the Heatpulse was pyrometrically controlled. The growth chamber was purged with oxygen prior to oxidation and during both the temperature ramps (up and down) and the oxidation

period. The Si wafers were Wacker <100> orientation, p-type boron doped (0.2-1 Ω cm) and were used as supplied by the manufacturer without further cleaning. The RTO oxidations were performed in 3 batches (over 3 days) and two boxes of new wafers were used. Wafer box 1 had been previously unsealed and thus the wafers had been exposed to clean room air (for some weeks). Six wafers of batch 1 were from box 1, i.e. exposed to air for some time. Wafer box 2 was unsealed just before the oxidation runs. A wafer from each batch was cycled in the Heatpulse prior to the oxide growths to check the installed recipe. The ramp-up time to growth temperature was approximately 5 seconds. The growth time noted in the data below is hold time at the growth temperature. A separate new box of wafers was used for the furnace oxidations. Again wafers were used as supplied. In batch 1 two wafers were oxidised for each hold time while for batch 2 only one wafer was oxidised for each hold time. Wafers from the third batch were grown under slightly different gas flow conditions but still nominally at 1050°C as determined by the pyrometer in the 2101.

Ellipsometric Analysis

All wafers were analysed without any post oxidation processing. The spectrometer was set nominally to 75° but the angle quoted in the results was arrived at by data fitting. This angle was chosen to maximise sensitivity (as discussed in the theory section). Measurements were taken at 113 wavelengths over the range 0.24-0.8 μ m. The experimental data were then compared with calculated $\tan\psi$ and $\cos\Delta$ spectra obtained from a single layer abrupt interface model using reference spectra for c-Si (Aspnes, 1983) and SiO₂ (Malitson, 1965).

Data fits were calculated using the commercial software provided by SOPRA and the J. Woollam Company. The former used a linear regression while the latter a Marquardt algorithm (as noted above) which calculated parameter correlations and 90% confidence limits. There were also some additional tests of fit quality that were available in the Woollam software. These were the mean deviation of model data points in

comparison to the experimental data, the mean square error, (MSE) sensitivity defined as the change in MSE when one of the fitted parameters was perturbed by $\pm 1\%$ while the others were held constant. This was calculated for all the fitted variables in turn and used to indicate whether the solution was good and also the relative importance of the perturbed parameter. MSE sensitivity was required to be large and positive to demonstrate that the fit was good. If, however, it was small then the value of the perturbed parameter was not very important and its error was also larger. The situation is illustrated in Fig.3.13 where a sharp minimum is observed for an important parameter, curve A, but is shallow for an unimportant parameter, curve B. Another situation can also occur which arises when there is weak dependence or correlation between some of the variables, curve C. Here there are a multitude of minima and the calculation can converge without reaching the correct solution. It is in these cases that the MSE sensitivity is useful and a good solution can be identified by ensuring that the MSE sensitivity is always positive.

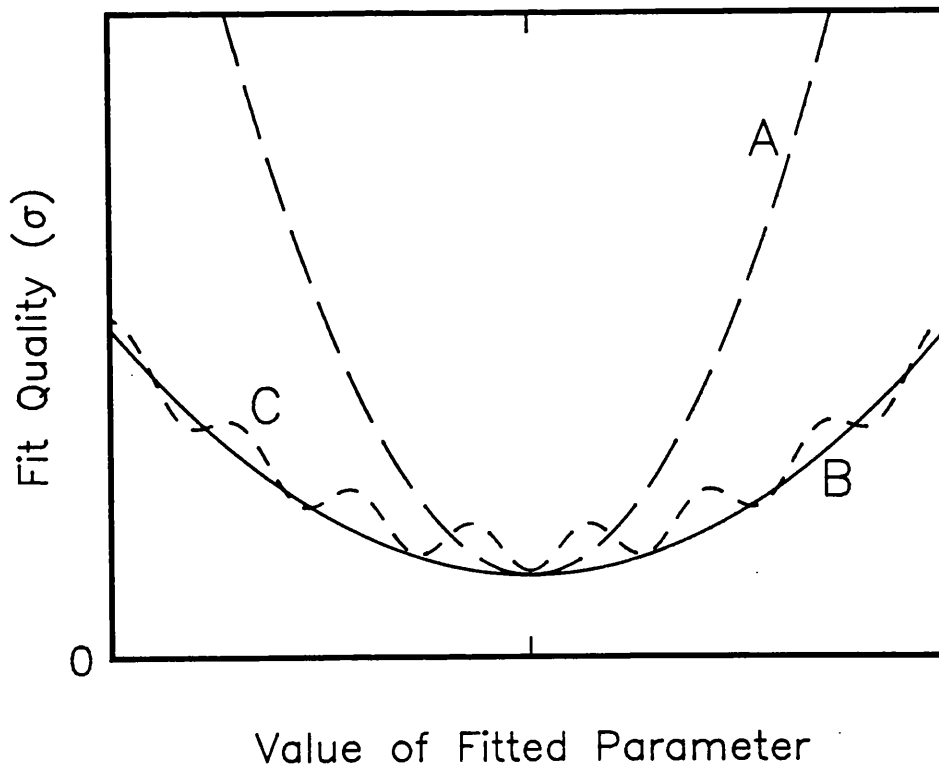


Fig.3.13 Fit quality (σ) dependence on fitted parameter showing the effects

of low sensitivity and/or correlations.

Results

This section is divided into two parts; the first presents the results from thermally grown oxides (RTO and FO) and the second for the UV/ozone oxides.

Thermal Oxides:

The results for the fits are shown in tables 3.I to 3.III (SOPRA software) and 3.IV (J. Woollam Co. software). Two typical fitted model and measured data sets are shown in Fig.3.14. In general very good fits were obtained as indicated by the low values of σ calculated for the fits. Both sets of software give similar results for thickness, density and quality of fit. RTO thickness versus growth time is plotted in Fig.3.15 and appears to be linear over most of the thickness range. A least squares fit to the data over the range 5-14nm produced an oxidation rate of $0.064 \pm 0.02 \text{ nm/s}$. Wafers from box 1 are not included in the least squares fit as they produced thicker oxides for the same growth time in comparison to the newly opened box. The growth data also indicates the reliability of the Heatpulse 2101 and the RTO process itself. The percentage difference in the oxide thicknesses for the same growth time in batch 1 is about 6%. With the high growth temperatures and short times normally used in RTO, any small variations in the growth cycle or the initial condition of the wafer surface can cause significant changes in the final oxide thickness.

Furnace oxides in the thickness range 8nm to 50nm were also analysed. Two wafers were grown simultaneously and the difference in oxide thickness between them was generally less 0.2nm (i.e. $\pm 1\%$). Thickness data for wafers grown at RSRE is shown in Fig.3.16. The data is plotted using ln-ln scales. However, this should not be taken to imply that the oxidation follows a power law even though it has been suggested by Reisman et al. (1988) and Wolters et al. (1989). A much more complete data set is necessary to study kinetics. There also appears to be a deviation from the straight line for shorter times.

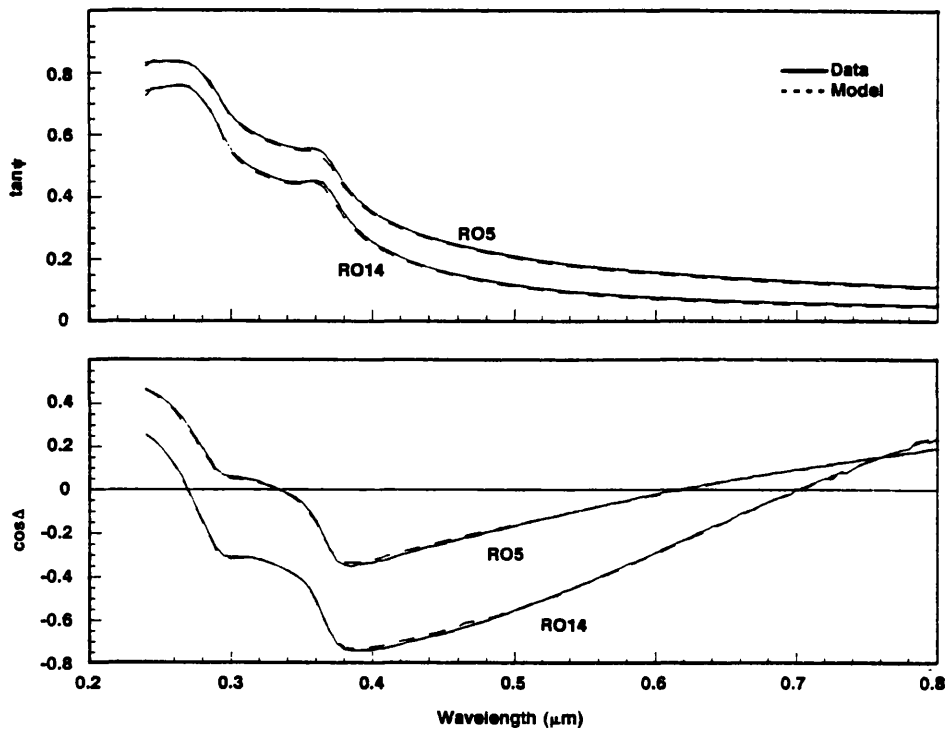


Fig.3.14 Two typical SE experimental and model data sets (see table 3.I).

The origin of this is probably because the growth period is short and thus influenced by the temperature ramp (load) period (see chapter 1).

Data, shown in Fig.3.17 for both RTO and FO indicate a trend towards increased oxide density for thinner oxides. Fitch et al. (1989) have also observed such a trend but were unable to analyse very thin oxides by infra-red spectroscopy due to the weak oxide absorption. They found it difficult to obtain data on very thin oxide layers with their dispersive IR instrument. Some Fourier transform IR data collected on thin oxides studied by SE also are discussed below.

Although it is difficult to define both thickness and density accurately when the sensitivity correlation is high (see table 3.IV) even for the much larger data set collected by SE. It is still possible to determine accurate thickness values. The density of the oxides appears to increase for thinner oxides down to ≈ 6 nm. Below ≈ 6 nm the sensitivity of the measurement is reduced so much that it is difficult to distinguish between density and thickness leading to a large scatter in the density values calculated.

Sample No.	Growth Time (s)	Oxide Thickness (Å)	Relative Density	σ
RO1	250	170	1.066	0.0066
RO2	"	182	1.002	0.0066
RO4	150	137	1.058	0.0068
RO5	"	143	1.041	0.0067
RO7	100	120	1.014	0.0073
RO8	"	112	1.057	0.0073
RO10	50	82	1.128	0.0075
RO11	"	78	1.122	0.0073
RO13	25	57	1.101	0.0074
RO14	"	58	1.215	0.0073
RO16	10	44	1.145	0.0080
RO17	"	47	1.050	0.0080
RO19	5	39	1.007	0.0077
RO20	"	42	1.051	0.0078

Table 3.I Results from batch one rapid thermal oxidation, shaded sample numbers indicate that the wafers were from box 1.

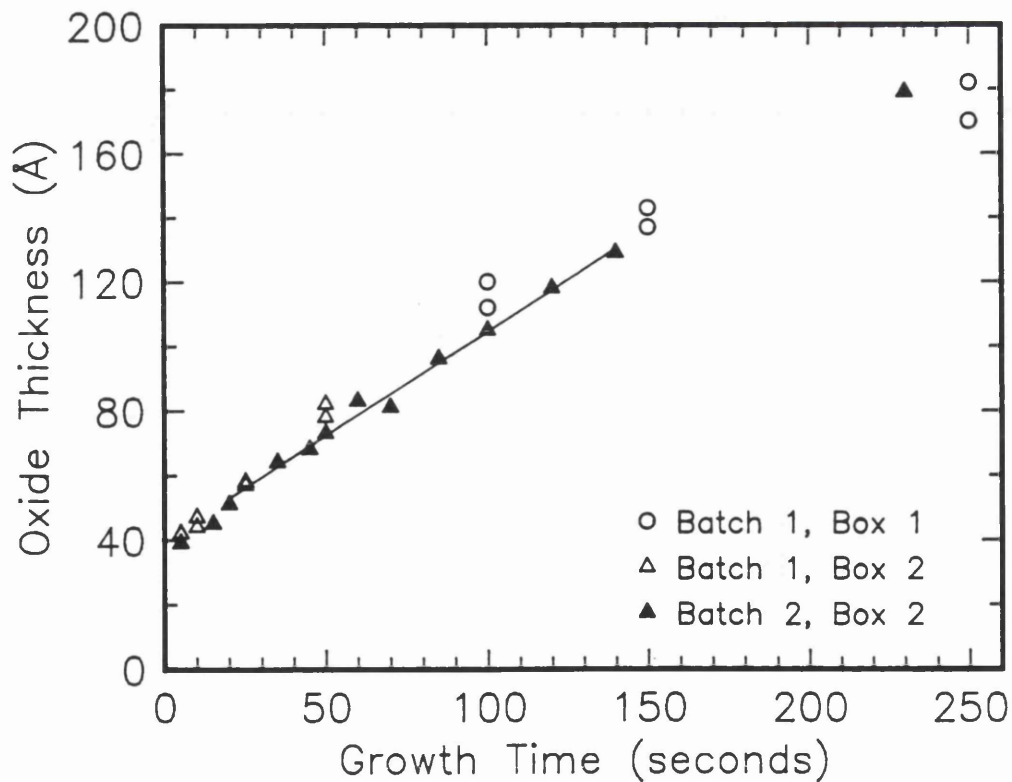


Fig.3.15 Rapid thermal oxide growth at 1050°C.

Sample No.	Growth Time (s)	Oxide Thickness (Å)	Relative Density	σ
RTO1	250	170	1.000	0.0073
RTO2	120	118	1.033	0.0073
RTO3	70	81	1.130	0.0071
RTO4	45	68	1.122	0.0074
RTO5	15	45	1.107	0.0076
RTO7	230	179	1.015	0.0062
RTO8	85	96	1.093	0.0071
RTO9	50	73	1.160	0.0071
RTO10	20	51	1.116	0.0076
RTO11	5	39	1.001	0.0080
RTO13	140	129	1.037	0.0068
RTO14	100	105	1.075	0.0070
RTO15	60	83	1.065	0.0075
RTO16	35	64	1.019	0.0074

Table 3.II Results from batch two oxidations.

Sample No.	Growth Time (mins.)	Oxide Thickness (Å)	Relative Density	σ
FO1	15	87	1.121	0.0070
FO2	"	85	1.135	0.0070
FO3	20	99	1.109	0.0069
FO4	"	101	1.070	0.0072
FO5	25	112	1.074	0.0069
FO6	"	112	1.117	0.0071
FO7	30	123	1.061	0.0070
FO8	"	123	1.091	0.0068
FO9	35	139	1.060	0.0068
FO10	"	139	1.076	0.0064
FO11	60	183	1.029	0.0061
FO12	"	184	1.030	0.0061

Table 3.III Results from furnace oxidations.

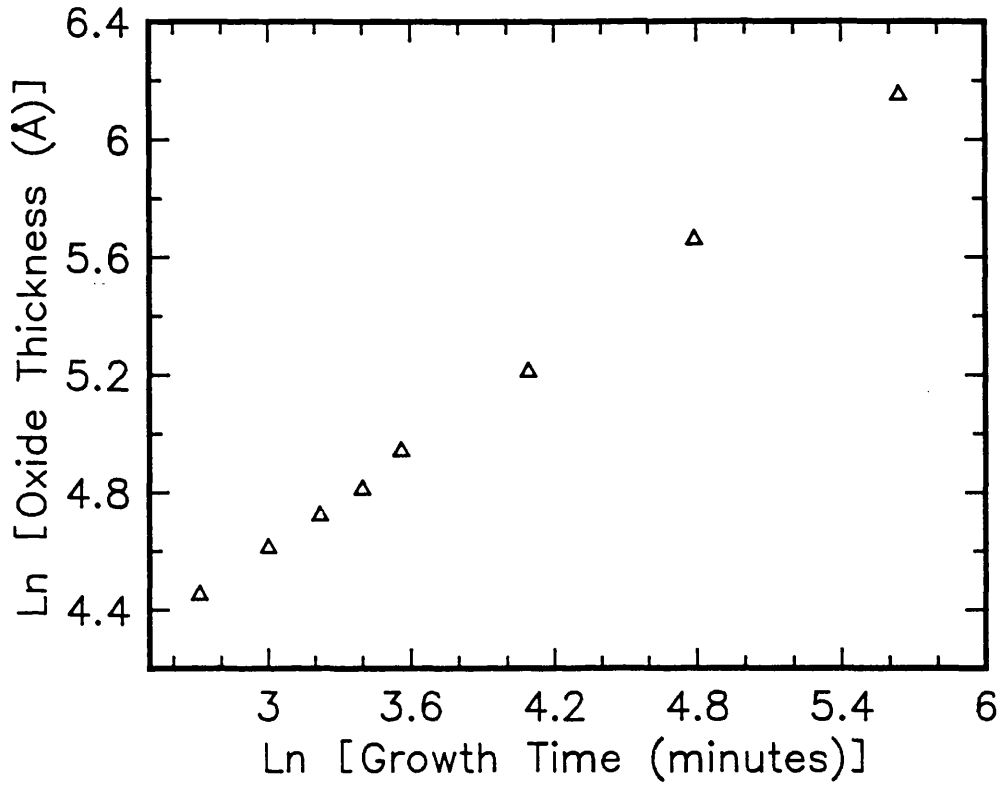


Fig.3.16 Ln-Ln plot of thermal oxide growth at 900°C.

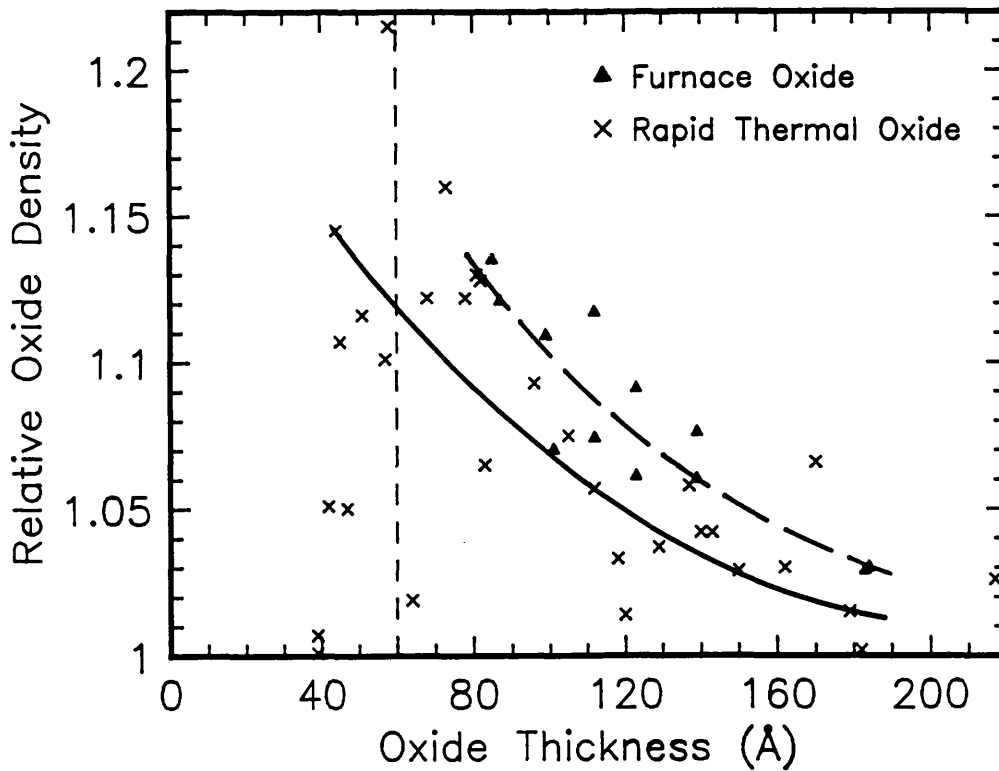


Fig.3.17 Relative oxide density of RTO and FO oxides.

Sample Number	Thickness (Å)	Relative Density	Correlation	σ
RO19	38.7 ± 1.7	$1.001 \pm .095$	0.995	0.0075
RO14	58.3 ± 1.4	$1.200 \pm .050$	0.993	0.0069
RO10	83.7 ± 3.4	$1.130 \pm .090$	0.992	0.0070
RO8	112.7 ± 0.8	$1.046 \pm .013$	0.992	0.0022
RO4	137.5 ± 2.9	$1.070 \pm .040$	0.990	0.0083
RO5	143.8 ± 2.3	$1.036 \pm .029$	0.989	0.0064
RO2	182.5 ± 2.4	$0.993 \pm .020$	0.986	0.0063

Table 3.IV Calculated results to selected data from batch 1 showing correlations and 90% confidence limits.

To more clearly illustrate that the oxide films under study are densified σ is plotted as a function of relative oxide density for oxides of thickness 14.3nm and 9.2nm in Fig.3.18. It is clear from these curves that the best fits (minima) are located away from a relative oxide density of 1 towards larger values. Although the correlations calculated are high (>0.98 is defined as high), it is possible to obtain reliable results by attempting many fits to the data using different starting parameters.

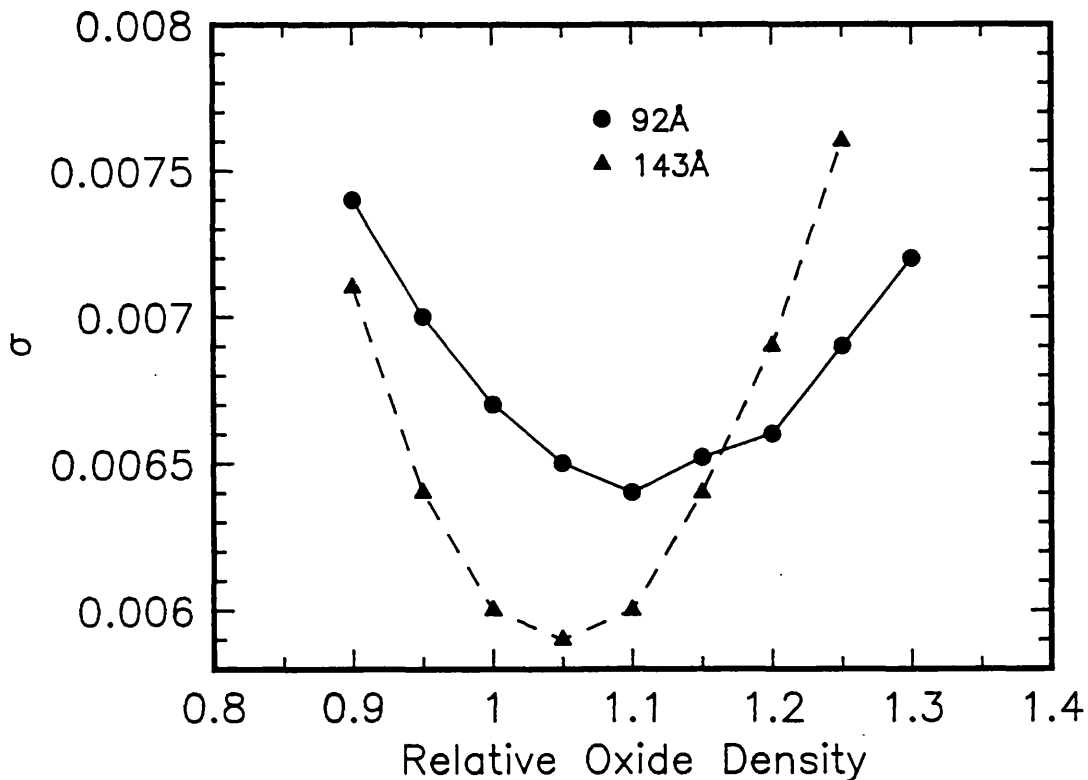


Fig.3.18 Fit quality as a function of relative oxide density.

With SWE the error in determining thickness is typically quoted to be at best 0.3nm even when n is fixed, for the thickness range under study here. As table 3.IV shows the errors are notably lower in the present study and moreover the density (and therefore n) is also determined. In conventional SWE it is not normally possible to calculate n for oxides of thickness less than 50nm with a high degree of confidence. The densities of the 900°C oxides are slightly greater than those grown at 1050°C for the same oxide thickness as expected from the work of Landsberger and Tiller (1987) and Ravindra et al. (1987). The FO also show much less scatter in the density values calculated than the RTO wafers. Clearly though, the dependence of density on oxide thickness is much stronger than on the growth temperatures used in this study.

Interfacial structure between the oxide and Si substrate has not been considered in the above discussion. Simulations of a two layer structure (i.e. with a sub-stoichiometric oxide interfacial layer) have not been very successful for the thinner layers under study. Both limits on instrumental sensitivity and the strong correlation between layers of similar optical properties mean that it is impossible to distinguish an interfacial layer with a high degree of confidence as was discussed in the theory section. A previous attempt by Ravindra et al. (1988) to identify interfacial layers using SE for thin oxides was also unsuccessful. From the work of Aspnes and Theeten (1980) it was evident that by including an interfacial layer the calculated density of the oxides decreased slightly. This was because the single layer model compensated for the interface by increasing the oxide density in the fit. Their inclusion of an interface also improved the quality of fitting to data. With single angle SE in the present study this was not the case and the value of σ was not reduced for layers of thickness less than 30nm. The change in density incurred in the two layer models was small and rather less than the errors calculated in table 3.IV. Recently a study of SWE data by Kalnitsky et al. (1990) has suggested that the high values of n that are often calculated for thin oxides can be explained by assuming that the oxide

density decreases (gradually) from the interface with the silicon, to an arbitrary point in the oxide. Their qualitative modelling is in accord with these results of increasing oxide density as thickness decreases. However, their n values are much higher, for example for a layer of approximately 9nm they calculated $n \approx 1.9$ whereas our maximum value for any thickness was less than 1.6 (see Fig.3.1). As noted above, SWE is not reliable for calculations of n for the thin oxides under study.

For oxides of about 30nm and greater σ was improved slightly by using an interfacial layer but the errors on the calculated values were large. The calculations using the Woollam software showed that not all the criteria of "good" fit quality were met. In particular the MSE sensitivity of interfacial parameters was found to be negative in the two layer modelling attempts. Additionally it should be noted that in the study by Aspnes and Theeten the interfacial layer was constructed from a calculation of the optical properties of a chemically mixed region. In the available software it was only possible to use the physical mixing model of a substoichiometric layer calculated from the Bruggeman effective medium approximation. This type of interlayer, while acceptable for situations of modelling rough interface induced sub-stoichiometry is not suitable for determining the nature of a chemically altered stoichiometry. Unfortunately due to the availability of time it was not possible to investigate the effect of a chemically mixed interlayer. The conclusion that is drawn from this study that density increases as oxide thickness falls is still valid because the high values of density observed are not likely to be accounted for by an interfacial layer as was also noted by Aspnes and Theeten.

UV/Ozone Low Temperature Oxides:

The results of SE analysis of some typical oxides are shown in table in table 3.V. From the discussion above of more conventionally grown oxides it is clear that the results from thin oxides are open to errors. This does not preclude the usefulness of SE in obtaining some information on the nature of the film grown. Here it has proved that the films grown are indeed

stoichiometric SiO_2 rather than some contaminant layer where the effect of such a film cannot be determined by SWE. The close fit of experimental data to model are shown in Fig.3.19 for the three layers of table 3.V.

Sample Number	Thickness (Å)	Relative Density	σ
512	74	1.20	0.0075
712	54	1.15	0.0072
412	42	1.15	0.0077

Table 3.V Typical UV/ozone oxide results.

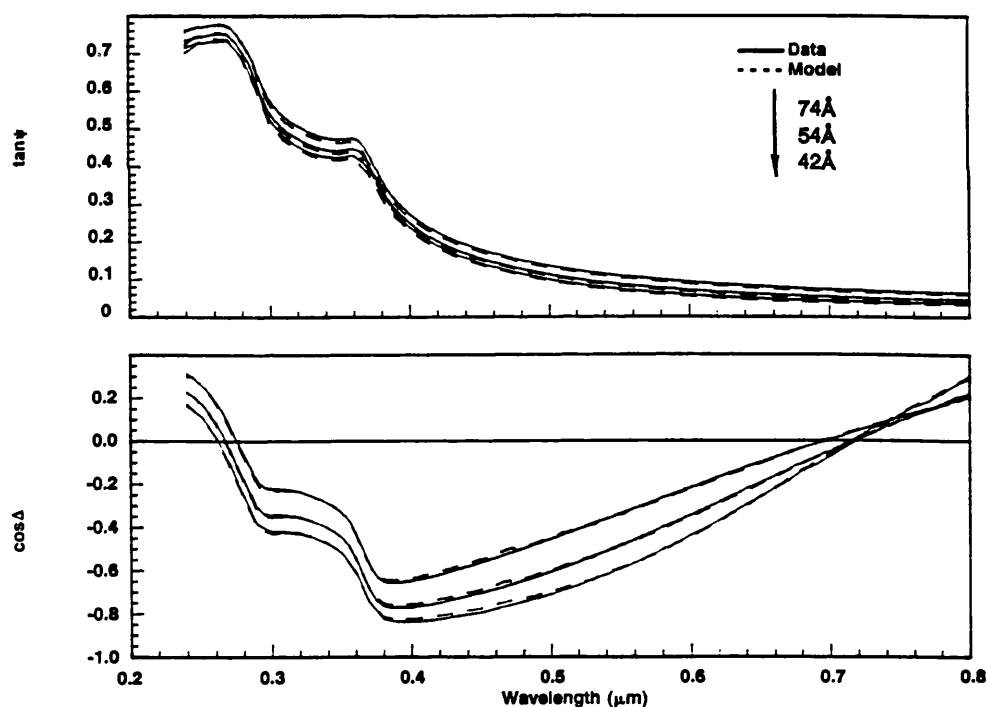


Fig.3.19 Experimental and model SE data for UV/ozone oxides, table 3.V. Additionally a plot of σ versus relative density, Fig.3.20 (similar to Fig.3.18) shows that although the variation in σ is smaller the minima are shifted to values of D greater than 1. In fact this was a common result for all the UV/ozone films whereas RTO oxides show much larger scatter. The very

low temperatures used in the UV/ozone growths suggest that the density of the oxides should be high in all cases because any thermally induced relaxation cannot occur.

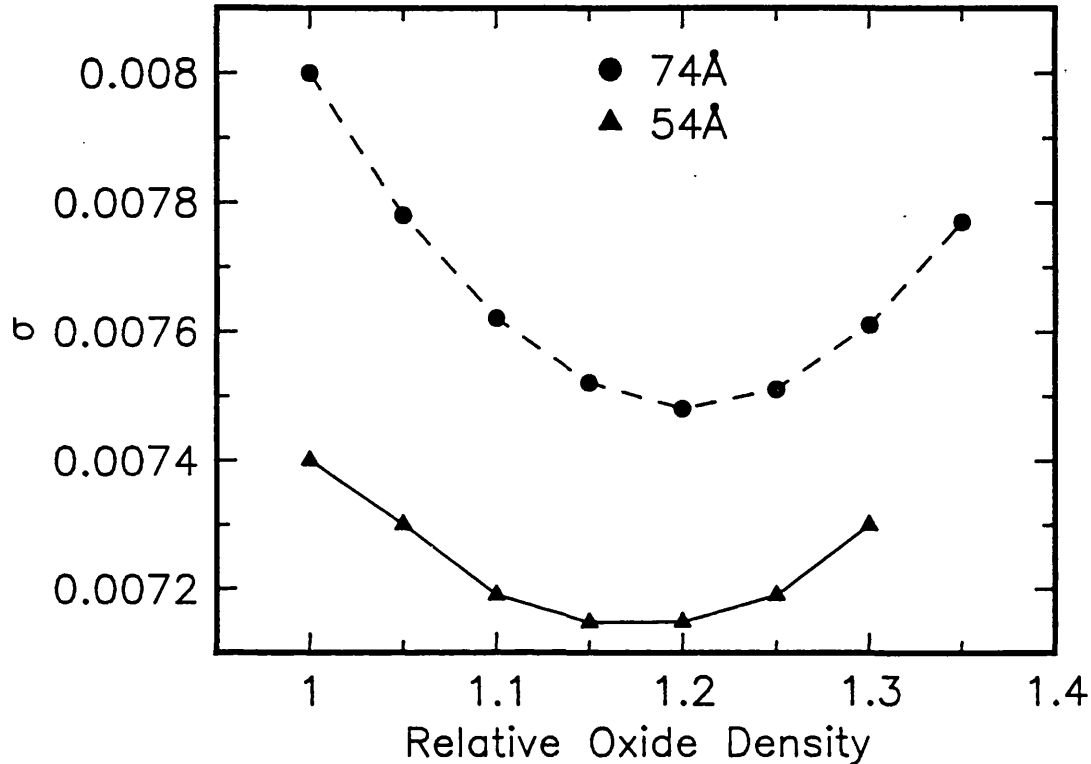


Fig.3.20 Fit quality as a function of relative oxide density for UV/O₃ oxides.

3.1.6 Multi-angle SE

A furnace grown oxide (FO1) was measured at 4 angles to test the multi-angle SE correlation breaking theory. The acquisition of variable angle data was quite time consuming and difficult. It was paramount to ensure that the angle of measurement was as precisely determined as possible as noted in the theory section.

If we look back to equations 3.20 to 3.22 we can calculate the values of L and k and try to ensure the sample under study will be sufficiently determined to allow unambiguous data extraction.

Unfortunately due to a limit on the data set that can be processed by the MASE programme the full data set collected could not be analysed. Again data was taken at 113 wavelengths at the 4 angles (nominally 73, 75, 77 and 79 degrees). The data was analysed with an increasing number of angles but

due to the upper bound on the data the number of wavelengths was simultaneously decreased. Although this did not allow one to achieve the best result possible with all the data collected it still demonstrated the effectiveness of the method. In table 3.VI the number of angles and wavelengths for the collated data are noted along with the results of the calculations.

Angles	No. of Wavelengths	Thickness (Å)	Relative Density	Correlation	L	K
75	113	91.7 ± 1.8	1.117 ± 0.044	0.992	226	453
75, 73	57	91.8 ± 1.6	1.112 ± 0.027	0.996	228	229
75, 73, 77	45	92.2 ± 1.5	1.106 ± 0.037	0.986	270	181
75, 73, 77, 79	31	92.5 ± 1.5	1.100 ± 0.039	0.986	248	128

Table 3.VI Multi-angle data set results.

What is important to note is the reduction in the number of wavelengths with increasing angles. Clearly though the fit quality is not drastically reduced and in fact the correlation decreases only slightly because thickness and density are so strongly correlated. This indicates that the multi-angle information has a large effect on correlation breaking in this situation. However it is important to emphasise that it is only the combined MASE data set that is truly deterministic. Thus the results of table 3.VI are an experimental demonstration of the correlation breaking theory discussed in section 3.1.3.

3.2 Infrared Absorption Spectroscopy

3.2.1 Introduction

It was demonstrated in the previous section that oxide properties are dependent upon both the layer thickness and growth conditions. Spectroscopic ellipsometry was used to study the physical nature of the oxide. In this and the following section a short discussion of the chemical nature of the thin oxides grown is presented. The two techniques used are infrared spectroscopy (IRS) and X-ray photoelectron spectroscopy.

Many studies have previously analysed bulk vitreous silica however it is only recently that the technique has been applied to thin grown oxides Boyd and Wilson (1982, 1987) and Grosse et al. (1986). Several characteristic absorption peaks have been observed and linked to various transverse-optical (TO) and longitudinal-optical (LO) vibration modes. These were theoretically studied by Galeener and Lucovsky (1976) and Kirk (1988). Four coupled pairs of TO-LO modes have been identified but most oxide analysis has concentrated on the TO mode at 1070cm^{-1} . This is the so-called stretching mode and has the largest absorption coefficient in transmission measurements. Both Boyd and Wilson (1987) and Fitch et al. (1989) have observed shifts in the peak positions and peak half widths as oxide thickness diminished. Devine (1988) collated data on the peak positions of densified bulk oxides and modelled peak ($1070, 800$ and 450cm^{-1}) shifts using a central force model. He found a linear variation of peak position with density as shown in Fig.3.21. Grosse et al. (1986) used reflection spectroscopy instead of transmission to overcome the difficulties of substrate effects and improve sensitivity. They also considered the effect of incident angle and polarisation on the observed spectra. With particular combinations of angle and polarisation they found that only certain absorption modes were active. This was also studied more recently by Olsen and Shimura (1989), Fig.3.22, for very thin ($\pm 1\text{nm}$) oxide layers.

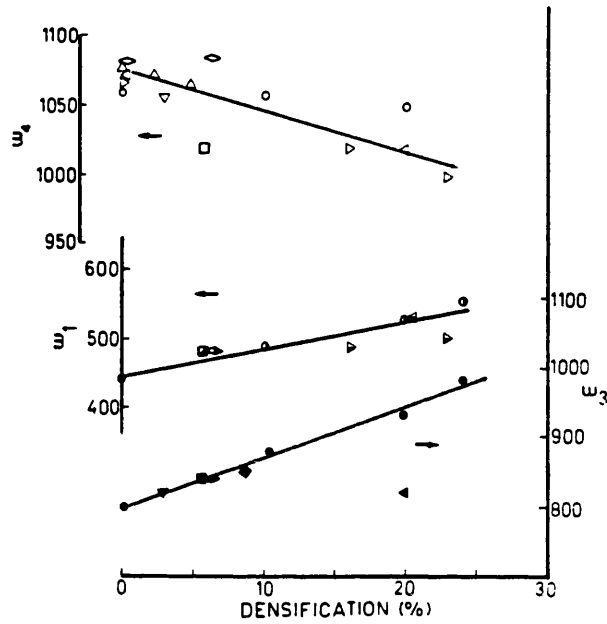
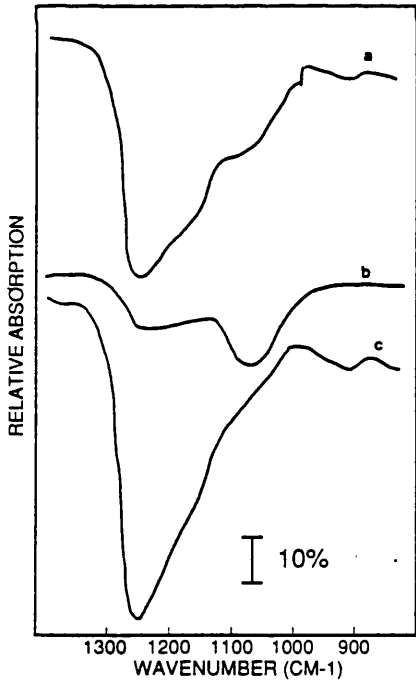


Fig.3.21 Variation of SiO₂ infrared peak positions with density, Devine (1988), ω_4 is the asymmetric stretching absorption peak.



Infrared reflection spectra of 1.2 nm SiO₂ film using (a) light with uncontrolled polarization, (b) light polarized perpendicular, and (c) light polarized parallel to the plane of incidence.

Fig.3.22 After Olsen and Shimura (1989).

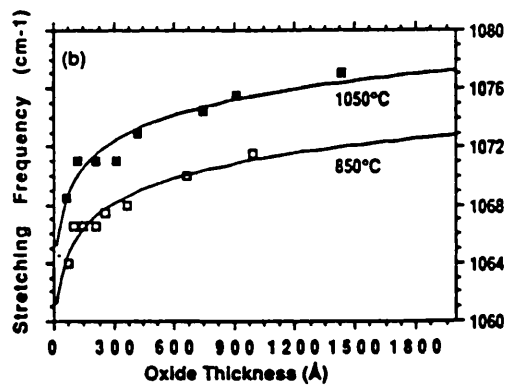
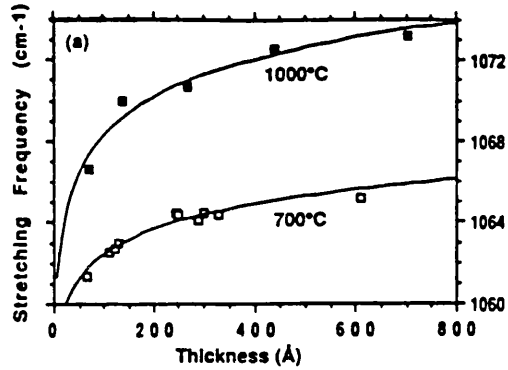


Fig.3.23 After Fitch et al. (1989).

For this report only a limited IRS study was possible. The aim was to confirm density results calculated from SE. Fig.3.23 illustrates the behaviour of the 1070cm^{-1} peak as a function of oxide thickness and growth temperature (as determined by Fitch et al.). The peak position decreases with both thickness and oxidation temperature. However, the behaviour below 10nm does not appear to follow that of thicker layers as was discussed by Boyd and Wilson (1987). They noted that the normally asymmetric peak, with a shoulder towards higher wavenumbers, observed for thick oxide layers (at 1080cm^{-1} , see Fig.3.25 below), becomes symmetric at approximately 10nm. Below 10nm the asymmetry appears towards lower wavenumbers, suggesting that the nature of thin oxides is significantly different from thick layers. Boyd also reported (1987) that the peak at 1070cm^{-1} could be deconvoluted into two peaks centred at 1050 and 1085cm^{-1} . However, care is necessary with the deconvolution method of identifying peaks because the result can depend upon the method of calculation. An alternative may be to take the approach of Grosse et al. (1986).

3.2.2 Experimental

A wide range of oxide thicknesses was analysed. The measurements were taken on a Digilab FTS40 with a spectral resolution of 4cm^{-1} and 2cm^{-1} for transmission and reflection measurements respectively. In transmission the beam diameter was 1mm but in reflection a 12mm diameter beam was incident on the sample. All reflection spectra were taken at an angle of incidence of 45 degrees. The raw transmission spectral response (arbitrary units) of the FTIR with a recently HF dipped Si sample is plotted in Fig.3.24 after signal averaging 128 scans. The range of the FTS40 is $400\text{-}4000\text{cm}^{-1}$. Therefore in the region of interest, $900\text{-}1500\text{cm}^{-1}$, the response of the spectrometer is high. The main peak observed is the O interstitial absorption at 1107cm^{-1} which overlaps the 1070cm^{-1} region. The effect of this peak was removed by subtracting the spectra of reference samples taken from the same wafer but with the oxide stripped off. Another difficulty with transmission measurements is the interference fringing commonly observed

with Si wafers. This was reduced in transmission by taking spectra at 4cm^{-1} resolution and applying some smoothing to the data. Finally the spectra were base line corrected and the peak positions determined. The effects of both smoothing and baseline correction are illustrated in the figures below. The level of smoothing was carefully limited to avoid any deleterious loss of spectral information.

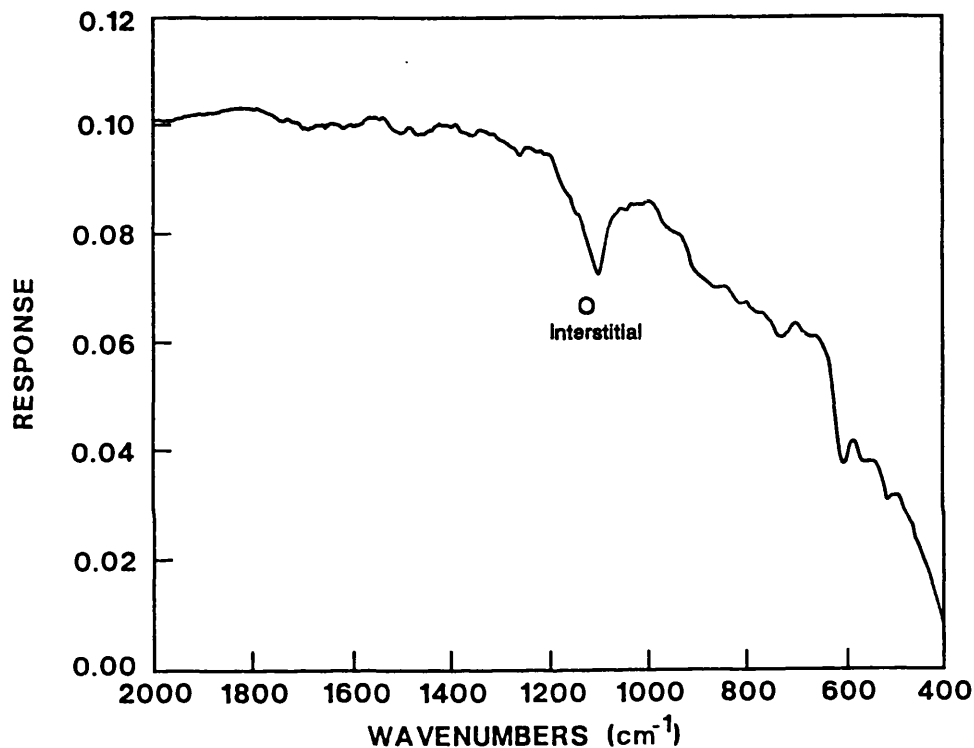
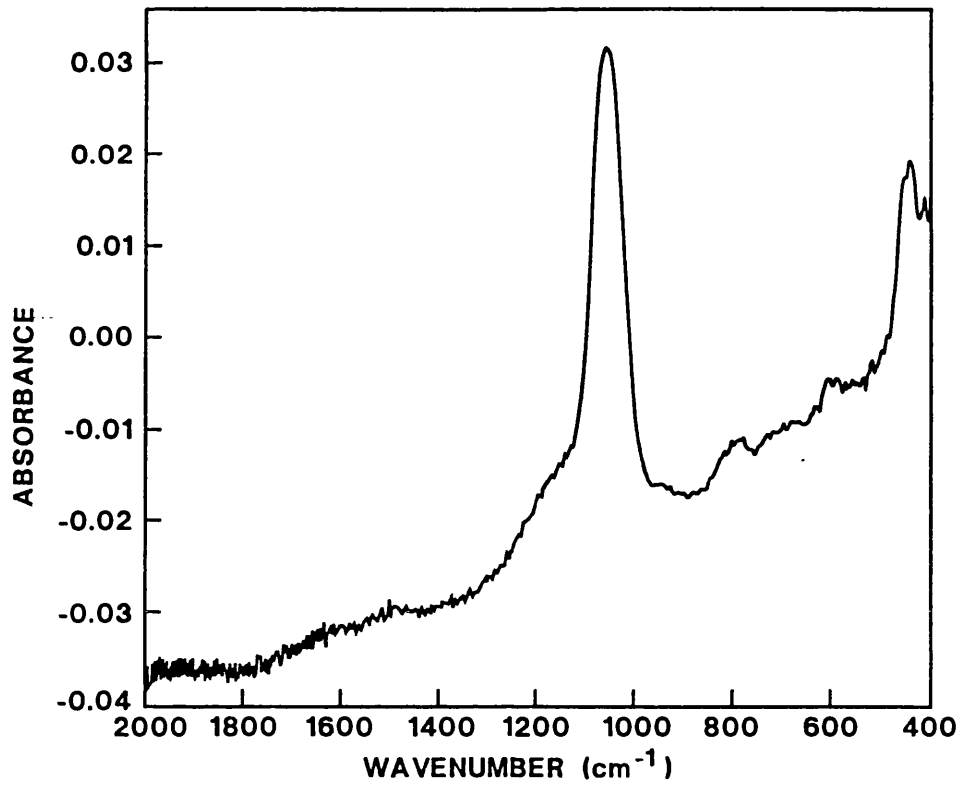


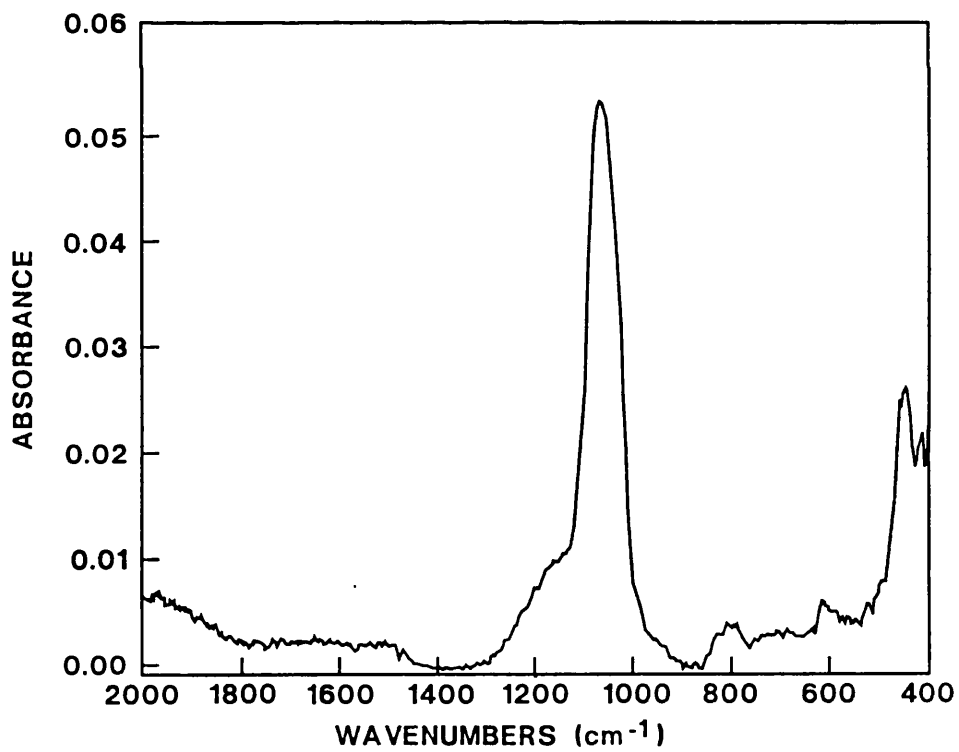
Fig.3.24 FTIR spectrometer detector response (arb. units) in the wavenumber range of interest.

3.2.3 Results

A typical thick oxide spectrum collected by averaging 300 scans is shown in Fig.3.25a,b. a) shows the raw spectrum as collected while b) shows the spectrum after smoothing and baseline correction. The three major TO peaks appear at approximately 1070cm^{-1} , 450cm^{-1} and 800cm^{-1} . A similar operation was also carried out on the raw spectra plotted in Fig.3.26. An expanded view, Fig.3.27a, of the UV/ozone oxide data both smoothed and unsmoothed shows that with care fringing effects can be reduced without undue loss of data. With baseline correction, Fig.3.27b, it becomes obvious that the peak is asymmetric as noted by Boyd (1987).



(a)



(b)

Fig.3.25 Typical thick (30nm) thermal oxide transmission spectrum, (a) raw data and (b) after smoothing and baseline correction.

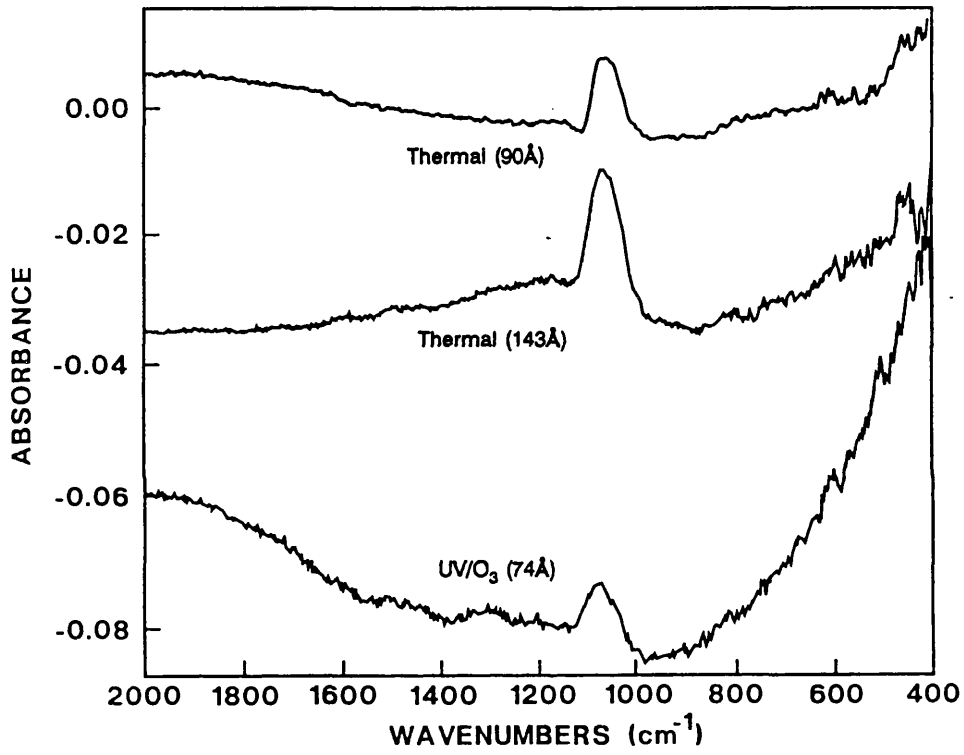
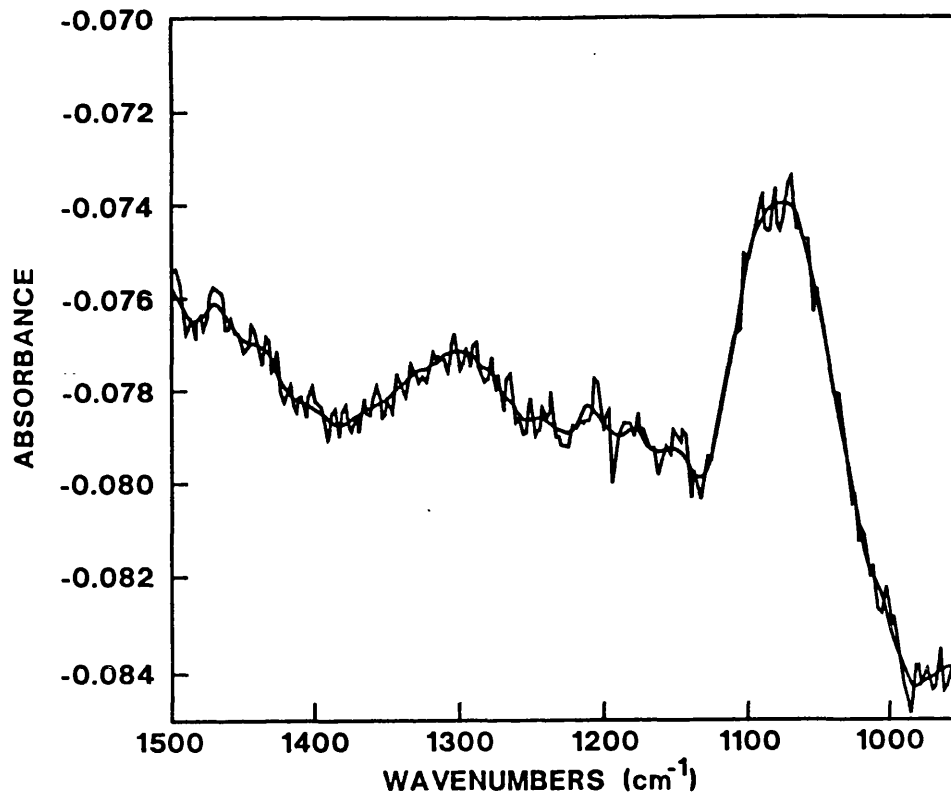
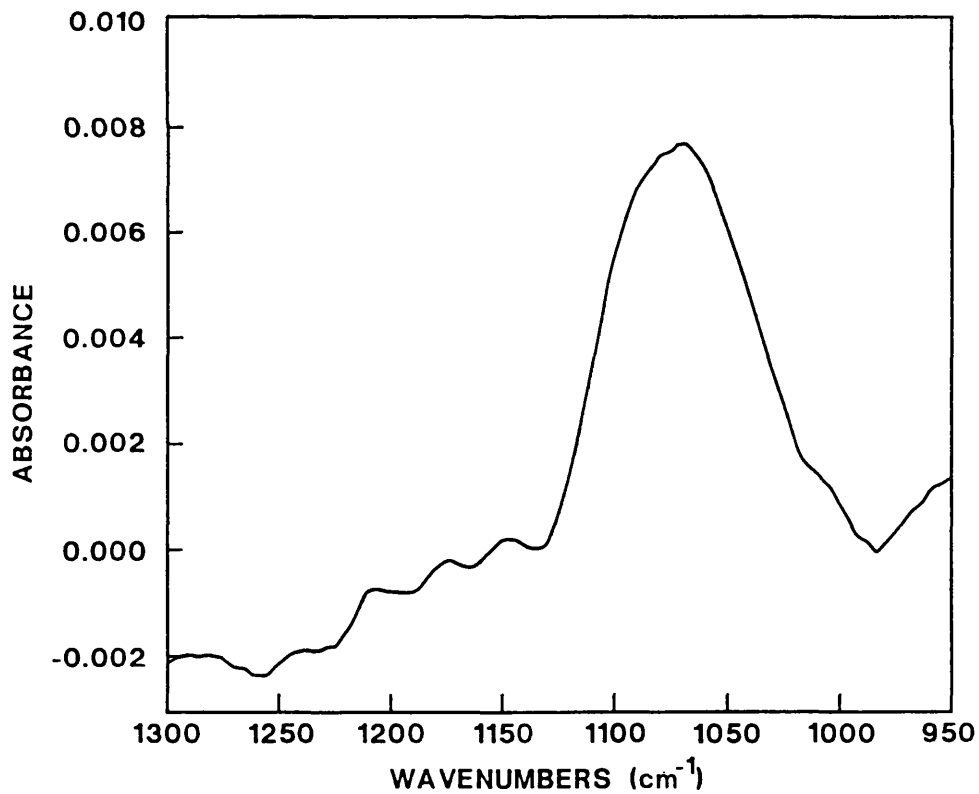


Fig.3.26 Raw transmission spectra for thermal oxides and a UV/ozone oxide.



(a) Smoothed and unsmoothed data.



(b) Smoothed data with baseline correction.

Fig.3.27 7.4nm UV/ozone low temperature oxide transmission spectra.

Peak positions and ellipsometrically determined oxide properties are collated in table 3.VII along with the implied densities determined from the expression given by Devine (1988), Fig.3.21.

$$\partial\omega/(\omega_1 \gamma) = -3.3 \times 10^{-3} \% \quad (3.27)$$

Where $\partial\omega = \omega_m - \omega_1$, ω_m is the measured peak position and $\omega_1 (= 1080\text{cm}^{-1})$ is its value for a fully relaxed oxide. γ is the fractional densification (in %) relative to a fully relaxed oxide. For samples A and B the results for density are quite close although the IR values are lower. It is important to note that a relative density is calculated based upon the assumed value of ω_1 . Higher values of the peak position have been observed (by Nakamura et al., 1984, Bench and Bergholz, 1990) for stoichiometric oxides prepared by slightly different methods. Quite clearly this would have the effect of increasing the calculated IR density.

Sample	Growth Process	Thickness (Å)	Relative Density (SE)	IR Peak (cm ⁻¹)	Relative Density (IR)
A	Thermal	326	1.033	1072	1.023
B	Thermal	143	1.05	1070	1.028
C	Thermal	93	1.10	1067	1.037
512	UV/O ₃	74	1.20	1071	1.025
712	UV/O ₃	54	1.15	1044	1.100

Shaded results are from reflection IR.

Table 3.VII Comparison of density data from IRS and SE. Assuming an error of $\pm 2\text{cm}^{-1}$ in the peak position the density error is ± 0.006 .

From table 3.VII it appears that the difference in density calculated using SE and IRS increases as the oxide thickness falls. This can be explained by several means. Either SE over estimates the density of thin oxides because an interfacial layer was not included in the modelling or alternatively for thinner layers the effect of the substrate becomes more important in IRS measurements due to both interference fringes and the absorption in the Si. Additionally if the observed peak for thin oxide is actually two overlapping peaks as suggested by Boyd (1987) then the peak

position of the mode cannot be determined precisely. The former proposition as discussed in section 3.1.3 seems unlikely because the density was not modified sufficiently to bridge the discrepancy in SE and IRS results. For very thin oxide layers (<10nm) the substrate does indeed influence the observed data, even though a reference spectra is removed, mainly due to scattering from the rough back surface and inhomogeneity in the bulk of the sample. In fact this was the main difficulty with the transmission measurement of sample 712 where the O interstitial absorbance was incompletely removed. The estimated oxide peak position was 1066cm^{-1} (which is equivalent to a density of 1.04). However, from the peak shifts one can conclude that the nature of the oxide does change as the thickness is reduced confirming previous studies.

Reflection spectra from three Si samples are plotted in Figs.3.28-30. It is immediately obvious from these that fringing effects are reduced if not removed altogether. This is due to the large beam diameter and because there is no interference from the substrate. Fig.3.28 shows a very recently etched Si sample. There are no oxide peaks except possibly a slight impression at $\approx 1250\text{cm}^{-1}$. The main feature observed is the O interstitial peak. The next figure displays the response of a native oxide formed over 2 months in air. In this case a recognisable peak occurs at 1256cm^{-1} but again there is no structure near 1070cm^{-1} as was observed in the transmission measurements on grown oxides. Moving on to Fig.3.30 taken from a UV/ozone grown oxide a distinct peak is observed at 1044cm^{-1} as well as a stronger (in comparison to the native oxide) absorption at 1256cm^{-1} . The 1044cm^{-1} is much sharper than that observed in transmission measurements of thin oxides. If one links this with the asymmetric stretching mode then the oxide density can be calculated to be about 10% greater than fully relaxed silica (see Table 3.VII). This result is much closer to the value determined using SE of 15%. Therefore the IR measurement in reflection corroborates the SE result.

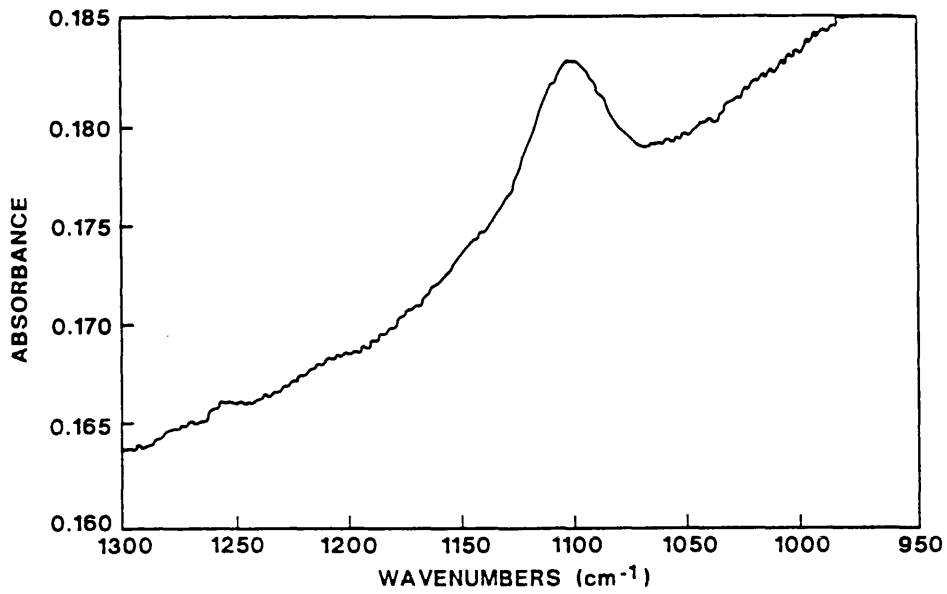


Fig.3.28 IR reflection spectrum from a recently HF etched Si sample.

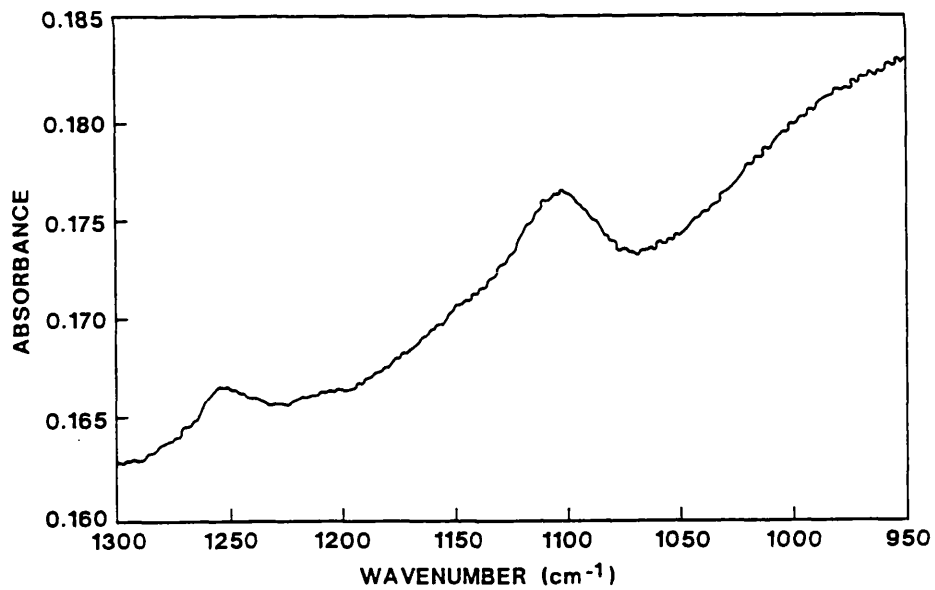


Fig.3.29 IR reflection spectrum from a native oxide layer.

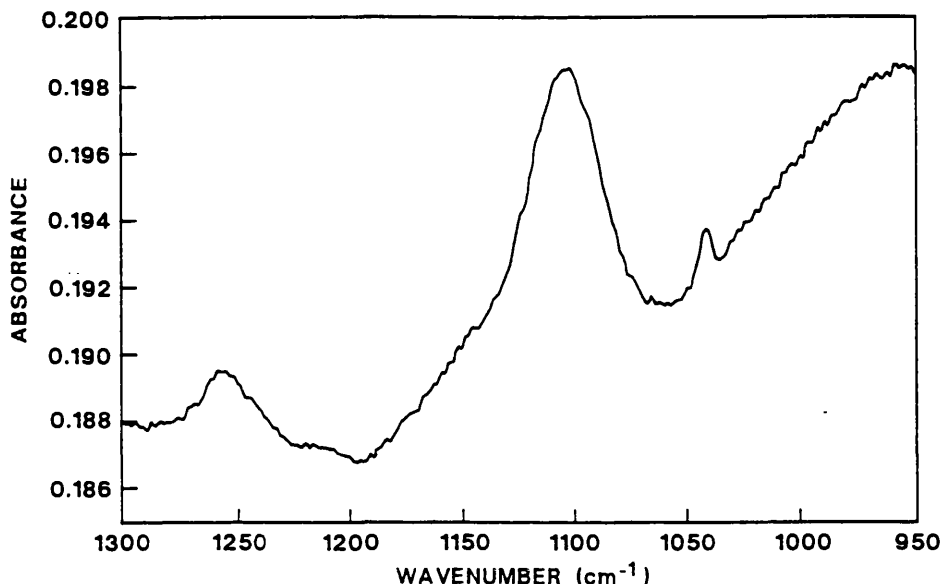


Fig.3.30 IR reflection spectrum from a 5.4nm UV/ozone oxide.

As noted above by selecting the angle of incidence and polarisation of the IR beam it is possible to sample particular vibration modes. The sharp peak at 1044cm^{-1} has a half maximum full width of $\approx 40\text{cm}^{-1}$ in comparison to the one observed in transmission of $>75\text{cm}^{-1}$. This suggests that the peak structure observed in transmission measurements is different to that in the reflection measurement. It is also evident that the native oxide may be different to the UV/ozone oxide which apparently follows the pattern of thermal oxide behaviour, because only a 1256cm^{-1} peak is observed.

3.3 X-Ray Photoelectron Spectroscopy

The previous sections in this chapter have identified the layers grown in this study as SiO_2 . However a more direct confirmation of the chemical constituents and bonding in the films is obtained from x-ray photoelectron analysis (XPS). Many studies have applied XPS to the SiO_2/Si system during the last 4-5 years. The very detailed article by Grunthaner and Grunthaner (1986) reviews the technique and much of the information in the literature. Some of their conclusions have been criticised in recent work from Hattori et al. (1989) and Takakura et al. (1989). Studies of the effects of different preparations on the nature of the oxide grown on Si surfaces have been carried out by Nakazawa et al. (1989) and Zazzera and

Moulder (1989) who observed that a short treatment in a UV/ozone environment was very effective in producing a thicker oxide in comparison to chemical treatments.

Here XPS has been used simply to identify the grown layer and compare it directly with a rapid thermal oxide of similar thickness. The x-rays used in the measurements were emitted from a $Mg(k_{\alpha})$ source with an average photon energy of 1253eV. A non-monochromatic beam was incident on the samples at an angle of 45° . The photoelectrons were collected at 90° to the sample surface. Fig.4.31 displays the Si_{2p} and O_{1s} photoelectron yield from the three samples examined; which were a) RTP oxide and b),c) UV/ozone oxides grown at $450^{\circ}C$. It is obvious that the thermal oxide is thicker than the UV/ozone layers because the Si_{2p} emission from the oxide is greater while the substrate signal is much reduced with respect to the other samples. The difference in the Si_{2p} binding energy peak maxima (ΔE in eV) between the substrate and SiO_2 and the relative (approximate) peak area ratios are collected together in table 3.VIII.

Growth Process	Thickness (SE)(Å)	ΔE (eV)	Relative Peak Area Ratios	
			Si_{2p} (SiO_2)	O_{1s}
Thermal	52	4.68	1.00	1.00
UV/ O_3	39	4.71	0.79	0.81
UV/ O_3	37	4.64	0.78	0.77

Table 3.VIII XPS data from thin thermal and UV/ozone oxides.

From table 3.VIII it can be seen that ΔE values for all the oxides are similar thus the UV/ozone process produces oxides of a chemical composition which are the same as thermal oxides. Most studies observe that ΔE is $>4.5eV$ for oxide films $>2nm$ as in the present case. The intensity of the signal between the two main Si_{2p} peaks (± 101 to $103eV$) is small indicating that the level of substoichiometric oxide in all the layers is negligible.

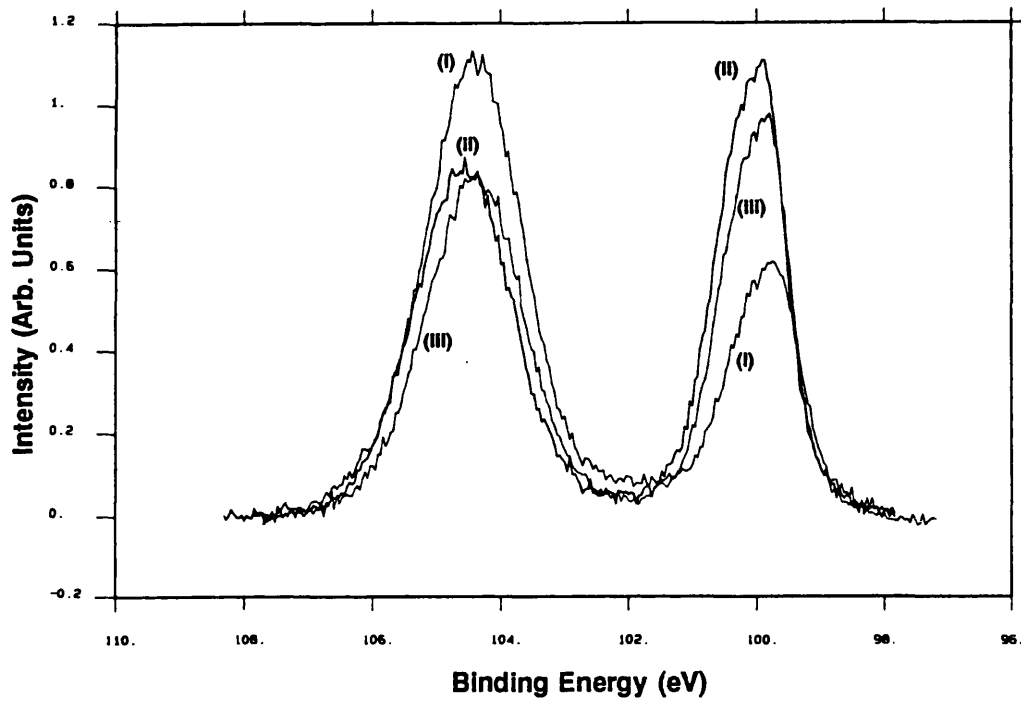
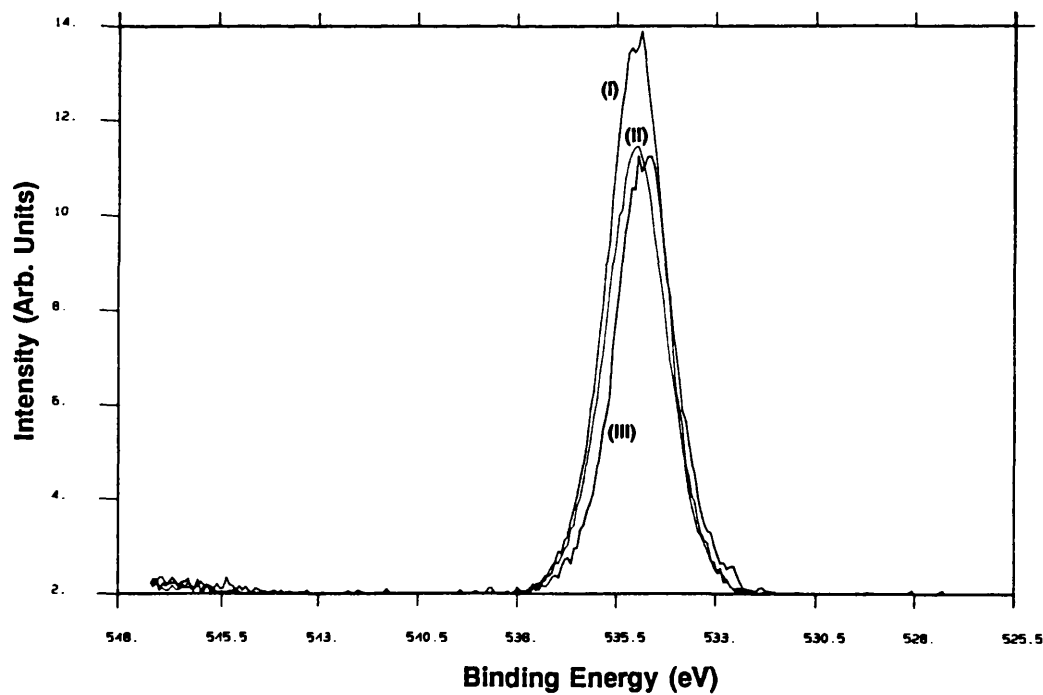
(a) Si_{2p} signal.(b) O_{1s} signal

Fig.3.31 XPS data from i, thermal oxide, ii, UV/ozone (uncovered growth) and iii, UV/ozone (covered growth).

The ratio of the peak areas are ≈ 0.8 for both the Si_{2p} and O_{1s} peaks. This is close to the ratio of the oxide thicknesses (from SE) of 0.75 and implies that the SE measurements are accurate.

3.4 Discussion and Summary

In this chapter three different methods, spectroscopic ellipsometry, infrared spectroscopy and x-ray photoelectron spectroscopy, were used to analyse thermal and UV/ozone grown oxides. The major part of the work concentrated on the development of SE. SE is capable of determining oxide thickness to an accuracy of better than 5% for layers of thickness down to 4nm, the error reduces to better than 1.5% for oxides of 150nm. From the analysis it can be concluded that the oxide density increases for decreasing film thickness. It was noted that the oxides grown at 900°C had on average a slightly higher density than those grown at 1050°C for similar thickness (Fig.3.17). At 1050°C the stress relaxation time for thick (100nm) or bulk oxides is much longer than the growth time (> 1 hour, see Landsberger and Tiller, 1987) so that the oxides formed should not have sufficient time to fully relax. However, it has been shown that the oxide density is a strong function of the film thickness even at high growth temperatures. The variation of oxide density is much more closely linked to the oxide thickness than the growth temperatures used in this study. This implies that the relaxation of thin oxides is quite different to that of bulk oxides. A recent study by Rafferty et al. (1989) of the relaxation of thermal oxides proposes that plastic flow occurs rather than the more commonly considered visco-elastic process. In the plastic flow model a critical stress is required to cause relaxation. Further studies are required to definitely identify which process is active. From the present study of thermal oxides it appears that the critical thickness at which relaxation starts is around 6-7nm thickness.

The UV/ozone oxides layers were stoichiometric and densified although as noted above oxide density was a much stronger function of film thickness than growth temperature. A direct comparison of UV/ozone and thermal oxides over a wide thickness range was not possible due to the

reduced confidence in density data for films of less than 6nm. However, the density of UV/ozone oxides was consistently high (typically 15%) and showed much less scatter than the RTO oxides for similar thickness.

It was demonstrated that multi-angle SE analysis of thin oxide layers produced improved confidence limits and reduced sensitivity correlations in comparison to SE (see note added in proof appendix b). The failure of attempts to model an interfacial region (on the basis of SE data) for these very thin layers is not surprising. MASE opens the door to the study of very thin layers and possibly interfacial structure.

IRS was used to obtain density values over the oxide thickness range studied by measuring the peak position of the asymmetric stretching absorbance. The data collected for UV/ozone oxides was similar to that for thermal oxide layers. It was found that for thick layers (>15nm) transmission IR gave similar results to SE. For thinner layers transmission and SE results diverged. Reflection IR spectra were also measured on several samples. It was found that the calculated density was much closer to the SE result for a thin (5.4nm) UV/ozone sample.

Direct evidence was obtained from XPS spectra on the chemical constituents of the layers. Predominantly stoichiometric SiO₂ spectra were observed for both the thermal and UV/ozone oxides. The three techniques collectively demonstrate that the UV/ozone growth process produces oxides which are physically indistinguishable from thermal oxides.

Further experiments to look at the effect of different growth processes and annealing are discussed in the concluding chapter. The application of SE, MASE and some recent developments of the IRS technique such as reflection spectroscopy to thin oxide films are discussed in the concluding chapter (chapter 5).

(Note added in proof with respect to MASE analysis, section 3.1.6, see appendix D).

Chapter 4

Electrical Analysis of UV/ozone Oxides

4.1 Introduction

It was noted in chapter 1 that the intensive study of the growth and nature of SiO₂/Si interfaces was essentially due to its unique electronic properties. The aim of this chapter is to investigate the electronic behaviour of low temperature UV/ozone oxides. The material analysis discussed in the previous chapter clearly demonstrates that these oxide layers are very similar to thermally formed films. The electronic properties were investigated using both high frequency capacitance-voltage (HFCV) and current-voltage (IV) measurements. The measurements were made on metal-oxide-semiconductor structures using an Al gate. Details of both techniques can be found in the very thorough book by Nicollian and Brews (1982) and also Sze (1981). Additionally more recent reviews of MOS electronic properties are given by Feigl (1983) and also Lefevre and Schulz (1988).

The ideal MOS band structure is shown in Fig.4.1. This assumes that the built-in field is due to the difference in work function of the metal (ϕ_m) and Si (ϕ_s). However this is not the case for real structures. Charge can exist in (MOS) structures in the form of fixed oxide charge (Q_f), oxide trapped charge (Q_{ot}), mobile ionic charge (Q_m) and interface trapped charge (Q_{it}). The type and distribution of charges is schematically shown in

Fig.4.2. The effect of these charges can be observed in HFCV characteristics as translation in the data along the voltage axis (see below). The aim of HFCV measurements was to obtain the flatband voltage (V_{fb}). V_{fb} is defined as the gate voltage required to induce "literally" flat bands in the silicon. This is controlled by the charge distribution in the structure. From the flat band voltage a weighted estimate of the total charge in the system (Q_{ss} see below) can be calculated. The oxide thickness can also be calculated from the HFCV capacitance in accumulation assuming a given dielectric permittivity for the oxide.

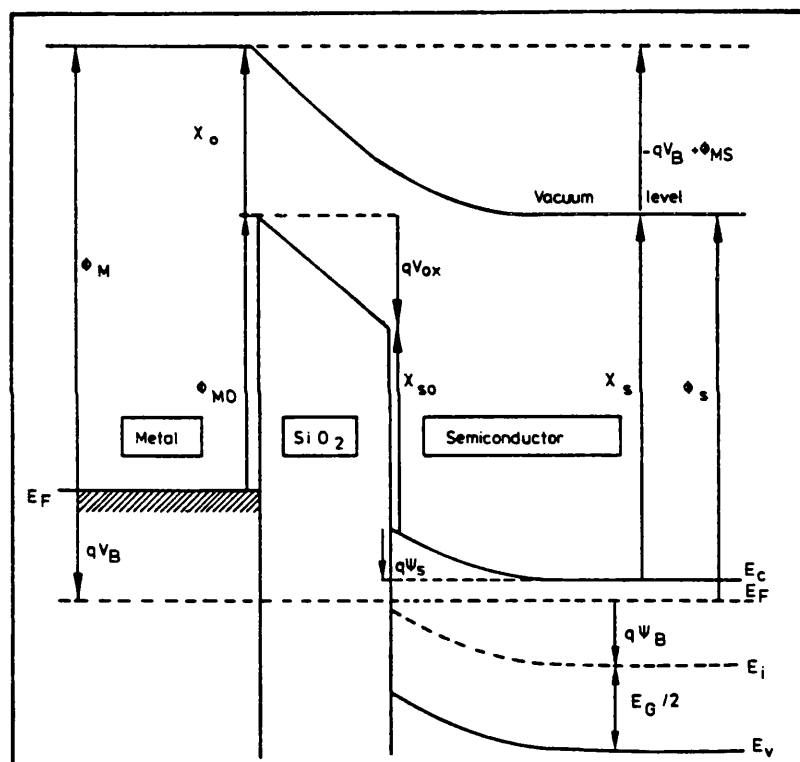


Fig.4.1 Ideal MOS band structure, after Lefevre and Schulz (1988) (see appendix E for related data).

From IV characteristics the charge conduction mechanism was identified and the barrier height to charge injection was determined. However the main aim of the IV tests was to obtain the breakdown field distribution. For the present study breakdown field was defined as the point when a catastrophic failure of the MOS IV characteristic occurred. HFCV and IV behaviour are discussed in sections 4.2 and 4.3 respectively.

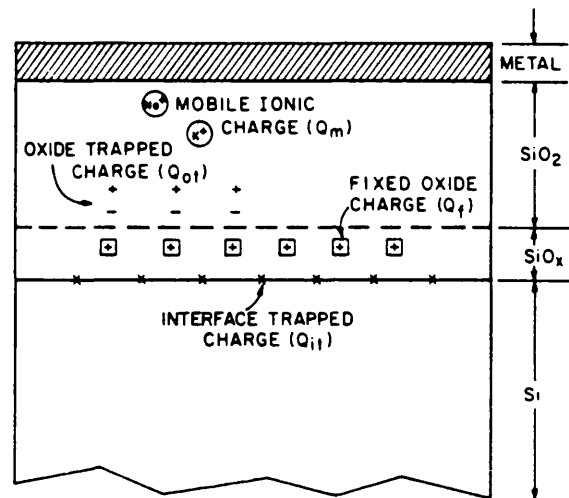


Fig.4.2 Distribution of charges in a realistic MOS structure (after Deal 1980).

4.2 High Frequency Capacitance Voltage Characterisation.

4.2.1 Capacitor Fabrication

After oxidation the samples for electrical characterisation were immediately inserted into a vacuum evaporator. Capacitor dots were defined by vacuum thermal evaporation of Al wire from a tungsten filament through a shadow mask. Prior to evaporation the system was pumped down to $<10^{-6}$ mbar. The circular dots were nominally 0.5mm in diameter. The metallisation was typically 300nm thick. To form back contacts the front surface was spin coated with positive resist, to a thickness of 3-4 μ m, and hard baked (at 80°C for 35 minutes). A dilute HF dip was then used to remove the back face oxide. With the resist still in place the Al back contact was deposited in a similar fashion to the dots but without the shadow mask. All electrical characterisation was carried out on oxides grown on high doping (0.2-1 Ω cm) p-type $<100>$ orientation substrates. The electrical behaviour was measured without any further processing. Since no forming gas anneal was available, only p-type substrates were used because of the well known difficulties in making good ohmic contacts to n-type material with Al.

4.2.2 HFCV Analysis

The measurements were carried out at both RSRE and UCL using Hewlett- Packard test equipment. HFCV measurements were taken at 1MHz typically over the voltage range -5,5V using the HP4275A. The voltage was always swept from inversion to accumulation. To allow the inversion layer to form immediately before measurement, the sample was held at 5V gate bias under illumination for up to 200 seconds. A probe station in an electrically screened and light tight box was used to contact the gate and substrate. During the measurement dry nitrogen was blown on to the device to avoid surface leakage currents. The data was taken on a number of samples with differing oxide thickness. All HFCV results quoted below are the average of 10 measurements. The effect of the oxide charges discussed in the introduction is to shift the HFCV curve as shown in Fig.4.3.

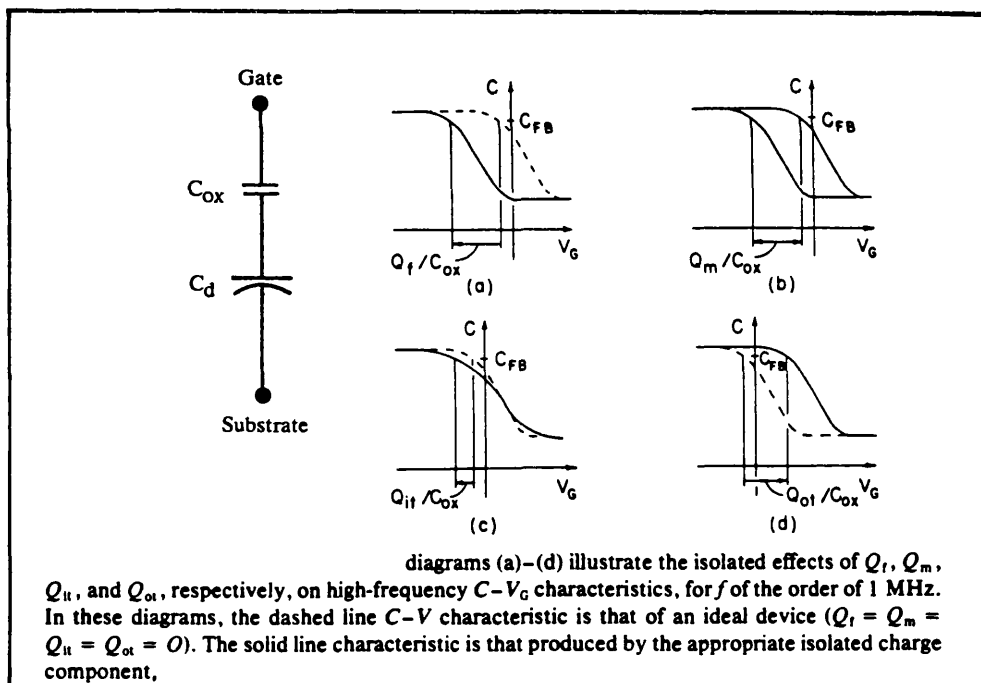


Fig.4.3 Modifications of HFCV characteristic due to trapped charges (after Feigl 1983).

V_{fb} was calculated assuming the capacitor to be represented by the insulator capacitance C_{ox} (oxide thickness, d_{ox} , area, A) and depletion layer capacitance C_d in series as inset in Fig.4.3. From this the flat band capacitance is defined as

$$C_{fb} = \frac{\epsilon_{ox} \epsilon_o A}{\sqrt{2} d_{ox} + \epsilon_{ox} L_d / \epsilon_{Si}} \quad (4.1)$$

$$\text{where } L_d \text{ is the Debye length} = \left[\frac{2kT \epsilon_o \epsilon_{Si}}{q^2 N_{subs}} \right]^{1/2} \quad (4.2)$$

and ϵ_{ox} and ϵ_{Si} are the relative dielectric permittivities of the oxide and Si respectively. V_{fb} is then taken to be the gate voltage at which C_{fb} is achieved. Q_{ss} is calculated using V_{fb} and the Fermi level.

$$Q_{ss} = C_{ox} (P_{ms} - V_{fb})/A \quad (4.3)$$

Where $P_{ms} = -0.6 - P_{Fermi}$ ($P_{Fermi} = kT \ln(N_{subs}/N_i)/q$, N_{subs} and N_i are dopant and intrinsic carrier densities). A typical HFCV characteristic for two different oxide thickness is shown in Fig.4.4. Normal behaviour is observed for negative voltage values. However, for positive voltages greater than about 1V the capacitance falls where it should reach a plateau. One possible explanation for this might be that under positive gate bias the Si becomes deeply depleted. For positive gate bias and highly doped p-type substrates the depletion layer is relatively thin. This in turn means that the volume available to generate minority carriers is very small resulting in a deficiency of minority carriers. Hence it takes a very long time to generate the equilibrium inversion charge. Therefore either the hold time prior to measurement was insufficient or there was a leakage across the oxide for positive gate bias leading to a fall in the capacitance. Measurements with varying hold time had little effect on the HFCV curves. Thus it is likely that some leakage across the oxide was the cause of the depletion effect. Averaged data from HFCV measurements are summarised in table 4.I.

Sample	d_{ox} (Å)	$-V_{fb}$ (V)	Q_{ss}/q ($\times 10^{12} \text{cm}^{-2}$)
2310HF	44.5 ± 1.0	1.41 ± 0.07	2.33 ± 0.41
2310BOMB	51.7 ± 1.2	1.11 ± 0.11	0.82 ± 0.41
612HF	70.0 ± 1.6	1.27 ± 0.08	1.20 ± 0.25
612BOMB	79.4 ± 1.7	1.39 ± 0.07	1.34 ± 0.19
512HF	82.8 ± 5.0	1.04 ± 0.15	0.41 ± 0.14
512BOMB	85.0 ± 2.7	1.22 ± 0.10	0.86 ± 0.23

Table 4.I HFCV data from UV/ozone grown oxides (mean and standard deviation of 10 capacitors).

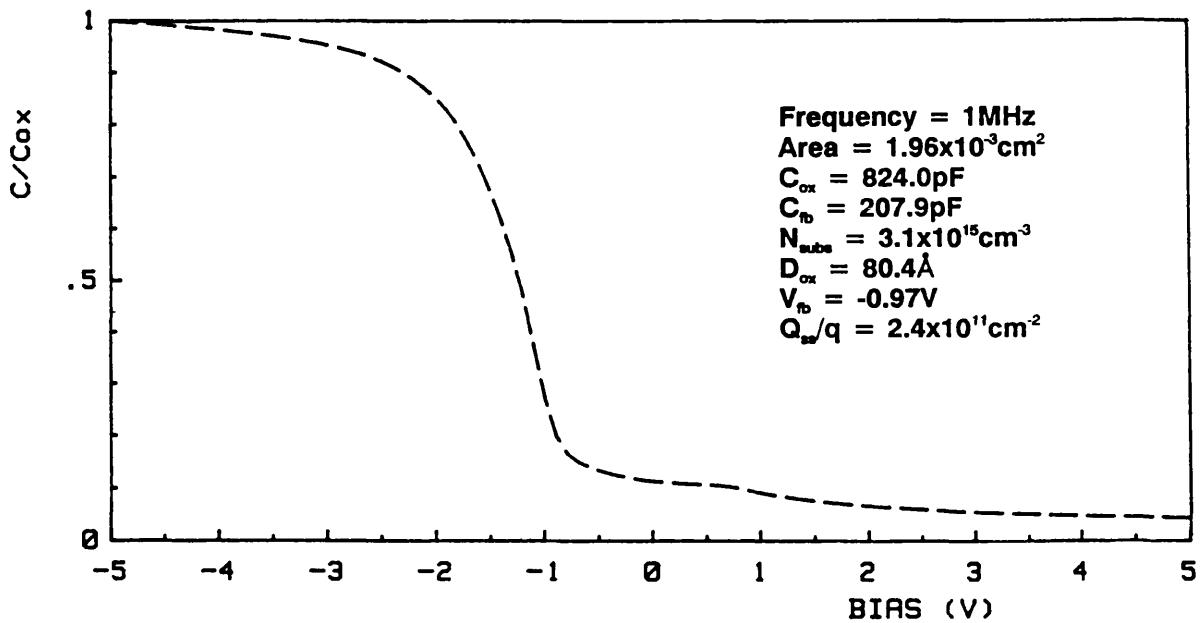
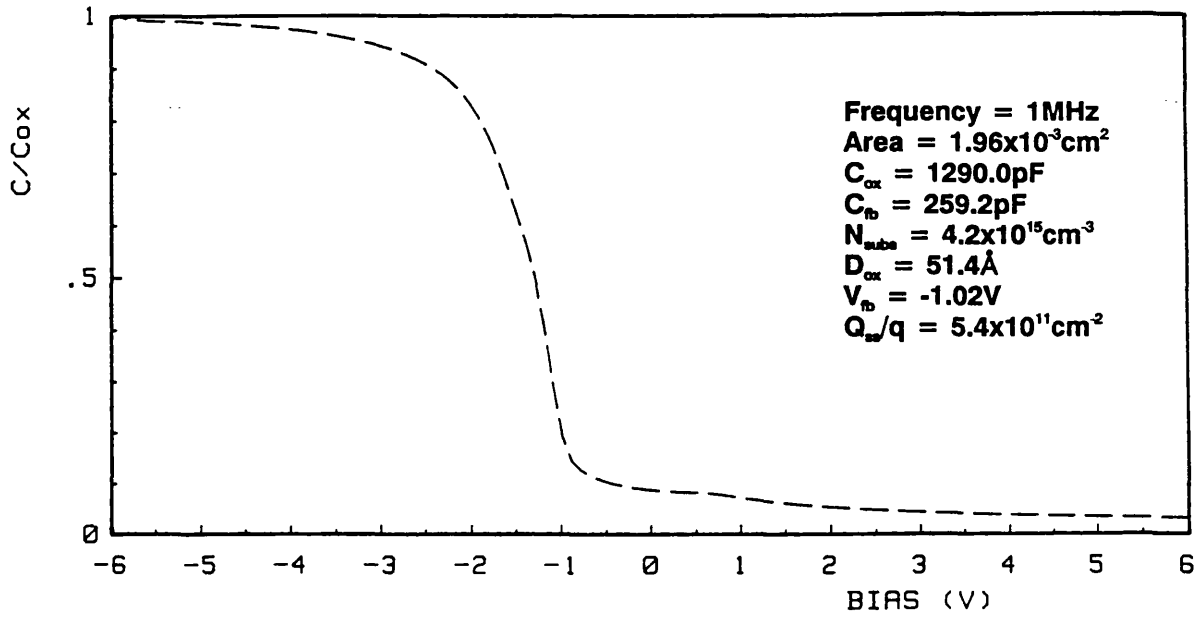


Fig.4.4 Typical HFCV characteristics for two UV/ozone oxide capacitors.

It is apparent (from table 4.I) that bomb prepared samples were notably thicker confirming the ellipsometric observation reported in chapter 2.

4.2.3 Errors in the Extraction of Parameters from HFCV

The data in table 4.I are average values and the errors noted on the parameters are just their standard deviation. The errors in extracted parameters have essentially 3 origins. These are,

- a) the area of the capacitor dots.
- b) the experimentally determined substrate doping density.
- c) the effect of interface trapped charge (Q_{it}) which is conventionally assumed to be low.

a) There appears to be a systematic error in the oxide thickness which is overestimated by the electronic technique (from C_{ox}) when compared to ellipsometric measurements. Test samples grown simultaneously for 612HF and 512HF were measured to be 6.7 and 7.5nm respectively using ellipsometry (these are lower than the values quoted in table 4.I). This discrepancy is probably due to a small error in the assumed area of the capacitor dot which was found to vary between 1.82 and $1.96 \times 10^{-3} \text{cm}^2$. The effect of such an error in the worst case would be an uncertainty of up to -0.5nm for an 8.0nm layer. This is similar to the difference observed. There is also another source of error in C_{ox} arising from the finite Si capacitance in accumulation which will result in an underestimated value of C_{ox} of about 4%. (Typically for the capacitor structures discussed C_{ox} is in error by approximately 10-20pF. Clearly the effect of this is small).

b) The flat band voltages of table I were calculated using the experimentally determined value of doping density, N_{subs} . As noted above C_{fb} is dependent upon N_{subs} via L_d . N_{subs} was found to be around $3-5 \times 10^{15} \text{cm}^{-3}$. However, this value in itself is inaccurate because it is inferred from the ratio of C_{min}/C_{ox} . As noted above the C_{min} varied with positive gate bias due to depletion effects and was therefore underestimated. The resistivity of the substrates was 0.2-1 Ωcm . This is equivalent to a carrier density of $10^{16}-10^{17} \text{cm}^{-3}$ (see p32 the Physics of Semiconductor Devices by S. M. Sze). At the growth

temperatures used in UV/ozone oxidation bulk dopants are unlikely to be grossly redistributed in the silicon. Hence L_d is in error leading to a low value of C_{fb} and V_{fb} . Taking the example of the two HFCV characteristics plotted above (Fig.4.4) C_{fb} can be recalculated using a more realistic value of N_{subs} which will be taken to be $4 \times 10^{16} \text{cm}^{-3}$. This is typically the value inferred from the capacitance plateau in HFCV before the dip in curve for positive gate bias. L_d for this carrier density is $2.88 \times 10^{-6} \text{cm}$ at 293K. Values of C_{fb} are presented in table 4.II showing the effect of a more appropriate substrate carrier concentration and also the worst case errors in the area and thickness.

d_{ox} (Å)	C_{fb} (Programme Calculation)	C_{fb} (with N_{subs} correction)	C_{fb} (with worst case A and d_{ox} errors)
51	259	405pF	385pF
80	208	325pF	310pF

Table 4.II Recalculated C_{fb} values taking into account corrections.

It is obvious that precise determination of the doping density is very important. From these new C_{fb} numbers V_{fb} is found to be -1.12 and -1.13V for the 5.1 and 8.0nm oxide respectively. The area and thickness correction just increases V_{fb} by about 0.05V. The resulting charge densities then become $5.9 \times 10^{11} / \text{cm}^2$ and $4.9 \times 10^{11} / \text{cm}^2$ for the 5.1 and 8.0nm oxides respectively. Q_{ss}/q is still of the same order of magnitude as previously determined, table 4.II.

c) Previously, it was noted that the capacitors did not receive a forming gas anneal. In conventional MOS capacitors the forming gas anneal hydrogenates interfacial dangling bonds reducing the interface trapped charge (Q_{it}) which can contribute to V_{fb} . The expression for C_{fb} above assumes that Q_{it} is negligible. To obtain an estimate of its possible contribution to V_{fb} the expression quoted on p486 of the book by Nicollian and Brews (1982) can be used. The distribution of states across the band gap was assumed to be uniform for simplicity in this expression.

$$\Delta V_{fb} = q Q_{it} [\phi_b + E_g/2q] A / C_{ox} \quad (4.4)$$

Q_{it} is the interface state density (/ev/cm²), $q\phi_b = - |E_f - E_{cb}|$, E_g = band gap energy (all energies are in eV). ΔV_{fb} for different Q_{it} are shown in Table 4.III.

Q_{it} (eV ⁻¹ cm ⁻²)	ΔV_{fb} (V)
10^{11}	0.01
10^{12}	0.12
10^{13}	1.18

Table 4.III The effect of trapped interface charges on V_{fb} .

It is unlikely that Q_{it} would greatly exceed $10^{12}/\text{cm}^2$ limiting the contribution to V_{fb} to around 0.1V. From the above discussion it can be concluded that the the HFCV technique is unreliable in determining Q_{ss}/q to high accuracy and will tend to underestimate the real value. There is no doubt however, that high charge densities exist in the capacitors studied.

4.3 Thermal Bias Stressing Behaviour

The value of Q_{ss}/q does not appear to be a strong function of either the oxide thickness or the surface preparation. This suggests that the charge originates either externally (i.e. as a contaminant e.g. sodium ions) or that a limiting amount is introduced by the growth process itself. To try to identify the origin of this charge several capacitors were thermal bias stressed at 200°C and a field of 1MV/cm (positive gate bias). Fig.4.5 shows HFCV curves for before (dashed) and after (solid) stressing. A large negative shift in the curve occurs. It is interesting to note that the curve is not stretched out by the stressing indicating that few new interface states are generated. The type of shift observed is normally ascribed to mobile positive charge in the oxide (normally Na⁺ or K⁺ ions).

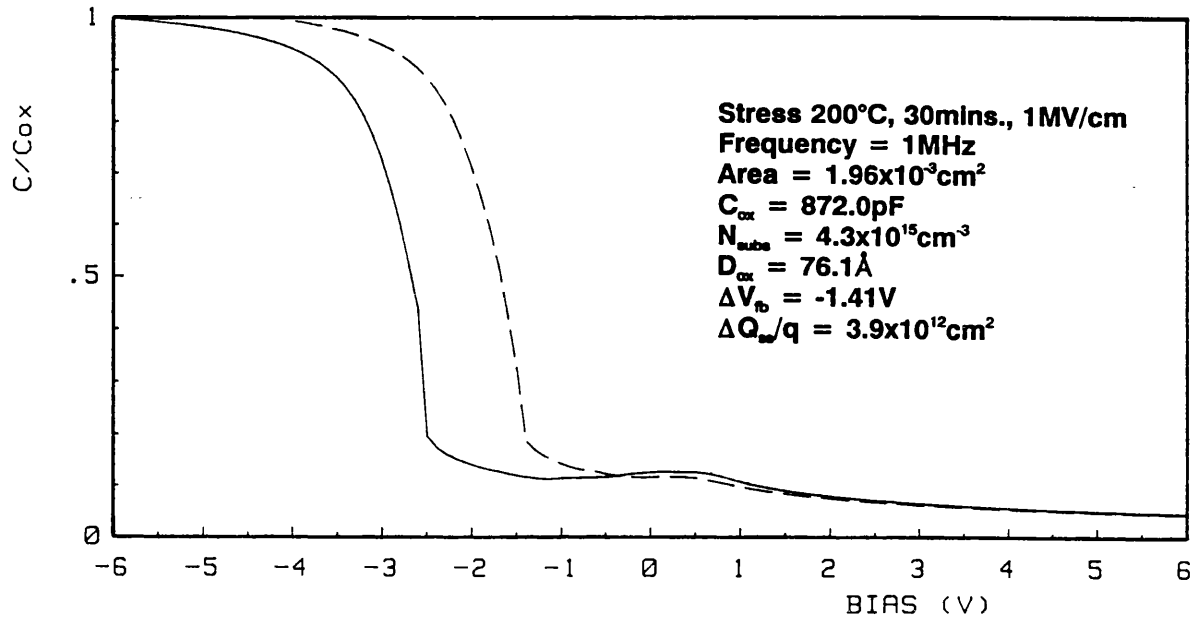


Fig.4.5 HFCV results before (- - -) and after (—) temperature bias stressing for a 7.6nm UV/ozone oxide grown at 500°C

It is well known that large concentrations of contaminants can be introduced during processing which can reside at interfaces. Upon thermal bias stressing these can drift through the oxide. Mobile charges already present in the oxide drift towards the Si interface (under positive bias) increasing the band bending. The very prominent shift of the HFCV characteristic provides strong evidence that an external contaminant is the cause of the high oxide charge density. The results do suggest that a high level of contamination exists on the Si surface prior to oxide growth.* HF acid is a known source of metallic impurities. Ultimately the surface condition was limited by the quality of chemicals and the requirement to transport and oxidise the sample in a non-clean room environment.

4.4 Current Voltage Characteristics

IV measurements were taken using a Keithley 236 programmable IV source. A voltage staircase of steps of 0.1V and a dwell time at each point of 0.1s was used to avoid any displacement current effects due to the

* See 4.5 (Summary) for an additional comment.

charging of the capacitors. In the present case of only p-type samples, only negative gate bias was used to avoid any voltage drop across the depletion layer in the Si. IV characteristics were taken to determine the breakdown fields for the thin oxides. The breakdown field was defined as the field required to cause a catastrophic failure of the oxide. Once this occurred the oxide no longer functioned as a dielectric and the IV curve could not be reproduced. In Fig.4.6 the point of breakdown is obvious from the discontinuous jump in current flowing through the capacitor.

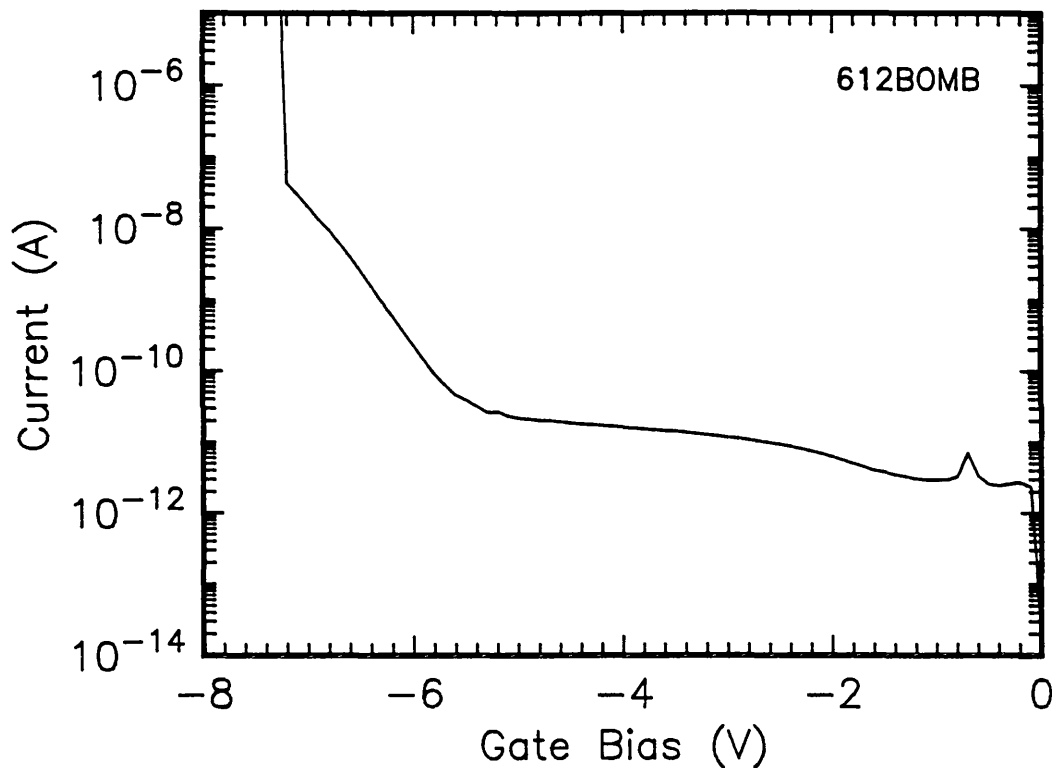


Fig.4.6 Typical IV characteristic for a UV/ozone oxide (grown at 500°C) capacitor.

The field necessary to cause breakdown is a basic test of oxide quality. Breakdown fields are noted below in table 4.IV.

	612HF	612BOMB	512HF	512BOMB
Mean E_{BD}	10.9 ± 0.7	9.5 ± 1.1	10.9 ± 1.5	9.5 ± 1.7
d_{ox} (Å)	70.0 ± 1.6	79.4 ± 1.7	82.2 ± 4.9	82.0 ± 2.7

Table 4.IV Mean break down fields for UV/ozone oxides grown at 500°C.

These were calculated using the oxide thickness determined electrically (to

ensure that any oxide thickness inhomogeneities were accounted for). As expected a wide distribution was obtained. However, the number of low field breakdowns (defined as those devices that showed no FN characteristic) was around 20 to 25% for all the samples measured. This is surprisingly low given the poor processing environment the material was subjected to and the very thin oxides studied. Generally it was observed that non-functioning devices were located in clusters. IV curves from a number of devices from one sample are plotted in Fig.4.7. Across the sample as a whole a wider variation in breakdown field and the voltage required to induce Fowler-Nordheim (FN) tunnelling was often observed. The cause of this effect is likely to be local variations in the initial surface oxide. A plot of cumulative breakdown against field is shown in Fig.4.8 for 27 capacitors with an average oxide thickness of 8.5nm. Values of breakdown field were calculated assuming the thickness value obtained from HFCV measurements to take into account any local variations in oxide thickness. As mentioned above the electrical thickness was higher than the ellipsometrically determined values. Hence it is likely that the breakdown fields are underestimated in the plot. The average breakdown field for all devices measured on all the samples was approximately 10MV/cm. This is a very respectable value, when compared to the best thermal oxides which have an average of 12-13MV/cm.

The IV data was also analysed for FN tunnelling behaviour according to the expression, (Wolters 1987),

$$J = J_{\max} \exp(-b/F) \quad (4.5)$$

$$\text{where } J_{\max} = q^3 m F^2 / (8\pi h m_{\text{ox}} \phi) = 3 \times 10^6 F^2 / \epsilon \text{ (A/cm}^2\text{)} \quad (4.6)$$

$$\text{and } b = (8\pi/3) (2m_{\text{ox}})^{1/2} \phi^{3/2} / qh = 48.3 \phi^{3/2} \text{ (MV/cm)}. \quad (4.7)$$

F is the electric field, J the current density, ϕ the barrier height to electron injection, h is Planck's constant and m_{ox} the electron effective mass in the oxide and m the free electron mass.

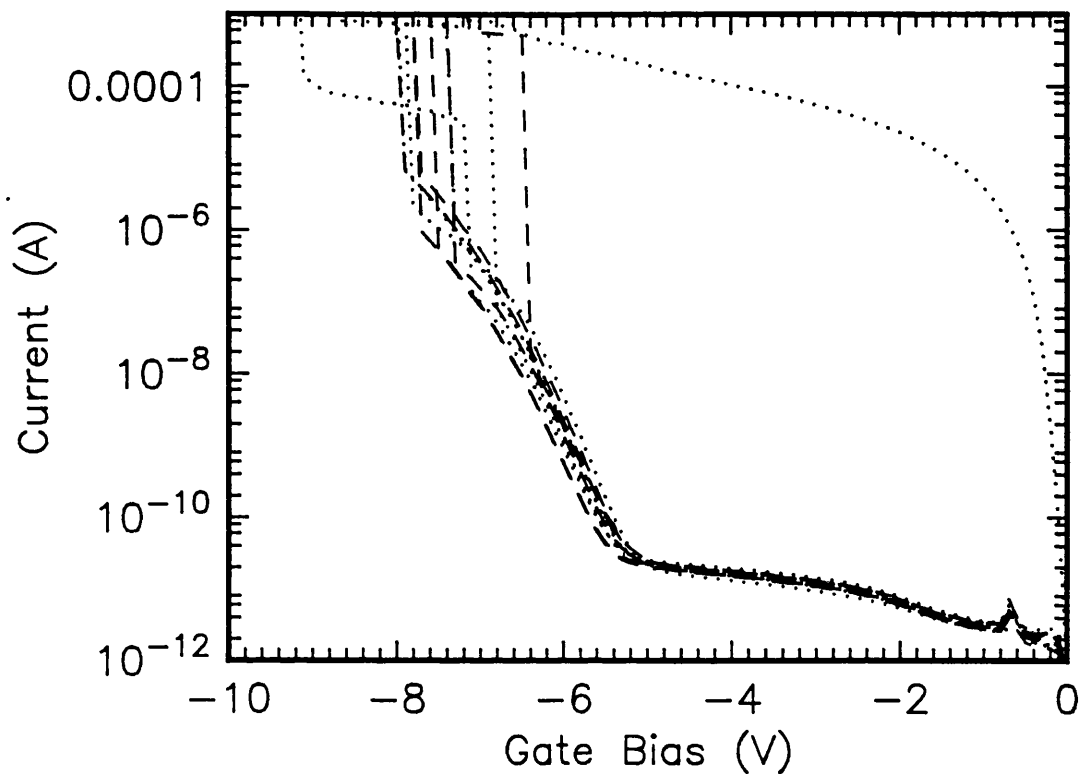


Fig.4.7 A collection of IV characteristics for sample 612Bomb showing different breakdown voltages.

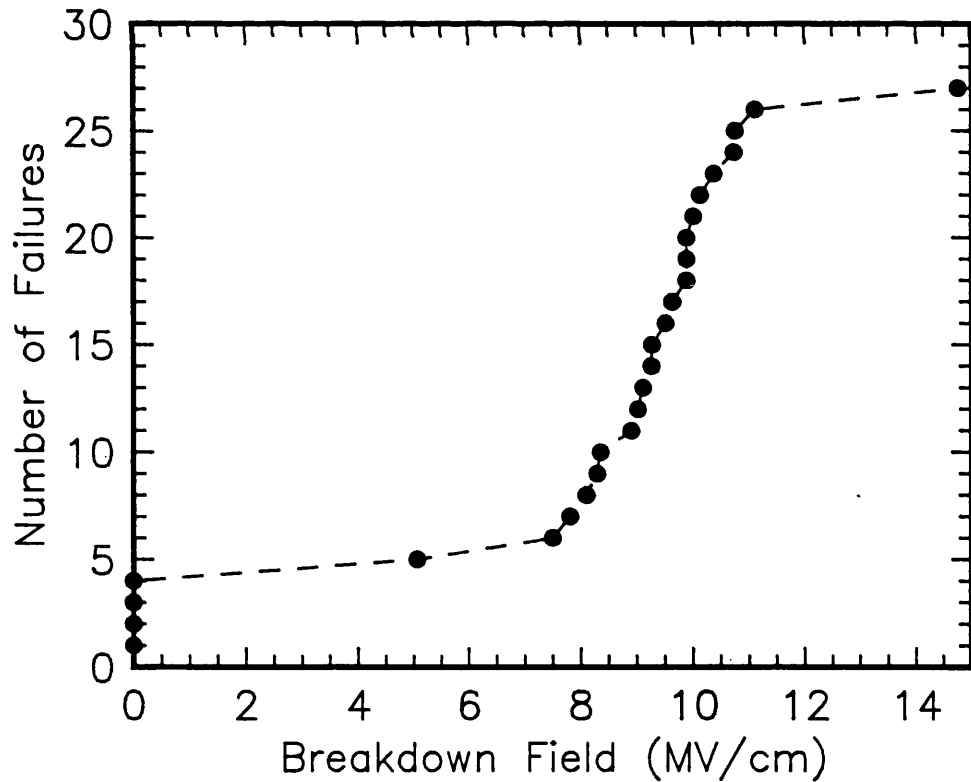


Fig.4.8 A plot of cumulative breakdown against field for sample 512Bomb.

This expression essentially describes the tunnelling current across a triangular barrier as shown in Fig.4.9. A plot of $\ln(I/V^2)$ against $-1/V$ should yield a straight line for FN conduction. ϕ can be calculated from the expression for b and the gradient of the FN plot using

$$\text{gradient} = 48.3 d_{\text{ox}} \phi^{3/2} 10^6 \quad (\text{V}) \quad (4.8)$$

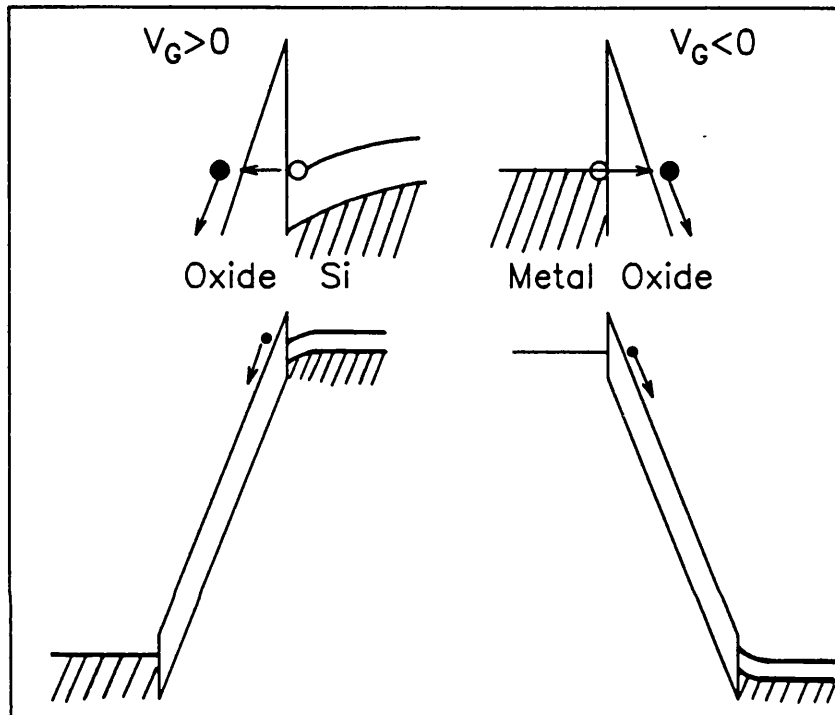


Fig.4.9 MOS band diagrams for Fowler-Nordheim tunnelling under high bias.

FN conduction was observed in the majority of devices over typically 4 orders of magnitude. The barrier height was calculated for both bomb and HF dipped samples from the gradient of the FN plots, and is shown in table 4.V.

Sample	ϕ (eV)
512HF	3.25
512BOMB	3.21
612HF	3.07
612BOMB	3.08

Table 4.V Calculated results for FN tunnelling barrier height (eV).

A representative FN characteristic is plotted in Fig.4.10. The barrier height

calculated was the difference between the Al Fermi level and the oxide conduction band. For negative gate bias electrons are injected from the Al into the oxide. The typical value for this barrier is 3.2eV which is close to those calculated above.

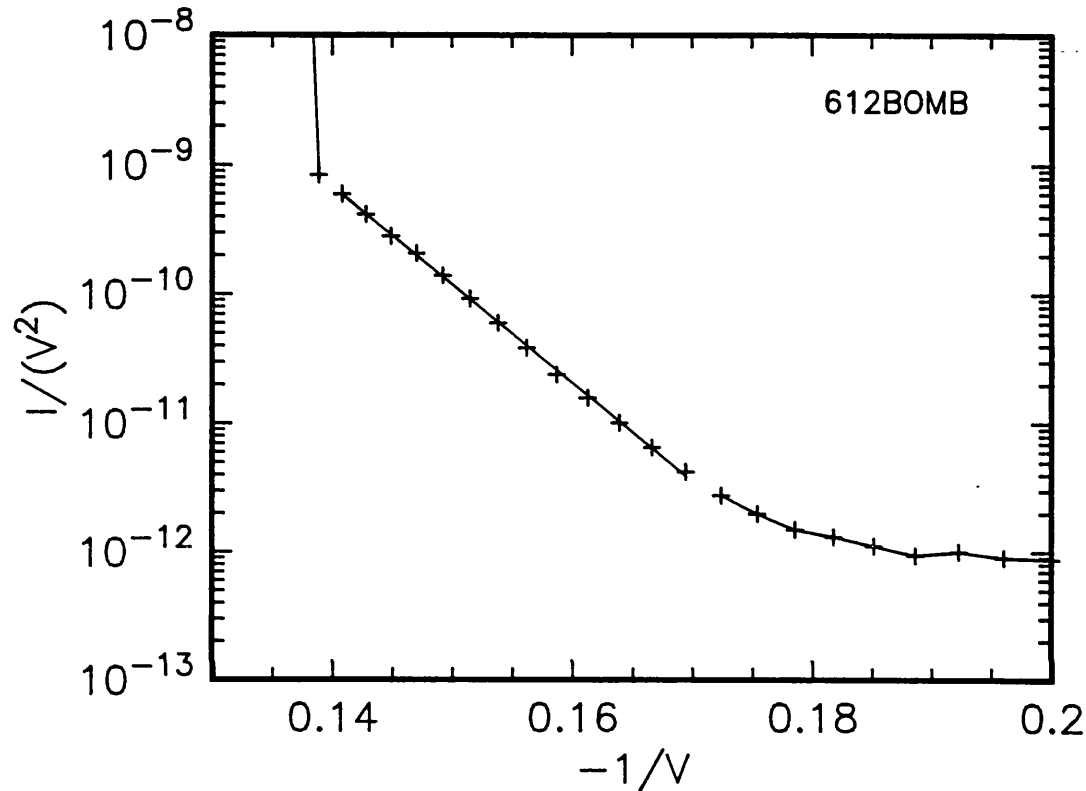


Fig.4.10 Typical FN characteristic from a UV/ozone oxide capacitor.

4.5 Summary

From the above discussion it is apparent that many of the electronic properties observed in thermal oxides are duplicated in the UV/ozone films. The observation of FN tunnelling strongly supports this conclusion. In fact a weak oscillation is also observed in the FN characteristic region (see Fig.4.10). This is only observed if the interface between the oxide and Si is abrupt (Maserjain, 1988) and emphasises that the grown layers are fully oxidised. It is especially important to note that breakdown fields averaging around 10MV/cm were observed which is comparable to good thermal oxides. All the samples were analysed without any forming gas anneals to satiate interface defects. Improved HFCV data may result by the reduction

of any "stretchout" of the HFCV characteristics due to these states. The density of positive oxide charges was in the high 10^{11}cm^{-2} to low 10^{12}cm^{-2} . To determine their nature temperature bias stress measurements were carried out in which high mobile positive charge density was observed. The most probable cause of this is contamination due to Na^+ or K^+ ions. The origins of this species are manifold*. Surface preparation prior to growth and the processing environment are the main factors which limit the quality of any oxide layer. In particular low temperature processes cannot supply the thermal energy required to desorb many surface impurities (Batey et al., 1989, recently reported that the effect of surface preparation on the performance of low temperature deposited oxides was critical). Chemical processing was carried out with only electronic grade reagents. Better chemicals and a cleaner environment are likely to have a beneficial effect.

* Prof. J. Robertson of Edinburgh University has also suggested that the high mobile ion density may have originated from the tungsten evaporation filament, which, on previous occasions, has been identified as a source of K^+ .

Chapter 5

Conclusions

In this final chapter the general conclusions and their implications are discussed particularly with respect to future avenues of research and applications. This chapter will also be used to speculate somewhat on further developments necessary to continue the present rapid rate of progress in the field of thin gate dielectrics. There are essentially two main parts to this thesis. These are the development of a new and possibly useful oxide growth technology and the application of SE and MASE in conjunction with other techniques to the analysis of thin oxides on Si.

In chapter 1 the requirements for future gate dielectrics were discussed. The decrease in gate oxide thickness means that both fabrication and characterisation become increasingly difficult. The nature of thin oxides was proposed to be somewhat different from thick fully relaxed layers. The high temperatures used in present conventional processing are believed to be incompatible with device scaling trends. Thus the success of this study can be partly gauged in the progress made in addressing these issues.

Initially studies of near UV oxidation proved that insufficient growth was induced to be technologically useful. However, it was found that deep UV was capable of inducing oxide growth at very low temperatures. From these studies the UV/ozone scheme of oxidation was proposed and investigated. It was demonstrated to be effective at temperatures less than 550°C. UV/ozone oxidation with the present arrangement (with a low

pressure Hg lamp) has several advantages. These are its simplicity, scalability (i.e. wafers of any size can be oxidised by just increasing the areas of the lamp grid and heater) and relatively low cost in comparison to high temperature systems which are more energy intensive. Additionally, for larger wafers the reduced thermal stresses due to lower temperature processing may be particularly beneficial. The final oxide thickness grown in 1 hour at 500°C in 1% ozone was equivalent to a thermal oxidation temperature of 775°C. In fact, the growth of very thin oxides (<5nm) was rapid but oxide growth at temperatures below 500°C appeared to be self-limiting (as in the case of native oxides). The thickest oxides grown were around 8nm. During the period of experiments the efficiency of the process was improved considerably, leading to faster growth rates and thicker oxides. This suggests that further growth rate increases should be possible by improving the experimental arrangement. However, to improve the growth rate it is important to understand the controlling mechanisms so that the process variables can be effectively manipulated.

The oxide growth mechanism was also studied and Cabrera-Mott (logarithmic) type kinetics identified. Growth was found to be a function of the substrate temperature, the UV output of the lamp and the ozone concentration in the ambient above the oxidising surface. A mechanistic description of the possible route to oxide formation was given in section 2.4. The same methods to test the mechanisms of growth can also be used to enhance growth rates. A simple extension of the trend of increasing the UV flux and ozone concentration (followed through the experimental period) would seem the best method of inducing faster reaction rates. The mechanism proposed points to the different effects of UV and ozone in the reaction. The Hg lamp acts as a combined source of both, however, it is feasible to use separate sources for UV and ozone. Commercial ozone generators are capable of producing higher concentrations which can be excited by a separate lamp. The lamp can be placed external to the chamber to avoid the overheating effects observed in the present

experimental arrangement. Additionally by using lamps of differing wavelength output it may be possible to determine the photoexcitation mechanism. It was perceived that photoexcitation of the Si surface played an important part especially once oxide thickness exceeded 3-4nm. However, the main UV emission line (254nm) of the lamp was strongly absorbed by the ozone (see Fig.2.3). Thus a UV source emitting radiation outside the strong ozone absorption band centred near 255nm which is still capable of exciting the Si surface (emitting electrons into the oxide) is likely to induce faster growth. Alternatively, if the mechanism is not surface driven and is dominated by the presence of atomic species in the ambient, growth should be restricted. Such an experiment would reveal more precisely the nature of the reaction. Hence a growth system of the type shown schematically in Fig.5.1 can be envisaged. The main difficulty lies in obtaining a UV emitting source which has the desired attributes. These are, the emission of photons over the desired wavelength range with a high energy density and a large area uniform flux. Very recently lamps with all these features have been reported in the literature by Eliasson et al. (1988, 1989). The principle of operation is to discharge gases such as those typically used in excimer lasers (for example KrF, XeCl and Xe) to produce an incoherent UV output. An important advantage of this type of lamp is that the output wavelengths can be varied by changing the gas. Indeed the excimer discharge lamps are more efficient and produce higher flux densities than low pressure Hg sources.

A better understanding of the growth kinetics is only possible by applying an in-situ oxide thickness measurement technique. This remains a very difficult task experimentally and theoretically because of the growth system and possible density variations in thin oxide layers. An in-situ spectroscopic ellipsometer with a very short measurement time would be vital for such a study (an instrument meeting these requirements is sold by SOPRA but at a typical cost of 100K pounds).

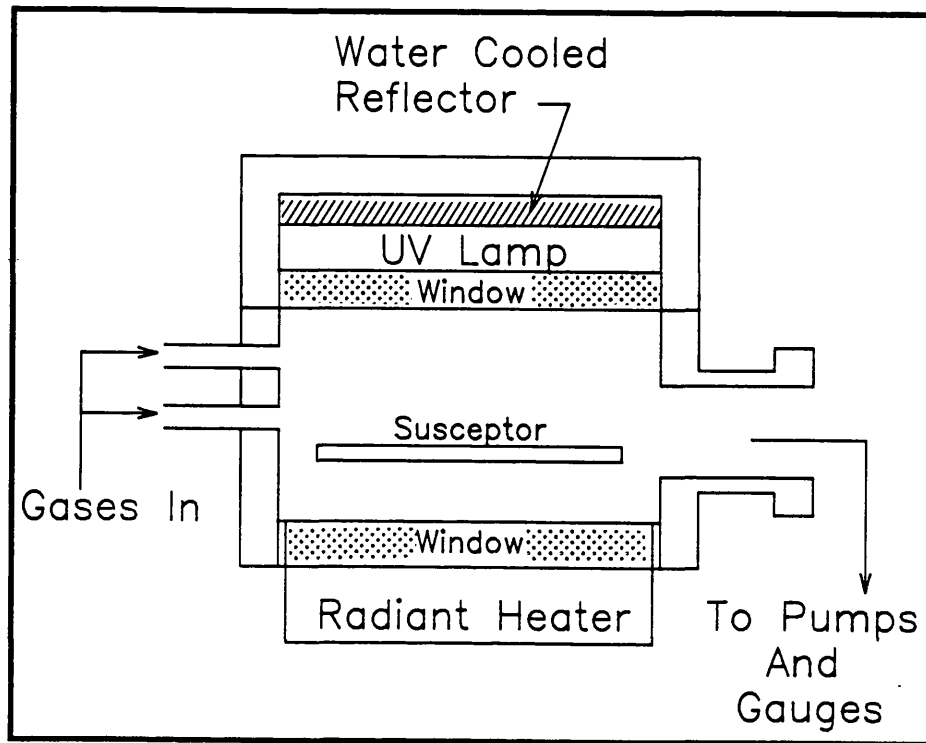


Fig.5.1 Schematic outline of improved growth system.

An alternative method of growth enhancement which was discussed in chapter 1 involved moving away from a pure oxygen chemistry. It was noted in section 1.3(vi) that UV laser excitation of O_2/NF_3 gas mixtures (Morita et al., 1986) resulted in rapid oxide growth at low temperature. This opens the possibility of using a UV lamp source to replace the laser with similar effect and thus overcome the limitation of the small area of material oxidised by the laser. A disadvantage of this method is the very corrosive nature of fluorine radicals and fluorine bearing species. Such species can attack the internal surfaces of the oxidation chamber (leading to contamination) and are known to etch SiO_2 . Thus they can also reduce the oxide and the suprasil window to the chamber.

The characteristics of the low temperature UV/ozone oxides were investigated by a number of commonly used techniques. Materials properties were analysed by SE, XPS and FTIR. All of these combined to demonstrate the close similarity between the low temperature UV/ozone grown layers and more conventional thermal oxides. It was established that

the density of these layers was higher than that of thermal oxides of similar thickness. The consequences of this on the long term electrical properties are unknown. It is interesting to note that interfacial compressive stress in any grown oxide (Fitch et al., 1989) and thus strain in the Si has several origins. These are the intrinsic bonding mismatch, the relaxation of the oxide during growth (by whatever mechanism) and the difference in thermal expansion coefficient between the Si and SiO₂. As the substrate cools from growth temperature the level of stress due to the latter is very much a function of the growth temperature. As the growth temperature falls this induced stress is reduced relatively. Quite clearly the use of UV/ozone growth may allow the impact of the different origins of stress on electrical properties to be analysed.

Electrical properties of the thin oxides were measured using IV and CV techniques and were again found to be similar to thermal layers. High breakdown field values (averaging around 10MV/cm) were observed and the lack of stretch out in the HFCV curves after temperature bias stressing indicated that the interface was stable (i.e. new interface states were not generated in significant numbers). It is very important to note that all electrical measurements were taken on devices without any forming gas anneal. Thus the stability of the interface and the high breakdown fields imply that good electrical properties can be achieved with UV/ozone oxides. It was also noted that a high mobile charge density existed in the oxide which was assigned to alkali metal contamination. The quality of the oxide appeared to be dominated by impurities. As noted in chapter 4 the poor processing chemicals and environment are largely responsible for this. The UV/ozone oxides appear unique in that they are in many ways so close in nature to thermal layers, especially when compared to the products of other low temperature processes.

SE and MASE have been used in a detailed study of grown oxide layers to demonstrate the existence of density variations. It was observed that for oxides of similar thickness growth at lower temperature resulted in a greater

degree of densification. The trend of increasing density was strongly related to decreasing thickness with layers of thickness $< 15\text{nm}$ exhibiting significant density increases. Rapid thermal oxidation was linear with growth time contrary to other studies (e.g. Ponpon et al. 1986). The differences were likely to be due to the reliance of most researchers on SWE which as demonstrated does not account for density variations. While a single layer model was used for data analysis the results do suggest that oxide density was graded. Further studies should address this issue. One method would be to measure the same sample as the oxide is progressively etched back.

MASE analysis opens up a wide avenue of future studies of the effects of annealing, the nature of the interface and density variations in very thin layers (down to 2.5nm). Trends in density are probably not simply explained by the viscoelastic relaxation process. By far the technologically most important aspect is the question of the relationship between the oxide materials properties and electrical performance. SE and MASE provide a non-destructive probe capable of delivering quantitative information. FTIR, particularly grazing angle FTIR (Brendel, 1990) is highly sensitive to chemical bonding in the oxide and interface region. A combined characterisation by MASE, FTIR and electrical techniques may be particularly fruitful.

The discussion above deals directly with derivative areas of further research. Here I would like to speculate and propose that if low temperature dielectric fabrication becomes vital for future generations of integrated circuits then a system combining the capabilities of inducing growth (UV/ozone) and deposition may be the most effective. At present there is much interest in oxynitrides (ON) and reoxidised nitroxides (ONO) because they are more resistant to hot electron and radiation damage. The fabrication of these inevitably requires very high temperatures. ONO structures could be produced by growing a thin oxide layer by UV/ozone followed by photo-deposition of oxide or oxynitride (this has already been demonstrated previously by Petitjean et al., 1990) and the application of the

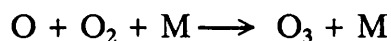
excimer discharge lamp to photodeposition is under investigation at University College London presently. Such a combination may be able to produce a low temperature dielectric rapidly with the interfacial properties of a grown layer. However, an oxidised layer retains the advantages of uniformity, simplicity of equipment and good stoichiometry over deposited films.

Finally, the quality of a thin oxides produced by any technique will be limited by the initial nature, both physical and chemical, of the Si surface prior to growth and its exposure to contaminants. It is thus all the more critical to prepare and control the initial Si surface and limit the period between preparation and growth. As discussed in chapter 1 high temperature furnace oxidation has advantages and disadvantages which have both fundamental and technological origins. If, the high thermal budget of furnace processing proves to be an important factor in the performance of devices then low temperature UV/ozone oxidation (which also has the capability to remove organic surface contaminants) may be a useful alternative. The electrical and physical properties of UV/ozone oxides were promisingly close to those of thermal layers and therefore do warrant further investigation.

Appendix A

Lifetime of Atomic Oxygen

A pseudo-first order estimate of the lifetime of atomic oxygen in molecular oxygen can be obtained if one considers the main reaction that leads to ozone formation (chapter 2 equation 3).



In this case the quantity M will be O₂. The reaction rate constant (k_o) for this process is 6.2x10⁻³⁴cm³molecule⁻¹s⁻¹ (Baulch et al., 1984). The average lifetime of an oxygen atom will thus be

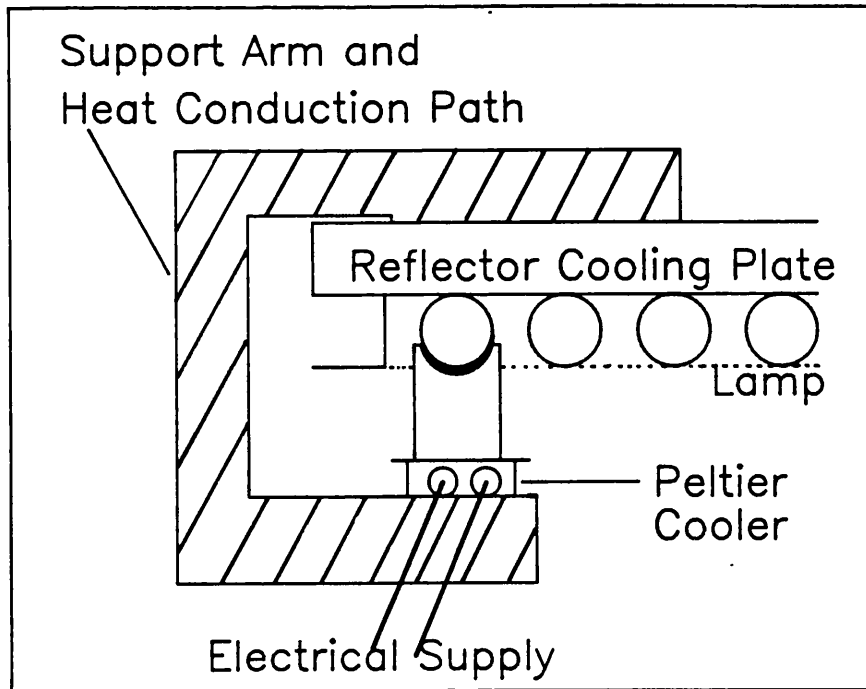
$$(k_o [\text{O}_2])^{-1} \text{ s.}$$

Hence the lifetime of an oxygen atom, given that the concentration of O₂ at atmospheric pressure is approximately 2.3x10¹⁹cm⁻³, is calculated to be 4.4x10⁻⁶s. Atomic oxygen is therefore a very short lived species in an atmosphere of oxygen.

Appendix B

Stabilisation of Lamp Emission

As was noted in chapter 2 the radiant flux from the lamp was severely affected by it becoming overheated. This had the effect of increasing the Hg vapour gas pressure and reducing current flow through the discharge. A simple method to limit the Hg gas pressure inside the lamp grid would be to just cool one point effectively, i.e. provide a sink for the vapour. Thus by controlling the proportion of Hg that is in the vapourised form one can control the internal pressure and avoid lamp destabilisation. In fact a device to carry this out was constructed but due to lack of time it was not possible to test it. Its basic structure is shown in the figure below.



A Peltier cooler is sandwiched between two conductive faces. As can be seen the upper part of the sandwich is in contact with the lamp while the lower part is a conduction path to remove heat to the reflector cooling plate. By adjusting the current flow in the Peltier device one can control the cooling rate and thus the lamp operation.

Appendix C

Bruggeman Effective Medium Approximation

Quite simply, if a material has several constituents of known optical behaviour then to obtain the optical functions of the mixed medium one can use effective medium theories. These have been discussed in detail by Aspnes et al. (1979). For the analyses of data in chapter 3 the Bruggeman approximation was used because of its self-consistent behaviour. The formulation is simple although its solution for more than two components is difficult. The expression is

$$\sum_{i=1}^n v_i \left(\frac{\epsilon_i - \epsilon}{\epsilon_i + 2\epsilon} \right) = 0$$

$$\sum_{i=1}^n \nu_i = 1$$

Where ν_i are the volume fractions and ϵ_i are the complex dielectric functions of each component i which is mixed into the material, n is the total number of constituents. The sum of ν_i must of course equal 1 for consistency. ϵ is the dielectric function of the mixed material. It is important to note here that this approximation is only applicable strictly for physical mixing and assumes that the wavelength of light is much larger than the dimensions of the mixed constituents. Chemically mixed layers i.e. with varying structure and bonding are not in general well described by this approximation.

Appendix D

Note Added in Proof To Corroborate Multi-Angle SE Results

In section 3.1.6 MASE analysis was carried out on a thin oxide. Post dating that a fuller analysis of data was carried out at the University of Nebraska. The results are summarised in the table below showing that although the final result appears largely unchanged the confidence limits and correlations were significantly reduced. The calculated results also did not exhibit any dependence upon the starting parameters for the larger data set. This is particularly important because the time required to achieve a good result is thus shortened. These results now open the door to the analysis of very thin oxides (<5nm) with high precision.

SE 1 angle and 113 wavelengths			MASE 3 angles and 113 wavelengths		
Thickness (Å)	Relative Density	Correlation	Thickness (Å)	Relative Density	Correlation
60.8 ± 1.4	1.20 ± .07	0.990	60.9 ± 0.7	1.20 ± .03	0.983
91.7 ± 1.8	1.12 ± .04	0.992	91.9 ± 0.8	1.13 ± .02	0.983

Appendix E

Electronic Data Relating to the Si/SiO₂ Interface

This data relates to Fig.4.1 taken from Lefevre and Schulz (1988) showing the ideal interface properties.

DATA RELATING TO THE IDEAL Si-SiO₂ SYSTEM

	Value	Unit	
<i>Silicon data</i>			
$E_g (T=0)$	1.1785	eV	
α (eqn. 8) (150<T<300 K)	-9.025×10^{-5}	eV K ⁻¹	
β (eqn. 8) (150K<T<300 K)	-3.07×10^{-7}	eV K ⁻²	
χ_s	4.23	eV	
ϵ_s/ϵ_0 (300 K, 750 MHz)	11.9	-	
N_c	$6.81 \times 10^{15} (T[K])^{3/2}$	cm ⁻³	
N_v (300 K)	2.23×10^{19}	cm ⁻³	
n_i (200 K<T<500 K)	$5.71 \times 10^{19} \left(\frac{T[K]}{300}\right)^{2.365} \times \exp\left(\frac{-6733}{T[K]}\right)$	cm ⁻³	
μ_n (300 K)	1350	cm ² V ⁻¹ s ⁻¹	
μ_p (300 K)	480	cm ² V ⁻¹ s ⁻¹	
<i>SiO₂ data</i>			
E_G	8.8	eV	
χ_{so}	3.23	eV	
χ_o	1.0	eV	
$\epsilon_{SiO_2}/\epsilon_0$	3.84	-	
μ_n	20 (bulk SiO ₂) ~2 (therm. SiO ₂) ~30 (therm. SiO ₂)	cm ² V ⁻¹ s ⁻¹ cm ² V ⁻¹ s ⁻¹ cm ² V ⁻¹ s ⁻¹	
<i>Gate electrode data</i>			
Work functions	ϕ_M	$(\phi_M - \chi_s)^a$	
Ag	4.97	0.76	eV
Al	4.13	-0.06	eV
Au	5.06	0.91	eV
Cr	4.18	0	eV
Cu	4.87	0.63	eV
Mg	3.19	-1.05	eV
Ni	4.6	0.4	eV
NiSi ₂	4.5	0.3	eV
Sn	3.42	-0.83	eV
poly-Si (Boron degenerate)	5.4	1.2	eV

Appendix F

References

Recent proceedings of relevant conferences and meetings.

Proc. A : "The Physics and Technology of SiO₂" ed. R. A. Devine, Les Arcs, Plenum Press (1988).

Proc. B : "SiO₂ and Its Interfaces" editors S. T. Pantelides and G. Lucovsky, Boston, Materials Research Society Symposium Proceedings 105, MRS (1988).

Proc. C : "The Physics and Chemistry of SiO₂ and the Si-SiO₂ Interface. editors C. R. Helms and B. E. Deal, Atlanta, Plenum Press (1988).

Proc. D : "Insulating Films on Semiconductors (INFOS'89)" editors F. Koch and A. Spitzer, Garching, North-Holland Press (1989).

Proc. E : "Rapid Thermal Annealing/Chemical Vapour Deposition and Integrated Processing" editors D. Hodul, J. C. Gelpey, M. L. Green and T. E. Seidel, San Diego, Materials Research Society Symposium Proceedings 146, MRS (1989).

Proc. F : "Semiconductor Cleaning Technology" editors J. Ruzyllo and R. E. Novak, Florida, 1st International Symposium on Cleaning Technology in Semiconductor Device Manufacturing, Electrochemical Society Proceedings 90-9 (1990).

Proc. G : "Semiconductor Silicon" editors H. R. Huff, K. G. Barraclough and J. Chikawa, Montreal, 6th International symposium of Silicon Materials Science and Technology, Electrochemical Society Proceedings 90-7 (1990).

ASPNES D. E., STUDNA A. A.: Phys. Rev. B 27, 985 (1983).

ASPNES D. E., THEETEN J. B.: J. Electrochem. Soc. 127, 1359 (1980): see also J. Vac. Sci. Technol. 16(5), 1374 (1979).

ASPNES D. E., THEETEN J. B., HOTTIER F.: Phys. Rev. B 20 No.8, 3292 (1979).

AZZAM R. M. A., BASHARA N. M: Ellipsometry and Polarised Light, North Holland, Amsterdam, 1977.

BAERI P., CAMPISANO U., FOTI G., RIMINI E.: J. Appl. Phys. 50(2), 788 (1979).

BARLOW K. J., KIERMASZ A., ECCLESTON W., MORUZZI J. L. : Appl. Phys. Lett. 53, 57 (1988).

BASU N., BHAT K.N.: Thin Solid Films 156, 243 (1988).

BAULCH D. L., COX R. A., HAMPSON JR. R. F., KERR J. A., TROE J., WATSON R. T.: J. Phys. Chem. Ref. Data 13 No.3, 1259 (1984).

BECK R. B., MAJKUSIAK B.: Phys. Stat Sol. (a) 116, 313 (1989).

BENCH W., BERGHOLZ W.: Semicond. Scie. Technol. 5, 421 (1990).

BOYD I.W.: Appl. Phys. Lett. 42(8), 728 (1983); Electronics Letters 24, 1062 (1988), "Deconvolution of infrared absorption".

BOYD I. W., MICHELI F.: Elec. Letters 23, 298 (1987).

BOYD I. W., WILSON J. I. B: J. Appl. Phys. 53, 4166 (1982); J. Appl. Phys. 62, 3195 (1987); Appl. Phys. Lett. 50, 320 (1987).

BRENDEL R.,: Appl. Phys. A50, 587 (1990).

BU-ABBUD G. H., BASHARA N. M.: Applied Optics 20 No.17, 3020 (1981).

BU-ABBUD G. H., BASHARA N. M. , WOOLLAM J. A.: Thin Solid Films 138, 27 (1986).

CABRERA N., MOTT N. F.: Rept. Progress Phys. 12, 163 (1948).

CALVERT J. C., PITTS Jr. J. N.: Photochemistry, J. Wiley and Sons Inc. (1966).

CARIM A. H., SINCLAIR R.: J. Electrochem. Soc. 134, 741 (1987).

CHAO S. C., PITCHAI R., LEE Y. H.: J. Electrochem. Soc. 136 No.9, 2751 (1989).

CHEN L., LIBERMAN V., O'NEILL J. A., WU Z., OSGOOD JR. J. M.: J. Vac. Sci. Tech. A6(3), 1426 (1988).

COLLINS R. W.: Rev. Scie. Instrum. 61(8), 2029 (1990).

COLLOT P., GAUTHERIN G., AGIUS B., RIGO S., ROCHET F. : Philos. Mag. B. 52, 1051 (1985).

DEAL B. E., GROVE A. S.: J. Appl. Phys. 36, 3770 (1965).

DEAL B. E.: IEEE Trans. Elec. Dev. ED-27, 606 (1980).

DEVINE R. A. B.: J. Vac. Scie. Technol. A6(6), 3154 (1988).

DILAC J. M.: Proc. E, 333 (1989).

DRESSENDORFER P. V., BARKER R. C.: Appl. Phys. Lett. 36, 933 (1980).

EASTMAN D. E., GROBMAN W.D., : Phys. Rev. Letts. 28 No.21, 1378 (1972).

ELIASSON B., KOGELSCHATZ U., STEIN H. J.: European Photochemistry Association Newsletter 32, 29 (1988).

ELIASSON B., KOGELSCHATZ U.: Appl. Phys. B46, 299 (1988): Proc. 2nd Int. Conf. on UV+Ozone in the treatment of water and other liquids, Berlin April 1989.

FEHLNER F. P.: J. Electrochem. Soc. 119, 1723 (1972); ibidem. 131, 1646 (1984).

FEHLNER F. P.: "Low Temperature Oxidation, The Role of Vitreous Oxides", J. Wiley and Sons (1986).

FEIGL F. J.: VLSI Electronics Volume 6, chapter 3, 147 (1983).

FIORI C.: Phys. Rev. Lett. 52, 2077 (1984).

FIORI C., DEVINE R. A. B.: Phys. Rev. B. 33, 2972 (1986).

FITCH J. T., LUCOVSKY G., KOBEDA E., IRENE E. A.: J. Vac. Sci. Technol. B7, 153 (1989); ibidem. B7(4), 775 (1989).

FITCH J. T., BJORKMAN C. H., LUCOVSKY G., POLLAK F.H., YIN X. :J. Vac. Sci. Technol. B 7, 775 (1989).

FOGARASSY E., UNAMUNO S., REGOLINI J. L., FUCHS F.: Phil. Mag. B55 No.2, 253 (1987) and in Proc. A, (1988).

FUKADA H., UCHIYAMA A., HAYASHI T., IWABUCHI T., OHNO S.: Japanese J. of Appl. Phys. 29 No.1, L137 (1990).

FUOSS P. H., NORTON L. J., BRENNAN S., FISCHER-COLBRIE A.: Phys. Rev. Lett. 60, 600 (1988).

GALEENER F. L., LUCOVSKY G.: Phys. Rev. Letts. 37 No.2, 1474 (1976).

GELPEY J., STUMP P., CAPODILUPO R.: Proc. Materials Research Society Symposium on RTP 52, 321 (1986).

GHEZ R. J.: J. Chem. Phys. 58, 1838 (1973).

GOSHO Y., SAKEI M.: Japanese J. Appl. Phys. 28 No.10, 1939 (1989).

GROSSE P., HARBECKE B., HEINZ B., MEYER R., OFFENBERG M.: Appl. Phys. A39, 257 (1986).

GRUNTHANER F. J., GRUNTHANER P. J.: Material Sci. Reports. 1,69 (1986).

HAHN P. O., GRUNDNER M., SCHNEGG A., JACOB H.: Proc. C, 401 (1988); also Appl. Surf. Sci. 39, 436 (1989).

HALBITTER J.: J. Mater. Res. 3, 506 (1988).

HAN C. J., HELMS C. R.: J. Electrochem. Soc. 135 No.7, 1824 (1988); also ibidem. 134, 1297 (1987) and 132, 516 (1985).

HASHIMOTO C., MURAMOTO S., SHIONO N., NAKAJIMA.: J. Electrochem. Soc. 127, 129 (1980).

HATTORI T., IGARASHI T., OHI M., YAMAGISHI H.: Japan. J. Appl. Phys. 28, L1436 (1989).

HATTORI T., TAKASE K., YAMAGISHI H., SUGINO R., NARA Y., ITO T.: Japan. Journal. Appl. Phys. 28, 296 (1989).

HECHT M. H., ORIENT O. J., CHUTJIAN A., VASQUEZ R. P.: Appl. Phys. Lett. 54, 421 (1989).

HEYNS M., HASENACK C., DE KEERSMAECKER R., FALSTER R.: Proc. F, 293 (1990).

HICKS J. M., URBACH L. E., PLUMMER E. W., DIA H-L.: Phys. Rev. Letts. 61 No.22, 2588 (1988).

HIRAMOTO K., SANO M., SADAMITSU S., FUJINO N.: Japanese J. of Appl. Phys. 28 No.12, L2109 (1989).

HO V. Q., SUGANO T.: Thin Solid Films 95, 315 (1982).

HODGE A., PICKERING C., PIDDUCK A., HARDEMAN R.: Proc. MRS Symp. on RTP 52, 313 (1986).

HOFF A. M., RUZYLLO J.: Appl. Phys. Letts. 52 (15), 1264 (1988)

HOFF A. M.: Thesis entitled "An investigation of the thermal oxidation of silicon in afterglow gas mixtures", Pennsylvania State University (1988).

HU S. M.: J. Appl. Phys. 45, 1567 (1974); Appl. Phys. Lett. 42, 872 (1983); J. Appl. Phys. 55, 4095 (1984).

IMAI K., YAMABE K.: Appl. Phys. Letts. 56 (3), 280 (1990).

IRENE,E.A., GHEZ,R.: Appl. Surf. Sci. 30, 1 (1987).

IRENE E. A., GHEZ R.: J. Electrochem. Soc. 124, 1757 (1977).

IRENE E. A., LEWIS E. A.: Appl. Phys. Lett. 51, 767 (1987).

IRENE E. A.: CRC Critical Reviews in Solid State and Materials Science

ISHIKAWA Y., TAKAGI Y., NAKAMICHI I.: Japanese J. of Appl. Phys. 28 No.8, L1453 (1989).

KALNITSKY A., TAY S. P., ELLUL J. P., CHONGSAWANGVIROD S., ANDREWS J. W., IRENE E. A.: J. Electrochem. Soc. 137 No.1, 234 (1990).

KIM U. S., WOLOWODIUK C. H., JACCODINE R. J., STEVIE F., KAHORA P.: J. Electrochem. Soc. 137 No.7, 2291 (1990).

KIMURA S., MURAKAMI E., WARABISAKO T., SUNAMI H.: J. Electrochem. Soc. 135, 2009 (1988).

KIMURA S., MURAKAMI E., MIYAKE K., WARABISAKO T., SUNAMI H., TOKUYOMA T.: J. Electrochem. Soc. 132, 1460 (1985).

KIRK C. T.: Phys. Rev. B 38 No.2, 1255 (1988).

KRUSOR B. S., BIEGELSEN D. K., YINGLING R. D., ABELSON J. R.: J. Vac. Soc. Technol. B7(1), 129 (1989).

LANDSBERGER L. M., TILLER W. A.: Appl. Phys. Lett. 51, 1416 (1987).

LEFEVRE H., SCHULZ M.: The Si-SiO₂ System ed. P. Balk, Elsevier, chapter 6, 273 (1988).

LING Z-M., DUPAS L. H., DE MEYER K. : J. Electrochem. Soc. 136 No.10, 3047 (1989).

LO G. Q., TING W. C., SHIH D. K., KWONG D. L.: Appl. Phys. Letts. 56(3), 250 (1990).

LUCOVSKY G., MANITINI M., SRIVASTAVA J. K., IRENE E. A.: J. Vac. Sci. & Technol. B5, 539 (1987).

MADIX R. J., SUSU A. A.: Surface Science 20, 377 (1970).

MALITSON I. H.: J. Optical Soc. Am. 55, 1205 (1965).

MARQUARDT D. L.: J. Soc. Ind. Appl. Math. 2, 431 (1963).

MASERJAIN J.: Proc. C, 497 (1988).

MASSOUD H.Z., PLUMMER J.D.: J. Appl. Phys. 62, 3416 (1987).

McGRUER N. E., SINGH R., WEISS J. A., RAJKANAN K.: J. Appl. Phys. 62, 3405 (1987).

McMARR P. J., VEDAM K., NARAYAN J.: J. Appl. Phys. 59(3), 694 (1986).

MICHELI F., BOYD I.W., Appl. Phys. Lett. 51, 1149 (1987); Appl. Phys. A 47, 249 (1988).

MIKI N., KIKUYAMA H., KAWANABE I., MIYASHITA M., OHMI T.,
IEEE Trans. on Elec. Dev. 37 No.1, 107 (1990).

MORITA M., KUBO T., ISHIHARA T., HIROSE M.: Appl. Phys. Letts.
45, 1312 (1984); also ibidem. 47(3), 253 (1985).

MORITA M., ARITOME S., TANAKA T., HIROSE M. : Appl. Phys.
Lett. 49, 699 (1986).

MOSLEHI M.: Appl. Phys. A 46, 255 (1988).

MOTT N. F., RIGO S., ROCHET F., STONEHAM A. M.: Phil. Mag. B
60, 189 (1989).

NAITO M., HOMMA H., MOMMA N.: Solid-State Electronics 29, 885
(1986).

NAMIKI A., TANIMOTO K., ZAMIA S., NAKAMURA N., SUZAKI T.:
Surface Science 193, 321 (1988), ibidem 222, 530 (1989).

NAKAMURA M., MOCHIZUKI Y., USAMI K., ITOH Y., NOZAKI T.:
Solid State Communications 50 No.12, 1079 (1984).

NAKAZAWA M., KAWASE S., SEKIYAMA H.: J. Appl. Phys. 65, 4014
(1989).

NAKAZAWA M., NISHIOKA Y., SEKIYAMA H., KAWASE S.: J. Appl.
Phys. 65, 4019 (1989).

NICOLLIAN E. H., BREWS J. R.: 'MOS (Metal Oxide Semiconductor)
Physics and Technology', J. Wiley & Sons, New York, 1982.

NICOLLIAN E. H., REISMAN A.: J. Electron. Materials 17, 263 (1988).

NULMAN J.: in NATO ASI Series 207, "Reduced Thermal Processing for
ULSI", editor R.A. Levy, 1989 Plenum Press New York.

OCAL C., FERRER S., GARCIA N.: Surf. Sci. 163, 335 (1985).

OELLIG E. M., MICHEL E. G., ASENSIO M. C., MIRANDA R.: Appl.
Phys. Lett. 50, 1660 (1987).

OKABE H.: 'Photochemistry of Small Molecules', John Wiley & Sons, New
York, 1978.

OLSEN J. E., SHIMURA F. S.: Appl. Phys. Lett. 53, 1934 (1988); J. Vac.
Sci. Technol. A 7, 3275 (1989).

ONG C. K., SIN E. H., TAN H. S.: J. Opt. Soc. Am. 3 No.5, 812 (1986).

OREN R., GHANDHI S.: J. Appl. Phys. 42, 752 (1971).

ORLOWSKI T. E., RICHTER H.: Appl. Phys. Lett. 45, 241 (1984).

ORLOWSKI T. E., MANTELL D. A.: J. Appl. Phys. 64(9), 4410 (1988).

OHSAWA A., HONDA K., TAKIZAWA R., NAKANISHI T., AOKI M., TOYOKURA N.: Proc. G, 601 (1990).

OURMAZD A., TAYLOR D. W., RENTSCHLER J. A.: Phys. Rev. Lett. 59, 213 (1987).

PEPPER M.: In proceedings of INFOS83 editors J. F. Verweij and D. R. Wolters, North-Holland Press, 32 (1983).

PETTITJEAN, M., PROUST, N., CHAPEAUBLANC, J-F., ALNOT, P., PERRIN, J., ALLAIN, B., Proc. EMRS Meeting Spring 1990, Symposium E, Strasbourg.

PHILIPPOSIAN A., JACKSON D., KAMIENIECKI E., RESNICK A.: Proc. F 357 (1989).

PICKERING C., HODGE A. M., DAW A. C., ROBBINS., PEARSON P. J., GREEF R.: Mat. Res. Soc. Symp., Boston, Vol.53, 317 (1986).

PICKERING C., SHARMA S., MORPETH A. G., KEEN J., HODGE A. M.: Proc. 4th International Symposium on SOI Technology and Devices, ed. D. N. Schmidt, V90-6, 175 (1990).

PICKERING C., SHAND B. A., SMITH G. W.: J. Electronic Materials 19, 51 (1990).

PIDDUCK A. J., NAYAR V.: Unpublished (1990). An apparatus similar to that described by T. Smith, J. Appl. Phys. 46 (4), 1553 (1975), was used to observe the real time emission of photoelectrons into air where they were collected. The photon source was similar to the Hg lamp used in the UV/ozone oxidation study. Silicon wafers with differing surface oxide thicknesses were tested. The emission current was found to be both time and oxide thickness dependent. As oxide thickness increased the emitted current decreased however significant current levels were observed even for oxides above 10nm. It is important to note that only electrons emitted into the air were observed. These electrons may however be few compared to the total number of electrons actually emitted into the oxide i.e. a relatively limited number of electrons have sufficient energy to be excited out of the surface. This observation appears to support the mechanism of oxide growth suggested in chapter 2.4.3.

PONPON J., GROB J., GROB A., STUCK, R.: J. Appl. Phys. 59, 3921 (1986).

QUENON P., WAUTELET M., DUMONT M.: J. Appl. Phys. 61, 3112 (1987).

RAFFERTY C. S., LANDSBERGER L. M., DUTTON R. W., TILLER W. A.: Appl. Phys. Letts. 54(2), 151 (1989); ibidem. 54(16), 1516 (1989).

RAVINDRA N. M., NARAYAN J., FATHY D., SRIVASTAVA J. K.,

- IRENE E. A.: J. Mater. Res. 2, 216 (1987).
- RAVINDRA N. M., RUSSO O. L., FATHY D., NARAYAN J., HEYD A. R., VEDAM K.: Proc. B, 169 (1988).
- RECHTIEN J. H., IMKE U., SNOWDON K. J., REIJNEN P. H. F., VAN DEN HOEK P. J., KLEYN A. W., NAMIKI A.: Surf. Sci. 227, 35 (1990).
- REISMAN A., NICOLLIAN E.H., WILLIAMS C.K., MERZ C.J.: J. Electron. Materials 16 No.1, 45 (1987).
- REISMAN A., EDWARDS S. T., SMITH P. L.: J. Electrochem. Soc. 135, 2848 (1988).
- REISMAN A., TEMPLE D., SMITH P. L.: J. Electrochem. Soc. 137, 284 (1990).
- ROCHET F., FROMENT M., D'ANTERROCHES C., ROULET H., DUFOUR.G.: Philos. Mag. B. 59, 339 (1989).
- ROCHET F., RIGO S., FROMENT M., D'ANTERROCHES C., MAILLOT C., ROULET, H., DUFOUR G. : Adv. Phys. 35, 237 (1986).
- ROWE J. E., IBACH H.: Phys. Rev. Letts. 32 No.8, 421 (1974).
- RUBLOFF G. W., HOFMANN K., LIEHR M., YOUNG D. R.: Phys. Rev. Letts. 58, 2379 (1987).
- RUZYLLO J., DURANKO G. T., HOFF A. M.: J. Electrochem. Soc. 134, 2052 (1987).
- SAI-HALASZ G. A., WORDEMAN M. R., KERN D. P., GANIN E., RISHTON S., ZICHERMAN D. S., SCHMID H., POLCARI M. R., NG H. Y., RESTLE P. J., CHANG T. H. P. DENNARD R. H.: IEEE Elec. Dev. Letts. 8 No.10, 463 (1987).
- SCHAFFER S. A., LYON S. A.: J. Vac. Sci. Technol. 19, 494 (1981); ibidem 21, 422 (1982); Appl. Phys. Lett. 47, 154 (1985).
- SHIRAI H., KANAYA K., YAMAGUCHI A., SHIMURA F.: J. Appl. Phys. 66, 5651 (1989).
- SINGH R. : J. Appl. Phys. 63, R59 (1988).
- SINGH R., McGRUER N. E., RAJAKANAN K., WEISS J. A.: J. Vac. Sci. Technol. A 6, 1480 (1988).
- SLAOUI A., PONPON J. P., SIFFERT P.: Appl. phys. A 43, 301 (1987).
- SNYDER P.G., ROST M. C., BU-ABBUD G. H., WOOLLAM J. A., ALTEROVITZ S. A.: J. Appl. Phys. 60(9), 3293 (1986).
- SRIVASTAVA J. K., PRASAD M., WAGNER J. B.: J. Electrochem. Soc. 132, 955 (1985); ibidem. 131, 1960 (1984).

STARNBERG H. I., SOUKIASSIAN P., BAKSHI M. H., HURYCH Z.:
Surface Science 224, 13 (1989).

STEINFELD J. I., ADLER-GOLDEN S. M., GALLAGHER J. W.: J.
Phys. Chem. Ref Data 16 No.4, 911 (1987).

STONEHAM A. M., TASKER P. W.: Phil. Mag. B 55, 237 (1987):
Semicond. Sci. Technol. 1 No.1, 93 (1986).

SZE, S.M. : 'Physics of Semiconductor Devices', John Wiley & Sons, New
York, (1981).

TABE M.: Appl. Phys. Letts. 45, 1073 (1984).

TAFT E.A.: J. Electrochem. Soc. 131, 2460 (1984).

TAKAKURA M., SUNADA T., MIYAZAKI S., HIROSE M.: Japan. J.
Appl. Phys. 28 No.12, L2324 (1989).

TAY S. P., ELLUL J. P., WHITE J. J., KING M. I. H.: J. Electrochem.
Soc. 134 No.6, 1484 (1987).

TAYLOR S., ECCLESTON W., BARLOW K. J.: J. Appl. Phys. 64, 6515
(1988)

TODOROV S. S., SCHILLINGER S. L., FOSSUM E. R.: IEEE Electron
Device Letts. 7 No.8, 468 (1986).

TODOROV S. S., FOSSUM E. R.: Appl. Phys. Lett. 52, 48 (1988).

UCHIDA Y., YUE J-H., KAMASE F., SUZUKI T., HATTORI T.,
MATSUMURA M.: Japanese J. of Appl. Phys. 25 No.11, 1633 (1986).

DE UNAMUNO S., FOGARASSY E.: Appl. Surf. Sci. 36, 1 (1989).

VANDENABEELE P., MAEX K., DE KEERSMAECKER R.:
Preceedings E 143 (1989).

VANHELLMONT J., MAES H. E., DE VEIRMAN A.: J. Appl. Phys. 65
No.11, 4454 (1989).

VIG J. R.: J. Vac. Sci. Technol. A3(3), 1027 (1985).

VINCKIER C., COECKELBERGHS P., STEVENS G., HEYNS M., DE
JAEGERE S. : J. Appl. Phys. 62, 1450 (1987).

VINCKIER C., COECKELBERGHS P., STEVENS G., DE JAEGERE S.:
Appl. Surf. Sci. 30, 40 (1987).

VINCKIER C., DE JAEGERE S.: J. Electrochem. Soc. 137 No.2, 628
(1990).

WAGNER L. F., SPICER W. E., : Phys. Rev. Letts. 28 No.21, 1381
(1972), Phys. Rev. B 9 No.4, 1512 (1974).

WAUTELET M., QUENON P., JANDIN A.: *Semicond. Sci. Technol.* 3 No.1, 54 (1988).

WEI L., YUAN-SEN X., YANG-SHU Z.: *Proc. C* 103 (1988).

WOLTERS D.R.: *Proc. A*, (1988).

WOLTERS D. R., ZEGERS-van DUYNHOVEN A. T. A.: *Phil. Mag. B* 55, 669 (1987); *J. Appl. Phys.* 65, 5126 (1989); *ibidem* 65, 5134 (1989).

WONG H., CHENG Y. C.: *J. Appl. Phys.* 64, 893 (1988).

YOUNG E. M., TILLER W. A.: *Appl. Phys. Lett.* 42, 63 (1983); *ibidem* 50, 80 (1987); *ibidem* 50, 46 (1987); *J. Appl. Phys.* 62, 2086 (1987).

YU C. F., SCHMIDT M. T., PODELESNIK D. V., OSGOOD R. M.: *J. Vac. Sci. Technol.* 5, 1087 (1987).

YU C. F., SCHMIDT M. T., PODELESNIK D. V., YANG E. S., OSGOOD R. M.: *J. Vac. Sci. Technol.* 6, 754 (1988).

ZAZZERA L. A., MOULDER J. F.: *J. Electrochem. Soc.* 136 No.2, 484 (1989).

ZHANG J. F., WATKINSON P., TAYLOR S., ECCLESTON W.: *Proc. D*, 374 (1989).

Appendix G

Publications

"Laser repair of faulty packaged VLSI chips", *Electronics Letters* 24 No.24, 1474 (1988), I. W. Boyd, A. J. Nolan, V. Nayar, F. Micheli, A. Overbury and A. Davidson.

"Low temperature oxidation of crystalline silicon using excimer laser radiation", *Applied Surface Science* 36, 134 (1989), V. Nayar, I. W. Boyd, F. N. Goodall and G. Arthur.

"Near ultraviolet (260-370nm) enhancement of silicon oxidation", *Chemtronics* 4, 101 (1989), V. Nayar and I. W. Boyd.

"Atmospheric pressure low temperature (<500°C) UV/ozone oxidation of silicon", *Electronics Letters* 26 No.3, 205 (1990), V. Nayar, P. Patel and I. W. Boyd.

"Determination of properties of thin thermal SiO₂ on silicon by spectroscopic ellipsometry", *Thin Solid Films* 195, 185-192 (1991), V. Nayar, C. Pickering and A. M. Hodge.